Vietnam Ministry of Science and Technology

P-ISSN 2525-2461 • E-ISSN 2615-9937

Vietnam Journal of Science, Technology and Engineering

SEPTEMBER 2023 • VOLUME 65 NUMBER 3

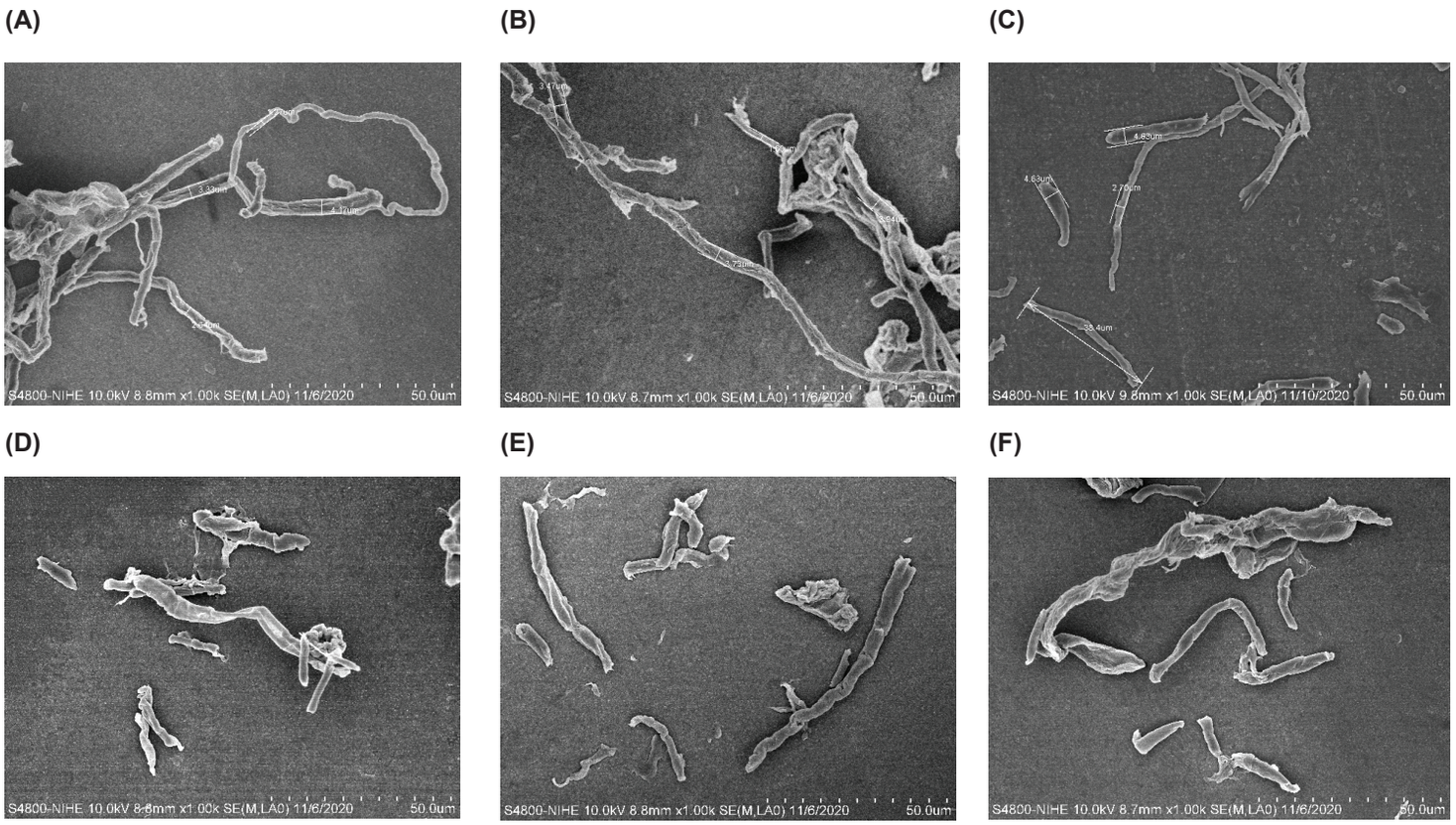

Study on synthesis of carboxymethyl cellulose from pineapple leaf waste and its potential applications as a thickener

VIETNAM JOURNAL OF SCIENCE, TECHNOLOGY AND ENGINEERING * SEPTEMBER 2023 * VOLUME 65 NUMBER 3

vietnamscience.vn or vietnamscience.vjst.vn

Vietnam Journal of Science, Technology and Engineering (VJSTE) **is a quarterly double-blind peer-reviewed academic journal. VJSTE publishes research articles and review articles in all areas of science, technology and engineering with the focus on the physical sciences, life sciences and environmental sciences including the following topics:**

- **Physical Sciences**
- **Agriculture**
- **Medicine**
- **Pharmacology**
- **Biology**
- **Biotechnology**
- **Biomedical Applications**
- **Ecology**
- **Climatology**
- **Environmental Science.**

CLASSIFICATION SCHEME

1. **Mathematics and Computer Science**
   - **1.1. Mathematics**
   - **1.2. Computer Science**
   - **1.3. Computational Science**
2. **Physical Sciences**
   - **2.1. Physics**
   - **2.2. Chemistry**
   - **2.3. Engineering**
3. **Life Sciences**
   - **3.1. Agriculture**
   - **3.2. Medicine**
   - **3.3. Pharmacology**
   - **3.4. Biology**
   - **3.5. Biotechnology**
   - **3.6. Biomedical Applications**
4. **Earth Sciences**
   - **4.1. Geography**
   - **4.2. Geology**
   - **4.3. Geophysics**
   - **4.4. Oceanography**
5. **Environmental Sciences**
   - **5.1. Ecology**
   - **5.2. Climatology**
   - **5.3. Environmental Science**

CONTENTS

SEPTEMBER 2023 • VOLUME 65 NUMBER 3

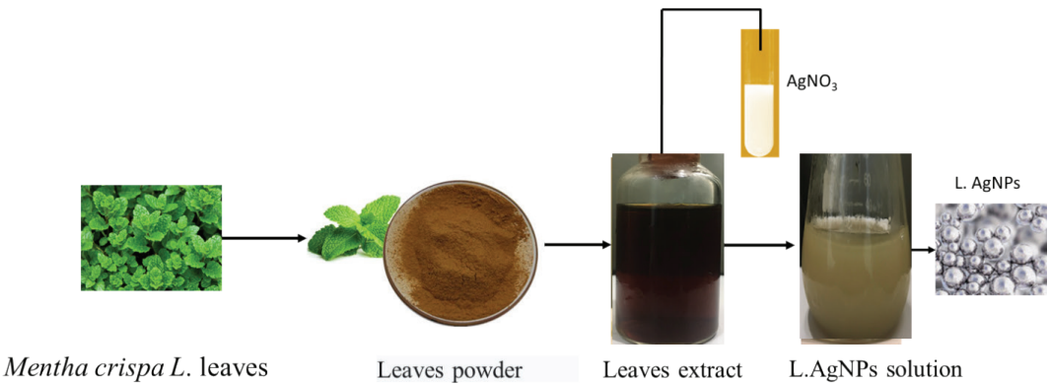

CONTENTS

SEPTEMBER 2023 • VOLUME 65 NUMBER 3

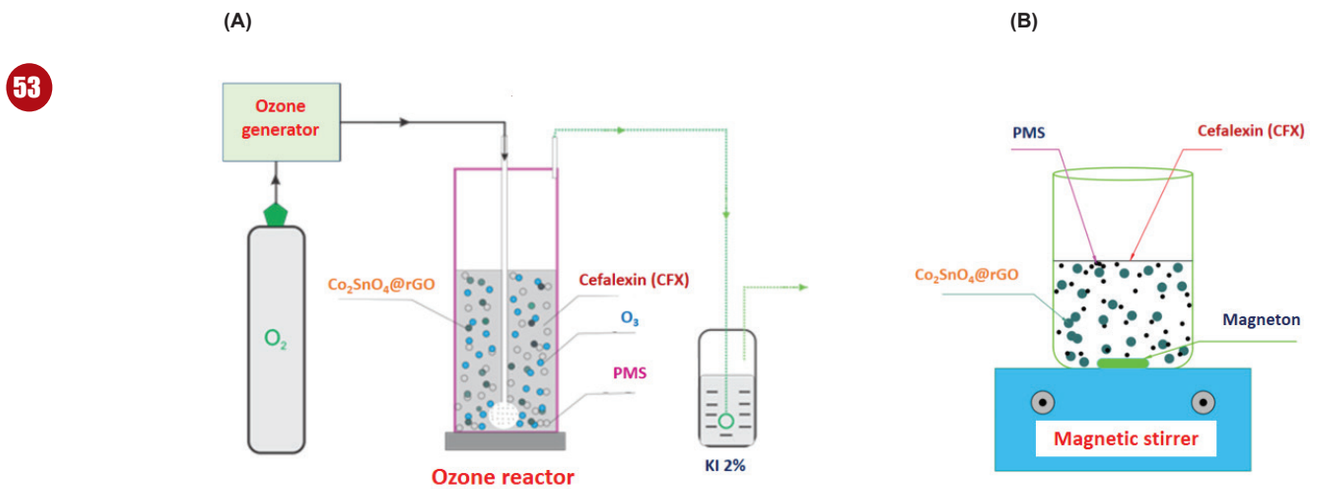

LIFE SCIENCES

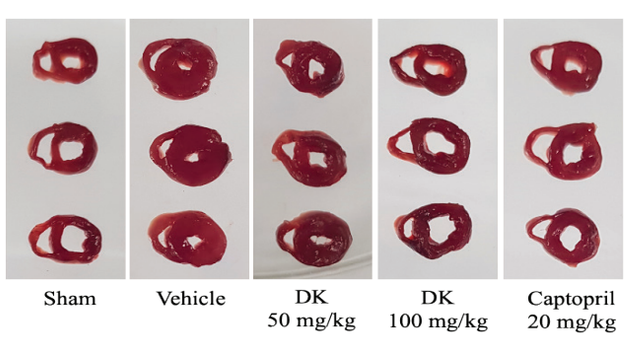

Integration of an RSA-2048-bit public key cryptography solution in the development of secure voice recognition processing applications

Nhu-Quynh Luc*, Duc-Huy Quach, Chi-Hung Vu, Hong-Truong Nguyen, Thanh-Long Vo-Khac

Academy of Cryptography Techniques, 141 Chien Thang Street, Tan Trieu Ward, Thanh Tri District, Hanoi, Vietnam

Received 20 October 2022; revised 20 December 2022; accepted 28 December 2022

Abstract:

The authors initially employs the fast Fourier transform (FFT) approach to transforming voice inputs into digital signals before integrating a speech recognition solution (which includes two models: the hidden Markov model (HMM) and the artificial neural network (ANN)). To achieve standard-tone identification of voice signals and digitally store speech, the authors then incorporated a 2048-bit Rivest-Shamir-Adleman (RSA) encryption method to encrypt and decrypt digital speech. The authors' building team constructed the program using a 256-bit advanced encryption standard - Galois counter mode (AES-GCM) encryption method to assure the application's effectiveness. The authors successfully created a voice recognition application according to the HMM of ANN. The collected findings suggest that the authors' secure speech recognition program (named soft voice - RSA) has improved in terms of safety, keeping speech material secret, and speed. It takes roughly 0.2 s to generate a 2048-bit RSA key pair that exceeds the National Institute of Standards and Technology (NIST) standard, 700-1070 ms to process speech, 1-4 ms to encrypt 2048-bit RSA, 6-8 ms to decrypt 2048-bit RSA.

Keywords: **artificial neural network, fast Fourier transform, hidden Markov model, Rivest-Shamir-Adleman.**

Classification number: **1.2**

1. Introduction

Speech recognition research and applications are now being investigated extensively, with practical applications in people's everyday lives. However, little research has been conducted on incorporating security measures to safeguard speech in voice recognition processing. The issue of speech recognition is a new development trend of the times, and numerous research papers on this subject have been developed and implemented in practice [1, 2]. Nevertheless, no security strategy has been put in place, putting speech recognition system users in danger of a number of things. The authors developed an application based on Markov's hidden model [3, 4], ANN [5-7], and the RSA cryptosystem [8] to handle the problem. The HMM will be integrated with ANN to handle the real-time speech recognition difficulty. To guarantee security, the RSA cryptosystem utilised for security must fulfill current NIST security criteria [9].

The authors include a 2048-bit RSA encryption technique in this research to preserve the user's voice data (voice utilises an HMM to identify speech-to-text data). The test team passed the NIST key evaluation criteria for the encryption key for the 2048-bit RSA cryptosystem. Following PKCS#1 (Public-Key Cryptography Standards-Version 2.1), an author-integrated 2048-bit RSA encryption and decryption solution assures security with today's real deployed applications. The specifics of cryptographic modules and the findings gained in this investigation are explained by the authors in the following parts of the publication.

2. Subject and methodology

2.1. Solution for converting and processing voice via FFT

Several voice processing algorithms have been used in practical applications [10, 11], most notably the audio-visual toolbox [12], the group delay [13], and the FFT. The FFT technique evolved from the discrete Fourier transform (DFT) approach, which overcomes the drawback that processing speech with a high sample length N takes a long time, and the complexity of the FFT is lowered to just N/2 log 2N. Although FFT has worse output information dependability than DFT in analogue-to-digital conversion, it is substantially faster, assuring real-time.

The authors selected FFT as the key approach in this research for converting speech to digital form and vice versa. The outputs of this FFT technique are essentially spectrum tables of the phonemes, which may be recognised on the computer using a hidden Markov-based machine learning model and an ANN [7]. ANN will investigate the possibility of any phoneme happening after another in this scenario, precisely identifying the phonemes reviewed by

*Corresponding author: Email: quynhln@actvn.edu.vn; lucnhuquynh69@gmail.com

HMM, and will then review and analyse whether the final output is accurate or not, based on a dictionary consisting of words and phrase meanings. Continue this approach until the output is quick and accurate.

2.2. Security solution for speech recognition applications

Following the conversion of voice to digital, the next phase in the study is to identify an encryption solution for digital data to assure the security of the received data against existing assaults. The authors have used the 2048-bit RSA public key cryptosystem in this work to conduct encryption and decryption for voice signal protection after converting it to digital form [14]. Furthermore, to test the speech recognition software module, the authors used an AES-256 cipher system to safeguard the voice in digital form for comparison. It follows that the efficiency in the speed of security implementation for speech communications is improved. The authors have analysed key parameter generation for the RSA cryptosystem to ensure that it meets NIST key quality testing criteria. The RSA cryptosystem is included in a software module that conforms to the PKCS#1 [15] standard and is certified to be safe against existing threats.

According to NIST standards, the RSA cryptosystem is considered safe with a length of nLen=1661 by 2022. At the time, the 2048-bit RSA cryptosystem was still guaranteed to be safe. The authors evaluate generating key parameters for use in the program for the AES 256 cryptosystem to surpass current NIST criteria. This demonstrates that the authors' method, which employs a 2048-bit RSA cryptosystem (or AES 256-bit), is sufficient to safeguard the speech signal against various assaults.

3. Results

3.1. Design and implement a secure voice recognition application

In this research, the secure voice recognition module (Soft voice-RSA) built by the authors incorporates the following modules: 2048-bit RSA key generation (according to PKCS#1 v2.1 standard) and has been tested to pass through NIST standards; the module converts speech into text and vice versa using the FFT method that applies HMM and ANN models; text-to-speech encryption module with RSA 2048 cryptography and software-generated public key; 2048-bit RSA decryption module with software generated RSA private key. Fig. 1 depicts the operational concept of 2048-bit RSA key generation, voice conversion, and protection utilising a 2048-bit RSA cryptosystem.

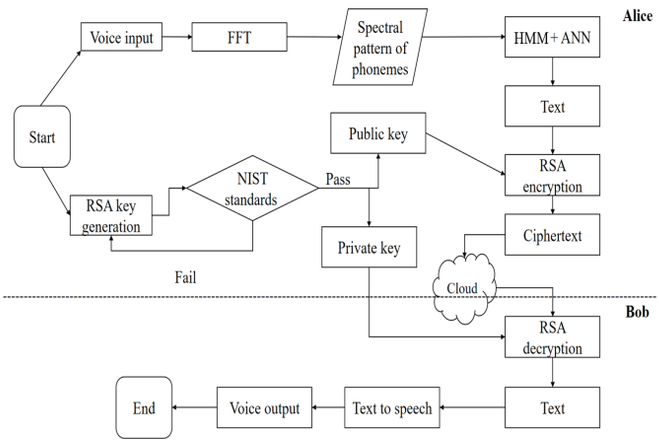

Fig. 1. Model of operation, conversion, and protection of voice using the RSA cryptosystem.

First, the speech recorded from the microphone is turned into signals that are transferred within the computer and processed into discrete samples. In the computer, the aforesaid samples travel via the HMM and ANN to compare and produce the standard text form matching the speech. Next, the resulting text is encrypted using the 2048-bit RSA cryptosystem. Then, transmit the freshly produced ciphertext to the recipient. At this moment, the receiver decodes the ciphertext and retrieves the plaintext, matching the original voice content. The text is transformed back to speech using a normal voice set.

3.2. Interface design for the soft voice-RSA module

In this research, the program module is created with two primary interfaces: Fig. 2A is a design detail for the implementation of 2048-bit RSA key generation (PKCS #1 v2.1 standard) to ensure that the key generated meets the NIST key quality assessment standard; Fig. 2B is an interface for performing speech-to-text and vice versa, as well as encrypting/decrypting speech signals in text using 2048-bit RSA cryptography.

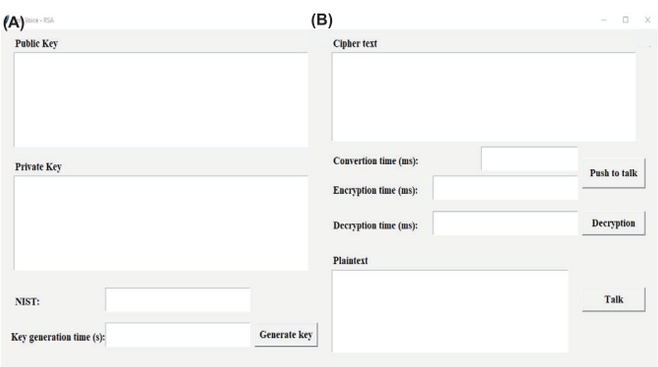

Fig. 2. (A) RSA key modulus generator interface; (B) Modular interface encrypts and decrypts voice using RSA cryptosystem.

3.2.1. The interface for key generation: To use the program, the user needs to prepare the private key and the public key of the RSA cryptosystem or use the key generated by the program with a minimum modulo length of 2048 bits by clicking the button "Generate key". After clicking, the machine will automatically generate a set of 2048-bit RSA keys. These keys will be checked through the NIST standard set. If they meet the standards, they will be printed on the screen and displayed throughout the entire processing time to produce the key.

3.2.2. The voice converter interface is secure: Once the needed security key is accessible, the user delivers his message via the microphone attached to the computer by clicking the "Push to talk" button. After pressing, the application will automatically record the portion of the voice we emit and stop when we finish talking. The analogue signal collected here from vibrations in the microphone is transformed into electrical impulses in the computer. Through the FFT transformation, electrical impulses are turned into spectral patterns. These spectral samples are processed using a language model (a mix of HMM and ANN) against the available sample sets to create the original spoken material in the form of text. The text here will be encrypted using the RSA cryptosystem using the public key created or prepared above. The ciphertext may then be communicated to the desired audience. When processing is complete, the ciphertext component will be displayed on the screen along with the conversion and encoding times. Then we hit "Decryption" to read the newly decoded segment and output the contents to the screen. The "Talk" button is used to play back the translated text.

4. Discussion

4.1. Analysis, assessment, and testing of the soft voice-RSA protected speech recognition module

In this research, to assess the operation of the soft voice-RSA software module, the authors did it on a computer with a configuration utilising Intel(R) Core i5-4200U, CPU @1.60GHz, up to 2.30 GHz; RAM: 8.00 GB. Fig. 3A displays the uptime results of the soft voice-RSA program module with 2048-bit RSA key generation that exceeds key assessment requirements. Fig. 3B displays the real-time results of speech conversion and voice encryption/decryption using 2048-bit RSA cryptography. Fig. 3C shows the execution time result of the soft voice program module (secure voice recognition with 256-bit AES-GCM encryption) (secure speech recognition with 256-bit AES-GCM cipher). To assess the performance, the process of creating 2048-bit RSA public and private key pairs; speech recognition by HMM and ANN models; execution time for speech conversion and encryption/decryption using 2048-bit RSA and AES-256-bit ciphers. The authors have run the program numerous times with varied input data for the software to run. Table 1 illustrates the results of running the soft voice-RSA program with varied input data and matching to the produced key set that is guaranteed to pass the key quality evaluation criteria of the NIST.

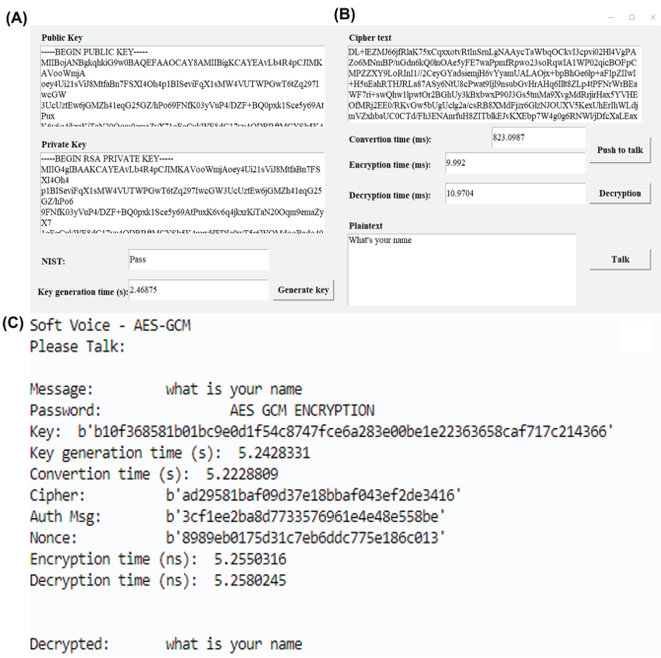

Fig. 3. Soft voice-RSA execution-time results. (A) NIST pass test and key generation; **(B)** Voice reception/conversion, speech encryption, and decryption using a 2048-bit RSA cryptosystem; **(C)** Voice capture/conversion, speech encryption, and decryption using a 256-bit AES-GCM cryptosystem.

Table 1. Execution time findings of soft voice-RSA and soft voice-AES-GCM.

The number of characters	Processing time (ms)	Encryption time (ms)	Decryption time (ms)	Key generation time (s)
Speech recognition using a 2048-bit RSA cryptosystem				
12	746.7266	3.991	7.0148	0.187500
35	1063.2608	1.9937	6.9827	0.328125
37	683.639	0.9993	5.9748	1.781250
40	830.3528	2.0288	7.9833	0.625000
Speech recognition uses 256-bit AES-GCM cryptography				
21	0.6907975	1.3045635	1.3075628	1.3005715
27	0.8660744	1.4963576	1.4993501	1.4933993
35	0.9356286	1.55198	1.5549542	1.5479727

The results show that the execution time of the soft voice-RSA seed when using the 2048-bit RSA cryptosystem is as follows: The process of generating a 2048-bit RSA key pair surpassing NIST's standards takes about 0.2-2 s; speech processing time ranges from 700-1070 ms; 2048-bit RSA encryption time takes between 1-4 ms; and the 2048-bit RSA decryption time takes about 6-8 ms. The execution time of the soft voice-RSA seed while utilising the 256-bit AES-GCM cryptosystem is as follows: the key generation process takes around 1-2 s; speech processing time is about

0.7-1 s; AES-GCM 256-bit encryption time takes about 1.5 s; decoding time takes about 1.6 s.

This enables the authors to notice that while increasing the length of the input, the processing pace varies differently. Because when we say it, while it may be a sentence of the same length, the pronunciation of phrases in it is different. Many clusters will grasp it, but some clusters have to be analysed into sections. So, while the length varies, the processing speed is often many times faster, and the encryption and decryption times are always in the range of 1-4 ms (for RSA 2048 encryption implementation. bit) and 6-8 s (for RSA 2048 decryption time). thus demonstrating that, even with a very large input processing, the software can process encoding and decoding in the time required to meet the user's demands.

In addition to the 2048-bit RSA technique, while constructing a secure speech recognition application, it is also feasible to substitute the security solution with any other cryptosystem, depending on the needs when utilising it. contemporary reality. Here, the authors have replaced the RSA 2048 cipher generation with the 256-bit AES-GCM cipher to prove that several other ciphers may be used to safely handle the speech signal after it has been translated, digital speech signal. Experimental findings reveal that the time for voice processing is identical to the above since both parties use the same processing technique, but the time of key creation, encryption, and decryption is slower if using AES-GCM 256 and faster with RSA. This demonstrates that the selected solution employing the 2048-bit RSA cryptosystem as a security solution for voice signals in digital form is suitable for the authors' application.

4.2. Testing the source code of soft voice-RSA software

The authors utilised the Fortify Static Code Analyzer toolkit (Version 22.1.0.0166) to examine and assess the source code of the soft voice-RSA software. Table 2 presents thorough findings while doing testing, assessment, and analysis of the source code of the soft voice-RSA program. The findings reveal that soft voice-RSA software has no faults during development. Here, the authors primarily discuss functions used in programming. In the software application soft voice-RSA, the authors have not constructed a protective solution for the process of producing keys and storing public keys and private keys of the 2048-bit RSA cryptosystem in compliance with key management and storage requirements of NIST [16-18]. These are also the solutions the authors' team hopes to enhance in future investigations.

Table 2. Soft voice-RSA software source code testing results using Fortify Static Code Analyzer toolkit.

Category	Fortify priority (audited/total)				Total issues
	Critical	*High*	*Medium*	*Low*	
Buffer overflow	0	0	0	0	0
Poor style: variable never used	0	0	0	0	0
Type mismatch: integer to character	0	0	0	0	0
Type mismatch: signed to unsigned	0	0	0	0	0
Unchecked return value	0	0	0	0	0
Weak cryptographic hash	0	0	0	0	0

Thus, via analysing, assessing, and testing the flaws in soft voice-RSA software using the Fortify Static Code Analyzer toolkit (Version 22.1.0.0166), it indicates that soft voice-RSA software authors established development and construction have also assured the safety of the source code. This is enough to prove that soft voice-RSA software can assure security against some of today's assaults when applied to these real-world commercial applications used by people every day.

5. Conclusions

The findings gained in this research have created a voice recognition application according to the HMM of ANN. In particular, the program has incorporated an RSA public key cryptography solution (according to PKCS#1 Version 2.1 standard) to secure the secrecy of speech material in digital form after identification. The execution speed of soft voice-RSA programs accomplishing encryption and decryption times is always between 1-4 ms (for 2048-bit RSA encryption implementation) and 6-8 s (for decryption time). These findings have been improved and have been compared with the solution while using the AES-GCM 256 cipher. Experimental findings reveal that the speech processing time is identical to that above because both sides utilise the same processing, but the time of key creation, encryption, and decryption for AES-GCM is several times slower than RSA. The authors concluded that the solution in this research also has certain drawbacks, such as the restricted voice recognition capabilities. This is also the research direction that the authors will concentrate on and will report on in the upcoming investigations.

CRediT author statement

Nhu-Quynh Luc: Conceptualisation, Methodology, Software, Resources, Writing - Review and Editing; Duc-Huy Quach: Data curation, Software, Writing - Original draft preparation; Chi-Hung Vu: Resources, Visualisation, Investigation; Hong-Truong Nguyen: Supervision; Thanh-Long Vo-Khac: Supervision, Software, Validation.

ACKNOWLEDGEMENTS

The authors thank the Academy of Cryptography Techniques for supporting this work.

COMPETING INTERESTS

The authors declare that there is no conflict of interest regarding the publication of this article.

REFERENCES

[1] N. Das, S. Chakraborty, J. Chaki, et al. (2021), "Fundamentals, present and future perspectives of speech enhancement", *Int. J. Speech Technol.*, **24(4)**, pp.883-901, DOI: 10.1007/s10772-020-09674-2.

[2] X. Han, Z. Zhang, N. Ding, et al. (2021), "Pre-trained models: Past, present and future", *AI Open*, **2**, pp.225-250, DOI: 10.1016/j.aiopen.2021.08.002.

[3] G.A. Fink (2008), *Markov Models For Pattern Recognition: From Theory to Applications*, Springer Berlin Heidelberg, 275pp, DOI: 10.1007/978-3-540-71770-6.

[4] Z. Han, Q. He, M.V. Davier (2019), "Predictive feature generation and selection using process data from PISA interactive problem-solving items: An application of random forests", *Front. Psychol.*, **10**, DOI: 10.3389/fpsyg.2019.02461.

[5] I. Farkaš, P. Masulli, S. Wermter (2020), *Artificial Neural Processing of the Networks and Machine Learning - ICANN 2020*, Springer, 918pp.

[6] G.R. Yang, X.J. Wang (2021), "Artificial neural networks for neuroscientists: A primer", *Neuron*, **107(6)**, pp.1048-1070, DOI: 10.1016/j.neuron.2020.09.005.

[7] R. Dastres, M. Soori (2021), "Artificial neural network systems", *Int. J. Imaging Robot.*, **21(2)**, pp.13-25.

[8] N. Bansal, S. Singh (2020), "RSA encryption and decryption system", *Int. J. Sci. Res. Comput. Sci. Eng. Inf. Technol.*, **6(5)**, pp.109-113, DOI: 10.32628/CSEIT206520.

[9] E. Barker (2020), *Guideline for Using Cryptographic Standards in The Federal Government*, National Institute of Standards and Technology Special Publication 800-175B Revision 1, 91pp.

[10] F. Ernawan, N.A. Abu, N. Suryana (2011), "Spectrum analysis of speech recognition via discrete Tchebichef transform", *Proceedings of SPIE - The International Society for Optical Engineering*, **8285**, DOI: 10.1117/12.913491.

[11] S. Sadhu, H. Hermansky (2021), "Radically old way of computing spectra: Applications in end-to-end ASR", *Proc. Interspeech 2021*, pp.1424-1428, DOI: 10.21437/Interspeech.2021-643.

[12] A. Abel, A. Hussain (2009), "Multi-modal speech processing methods: An overview and future research directions using a MATLAB based audio-visual toolbox", *Multimodal Signals: Cognitive and Algorithmic Issues*, **1177**, pp.121-129, DOI: 10.1007/978-3-642-00525-1_12.

[13] T. Drugman, T. Dubuisson, T. Dutoit (2011), "Phase-based information for voice pathology detection", *2011 IEEE Int. Conf. Acoust. Speech Signal Process. (ICASSP)*, Prague, Czech Republic, pp.4612-4615, DOI: 10.1109/ICASSP.2011.5947382.

[14] RSA Laboratories (2002), *PKCS #1 v2.1: RSA Cryptography Standard*, 61pp.

[15] G. McGraw (2006), "Software security: Building security in", *Proceedings of The 17th International Symposium on Software Reliability Engineering*, DOI: 10.1109/ISSRE.2006.43.

[16] A. Apvrille, M. Pourzandi (2005), "Secure software development by example", *IEEE Secur. Priv. Mag.*, **3(4)**, pp.10-17, DOI: 10.1109/MSP.2005.103.

[17] J. Koziol, D. Litchfield, D. Aitel, et al. (2004), *The Shellcoder's Handbook: Discovering and Exploiting Security Holes*, 2nd Edition, Wiley Publishing, 744pp.

[18] M. Howard, D. Leblanc (2008), *Writing Secure Code*, 2nd Edition, Microsoft Press, 737pp.

DOI: 10.31276/VJSTE.65(3).08-13

Development of a PCB-based passive capacitive sensor for fluidic flow detection

Nhu Cuong Nguyen[1], Bao Anh Hoang[1], Trung Kien Do[2], Thanh Tung Bui[1], Duc Trinh Chu[1], Quang Loc Do[2*]

[1]*Faculty of Electronics and Telecommunications, VNU University of Engineering and Technology, 144 Xuan Thuy Street, Dich Vong Hau Ward, Cau Giay District, Hanoi, Vietnam*
[2]*Faculty of Physics, VNU University of Science, 334 Nguyen Trai Street, Thanh Xuan Trung Ward, Thanh Xuan District, Hanoi, Vietnam*

Received 24 August 2022; revised 26 September 2022; accepted 3 October 2022

Abstract:

A passive wireless sensor system integrated with capacitive fluidic flow detection is proposed and developed based on the printed circuit board (PCB) technique. The capacitive sensing structure consists of PCB-based electrodes enclosing an insulating pipe that contains the fluidic flow of interest. The conductivity of the fluidic flow and the appearance of foreign objects within the flow can be determined by analysing the resonant frequency of the detection path in the proposed system. Experimental results demonstrate that the resonant frequency increases according to the increase in electrical conductivity of the fluidic flow. In addition, the sensing performance is also confirmed by the detection of sizes and electrical conductivities of NaCl droplets passing through the detection zone. Furthermore, this work indirectly verifies the effectiveness and feasibility of the integration of passive wireless sensing technique into the fluidic flow detector by using the PCB fabrication technique and demonstrates great potential for use in various applications in biomedical and chemical fields, especially in biomedical applications.

Keywords: **fluidic flow detection, passive capacitive detection, printed circuit board.**

Classification numbers: **2.1, 2.3**

1. Introduction

Fluidic flow detection refers to the measurement and detection of the properties of fluidic flow including conductivity, permittivity, and the appearance of foreign objects inside the fluidic flow. This technique has become an integral part of several systems in pharmaceutical [1], chemical analysis [2, 3], and biomedical systems [4]. Due to its vital roles in these fields, several methods have been proposed to improve fluidic flow detection such as optical, ultrasonic, and electrical sensing. When fluidic flow detection is based on the change of physical properties that are directly or indirectly related to electrical properties, the capacitively coupled contactless conductivity detection (C^4D) sensor structure [5-7] first proposed by A.J. Zemann, et al. (1998) [8]; J.A.F.D Silva, C.L.D Lago (1998) [9] is among the most prevalent methods. This method employs a conductivity detection technique in which a two-electrode configuration is utilized. These electrodes constitute a sensing capacitor including one electrode that acts as an exciting electrode in which the electrical signal is applied, and the other electrode function as a pick-up electrode where the electrical signal is sensed. Thus, any change in the electrical properties of the fluidic flow in the sensing area results in a change of the pick-up signal. This detection method has potential in many areas and has been employed in several detection and measurement applications [10-14]. However, stray capacitances can be generated by various sources, such as background noise, which can significantly influence the output sensitivity of the C^4D structure and thus impede the ability to detect objects or particles on the microscale.

Inductor-capacitor (LC) passive wireless sensing is based on the principle of resonance frequency shift detection. This is a high sensitivity technique that has been applied in several applications such as speed, position, and pressure detection [15, 16]. A potential technique to overcome the limits and difficulties of the conventional C^4D structure is its integration with LC sensing, resulting in a passive capacitively coupled contactless conductivity detection (PC^4D) sensor [17]. In this study, the C^4D structure, which acts as the sensing component, was connected to a PCB planar helical inductor to constitute a detection path whose resonant frequency is utilized for fluidic flow detection. LC sensors require no direct power connection to electrodes, thus minimizing any inadvertent change in electrical and chemical properties of the measured fluidic flow. The C^4D structure, as well as the planar inductors, were successfully fabricated using PCB technology. The fabricated PCB-based PC^4D structure was experimentally examined and the performance of the proposed method was evaluated by detecting the conductivity of the fluid and the presence of foreign objects in the fluidic flow.

2. Working principle and design

Figure 1A shows the design of the proposed PCB-based PC^4D sensor for fluidic flow detection. The proposed structure comprises two through-hole electrodes enclosing the conduit or the insulating pipe that contains the fluidic flow to be measured. The two electrodes create a sensing capacitor with the materials inside the channel wall acting as the dielectric material (Fig. 1B). An equivalent electrical circuit of the C^4D structure is shown in Fig. 1C. The resistance of the fluid inside the channel is R_S. The

*Corresponding author: Email: locdq@hus.edu.vn

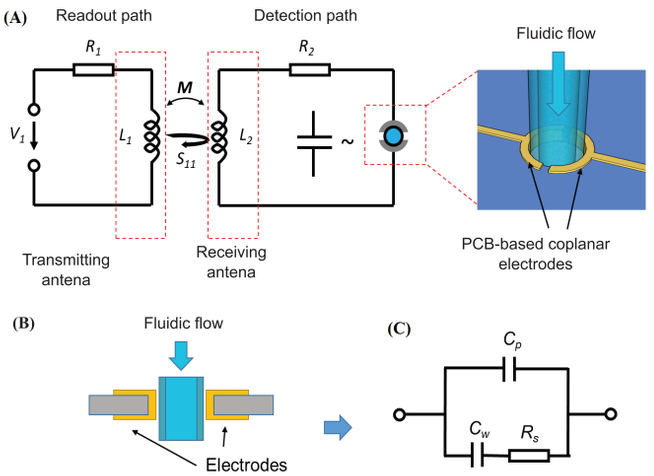

Fig. 1. Design of the proposed PCB-based PC⁴D sensor (A), a cross-section of a C⁴D structure (B), and the simplified equivalent circuit of the C⁴D structure (C).

wall capacitance is C_w. The configuration of the two electrodes also creates a stray capacitance C_p. Therefore, the impedance of the C⁴D cell, Z, can be determined by Q.L. Do, et al. (2019) [17]:

$$Z = \frac{R_S C_w^2 \omega^2 - j\left[\omega\left(C_w + C_p\right) + R_S^2 C_w^2 C_p \omega^3\right]}{\left(R_S C_p C_w w^2\right)^2 + \left[\omega\left(C_w + C_p\right)\right]^2} \quad (1)$$

where R_S is the solution resistance; $\omega=2\pi f$, f is the measurement frequency; j is the imaginary unit. As can be seen from the above equation, the imaginary part of the impedance is a function of ω, C_w, C_p, and R_s. The wall capacitance C_w depends on the dielectric layer's thickness and permittivity and the electrode's size. Thus, any change in the permittivity of the fluid material inside the conduit would give rise to a change in impedance of the sensing capacitor formed by the two electrodes.

As discussed above, two electrodes in the C⁴D structure constitute a capacitor with the dielectric material being the fluid flow. The sensing capacitor is connected to an inductor L_2, forming an LC resonator. The resonant frequency f_{res} of the detection path and quality factor Q can be expressed as Q.L. Do, et al. (2019) [17]:

$$f_{res} = \frac{1}{2\pi\sqrt{L_2 C}} \quad (2)$$

$$Q = \frac{1}{R_2} \times \sqrt{\frac{L_2}{C}} \quad (3)$$

where C is the capacitance of the sensing component in the detection path. The presence of an object or a change in the conductivity of the fluid gives rise to a change in the capacitance of the sensing capacitor. This in turn leads to a change in the resonant frequency of the LC resonator. The detection path is then wirelessly connected to the network analyser via a pair of antennae to detect such a change. The primary inductor L_1 works as the transmitting antenna. This antenna functions as the energy transmitting terminal by sending signals to the receiving antenna, which is the receiving inductor L_2 at the detection path with the C⁴D structure. The electrical signals from the network analyser are reflected through the pair of transmitting and receiving inductors. R_1 and R_2 are the parasitic resistances of the inductors. The input impedance Z_i of the network analyser is the combination of the reader path impedance Z_R and the detection path impedance Z_d, which is given by Q.L. Do, et al. (2019) [17]:

$$Z_i = Z_R + Z_d = R_1 + j\omega L_1 + \frac{(\omega M)^2}{R_2 + j\omega L_2 - j\left(\frac{1}{\omega C}\right)} \quad (4)$$

where ω is the angular frequency; R_1 and L_1 are the resistance and inductance of the readout coil, respectively; M is the mutual inductance between the transmitting antenna and the receiving antenna. The mutual inductance M of the coil is given by Q.A. Huang, et al. (2016) [18]:

$$M = k\sqrt{L_1 L_2} \quad (5)$$

where k is the geometry-dependent coupling coefficient with a value that varies between 0 (no coupling) and ±1 (maximum coupling).

As can be seen from Eq. 4, with the values of the primary and secondary inductors (L_1 and L_2) and the mutual inductance M between two coils considered constant during the measurement, the input impedance to the network analyser Z_i depends on the capacitance of the C⁴D sensor as well as the operating frequency. The input impedance of the detection path will experience changes corresponding to a change of the fluidic flow. This results in a change of the input reflection coefficient S_{11}, i.e., the ratio of reflected and incident power. As the excitation frequency corresponds to the resonant frequency of the LC detection path, the reflection coefficient S_{11} hits a low. Therefore, the change in the resonant frequency of the LC circuit can be detected by analysing the reflection coefficient S_{11}.

3. Measurement setup

Figure 2A shows the experimental measurement setup. A network analyser (E5061A, ENA Agilent) was used as a vector network analyser to detect the resonant frequency of the LC wireless passive sensor by analysing the reflection coefficient S_{11}. At the resonant frequency of the detection path, the parameter S_{11} reaches a minimum value. The fluidic channel was a silicon tube. A syringe micropump (AS ONE - CT10) was used to inject the solution into the fluidic channel. In addition, several experiments were conducted to determine the resonance frequency change while air bubbles move through the detection zone. The Y-channel configuration was employed in conjunction with two syringes. One syringe contained a sodium chloride (NaCl) solution, while the other was filled with air. As the micropump was activated, liquid droplets and air bubbles were generated inside the main channel. By altering the liquid and air phase flow rate, liquid droplets and air bubbles of different sizes can be achieved.

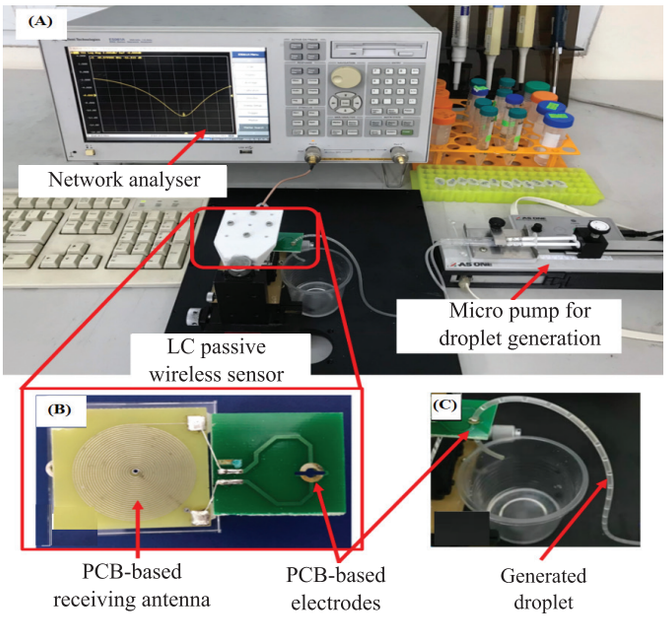

Fig. 2. Measurement setup (A), the fabricated detection path including the receiving antenna and the PCB-based electrodes of the C⁴D structure (B), and the experimental generated droplets (C).

Both the electrodes of the C⁴D structure as well as the primary and secondary inductors were fabricated by the (PCB) technique. Fig. 2B shows the design of the transmitting and receiving antennae as well as the design of the two electrodes that constitute the sensing component of the C⁴D structure. The electrodes of the C⁴D structure were designed as through-hole semicircles facing each other. Each electrode has an inner radius of 1.15 mm and an outer radius of 2.5 mm. The two electrodes are separated by a cavity where the fluidic channel is placed for measurements, as shown in Fig. 2C. Similar to the capacitance sensing electrodes, the receiving antenna was designed as helical coplanar inductors on a PCB board. The inductor at the detection path has a radius of 12.3 mm, which is composed of 23 turns, as shown in Fig. 2B. Meanwhile, the transmitting antenna has a dimension of 20x20 mm with a width of 1 mm. Two inductors are placed in air and separated by a fixed distance of 8.0 mm.

4. Results and discussion

4.1. Fluidic flow conductivity detection

NaCl solutions with concentrations ranging from 10 mM to 1 M were utilized to examine the ability to detect changes in the conductivity of the fluid flow. The network analyser detects the resonant frequency of the detection path by parametrically sweeping the stimulating frequencies. The reflection coefficient S_{11} corresponding to the sweeping frequency of the excitation signals was acquired. At the resonant frequencies, the reflection coefficient S_{11} experiences a minimum. Fig. 3A shows the relationship between the reflection coefficient S_{11} and the stimulating frequency with several values of the NaCl concentration solution. In the experiments with each concentration, the acquired values of resonant frequency at which S_{11} was a minimum were extracted. The experimental results show that when the concentration of the NaCl solution filling the fluidic channel increases from 10 mM to 1 M, the resonant frequency of the proposed sensor decreases from 49.32 to 49.12 MHz, respectively. At the same time, the value of the reflection coefficient S_{11} changes from -10.04 to -11.01 dB. Therefore, it can be concluded that the change in the measured solution not only caused a shift in the resonant frequency but also the value of the reflection coefficient S_{11}. Fig. 4 also demonstrates that the resonant frequency varies with the concentration of the solution. On a logarithmic scale of NaCl concentration, the dependence of the resonant frequency on the NaCl concentration is considered roughly linear with a decreasing rate of approximately 0.098 MHz/decade. Therefore, it is possible to utilize the proposed LC wireless passive sensor to detect the

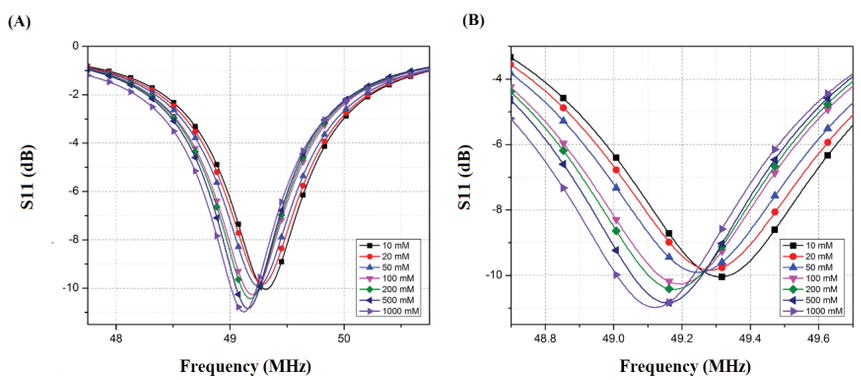

Fig. 3. Dependence of the reflection coefficient S_{11} on the NaCl concentration ranging from 10 mM to 1 M over frequencies ranging from 48 to 50.5 MHz (A) and over the frequency range from 48.8 to 49.8 MHz (B).

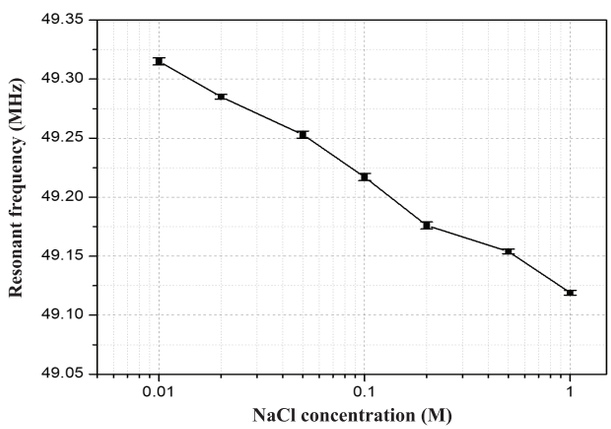

Fig. 4. The dependence of the resonant frequency on the concentration of NaCl solution.

electrical properties of the solution by measuring the resonant frequencies of the detection path.

4.2. Detection of liquid drops and air bubbles passing through the sensor

An air bubble generation structure utilizing a Y-junction configuration was conducted to investigate the ability to detect the appearance of foreign objects in the fluidic flow. Two syringes with a volume of 1 ml were employed to generate the same flow rate for the two phases. The syringe micropump speed was set at 6 mm/min. With such configurations, the length of the droplets and air bubbles generated in the main channel were equal. The resonance frequency of the detection path was monitored and tracked while air bubbles and droplets moved along the main fluidic channel through the detection zone.

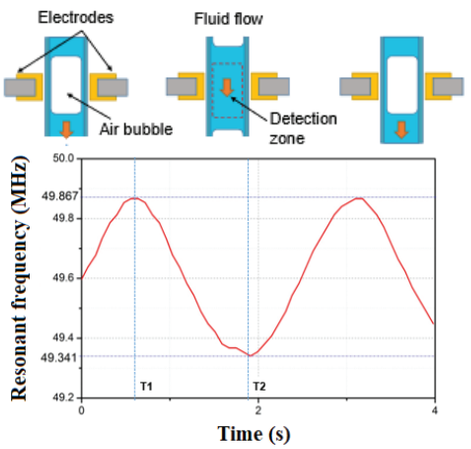

Fig. 5. Resonant frequency of the detection path as bubbles pass through the detection zone with the channel filled with 1 M NaCl.

The alternation of the resonant frequency according to the passage of air bubbles through the detection zone is shown in Fig. 5. The results show the resonant frequency's dependence on air bubble position inside the fluidic channel, which causes a change in the resonance frequency of the detection path circuit. When the droplets and air bubbles pass through the sensing region of the C^4D structure, the measured resonant frequency of the detection path changes. As the air bubbles travel through the detection region at T_1, the acquired resonant frequency increases. In contrast, the resonant frequency value drops at the appearance of liquid droplets passing the detection zone (T_2). Since the Y-junction droplet generation configuration generates air bubbles and liquid droplets consecutively, the acquired resonant frequency changed harmonically. These primary results demonstrate that the detection system can recognize the appearance of foreign objects or air bubbles. Compared to the C^4D technique proposed by X.Y. Tang, et al. (2020) [19], which used the C^4D technique with capacitive reactance elimination, the LC passive wireless detection method appears to be more precise. The observed data seems to be less influenced by background noise. In addition, this flow detection approach does not require a complex circuit for signal conditioning or a processing unit.

Object detection performance of the proposed system was experimentally studied. The sizes of droplets and air bubbles were altered by modifying the input flow rate into the Y junction. The length ratio (LR) of a generated droplet is defined as the ratio of the length of the liquid droplet over the length of an air bubble generated in the main fluidic channel:

$$LR = \frac{L_{liquid\ droplet}}{L_{air\ bubble}} \quad (6)$$

In this study, two syringes of different volumes, including 1 and 3 ml, were employed to produce a LR of approximately 1:5. Fig. 6 shows the variation of resonant frequency in the detection path when 1 M NaCl droplets and air bubbles passed through the sensor with LRs of 1:1 and 1:5. It can also be seen from the results that in the case of LR=1:5, the average value of resonant frequency was higher than that of LR=1:1. In the case of LR=1:5, the resonant frequencies varied from approximately 49.5 to 50.25 MHz. Meanwhile, the resonant frequencies changed in the range of 49.34 and 49.85 MHz in the case of LR=1:1. In addition, it can also be observed that the peak of the signals with LR=1:5 lasted longer than the minimum signal peaks at LR=1:1. This can be explained by the fact that the air bubbles were longer in the case of LR=1:5. Therefore, it took the air bubbles more time to pass through the detection zone, which resulted in the maximum peaks of the acquired signals lasting longer.

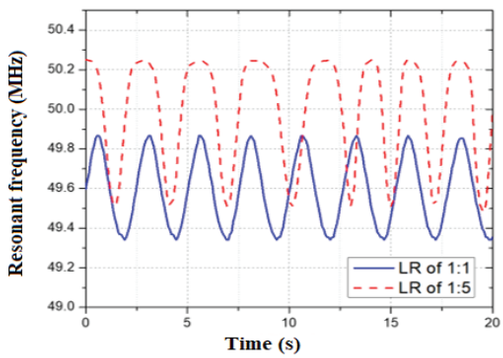

Fig. 6. The acquired resonant frequency of the system with 1 M NaCl droplet-air bubble experiments with LRs of 1:1 and 1:5.

With each LR value, the influence of solution concentration was studied. Specifically, five concentrations of the NaCl solution, including 0.01, 0.05, 0.1, 0.5, and 1 M, were investigated. The resonant frequencies reached a minimum when the NaCl droplets passed through the sensor. This passage corresponds to the minimum peaks of the acquired resonant frequency. Fig. 7A shows the dependence of the resonant frequency minima on the concentration of NaCl solution with LRs of 1:1 and 1:5, respectively.

In the case of LR=1:1, the passage of 0.01 M NaCl droplets resulted in a resonant frequency of 49.419 MHz. As the NaCl droplet concentration increased, the minimum peak values also decreased on a logarithmic scale with a rate of 0.041 MHz/decade. The minimum was approximately 49.338 MHz with the passage of

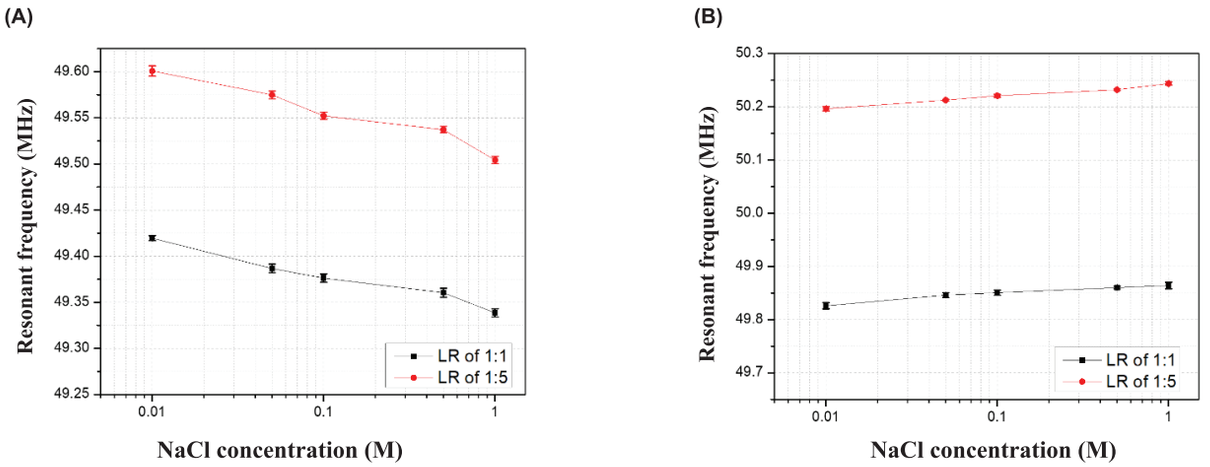

Fig. 7. Dependence of minimum (A) and maximum (B) peaks on the concentration of NaCl with the LR of 1:1 and 1:5.

1 M NaCl droplets. Similarly, the passage of 0.1 M NaCl droplets with LR=1:5 resulted in a minimum peak of 49.504 MHz, while the 1 M NaCl droplets resulted in a resonant frequency of 49.5043 MHz with the declining rate being 0.048 MHz/decade. In contrast, when the concentration of NaCl increased, the resonant frequency maxima corresponding to the passage of air bubbles through the detection zone increased as well, as shown in Fig. 7B. The maximum peak value for LR=1:1 was 49.8259 MHz with 0.01 M NaCl droplets. As the NaCl concentration grew to 1 M, the resonant frequency increased to 49.864 MHz with a rate of 0.0192 MHz/decade. Meanwhile, the maximum resonant frequency also increased with the NaCl concentration, but at a higher rate of 0.0237 MHz/decade in the case of LR=1:5. It can be seen from both Fig. 7A and Fig. 7B that the increase of resonant frequency with molar concentration is less significant when measuring maximum peaks. This is because peak maxima represent the appearance of air bubbles, as illustrated in Fig. 5, thus, if the air bubble already occupies a large area of the detection region, the concentration of NaCl does not have much influence.

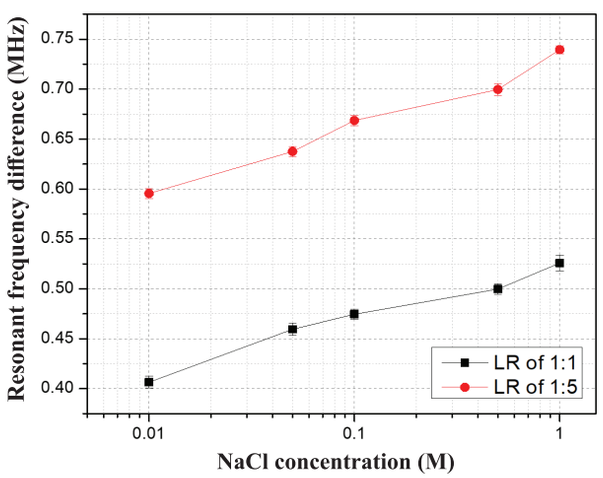

Fig. 8. Difference between maximum and minimum peaks of the resonant frequencies according to the passage of NaCl droplets at different LRs.

Figure 8 shows the difference between maximum and minimum peaks (Δ_{fres}) of the resonant frequencies according to the passage of NaCl droplets at different LRs. As can be seen from the graph, the differences, given by Δ_{fres}, for LR=1:1 and 1:5 seem to be quite clear. The frequency gap between the signal of LR=1:1 and LR=1:5 is approximately 0.18 MHz. As the NaCl concentration increased, Δ_{fres} also increased in both cases. At the same time, the frequency gap broadened but not significantly. It can be implied that Δ_{fres} certainly indicates the ratio between the length of droplets and air bubbles as well as the conductivity of the droplets. Although the proposed system is currently limited in characterizing different substances in the fluidic flow, the difference in Δ_{fres} in these experiments has demonstrated that implementation of the resonant frequency of the proposed sensing structure comprising the C^{4}D structure coupled with a coplanar inductor can detect not only the conductivity of the solution but also the size and electrical conductivity of the particles or objects inside the fluidic channel.

5. Conclusions

This paper proposed and developed a PCB-based PC^{4}D sensor for fluidic flow detection. The sensing structure integrates a C^{4}D structure with a coplanar inductor to form a detection path with its resonant frequencies varying with fluid flow. The obtained results show that the conductivity of the fluidic flow can be determined by measuring the resonant frequency of the detection path utilizing the reflection coefficient S_{11}. The resonant frequency experiences a linear increase according to the increase in the electrical conductivity of the fluidic flow. Experiments were also carried out to investigate droplet-air bubble detection. The frequency gap between the case of LR=1:1 and LR=1:5 was approximately 0.18 MHz. The experimental results indicated that by using the proposed method, the size and electrical conductivity of the particles or objects inside the fluidic flow could be estimated. The results show this scheme has great potential for use in various applications in biomedical and chemical fields but especially in biomedical applications.

CRediT author statement

Nhu Cuong Nguyen: Simulation Implementation, Writing the manuscript; Bao Anh Hoang: Experiment implementation; Trung Kien Do: Data analysis, Data presentation; Thanh Tung Bui: Supporting data analysis, Literature review; Duc Trinh Chu: Review manuscript and Supervise the project; Quang Loc Do: Supervise and Editing.

ACKNOWLEDGEMENTS

This research is funded by Vietnam National Foundation for Science and Technology Development (NAFOSTED) under grant number 103.99-2020.40.

COMPETING INTERESTS

The authors declare that there is no conflict of interest regarding the publication of this article.

REFERENCES

[1] A.L. Campana, S.L. Florez, M.J. Noguera, et al. (2019), "Enzyme-based electrochemical biosensors for microfluidic platforms to detect pharmaceutical residues in wastewater", *Biosensors*, **9(1)**, DOI: 10.3390/BIOS9010041.

[2] S. Motomizu (2012), "Computer-controlled fluid-flow chemical analysis (CC-FCA) and its application to environmental analytical chemistry", *Pure and Applied Chemistry*, **84(10)**, pp.1999-2013, DOI: 10.1351/PAC-CON-12-02-09.

[3] D. Janasek, J. Franzke, A. Manz (2006), "Scaling and the design of miniaturized chemical-analysis systems", *Nature*, **442(7101)**, pp.374-380, DOI: 10.1038/nature05059.

[4] P. Sengupta, K. Khanra, A.R. Chowdhury, et al. (2019), "Lab-on-a-chip sensing devices for biomedical applications", *Bioelectronics and Medical Devices: From Materials to Devices - Fabrication, Applications and Reliability*, pp.47-95, DOI: 10.1016/B978-0-08-102420-1.00004-2.

[5] W.K.T. Coltro, R.S. Lima, T.P. Segato, et al. (2012), "Capacitively coupled contactless conductivity detection on microfluidic systems - Ten years of development", *Analytical Methods*, **4(1)**, pp.25-33, DOI: 10.1039/C1AY05364G.

[6] P. Kuban, P.C. Hauser (2011), "Capacitively coupled contactless conductivity detection for microseparation techniques - recent developments", *Electrophoresis*, **32(1)**, pp.30-42, DOI: 10.1002/ELPS.201000354.

[7] P. Kuban, P.C. Hauser (2008), "A review of the recent achievements in capacitively coupled contactless conductivity detection", *Analytica Chimica Acta.*, **607(1)**, pp.15-29, DOI: 10.1016/j.aca.2007.11.045.

[8] A.J. Zemann, E. Schnell, D. Volgger, et al. (1998), "Contactless conductivity detection for capillary electrophoresis", *Anal. Chem.*, **70(3)**, pp.563-567, DOI: 10.1021/ac9707592.

[9] J.A.F.D. Silva, C.L.D. Lago (1998), "An oscillometric detector for capillary electrophoresis", *Anal. Chem.*, **70(20)**, pp.4339-4343, DOI: 10.1021/ac980185g.

[10] T.V. Quoc, H.N. Dac, T.P. Quoc, et al. (2015), "A printed circuit board capacitive sensor for air bubble inside fluidic flow detection", *Microsystem Technologies*, **21(4)**, pp.911-918, DOI: 10.1007/s00542-014-2141-8.

[11] H.N. Dac, H.T.T. Thuy, T.V. Quoc, et al. (2020), "Study on design optimization of a symmetry two-axis tilt angle capacitive sensor", *IETE J. Res.*, **69(1)**, pp.264-271, DOI: 10.1080/03772063.2020.1816224.

[12] A.A. Elbashir, H.Y. Aboul-Enein (2010), "Applications of capillary electrophoresis with capacitively coupled contactless conductivity detection (CE-C4D) in pharmaceutical and biological analysis", *Biomedical Chromatography*, **24(10)**, pp.1038-1044, DOI: 10.1002/bmc.1417.

[13] K.A. Mahabadi, I. Rodriguez, C.Y. Lim, et al. (2010), "Capacitively coupled contactless conductivity detection with dual top - bottom cell configuration for microchip electrophoresis", *Electrophoresis*, **31(6)**, pp.1063-1070, DOI: 10.1002/elps.200900578.

[14] J.P. Hutchinson, C. Johns, M.C. Breadmore, et al. (2008), "Identification of inorganic ions in post-blast explosive residues using portable CE instrumentation and capacitively coupled contactless conductivity detection", *Electrophoresis*, **29(22)**, pp.4593-4602, DOI: 10.1021/ac2020195.

[15] H. Wen, C. Chen, S. Li, et al. (2021), "Array integration and far-field detection of biocompatible wireless LC pressure sensors", *Small Methods*, **5(3)**, DOI: 10.1002/SMTD.202001055.

[16] C.S. Lee, C.Y. Wu, Y.L. Kuo (2017), "Wearable bracelet belt resonators for noncontact wrist location and pulse detection", *IEEE Transactions on Microwave Theory and Techniques*, **65(11)**, pp.4475-4482, DOI: 10.1109/TMTT.2017.2684118.

[17] Q.L. Do, T.T. Bui, B.A. Hoang, et al. (2019), "Development of a passive capacitively coupled contactless conductivity detection (PC4D) sensor system for fluidic channel analysis toward point-of-care applications", *IEEE Sensors Journal*, **19(15)**, pp.6371-6380, DOI: 10.1109/JSEN.2019.2908179.

[18] Q.A. Huang, L. Dong, L.F. Wang (2016), "LC passive wireless sensors toward a wireless sensing platform: Status, prospects, and challenges", *Journal of Microelectromechanical Systems*, **25(5)**, pp.822-841, DOI: 10.1109/JMEMS.2016.2602298.

[19] X.Y. Tang, J. Huang, H. Ji, et al. (2020), "New method for bubble/slug velocity measurement in small channels", *Review of Scientific Instruments*, **91(5)**, DOI: 10.1063/1.5134548.

DOI: 10.31276/VJSTE.65(3).14-20

Green synthesis of silver nanoparticles using *Mentha crispa* L. leaf extract for treatment of dye wastewater

Thi Minh Dinh[1], Khac Khoi Tran[2, 3], Anh Trung Le[2], Thi Minh Nguyet Nguyen[2], Thi Hue Do[2*], Ian Liau[4]

[1]*Dai Tu High School, Hung Son Town, Dai Tu District, Thai Nguyen Province, Vietnam*
[2]*Faculty of Physics, Thai Nguyen University of Education, 20 Luong Ngoc Quyen Street, Quang Trung Ward, Thai Nguyen City, Thai Nguyen Province, Vietnam*
[3]*Faculty of Fundamental Science, Phenikaa University, Nguyen Van Trac Street, Yen Nghia Ward, Ha Dong District, Hanoi, Vietnam*
[4]*Department of Applied Chemistry, National Yang-Ming Chiao-Tung University, 1001, University Road, Hsinchu 300, Taiwan*

Received 25 October 2022; revised 29 December 2022; accepted 5 January 2023

Abstract:

***Mentha crispa* L. is one of Vietnam's most precious folk medicines and is also a spice used in many delicious dishes in Vietnam and around the world. The use of *Mentha crispa* L. leaf extract as a reducing agent for Ag^+ ions to synthesize silver nanoparticles is discussed in this paper. Single silver nanospheres were dispersed in biological media and their sizes were controlled in the range of 20-80 nm. Factors affecting particle size and shape such as extract concentration, $AgNO_3$ concentration, reaction time, and temperature were investigated to determine the optimal parameters for particle synthesis. The optical properties, dispersion, crystal structure, morphology, and sizes of silver nanoparticles were investigated through UV-Vis absorption spectroscopy, dynamic light scattering (DLS) measurements, X-ray diffraction, and transmission electron microscopy (TEM). The functional groups on the L.AgNPs were determined by Fourier-transform infrared (FTIR) transmittance spectra. The synthesised silver nanoparticles were used to treat methylene blue (MB) dye, the main component of dye wastewater, based on their photocatalytic properties. The results show that in the presence of L.AgNPs, the photodegradation efficiency of $NaBH_4$ or H_2O_2 reducing agents is much higher, up to 95% of illumination.**

Keywords: **dyeing wastewater, green synthesis, *Mentha crispa* L., silver nanoparticles, sweet basil.**

Classification number: **2.2**

1. Introduction

Nanotechnology has been asserting its importance in many areas of science and life in almost every country in the world. Undeniably, nanomaterials are present in many products of science and technology. Silver nanoparticles are particularly interesting to scientists because of their unique properties such as their plasmon resonance frequency being located in the visible light region, non-toxicity, and high biocompatibility [1-3]. They are widely exploited in fields ranging from medicine and pharmacy, to agriculture and forestry, and to diagnostic imaging with applications such as drug delivery, cellular imaging, sensors, biological probes, and surface-enhanced Raman scattering (SERS) [4-9]. In particular, silver nanoparticles exhibit some of the best antibacterial and bactericidal activities thanks to their characteristic mechanisms [10-16]. While the antibacterial mechanism of silver nanoparticles remains controversial, observations have shown silver ions destroying respiratory function, the function of cell walls, as well as binding to the DNA of microbial cells and destroying their function [17-22]. In addition, silver nanoparticles have been shown to have redox properties that catalyse biological agents such as dyes and chemical agents like benzene under the influence of light [23-27].

Because of the wide applicability of silver nanoparticles, they have been synthesized by many different methods such as chemical reduction, electrochemistry, radiation, photochemistry, and biological reduction [28-32]. Each method creates nanoparticles with different shapes, structures, and sizes. Depending on the intended use and specific conditions, different methods are selected. Recently, synthesizing silver nanoparticles by using reducing agents of biological origin such as microorganisms and plant extracts has attracted much attention from researchers [33-36]. This method synthesizes particles with high concentration, relatively uniform size, and, especially, with abundant raw materials, low economical cost, and environmentally friendly products. The synthesis of silver nanoparticles from plant extracts has advantages over synthesis from biological microorganisms because it eliminates the elaborate process of cell culture and simplifies large-scale particle synthesis thereby saving time and cost [34-36]. There are many types of plants selected for the synthesis of silver nanoparticles such as Azadirachta indica [37], green tea leaves [38], *Aloe vera* [39], *Capsicum annuum* L. [40], *Jatropha curcas* [41], *Magnolia kobus* [42], *Carica papaya* [43], *Hibiscus rosa* Sinensis [44], *Mentha piperita* [45], *Morinda citrifolia* [46], *Sesbania grandiflora* [47], *Albizia adianthifolia* [48], and *Ziziphora tenuior* [49]. However, there have been no reports on the use of *Mentha crispa* L. leaf extract to synthesize silver nanoparticles.

Sweet basil (*Mentha crispa* L.) is a common herb in Europe, northwest Africa, and Asia. This vegetable belongs to *Mentha*

*Corresponding author: Email: huedt@tnue.edu.vn

aquatica, which is relatively similar in appearance to mint (*Mentha arvensis* L.). Many people often confuse these two herbs with each other. However, in fact, sweet basil and mint are two different vegetables. Not only is it used as a spice, sweet basil can also be used as a medicine with many effects on human health. Sweet basil can strengthen the digestive system, prevent cancer, help brighten skin, protect skin from acne, effectively fight inflammation, treat insect bites, treat sore throats, relieve colds, and treat asthma from colds [50]. In this paper, we synthesize silver nanoparticles using *Mentha crispa* L. leaf extract and study the application of these synthesized silver nanoparticles in the treatment of dye wastewater and antibacterial activity.

2. Materials and methods

2.1. Materials

Silver nitrate ($AgNO_3$, >99%) and methylene blue dye ($C_{16}H_{18}ClN_3S$, 97%) were purchased from Sigma Aldrich. Sodium borohydride ($NaBH_4$, >99%) and hydrogen peroxide (H_2O_2, 30%) were purchased from Merck, Germany. Chemicals were used without any purification. Sweet basil leaves were collected from the medicinal garden at Thai Nguyen University of Education. Deionized water (DI) with a resistance of 18.2 MΩ was used in all processes.

2.2. Mentha crispa L. leaf extract preparation

The sweet basil leaves were collected and washed several times with water and then deionized water to remove dirt adhered to the leaves. They were dried at room temperature (27^0C) for 24 hours and then ground into a powder with an agate mortar. Then, 10 g of leaf powder was mixed with 100 ml of sterilised, deionized water. The mixture was steamed in a water bath at 100^oC for about 30 min. The solution was cooled and centrifuged at 5000 rpm for about 15 min. The residue was removed and the solution extract was filtered with Whatman No. 1 filter paper. The final extract was obtained by filtering the solution through a 0.22-µm Ministart filter and was stored refrigerated (4^oC) for future use.

2.3. Green synthesis of silver nanoparticles (L.AgNPs)

An amount of *Mentha crispa* L. leaf extract in respective volumes was mixed into a 1.0 mM $AgNO_3$ solution. The reaction mixture was continuously magnetically stirred in the dark at room temperature for about 24 hours. The reactions of the solution were monitored at different time intervals. To optimize the synthesis of L.AgNPs, the influences of $AgNO_3$ concentration, reaction time, and extract volume were investigated. The volumes of $AgNO_3$ in the series of experiments to investigate the effect of $AgNO_3$ concentration were 6, 8, 10 and 14 ml, respectively, corresponding to $AgNO_3$ concentrations varying from 0.43 to 0.8 mM while the volume of extract solution was 0.25 ml. To investigate the effect of the amount of extract on the particle synthesis yield, different volumes of extract were used: 0.15, 0.25 and 0.35 ml while the volume of 1 mM $AgNO_3$ solution was 14 ml. At the same time, to monitor the development of L.AgNPs over time, each solution was withdrawn from the reaction vessel at certain times such as 0.5, 2, 4, 6, 8,10, 12, 14, 16 and 24 hours. The synthesis process of the L.AgNPs is shown in Fig. 1.

2.4. Application of L.AgNPs

L.AgNPs were used as photocatalysts to treat MB, an ingredient in dye wastewater in either 30% H_2O_2 or 0.2 M $NaBH_4$. To examine the role of L.AgNPs in improving the degradation efficiency of MB pigment, experiments were conducted independently in the presence or absence of L.AgNPs as a catalyst. Specifically, 10 ml of L.AgNP solution, after centrifugation to remove impurities, was placed into 100 ml of 10-ppm MB solution and magnetically stirred in the dark for about 2 hours to balance absorption. Then, 1 ml of 30% H_2O_2 or 2 ml of 0.2 M $NaBH_4$ were added to the solution. The mixture was continuously illuminated with a 30 W LED with a colour temperature of 6500 K (Philips, Amsterdam, The Netherlands). The photodegradation rate was monitored by observing the absorption reduction at the characteristic peak of MB pigment after each illumination time period: 5, 30, 60, 90, and 120 min.

2.5. Characterisation

A Jasco V-770 UV-Vis spectrophotometer was used to investigate the optical properties of the synthesised silver nanoparticles at wavelengths between 250-1000 nm. Morphology and particle size were determined by TEM on a JEOL JEM-2100 at an accelerating voltage of 200 kV. The particle size distribution of the L.AgNPs in media was evaluated by a particle size analyser (PSA, Delta Nano C, Beckman) using DLS. The XRD spectra were collected using an X-ray diffractometer (Bruker D8 Advance, Germany) operated at 30 kV with Cu-K_α radiation (wavelength of λ=0.154056 nm) with a parallel-beam geometry between 30 to 80^o. The main functional groups of the *Mentha crispa* L. leaf extract and L.AgNPs were analysed by FTIR spectra using an FTIR spectrophotometer (Nicolet 6700, Thermo Scientific) (Fig. 1).

Fig. 1. Process for synthesising L.AgNPs from *Mentha crispa* L. leaf extract.

3. Results and discussion

The influence of $AgNO_3$ concentration, amount of extract, and reaction time on the morphology and size of the L.AgNPs is shown through the absorption spectrum of the solutions (Fig. 2). Figs. 2A and 2B are the absorption spectra and the normalised absorption spectra of the L.AgNPs solutions when the $AgNO_3$ concentration was varied from 0.43 to 0.8 mM. It can be seen that $AgNO_3$ concentration has a great influence on the formation and growth of particles as both the absorbance and resonance peak

wavelengths change with $AgNO_3$ concentration. When the $AgNO_3$ concentration is below 0.75 mM, the produced L.AgNPs are not uniform in size. This is shown by the half-width of the normalised absorption spectra. When $AgNO_3$ concentration is 0.8 mM, the half-spectral width is much narrower, and the absorption spectrum at its lowest. It was demonstrated that the synthesised L.AgNPs have a relatively uniform size of around 40 nm (corresponding to the absorption peak at 445 nm). The effect of $AgNO_3$ concentration on particle formation and growth was explained by a kinetic mechanism according to Lamer's model [51]. When the $AgNO_3$ concentration is high, the reaction rate is fast during the first stage and the concentration of monomers rapidly increases, facilitating the formation of small-size particles and relatively uniform size development in the later stages.

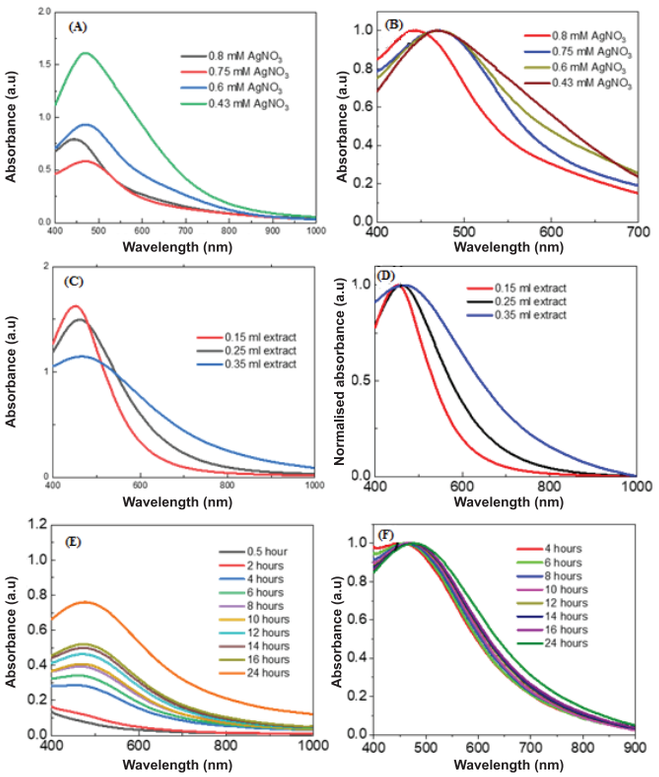

Fig. 2. The dependence of UV-VIS and normalised absorption spectra of L.AgNP solutions on $AgNO_3$ concentration (A, B), extract volume (C, D), and reaction time (E, F).

Extraction volume also greatly influenced the formation and growth of the L.AgNPs (Figs. 2C and 2D). With extraction volumes of 0.25 and 0.35 ml, the absorbance spectra showed a large amount of excess extract after the reaction as shown by the high absorbance in the region below 400 nm. At the same time, L.AgNPs formed in different sizes, especially when the extract volume was 0.35 ml. Thus, in this survey, an extract volume of 0.15 ml synthesised the best quality L.AgNPs. The extract acts as a reducing agent in particle fusion. In these reactions, the volume of extract used was in excess of the amount of precursor $AgNO_3$, so it can be seen that the larger the extract volume, the more inhibited the incorporation of monomers in solution during the early stages of the reaction. This leads to heterogeneous formation of particles in the solution and a larger size distribution. On the other hand, as the kinetic processes behind the formation and growth of particles go through each stage, time plays an important role in the synthesis reaction. In this study, the volume of extract used was 0.5 ml and the volume of 1 mM $AgNO_3$ was 20 ml. After a certain period of time, 2 ml of the solution was withdrawn to investigate the optical characteristics, morphology, and size. In the first 4 hours of the reaction, the L.AgNPs in solution began to form but with low concentration and small size corresponding to an absorption spectrum that had no clear resonance peak (characteristic spectrum of metal nanoparticles as small as 10 nm in diameter) [52]. As the reaction time increased, the absorbance increased and the resonance peak shifted towards longer wavelengths, indicating more particles were formed and the size increased. However, in the absorption spectrum at 24 hours, it can be seen that the half-width of the peak tended to increase and large particles formed as evidenced by the increased absorption at longer wavelengths. The formation and growth of AgNPs over time are also explained by the Lamer mechanism [51]. However, the initial phase of this kinetic process is long because the reduction reaction rate is slow. When the reaction time lasts more than 24 hours, to the point where no new monomers are generated, particles will agglomerate together to form larger particles in the solution.

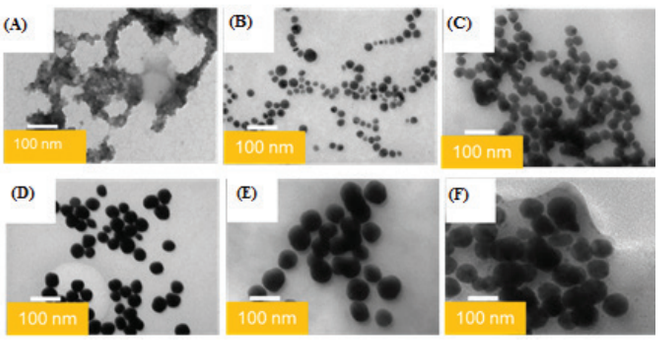

Fig. 3. TEM image of L.AgNPs by reaction time. (A) 4 hours, **(B)** 6 hours, **(C)** 10 hours, **(D)** 14 hours, **(E)** 16 hours, **(F)** 24 hours.

This process is shown by observing the TEM images of the particles obtained at different time intervals (Fig. 3). A reaction time of fewer than 2 hours yielded hardly any L.AgNPs. An appearance of beads in the TEM measurement was obtained when the reaction time was over 4 hours. However, after 4 hours of reaction, mainly small particles (several nm) were formed and tended to clump together. When reaction time increased from 6 to 24 hours, the average size of the L.AgNPs particles increased from 20 to 80 nm. Fig. 3F shows 24 hours of reaction time and the obtained particles are of unequal size, agglomerating to form large-sized particles, and at the same time very small particles appear. From this data, it seems that a synthesis time of 16 hours for L.AgNPs from the extract of basil leaves is the most suitable (Fig. 3E). These results prove that using organic compounds to reduce Ag^+ ions is much faster than using fungi or bacteria to synthesise silver particles [53].

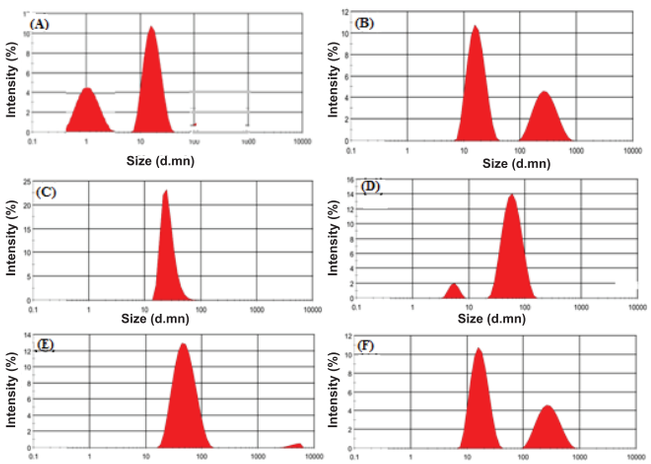

Fig. 4. Dependence of particle size distribution spectra of L.AgNPs on reaction time. (A) 2 hours, **(B)** 6 hours, **(C)** 10 hours, **(D)** 14 hours, **(E)** 16 hours, **(F)** 24 hours.

Fig. 4 shows the particle size distribution spectra of the L.AgNPs obtained after different reaction times. It can be seen that silver nanoparticles synthesised from plant extracts have a wider size distribution than silver nanoparticles synthesised by chemical reduction because of slower biological reduction reactions. Even so, the results obtained show that synthesis efficiency as well as the particle size uniformity are better than those previously published using green synthesis methods [33-35]. The XRD spectra of the L.AgNPs synthesised at 10, 14, 16, and 24 hours are shown in Fig. 5. It can be seen that the samples all have the same peaks at 2θ angles 27.8, 32.2, 38.1, 43.6, 46.4, 64.4, and 77.5° corresponding to the lattice planes (211), (122), (111), (200), (231), (220), and (311), respectively, of face-centred cubic (fcc) Ag crystals [52]. No peaks from any other phase appeared in the XRD spectrum, indicating that a single phase of Ag with cubic structure nanoparticles was synthesised directly from the extract. The average crystal size was determined based on the width of the diffraction peaks using the Debye-Scherrer formula: $D=(k\lambda)/(\beta \cos \theta)$, where D is the average crystal size of the powder sample; K=0.9 is the geometric factor or Scherrer constant; β is the angular full-width at half maximum (FWHM) of the XRD peak (rad), λ=0.154056 nm is the wavelength of Cuk_{α}, and θ is the Bragg diffraction angle of the corresponding peak. For the samples surveyed, the diffraction peak with the highest intensity occurred at 2θ=38.1°, corresponding to the (111) lattice plane. The average crystal size determined according to this diffraction peak is 0.44 nm.

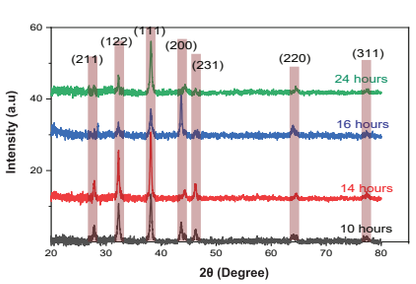

Fig. 5. XRD spectrum of the L.AgNPs at different reaction times.

The FTIR spectra of the L.AgNPs showed the presence of functional groups on the particles in the wavenumber range from 540 to 3444 cm^{-1} (Fig. 6). The region of greatest intensity at 3444 cm^{-1} is attributed to the presence of -OH functional groups of alcohol and phenolic compounds, which exist in the basil leaf extract [44, 45]. Peaks in the region of 1631 to 1387 cm^{-1} are attributed to the stretching vibrations of the C-N bonds of amide functional groups.

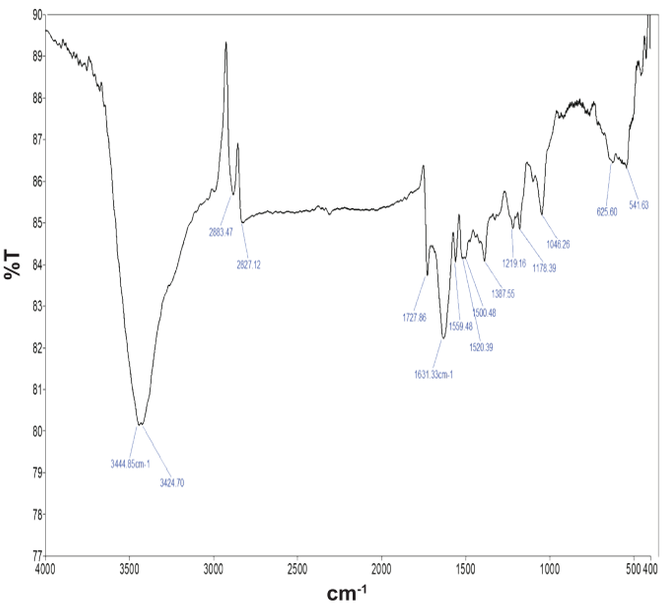

Fig. 6. FTIR spectrum of L.AgNPs.

Peaks in the 1178 and 1220 cm^{-1} regions are attributed to the C-N stretching mode of aromatic amine groups. The peak at 1048 cm^{-1} is related to the presence of C-O bonds. The band at 1048 cm^{-1} is also related to the presence of C-O bonds. The peaks in the 541 to 625 cm^{-1} region represent fluctuations of metallic Ag [47, 48].

L.AgNPs were used as a catalyst to study the ability to degrade MB organic pigment in the presence of either H_2O_2 or $NaBH_4$ reducing agents. The experiments were conducted under the condition that the solution was illuminated with a 30 W LED white light source of colour temperature 6500 K. The illumination was carried out continuously for 2 hours to monitor the photodegradation efficiency of the L.AgNPs. Fig. 7 shows the absorption spectra of the 10 ppm MB solution over the illumination time in the cases of using only 0.2 M $NaBH_4$ (Fig. 7A), only L.AgNPs (Fig. 7B), only 30% H_2O_2 (Fig. 7C), 30% H_2O_2 reducing agent catalysed by L.AgNPs (Fig. 7D), and 0.2 M $NaBH_4$ reducing agent catalysed by L.AgNPs (Fig. 7E). In the spectroscopic determination of the decrease in relative absorbance of MB pigment in the cases over time of illumination (Fig. 7F), the colour of the solution changed with the exposure time when using H_2O_2 reducing agent (Fig. 7G) and $NaBH_4$ reducing agent (Fig. 7H) with the catalyst L.AgNPs. Monitoring the decrease of

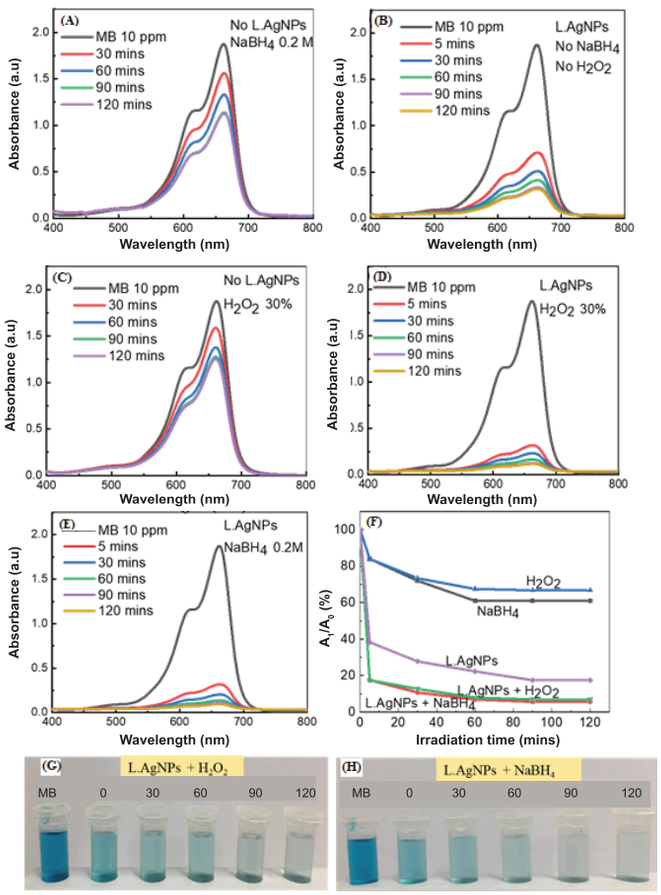

Fig. 7. Absorption spectrum of MB over time in the following cases: (A) only $NaBH_4$, (B) only L.AgNPs, (C) only H_2O_2, (D) L.AgNPs + H_2O_2, (E) L.AgNPs + $NaBH_4$, (F) the decrease in relative absorbance of MB with time, (G, H) changes to the colour of the solutions with time.

absorbance of MB at 662 nm with irradiation time, it can be seen that when the reducing agents H_2O_2 or $NaBH_4$ and L.AgNPs are not used simultaneously, an absorbance of MB at the solid peak is observed. The 662 nm peak also decreased when illuminated. However, the absorbance can only be reduced to a certain value and cannot be further reduced. This shows that under the effect of light and reducing agents, MB is also partially discoloured (Figs. 7A and 7C). In the case where the MB colorant solution contains only L.AgNPs and is illuminated, the photodegradability is better than that of the solutions without L.AgNPs. In 2 hours, the absorbance of MB decreased from 1.87 to 0.34 when catalysed by L.AgNPs. This clearly demonstrates the role of Ag nanoparticles in the degradation of MB pigment. To demonstrate this, experiments monitoring the photodegradability of Ag nanosheets were performed using both reducing agents and L.AgNPs (Figs. 7D and 7E). The results showed that after irradiation for about 1 hour, the absorption concentration of MB in the solution decreased significantly, and after 2 hours of illumination, almost all the pigments were decomposed. This can be seen by the colour of the solutions over time (Figs. 7G and 7H). There is a slight difference between using H_2O_2 and $NaBH_4$ reducing agents in terms of photodegradation efficiency (Fig. 7F). The photodegradation efficiency is better when using $NaBH_4$, although the concentration of $NaBH_4$ reducing agent is much lower than that of H_2O_2. The photodegradation efficiency was determined by the following formula:

$$H = \frac{A_0 - A_t}{A_0} \times 100\%$$

where A_o is the absorbance of the initial MB and A_t is the absorbance of the MB at the peak of 662 nm after the illumination time t. Therefore, from the data on the absorption spectrum, it can be determined that the photodegradation efficiency in the case of L.AgNPs and 30% H_2O_2 is 92.6% and in the case of 0.2 M L.AgNPs and $NaBH_4$ it is 95.6%. The photodegradation mechanism of the L.AgNPs is explained by the light absorption of silver nanoparticles along with the presence of NaBH4 reducing agent, making the colour degradation reaction speed faster.

$$AgNPs + h\nu \rightarrow Ag^+ (e^-, h^+)$$

$$h^+ + MB + NaBH_4 \rightarrow \text{colourless products}$$

4. Conclusions

In this article, spherical L.AgNPs with sizes ranging from 20 to 80 nm in diameter were synthesised by a simple de-greening method using basil leaf extract. The size, as well as the particle size distribution, depended on the extract volume, $AgNO_3$ concentration, and reaction time. The survey results of factors affecting the formation and growth of L.AgNPs showed that when the concentration of $AgNO_3$ was 0.8 mM and the extraction volume was 0.15 ml, the L.AgNPs had an average size of 40 nm and the particles were relatively uniform in shape and size. The synthesis time of the L.AgNPs by the extraction method is about 6 hours, which is much shorter than the synthesis time using bacteria or fungi. Increasing synthesis time from 6 to 24 hours caused the average size of the L.AgNPs to increase from 20 to 80 nm. However, the most reasonable time to obtain L.AgNPs with the best quality was between 10 and 16 hours. The L.AgNPs were used to study photocatalytic ability of colour degradation of MB. Comparing the results of MB's absorbance attenuation at the 662 nm peak in cases with and without L.AgNPs, it was seen that the L.AgNPs have an important role in photodegradation. The highest photodegradation efficiency was 95% when using 0.2 M $NaBH_4$ reducing agent together with the Ag catalyst.

CRediT author statement

Thi Minh Dinh: Methodology, Formal analysis, Writing, Editing; Khac Khoi Tran: Material synthesis, Data analysis, Editing; Anh Trung Le: Material synthesis, Writing, Review;

Thi Minh Nguyet Nguyen: Review, Data analysis; Thi Hue Do: Material synthesis, Data analyst, Review, Writing, Editing; Ian Liau: Editing, Data analyst.

ACKNOWLEDGEMENTS

The present research was supported by Vietnam Ministry of Education and Training under grant code B2023-TNA-06.

COMPETING INTERESTS

The authors declare that there is no conflict of interest regarding the publication of this article.

REFERENCES

[1] M. Asif, R. Yasmin, S. Umbreen (2022), "Green synthesis of silver nanoparticles (agnps), structural characterization, and their antibacterial potential", *Dose-Response*, **20(2)**, DOI: 10.1177/15593258221088709.

[2] C. Liao, Y. Li, S.C. Tjong (2019), "Bactericidal and cytotoxic properties of silver nanoparticles", *International Journal of Molecular Sciences*, **20(2)**, pp.449-452, DOI: 10.3390/ijms20020449.

[3] E.Y. Ahn, H. Jin, Y. Park (2019), "Assessing the antioxidant, cytotoxic, apoptotic and wound healing properties of silver nanoparticles green-synthesized by plant extracts", *Materials Science and Engineering C*, **101**, pp.204-216, DOI: 10.1016/j.msec.2019.03.095.

[4] R.A. Bapat, T.V. Chaubal, C.P. Joshi, et al. (2018), "An overview of application of silver nanoparticles for biomaterials in dentistry", *Materials Science and Engineering C*, **91**, pp.881-898, DOI: 10.1016/j.msec.2018.05.069.

[5] S. Nakamura, M. Sato, Y. Sato, et al. (2019), "Synthesis and application of silver nanoparticles (ag nps) for the prevention of infection in healthcare workers", *International Journal of Molecular Sciences*, **20(15)**, DOI: 10.3390/ijms20153620.

[6] K. Chand, D. Cao, D.E. Fouad, et al. (2020), "Green synthesis, characterization and photocatalytic application of silver nanoparticles synthesized by various plant extracts", *Arabian Journal of Chemistry*, **21(11)**, pp.8248-8261, DOI: 10.1016/j.arabjc.2020.01.009.

[7] A. Akbarzadeh, L. Kafshdooz, Z. Razban, et al. (2018), "An overview application of silver nanoparticles in inhibition of herpes simplex virus", *Artificial Cells, Nanomedicine, and Biotechnology*, **46(2)**, pp.263-267, DOI: 10.1080/21691401.2017.1307208.

[8] K. Zhang, V.C.H. Lui, Y. Chen, et al. (2020), "Delayed application of silver nanoparticles reveals the role of early inflammation in burn wound healing", *Scientific Reports*, **10(1)**, DOI: 10.1038/s41598-020-63464-z.

[9] S. Lee, B.H. Jun (2019), "Silver nanoparticles: Synthesis and application for nanomedicine", *International Journal of Molecular Sciences*, **20(4)**, DOI: 10.3390/ijms20040865.

[10] A.S. Anees, S.S. Das, A. Khatoon, et al. (2020), "Bactericidal activity of silver nanoparticles: A mechanistic review", *Materials Science for Energy Technologies*, **3(1)**, pp.756-769, DOI: 10.1016/j.mset.2020.09.002.

[11] S.K. Kailasa, T.J. Park, J.V. Rohit, et al. (2019), "Antimicrobial activity of silver nanoparticles", *Nanoparticles in Pharmacotherapy*, **2019**, pp.461-484, DOI: 10.1016/b978-0-12-816504-1.00009-0.

[12] A. Roy, O. Bulut, S. Some (2019), "Green synthesis of silver nanoparticles: biomolecule-nanoparticle organizations targeting antimicrobial activity', *RSC Advances*, **9(5)**, pp.2673-2702, DOI: 10.1039/c8ra08982e.

[13] J.Y. Cheon, S.J. Kim, Y.H. Rhee, et al. (2019), "Shape-dependent antimicrobial activities of silver nanoparticles", *International Journal of Nanomedicine*, **14**, pp.2773-2780, DOI: 10.2147/IJN.S196472.

[14] C.G.A. Das, V.G. Kumar, T.S. Dhas, et al. (2020), "Antibacterial activity of silver nanoparticles (biosynthesis): A short review on recent advances", *Biocatalysis and Agricultural Biotechnology*, **27**, DOI: 10.1016/j.bcab.2020.101593.

[15] M.G. Gordienko, V.V. Palchikova, S.V. Kalenov, et al. (2019), "Antimicrobial activity of silver salt and silver nanoparticles in different forms against microorganisms of different taxonomic groups", *Journal of Hazardous Materials*, **378**, DOI: 10.1016/j.jhazmat.2019.120754.

[16] T. Bruma, F.M. Bravo, P. Jara, et al. (2021), "Silver nanoparticles and their antibacterial applications", *International Journal of Molecular Sciences*, **22(13)**, DOI: 10.3390/ijms22137202.

[17] X. Yan, B. He, L. Liu, et al. (2018), "Antibacterial mechanism of silver nanoparticles in pseudomonas aeruginosa: Proteomics approach", *Metallomics*, **10(4)**, pp.557-564, DOI: 10.1039/C7MT00328E.

[18] Y. Qing, L. Cheng, R. Li, et al. (2018), "Potential antibacterial mechanism of silver nanoparticles and the optimization of orthopedic implants by advanced modification technologies", *International Journal of Nanomedicine*, **13**, pp.3311-3327, DOI: 10.2147/ijn.s165125.

[19] S. Tang, J. Zheng (2018), "Antibacterial activity of silver nanoparticles: Structural effects", *Advanced Healthcare Materials*, **7(13)**, DOI: 10.1002/adhm.201701503.

[20] S. Liao, Y. Zhang, X. Pan, et al. (2019), "Antibacterial activity and mechanism of silver nanoparticles against multidrug-resistant Pseudomonas aeruginosa", *Int. J. Nanomedicine*, **25(14)**, pp.1469-1487, DOI: 10.2147/IJN.S191340.

[21] G. Navarro, E. Alpaslan, M. Wang, et al. (2019), "Characterization and study of the antibacterial mechanisms of silver nanoparticles prepared with microalgal exopolysaccharides", *Materials Science and Engineering C*, **99**, pp.685-695, DOI: 10.1016/j.msec.2019.01.134.

[22] A. Salleh, R. Naomi, N.D. Utami, et al. (2020), "The potential of silver nanoparticles for antiviral and antibacterial applications: A mechanism of action", *Nanomaterials*, **10(8)**, pp.1566-1572, DOI: 10.3390/nano10081566.

[23] R. Rajkumar, G. Ezhumalai, M. Gnanadesigan (2020), "A green approach for the synthesis of silver nanoparticles by *Chlorella vulgaris* and its application in photocatalytic dye degradation activity", *Environmental Technology & Innovation*, **21**, DOI: 10.1016/j.eti.2020.101282.

[24] M.A. Kareem, I.T. Bello, H.A. Shittu, et al. (2020), "Green synthesis of silver nanoparticles (AgNPs) for optical and photocatalytic applications: A review", *IOP Conference Series: Materials Science and Engineering*, **805**, DOI: 10.1088/1757-899X/805/1/012020.

[25] J. Singh, S.S. Jolly, K.H. Kim, et al. (2019), "Biogenic synthesis of silver nanoparticles and its photocatalytic applications for removal of organic pollutants in water", *Journal of Industrial and Engineering Chemistry*, **80(1)**, pp.247-257, DOI: 10.1016/j.jiec.2019.08.002.

[26] G.B. Strapasson, A.G. Kontos (2021), "Microwave assisted synthesis of silver nanoparticles and its application in sustainable photocatalytic hydrogen evolution", *International Journal of Hydrogen Energy*, **46(69)**, pp.34264-34275, DOI: 10.1016/j.ijhydene.2021.07.23.

[27] M.S. Samuel, S. Jose, E. Selvarajan, et al. (2019), "Biosynthesized silver nanoparticles using Bacillus amyloliquefaciens; Application for cytotoxicity effect on A549 cell line and photocatalytic degradation of p-nitrophenol", *Journal of Photochemistry and Photobiology B*, **202**, DOI: 10.1016/j.jphotobiol.2019.111642.

[28] K. Gudikandula, S. Charya Maringanti (2016), "Synthesis of silver nanoparticles by chemical and biological methods and their antimicrobial properties", *Journal of Experimental Nanoscience*, **11(9)**, pp.1-8, DOI: 10.1080/17458080.2016.1139196.

[29] M. Rafique, I. Sadaf, M.S. Rafique, et al. (2016), "A review on green synthesis of silver nanoparticles and their applications", *Artificial Cells Nanomedicine, and Biotechnology*, **45(7)**, pp.1-20, DOI: 10.1080/21691401.2016.1241792.

[30] D.T. Hue, N.T.P. Thao, T.K. Khoi, et al. (2021), "Multi-shaped silver meso-particles with tunable morphology for surface enhanced Raman scattering", *Optics Communications*, **497**, DOI: 10.1016/j.optcom.2021.127200.

[31] A. Ahmed, M. Ahmad, B.L. Swami, et al. (2015), "A review on plants extract mediated synthesis of silver nanoparticles for antimicrobial applications: A green expertise", *Journal of Advanced Research*, **7(1)**, pp.17-28, DOI: 10.1016/j.jare.2015.02.007.

[32] R. Shanmuganathan, I. Karuppusamy, M. Saravanan, et al. (2019), "Synthesis of silver nanoparticles and their biomedical applications - A comprehensive review", *Current Pharmaceutical Design*, **25(24)**, pp.2650-2660, DOI: 10.2174/1381612825666190708185506.

[33] M. Ahmed, G. Murtaza, A. Mehmood, et al. (2015), "Green synthesis of silver nanoparticles using leaves extract of Skimmia laureola: Characterization and antibacterial activity", *Materials Letters*, **153**, pp.10-13, DOI: 10.1016/j.matlet.2015.03.143.

[34] S. Kumar, B. Ankamwar, S. Karmakar, et al. (2018), "Green synthesis of silver nanoparticles using the plant extract of Shikakai and Reetha", *Materials Today: Proceedings*, **5(1)**, pp.2321-2329, DOI: 10.1016/j.matpr.2017.09.236.

[35] P. Tamilarasi, P. Meena (2020), "Green synthesis of silver nanoparticles (Ag NPs) using Gomphrena globosa (Globe amaranth) leaf extract and their characterization", *Materials Today: Proceedings*, **33(5)**, pp.2209-2216, DOI: 10.1016/j.matpr.2020.04.025.

[36] T. Varadavenkatesan, R. Selvaraj, R. Vinayagam (2019), "Green synthesis of silver nanoparticles using Thunbergia grandiflora flower extract and its catalytic action in reduction of Congo red dye", *Materials Today: Proceedings*, **23(1)**, pp.39-42, DOI: 10.1016/j.matpr.2019.05.441.

[37] N. Namratha, P.V. Monica (2013), "Synthesis of silver nanoparticles using *Azadirachta indica* (Neem) extract and usage in water purification", *Asian Journal of Pharmacy and Technology*, **3(4)**, pp.170-174.

[38] H.A. Widatalla, L.F. Yassin, A.A. Alrasheid, et al. (2022), "Green synthesis of silver nanoparticles using green tea leaf extract, characterization and evaluation of antimicrobial activity", *Nanoscale Advances*, **4(3)**, pp.911-915, DOI: 10.1039/D1NA00509J.

[39] P.J. Burange, M.G. Tawar, R.A. Bairagi, et al. (2021), "Synthesis of silver nanoparticles by using *Aloe vera* and *Thuja orientalis* leaves extract and their biological activity: A comprehensive review", *Bull. Natl. Res. Cent.*, **45**, DOI: 10.1186/s42269-021-00639-2.

[40] S. Li, A. Xie, X. Yu (2007), "Green synthesis of silver nanoparticles using Capsicum *annuum* L. extract", *Chemistry*, **9(8)**, DOI: 10.1039/b615357g.

[41] S. Nayak, S.P. Sajankila, C.V. Rao, et al. (2019), "Biogenic synthesis of silver nanoparticles using *Jatropha curcas* seed cake extract and characterization: Evaluation of its antibacterial activity", *Energy Sources, Part A: Recovery, Utilization, and Environmental Effects*, **43(24)**, pp.1-9, DOI: 10.1080/15567036.2019.1632394.

[42] H.J. Lee, J.Y. Song, B.S. Kim (2013), "Biological synthesis of copper nanoparticles usingMagnolia kobusleaf extract and their antibacterial activity", *Journal of Chemical Technology & Biotechnology*, **1**, DOI: 10.1002/jctb.4052.

[43] S.P. Singh, A. Mishra, R.K. Shyanti, et al. (2021). "Silver nanoparticles synthesized using carica papaya leaf extract ($AGNP_S$-PLE) causes cell cycle arrest and apoptosis in human prostate (du145) cancer cells", *Biol. Trace Elem. Res.*, **199**, pp.1316-1331, DOI: 10.107/s12011-020-02255-2.

[44] L. Le, M. Fan, B. Liu, et al. (2022), "Green formulation of Ag nanoparticles by Hibiscus rosa-sinensis: Introducing a navel chemotherapeutic drug for the treatment of liver cancer", *Arabian Journal of Chemistry*, **15(2)**, DOI: 10.1016/j.arabjc.2021.103602.

[45] W. Wenzhi, P. Ma, Q. Zhao, et al. (2022), "Beneficial properties of the biosynthesized silver/chitosan nanoparticles mediated by *Mentha piperita* in rats with heart failure following myocardial infarction", *Inorganic Chemistry Communications*, **141**, DOI: 10.1016/j.inoche.2022.109581.

[46] L.V. Morales, H.E. Gómez, L.Z.F. López, et al. (2020), "Study of the effect of the different parts of *Morinda citrifolia* L. (noni) on the green synthesis of silver nanoparticles and their antibacterial activity", *Applied Surface Science*, **537**, DOI: 10.1016/j.apsusc.2020.147855.

[47] D.N.P. Sudarmani, S.S. Saravana, C. Sundareswari, et al. (2021), "Bioefficacy of sesbania grandiflora leaves silver nanoparticles against aedes aegypti larvae", *Journal of Advanced Scientific Research*, **12(4)**, pp.176-184, DOI: 10.55218/JASR.s1202112419.

[48] M. Dadashpour, A.F. Amandi, M.P. Moghaddam, et al. (2018), "Biomimetic synthesis of silver nanoparticles using *Matricaria chamomilla* extract and their potential anticancer activity against human lung cancer cells", *Materials Science and Engineering C*, **92**, pp.902-912, DOI: 10.1016/j.msec.2018.07.053.

[49] B. Sadeghi, F. Gholamhoseinpoor (2015), "A study on the stability and green synthesis of silver nanoparticles using Ziziphora tenuior (Zt) extract at room temperature", *Spectrochimica Acta. Part A, Molecular and Biomolecular Spectroscopy*, **134**, pp.310-315, DOI: 10.1016/j.saa.2014.06.046.

[50] K. Bączek, O. Kosakowska, M. Gniewosz, et al. (2019), "Sweet basil (*Ocimum basilicum* L.) productivity and raw material quality from organic cultivation", *Agronomy*, **9(6)**, 15pp, DOI: 10.3390/agronomy9060279.

[51] E.C. Vreeland, J. Watt, G.B. Schober, et al. (2015), "Enhanced nanoparticle size control by extending LaMer's mechanism", *J. Chemistry of Materials*, **27(17)**, pp.6059-6066, DOI: 10.1021/acs.chemmater.5b02510.

[52] K.L. Kelly, E. Coronado, L.L. Zhao, et al. (2003), "The optical properties of metal nanoparticles: The influence of size, shape, and dielectric environment", *The Journal of Physical Chemistry B,* **107(3)**, pp.668-677, DOI: 10.1021/jp026731y.

[53] M. Alavi (2022), "Bacteria and fungi as major bio-sources to fabricate silver nanoparticles with antibacterial activities", *Expert Review of Anti-infective Therapy*, **20(6)**, pp.897-906, DOI: 10.1080/14787210.2022.2045194.

Degradation of acrylic-melamine based varnish containing Tinuvin 292 with accelerated exposure in fluorescent UV and condensation

Trung Thanh Nguyen*

Institute of Technology, General Department of Defence Industry, Dong Ngac Ward, Bac Tu Liem District, Hanoi, Vietnam

Received 1 July 2022; revised 22 September 2022; accepted 28 September 2022

Abstract:

The durability of an acrylic-melamine (AC-ML) based varnish containing Tinuvin 292 when exposed to 100 cycles of accelerated exposure testing in fluorescent UV and condensation was investigated. Fourier-transform infrared (FT-IR) spectroscopy, thermal gravimetric analysis (TGA), and scanning electron microscope (SEM) were used to evaluate the changes between the initial and aged coatings. The obtained results showed that gloss loss, adhesion, flexibility, impact resistance, and relative hardness of the AC-ML varnish were enhanced with 2.5 wt.% of Tinuvin 292. FT-IR spectrums of the initial and aged samples without Tinuvin 292 illustrated strong changes in intensity of CH_2 and C=O (ester) groups. AC-ML varnish with 2.5 wt.% of Tinuvin 292 exhibited changes in the peaks of the CH_2 and ester groups after accelerated exposure testing. SEM images showed that the surface of the aged AC-ML varnish without Tinuvin 292 was rougher than that of the coating with Tinuvin 292. TGA results also showed that 2.5 wt.% of Tinuvin 292 had improved thermal oxidation stability of the AC-ML based varnish.

Keywords: **accelerated exposure testing, acrylic-melamine varnish coating, degradation, FT-IR, physico-mechanical properties, thermal oxidation resistance, Tinuvin 292.**

Classification numbers: **2.2, 2.3**

1. Introduction

Degradation of polymers, in general, and paint coatings, in particular, under high temperature, humidity, oxygen, thermal changing, and UV radiation result in the damage of polymers or adhesion loses, chalking, or blistering, etc. [1-4]. Many authors have studied how to reduce coating degradation under UV light by using carbon black, graphene oxide, nanosilica, zinc oxide (ZnO), and inorganic pigments [5-8]. Unfortunately, these above anti-UV additives tend to agglomerate or cluster, so they are difficult to disperse in coatings and thus cannot be used for varnishes due to losing their transparency [9-11].

AC-ML paint with its high relative hardness, polish, and chemical resistance is widely used for electrical details, household items, insulating metarials, and automotive products [12-15]. Even baking acrylic- melamine coatings are widely used for outdoor purposes, but publications on their degradation have been limited [14-16]. In our last article, the authors studied the effects of acrylic/melamine ratio and baking temperature on mechanical properties, thermal resistance, and chemical resistance to determine the optimal ratio and drying temperature for the AC-ML varnish coating. From which, the conditions of acrylic/melamine ratio (wt.%) of 35/15, baking temperature of 140^{o}C, and baking time of 60 min were determined as optimal. Results also showed that the AC-ML varnish was capable of being used to protect metal parts under several chemical conditions [17].

Tinuvin 292 is a liquid hindered amine light stabilizer that is especially developed for protecting coatings from UV radiation. It is useful for varnish in UV radiation protection [18].

This article will address the effect of Tinuvin 292 on the degradation of AC-ML varnish when subjected to accelerated exposure in fluorescent UV and condensation with FT-IR analysis. Besides that, mechanical properties, gloss loss, surface morphology, and thermal oxidation resistance of initial and aged AC-ML varnish coatings were also investigated.

2. Materials and methods

2.1. Materials

Acrylic resin (trade name of Eterac 7108-X-54) was supplied by Eternal Chemical Co., Ltd (Taiwan), with an appearance of clear/clean, acid value (mg KOH/g): 5-9, and solid content of (60±1)%.

Melamine resin (trade name of MF268) was purchased from Synpol Products Private Ltd. (India), with free formaldehyde ≤3%, acid value (mg KOH/g) ≤3%, and solid content (60±2)%.

Xylene, acetone, and butyl acetate were purchased from Industrial Products (China).

Tinuvin 292 (Bis(1,2,2,6,6-pentamethyl-4-piperidinyl)-sebacate and 1-(Methyl)-8-(1,2,2,6,6-pentamethyl-4-piperidinyl)-sebacate) was supplied by Kremer Pigmente GmbH & Co. KG (Germany).

*Email: nguyentrungthanhk42@gmail.com

2.2. Varnish preparation [17]

Raw materials were prepared as given in Table 1. Acrylic resin and melamine resin were dissolved in xylene, then acetone and butyl acetate was added. The varnish was well mixed and the samples were formed (according to ISO 15528:2013) on steel panels according to ISO 1514:2016 for testing of mechanical properties.

Table 1. Composition of AC-ML varnish.

No.	Components	Weight percent (wt.%)
1	Acrylic, Eterac 7108-X-54	35
2	Melamine, MF268	15
3	Xylene	30
4	Butyl acetate	12-15
5	Acetone	5
6	Tinuvin 292	0-3.0

2.3. Sample preparation

Samples for mechanical properties measurement and salt mist testing were prepared on steel panels (ISO 1514:2016). Paint coatings were deposited on the cleaned panels by using a spray gun with pressure of 4 kg/cm^2.

These coatings were prepared and kept at a temperature of (25±2)^{o}C and humidity of (50±5)% for one day, then baked at 140^{o}C for 60 min, and then kept at room temperature for five days before testing [17]. The thickness of the dried coatings was (30±3) µm as measured with a Minitest 600 Erichsen digital meter.

2.4. Analysis methods

Accelerated exposure testing was performed in a UV/condensation weathering chamber (Atlas UVCON UC-327-2) with UVB-313 fluorescent lamps and operated under conditions of one cycle including 8 h of UV irradiation at 60°C following by 4 h of dark with water condensation at 50°C in accordance ASTM D4587-11. FT-IR spectroscopy was conducted on a Fourier FTIR-8700 series converter.

Morphology of the coating film was observed by FE-SEM (Hitachi S4800) with a magnification of 1,000 times and voltage of 5 kV.

Gloss of the coating was determined according to ISO 2813:2014 with an angle of 60 degrees. Adhesion of the coating was determined according to ISO 2409:2013. Flexibility of the coating was determined according to ISO 1519:2011. Impact resistance of the coating was determined according to ISO 6272-1:2011. Finally, relative hardness of the coating was determined according to ISO 1522:2006.

Thermal oxidation resistance was determined by TGA as analysed by a NETZSCH TG 209F1 LIBRA with a heat rate of 10^{o}C/min from ambient temperature to 600^{o}C in air atmosphere.

3. Results and discussion

3.1. Effect of Tinuvin 292 content on physico-mechanical properties of AC-ML varnish when subjected to accelerated exposure of fluorescent UV and condensation

To study the effect of Tinuvin 292 content on gloss loss and mechanical properties in AC-ML varnish after accelerated exposure testing, samples with thickness of 30±3 µm were prepared with Tinuvin 292 content of 0, 1.0, 2.0, 2.5, and 3.0, which were named M0, M1, M2, M3, and M4, respectively. Results from 100 cycles of ageing testing are shown in Tables 2 and 3.

Table 2. Gloss and mechanical properties of initial AC-ML varnish coatings.

Samples	Gloss at 60^o	Mechanical properties of coating			
		Adhesion (points)	*Flexibility (mm)*	*Impact resistance (kg.cm)*	*Relative hardness*
M0	81	1	2	200	0.59
M1	81	1	2	200	0.59
M2	81	1	2	200	0.59
M3	80	1	2	200	0.59
M4	80	1	2	200	0.59

Table 3. Gloss and mechanical properties of aged AC-ML varnish coatings.

Samples	Gloss at 60^o	Mechanical properties of coating			
		Adhesion (points)	*Flexibility (mm)*	*Impact resistance (kg.cm)*	*Relative hardness*
M0	43	5	6	80	0.71
M1	49	4	5	140	0.68
M2	61	2	3	180	0.64
M3	76	1	2	200	0.60
M4	77	1	2	200	0.60

Table 2 showed that Tinuvin 292 did not affect the mechanical properties and gloss of AC-ML varnish. Table 3 showed that after 100 cycles of ageing testing, as the content of Tinuvin 292 increased, adhesion, flexibility, impact resistance, and gloss of coatings had less of a reduction. After ageing testing, impact resistance of M0 (the sample without Tinuvin 292) decreased strongly from 200 to 80 kg.cm, relative hardness increased from 0.60 to 0.71, and flexibility increased from 2 to 6 mm. This meant that the coating became more brittle and lost its adhesion. Meanwhile, samples M3 (sample with 2.5 wt.% of Tinuvin 292) and M4 (sample with 3 wt.% of Tinuvin 292) only showed slight changes to adhesion, flexibility, impact resistance, and gloss loss. The results also showed that for Tinuvin 292 content over 2.5 wt.%, the relative hardness of aged coatings did not increase. This can be explained that Tinuvin 292 (light stabilizer) had prevented polymer chains from breaking down and being severed, so ageing of the polymers by UV rays was limited [18-20]. Hence, with Tinuvin 292, mechanical properties of AC-ML varnish are better than those without Tinuvin 292 after 100 cycles of accelerated exposure testing, and the same also occurred with the gloss value

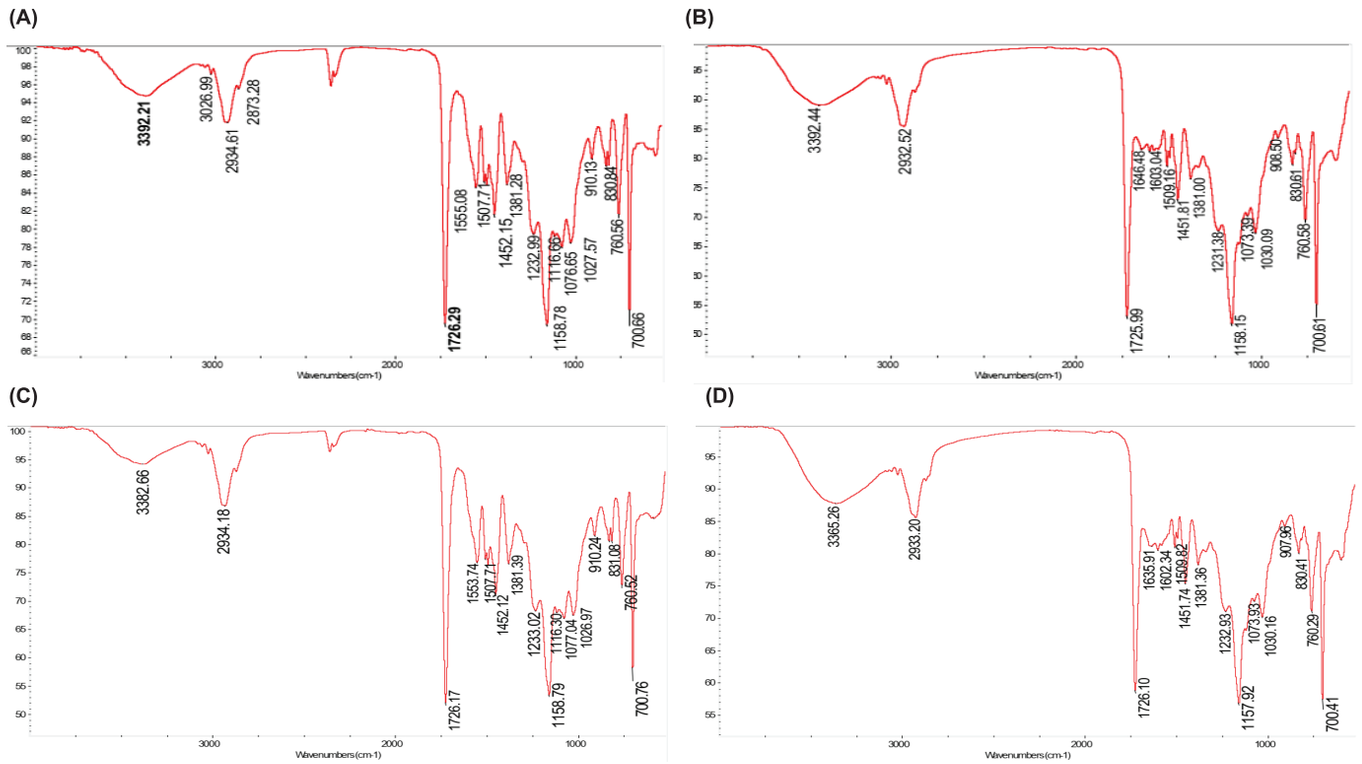

Fig. 1. IR spectra of M0 (A) before and (B) after accelerated exposure testing and M3 (C) before and (D) after accelerated exposure testing.

of AC-ML varnish [21, 22]. Therefore, Tinuvin 292 enhanced the mechanical properties and gloss of the AC-ML varnish under UV radiation conditions. Based on above results, M3 was chosen for further study.

3.2. FT-IR spectroscopy analysis

In general, degradation of polymers may not be seen by their appearance but through the chemical changes of their functional groups. Therefore, to investigate the chemical changes of the initial and aged coatings' functional groups, FT-IR spectroscopy was performed on M0 and M3 of before and after ageing with 100 cycles of accelerated exposure. The results are shown in Figs. 1A-D and Table 4.

Figures 1A and 1B showed that the peak intensity of CH_2 (3026 or 2934) sharply decreased and even peak 2873 of CH_2 in Fig. 1A disappeared in Fig. 1B. This can be explained that the polymer molecular chain had been severed and the molecular length became much shorter. At the same time, the intensities of the ester group peaks (1726 of C=O and 1232 of C-O) decreased as the ester bond was destroyed to form new bonds such as ketones due to optical oxidation or as C=O and C-O groups were stretched and rocked [19, 21]. As can be seen in Figs. 1C and 1D, there was only a small difference in intensities of peaks between the before- and after-aging samples. These results show that in varnish with Tinuvin 292, peak intensities of CH_2 (2934) and ester groups (1726 of C=O and 1233 of C-O) also stretched but intensities and vibrations of these peaks reduced insignificantly compared to the initial sample. Photo-degradation of polymers may occur to chain scissions or macroradical disproportionation, leading to terminal double bonds [20, 21]. In the sample with Tinuvin 292 (M3), there was little difference in peak intensities between before and after ageing. In the sample without Tinuvin 292, macroradical disproportionation attacked polymer chains to produce C=C bonds. In the case of AC-ML varnish containing Tinuvin 292, macroradicals would attack the conjugated double bonds of Tinuvin 292. In other words, Tinuvin 292 absorbed the UV rays and, thus, reduced coating degradation [23-25].

Table 4. Fluctuations in infrared AC-ML varnish coatings.

No.	Typical spectrum	Wavenumbers (cm^{-1})
1	vCH, stretch	3392
2	vas(CH_2=), asymmetry in vinyl group	3026
3	vas(CH_2=), asymmetry in carbon chain	2934
		2932
4	v(CO) of fat acid	1726
		1725
5	v(C=C) in vinyl group	1646
6	vC=C (epoxy aromatic ring)	1555
7	vCH	1232
		1231
8	vC-O stretch, vibrations	1158
9	vaC-O-C (asymmetry)	1076
		1073
10	ω(CH_2), oscillation of CH_2 near vinyl group	910
		908
11	□(CH), oscillation deformation of CH in aromatic ring	760

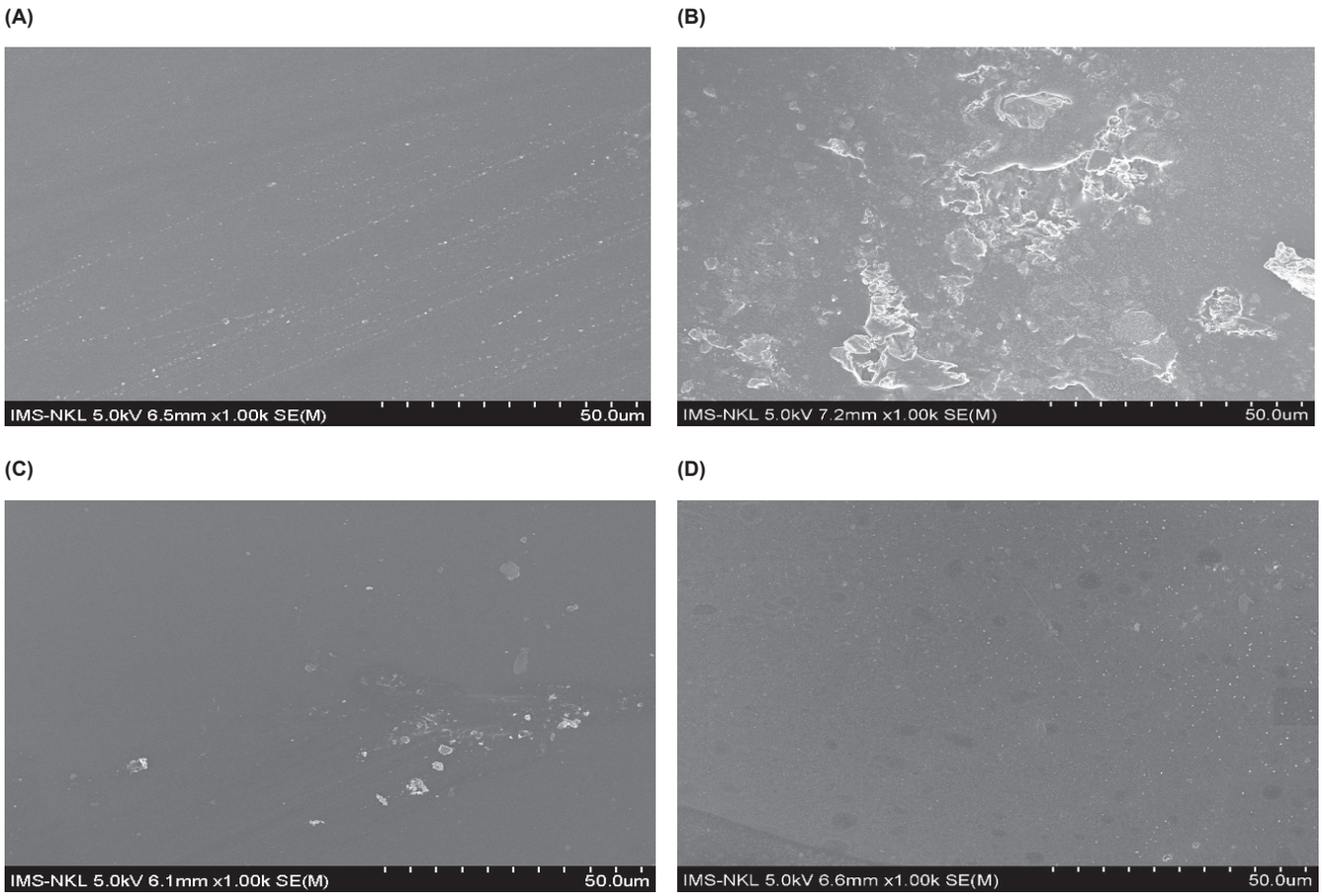

Fig. 2. Surface SEM images (A) before and (B) after accelerated exposure testing and M3 (C) before and (D) after accelerated exposure testing.

3.3. Morphology of varnish coating surface

Samples M0 and M3, as mentioned in Table 2, were selected to investigate the effect of 100 cycles of the accelerated exposure testing on the surface of AC-ML varnish coatings. The obtained results are shown in Fig. 2.

Figure 2D showed that after ageing testing, there were no cracks, blisters, or surface changes on M3. The surface of M0 and M3 after 100 cycles of accelerated exposure testing were rougher when compared with the initial sample surfaces. For M0, in comparison with initial sample, the sample surface after the aging testing was strongly damaged and had pinholes. This can be explained by the oxidation process that occurred, which led to the generation of micro-cavities and micro-holes on coating's surface [21, 23, 25]. These results indicate that Tinuvin 292 with a content of 2.5 wt.% is suitable for protecting AC-ML varnish from the effect of UV irradiation and humidity condensation impacts for long time (about 100 cycles).

3.4. Effect of Tinuvin 292 on thermal oxidation resistance of coating

To study the effect of Tinuvin 292 on thermal oxidation resistance of AC-ML varnish, TGA was carried out on M0 and M3 before and after testing with 100 cycles of accelerated exposure. Results are shown in Table 5 and Fig. 3.

Table 5. Effect of Tinuvin 292 on thermal oxidation resistance of AC-ML varnish.

Samples	Weight loss (%)		
	300°C	*400°C*	*500°C*
M0 (initial)	6.81	56.05	85.25
M0 (aged)	9.53	59.58	90.68
M3 (initial)	3.56	41.35	85.06
M3 (aged)	8.05	53.18	87.82

Table 5 and Fig. 3 showed that the samples had different curve slopes. At different temperatures, weight loss of samples was different, too. The TGA curve slope of aged M0 was the highest. The results also showed that Tinuvin 292 had remarkably enhanced thermostability of the coating [5, 19-21]. This can be explained that under 200°C, decomposition occurred with low molecular substances and residual solvents with a decomposition volume of about 2-4%. Up to 400°C, decomposition occurred with residual functional groups in polymer branches, which are low molecular substances. The decomposition of M0 and M3 was the

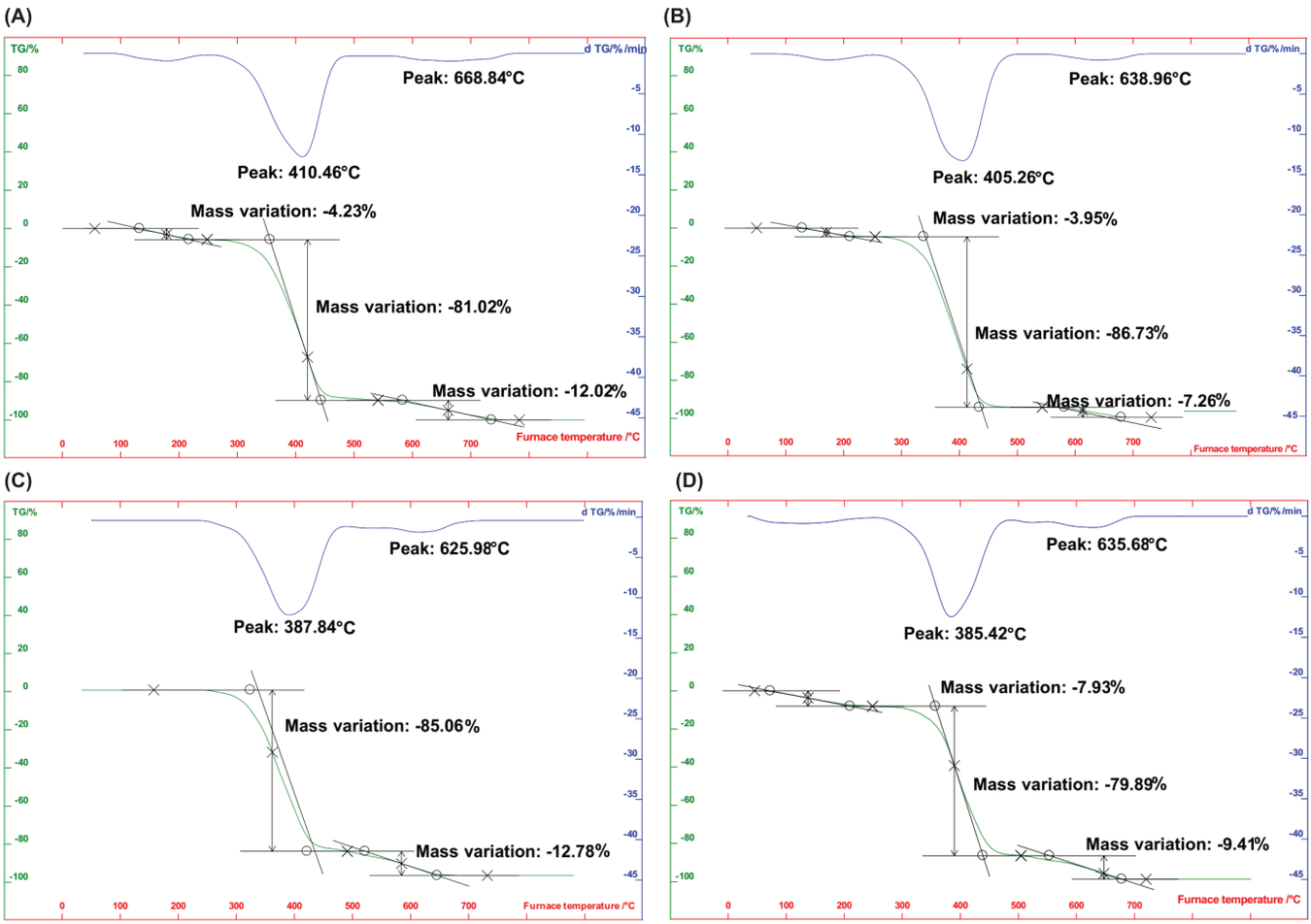

Fig. 3. TGA diagrams of (A) before and (B) after accelerated exposure testing and M3 (C) before and (D) after accelerated exposure testing.

same. Meanwhile, aged M0 decomposed more than aged M3 and was the strongest of all. This can be explained that after aging, polymer chains of M0 had been broken and while the Tinuvin 292 in sample M3 had prevented polymer chains from breaking, lowering its decomposition [20, 21]. By Tinuvin 292 preventing chemical bonds of the polymers from breaking, slits in the material structure were reduced thereby reducing oxygen permeation in the material and increasing thermal oxidation resistance of the coating. Up to 500°C and above, the decomposition of the two samples were similar because at high temperatures all organic components were burnt or decomposed and inorganic parts of samples remained the same [26-28].

4. Conclusions

Investigations indicated that the presence of Tinuvin 292 improved adhesion, flexibility, impact resistance, relative hardness, and gloss loss of AC-ML varnish after 100 cycles of accelerated exposure testing. The suitable content of Tinuvin 292 for this varnish was determined to be 2.5 wt.%. Under UV irradiation, bonds of ~CH_2 and ester groups of the samples without Tinuvin 292 strongly decreased. Meanwhile, the sample with Tinuvin 292 found the breakage of those groups to be limited. AC-ML varnish with 2.5 wt.% of Tinuvin 292 could withstand 100 UV-thermo-humidity complex cycles without cracks, blisters, or visible surface changes. Thus, Tinuvin 292 improved the thermal oxidation resistance of AC-ML varnish. From room temperature to 400°C, with Tinuvin 292, the decomposition of the sample was 53.18 compared to a value of 59.58 from the sample without Tinuvin 292.

COMPETING INTERESTS

The author declares that there is no conflict of interest regarding the publication of this article.

REFERENCES

[1] M.M.D. Crescenzo, E. Zendri, M.S. Pons, et al. (2014), "The use of waterborne paints in contemporary murals: Comparing the stability of vinyl, acrylic and styrene-acrylic formulations to outdoor weathering conditions", *Polym. Degrad. Stab.*, **107**, pp.285-293, DOI: 10.1016/j.polymdegradstab.2013.12.034.

[2] C. Queant, P. Blanchet, V. Landry, et al. (2019), "Comparison of two encapsulation systems of UV stabilizers on the UV protection efficiency of wood clear coats", *J. Polym. Eng.*, **39(1)**, pp.94-103, DOI: 10.1515/polyeng-2018-0026.

[3] E. Kızılkonca, F.B. Erim (2019), "Development of anti-aging and anticorrosive nanoceria dispersed alkyd coating for decorative and industrial purposes", *Coatings*, **9(10)**, DOI: 10.3390/coatings9100610.

[4] A. Cogulet, P. Blanchet, V. Landry (2019), "Evaluation of the impacts of four weathering methods on two acrylic paints: Showcasing distinctions and particularities", *Coatings*, **9(2)**, DOI: 10.3390/coatings9020121.

[5] A.G. Kahrizsangi, J. Neshati, H. Shariatpanahi, et al. (2015), "Improving the UV degradation resistance of epoxy coatings using modified carbon black nanoparticles", *Prog. Org. Coat.*, **85**, pp.199-207, DOI: 10.1016/j.porgcoat.2015.04.011.

[6] M.S. Selim, M.A. Shenashen, A. Elmarakbi, et al. (2017), "Sunflower oil-based hyperbranched alkyd/spherical ZnO nanocomposite modeling for mechanical and anticorrosive applications", *RSC Adv.*, **7(35)**, pp.21796-21808, DOI: 10.1039/C7RA01343D.

[7] S. Das, P. Pandey, S. Mohanty, et al. (2017), "Investigation into the influence of UV aging on green polyurethane/nanosilica composite coatings based on transesterified castor oil and palm oil isocyanate", *J. Inorg. Organomet. Polym. Mater.*, **27(3)**, pp.641-657, DOI: 10.1007/s10904-017-0506-z.

[8] N.T. Thanh (2022), "Improvement of environmentally friendly alkyd composite coating with graphene oxide", *MJCSM*, **7(1)**, pp.1-10, DOI: 10.37934/mjcsm.7.1.110.

[9] V. Pintus, S. Wei, M. Schreiner, et al. (2016), "Accelerated UV ageing studies of acrylic, alkyd, and polyvinyl acetate paints: Influence of inorganic pigments", *Microchem. J.*, **124**, pp.946-961, DOI: 10.1016/j.microc.2015.07.009.

[10] S. Pourhashem, M.R. Vaezi, A. Rashidi, et al. (2017), "Exploring corrosion protection properties of solvent based epoxy-graphene oxide nanocomposite coatings on mild steel", *Corros. Sci.*, **115**, pp.78-92, DOI: 10.1016/j.corsci.2016.11.008.

[11] N.K. Akafuah, S. Poozesh, A. Salaimeh, et al. (2016), "Evolution of the automotive body coating process-a review", *Coatings*, **6(2)**, DOI: 10.3390/coatings6020024.

[12] G. Nishino, H. Sugimoto, E. Nakanishi et al. (2012), "Preparation and properties of acrylic melamine hard coating", *J. Appl. Chem.*, **123(1)**, pp.307-315, DOI: 10.1002/app.33727.

[13] Z. Bahreini, V. Heydari, Z. Namdari (2017), "Effects of nano-layered silicates on mechanical and chemical properties of acrylic-melamine automotive clear coat", *Pigment. Resin Technol.*, **46(2)**, pp.333-341, DOI: 10.1108/PRT-07-2016-0077.

[14] R. Han, Y. Zhang (2011), "Studies on performance of cured water-borne melamine-acrylic emulsion coatings", *J. Adhes. Sci. Technol.*, **25(8)**, pp.883-892, DOI: 10.1163/016942410X520916.

[15] B. Likozar, R.C. Korošec, I. Poljanšek, et al. (2011), "Curing kinetics study of melamine-urea-formaldehyde resin", *J. Therm. Anal. Calorim.*, **109(3)**, pp.1-10, DOI: 10.1007/s10973-011-1883-0.

[16] G. Nishino, S. Kanda, H. Sugimoto, et al. (2012), "Preparation and coating properties of an acrylic melamine resin containing silicone segments", *Polym. Bull.*, **68(7)**, pp.2049-2060, DOI: 10.1007/s00289-012-0716-z.

[17] N.T. Thanh (2021), "Influence of acrylic/melamine ratio on some properties of acrylic-melamine coating", *TNU J. Sci. Tech.*, **226(15)**, pp.53-59, DOI: 10.34238/tnu-jst.4783 (in Vietnamese).

[18] N.T. Vuong, D.P. Hung, D.K. Linh, et al. (2017), "Effect of R-TiO_2 and ZnO nanoparticles on the UV-shielding efficiency of water-borne acrylic coating", *Prog. Org. Coat.*, **110**, pp.114-121, DOI: 10.1016/j.porgcoat.2017.02.017.

[19] C. Queant, P. Blanchet, V. Landry, et al. (2018), "Effect of adding UV absorbers embedded in carbonate calcium templates covered with light responsive polymer into a clear wood coating", *Coatings*, **8(8)**, DOI: 10.3390/coatings8080265.

[20] E. Yousif, R. Haddad (2013), "Photodegradation and photostabilization of polymers, especially polystyrene: Review", *Springerplus*, **2(1)**, pp.1-32, DOI: 10.1186/2193-1801-2-398.

[21] M.A. Shenoy, Y.D. Marathe (2007), "Studies on synergistic effect of UV absorbers and hindered amine light stabilisers", *Pigment. Resin Technol.*, **36(2)**, pp.83-89, DOI: 10.1108/03699420710733510.

[22] A.Z.M. Rus, K. Terence, J.C. Andrew (2008), "Degradation studies of polyurethanes based on vegetable oils. Part 1. Photodegradation", *Prog. React. Kinet.*, **33(4)**, pp.363-391, DOI: 10.3184/146867808X377140.

[23] E. Moore (2017), *Fourier Transform Infrared Spectroscopy* (*FTIR*): *Methods, Analysis, And Research Insights*, Nova Science Publishers, 129pp.

[24] S. Nikafshar, O. Zabihi, M. Ahmadi, et al. (2017), "The effects of UV light on the chemical and mechanical properties of a transparent epoxy-diamine system in the presence of an organic UV absorber", *Materials*, **10(2)**, DOI: 10.3390/ma10020180.

[25] A. Kozak (2015), "Multi-criteria assessment of an acrylic coating exposed to natural and artificial weathering", *Procedia Eng.*, **108**, pp.664-672, DOI: 10.1016/j.proeng.2015.06.197.

[26] J. Hu, X. Li, J. Gao, et al. (2009), "Ageing behavior of acrylic polyurethane varnish coating in accelerated weathering environments", *Prog. Org. Coat.*, **65(4)**, pp.504-509, DOI: 10.1016/j.porgcoat.2009.05.002.

[27] Y. Liu, Z. Li, X. Ren (2014), "UV-protective treatment for Vectran (R) fibers with hybrid coatings of TiO_2/organic UV absorbers", *J. Adhes. Sci. Technol.*, **28(18)**, pp.1773-1782, DOI: 10.1016/j.colsurfa.2019.06.030.

[28] X.Y. Wei, Z.B. He, S.Q. Yuan, et al. (2022), "Enhancement of ultraviolet light resistance of colorless and transparent semi-alicyclic polyimide nanocomposite films via the incorporation of hindered amine light stabilizers for potential applications in flexible optoelectronics", *Polymers*, **14(6)**, DOI: 10.3390/polym14061091.

Fabrication of transparent flexible electrodes on polyethylene terephthalate substrate with high conductivity, high transmittance, and excellent stability

Tien Dat Doan[1, 2], Nhung Hac Thi[1, 2], Ho Thi Oanh[1], Tuyen Nguyen Duc[1], Dong Hoon Choi[3], Mai Ha Hoang[1, 2*]

[1]*Institute of Chemistry, Vietnam Academy of Science and Technology, 18 Hoang Quoc Viet Street, Nghia Do Ward, Cau Giay District, Hanoi, Vietnam*
[2]*Graduate University of Science and Technology, Vietnam Academy of Science and Technology, 18 Hoang Quoc Viet Street, Nghia Do Ward, Cau Giay District, Hanoi, Vietnam*
[3]*Department of Chemistry, Research Institute for Natural Science, Korea University, 145 Anam-ro, Seongbuk-gu, Seoul 02841, Korea*

Received 29 September 2022; revised 17 November 2022; accepted 23 November 2022

Abstract:

Transparent flexible electrodes based on silver nanowires (AgNWs) have great potential for practical applications and many studies have been carried out to improve their conductivity, transparency, and surface roughness. In this study, we demonstrate a new approach for the fabrication of high-performance transparent flexible electrodes based on AgNWs and graphene oxide (GO) on polymer substrates using the pressing method. The surface morphology of the pressed AgNW/GO electrode was characterised by atomic force microscopy (AFM) and observed by scanning electron microscope (SEM). The electrode had a low surface roughness with the root mean square (Rq) of 7 nm. The electrode exhibits a low sheet resistance of 22 Ω/sq, a high transmittance of ~88%, resulted in a figures-of-merit (FoM) value of ~12.6. The optical and electrical properties of the electrode are comparable to that of the flexible ITO electrode. In addition, the electrodes also displayed outstanding durability and mechanical stability. This simple and scalable fabrication method is expected to contribute to future studies on flexible transparent conductive electrodes.

***Keywords*:** **flexible conducting electrodes, graphene oxide, pressing method, silver nanowires.**

Classification numbers: **2.2, 2.3**

1. Introduction

Transparent electrodes are an important element of various optoelectronic devices such as organic light-emitting diodes (OLEDs) and organic solar cells (OSCs) [1]. So far, indium tin oxide (ITO) is the most common material utilized for transparent electrodes because of its low sheet resistance (<20 Ω/sq) and high transmittance (~90%) [2]. However, it has several disadvantages including brittleness, necessity for high-temperature treatment, and limited optical transmittance in near-infrared (NIR). The brittle property of ITO makes its unsuitable for flexible optoelectronic devices. In addition, the depletion of indium sources is also a major problem for the production of ITO electrodes. Therefore, the development of new flexible materials at low cost to replace ITO has become an important subject [3].

Nowadays, several types of materials can be used to fabricate transparent electrodes such as metal nanowires, graphene, carbon nanotubes, and conductive polymers [4, 5]. Among these, AgNWs have attracted significant attention and are studied extensively. AgNW electrodes show excellent electrical conductivity and transparency, which are comparable to ITO electrodes. Moreover, AgNW electrodes are flexible and have low manufacturing costs and a low level of inherent toxicity. Nevertheless, AgNW electrodes have two main disadvantages: (i) high surface roughness (Rq) due to pile-up at cross points and (ii) weak adhesion between the AgNWs and its polymer substrate. In order to increase the contact between the AgNWs as well as its interaction with the substrate, the spin-coated electrode is usually thermally annealed. However, the annealed electrodes still have large surface roughness, which hampers their applications. Furthermore, the thermal annealing process may cause damage to polymer substrates such as polyethylene terephthalate (PET) or polyethylene naphthalate (PEN). In order to solve this problem, a researcher successfully fabricated AgNW electrodes by mechanical pressing at room temperature [6, 7]. However, in that study, the AgNW had a large diameter (about 70 nm), resulting in fabricated electrodes with low transmittance, resulting in a low figures-of-merit (FoM) value even when they were fabricated on a glass substrate. Lately, many studies have also used GO to improve electrical conductivity and the surface roughness of AgNW electrodes [8-10]. However, this solution only partially overcomes the problems mentioned above. Therefore, in this paper, we fabricated flexible electrodes with small-diameter AgNWs (~35 nm) and GO using a mechanical pressing method. The obtained electrode displayed high electrical conductivity, low surface roughness, and excellent stability.

2. Materials and methods

2.1. Materials

Silver nitrate ($AgNO_3$): purity ≥99.8% (Fisher Scientific); ethylene glycol (EG): 99% purity (Fisher Scientific); nickel(II) chloride: 99% purity (Sigma); graphite (size less than 20 μm, Sigma); polyvinylpyrrolidone (PVP) M_w=360,000 Da, purity 99% (Sigma); isopropanol: 99.7% purity (Sigma); sheet of

*Corresponding author: Email: hoangmaiha@ich.vast.vn

PET: size 300×300×0.25 mm (Sigma); absolute alcohol, sodium nitrate, potassium permanganate, hydrogen peroxide, concentrated hydrochloric acid solutions were used without further purification.

2.2. Synthesis of AgNWs

AgNWs were synthesised by the polyol method, using EG as a reducing agent in the presence of PVP surfactant [11, 12], with some modifications from the procedure reported in 2013 [10]. Firstly, 1.02 g $AgNO_3$, 1.66 g PVP, 200 ml EG, and 3.12 mg $NiCl_2$ were added to a flask and well-mixed under stirring. The mixture was heated and kept at 140ºC for 6 h. After the reaction, the AgNWs were filtered and washed several times with isopropanol by centrifugation and then dispersed in 100 ml of isopropanol to obtain an AgNWs dispersion with a concentration of 4 mg/ml. The synthesised AgNWs had an average diameter of 35 nm and an average length of 20 µm.

2.3. Synthesis of GO

GO was synthesised from graphite by the Hummer method [13]. The specific procedure included the following steps. Firstly, 48 ml of concentrated H_2SO_4 was cooled to below 5ºC, then 1 g of graphite and 0.5 g of $NaNO_3$ were added. The mixture was stirred at 5ºC for 60 minutes. Then, 6 g of $KMnO_4$ was slowly added to peel off the graphene layers. Finally, 10 ml H_2O_2 was added to the reaction to reduce excess Mn^{+7} ions to Mn^{+2} ions. The resultant GO was filtered and washed with distilled water by centrifugation to obtain a final solution with a concentration of 0.05%. The GO solution had high transparency and high durability, suitable for use in electrode fabrication.

2.4. Electrode fabrication

Four types of electrodes were fabricated: electrodes E1 (AgNWs) and E2 (AgNWs pressed) were fabricated by spin-coating only the AgNW dispersion onto the PET substrate (2000 rpm, 40 s) and electrodes E3 (AgNW/GO) and E4 (AgNW/GO pressed) were fabricated with a layer-by-layer spin-coating method using the AgNW dispersion and GO solution (2000 rpm, 40 s). After spin-coating, electrodes E2 and E4 were pressed at a pressure of 10 MPa for 20 s.

2.5. Characterisation

The surface morphology of the electrodes was characterised by atomic force microscopy (AFM, XE-100) using non-contact mode. The size and distribution of AgNWs on the electrode were observed by scanning electron microscope (SEM, S-4800, Hitachi, Japan). The sheet resistance of the electrode was measured with a Jandel RM3000 four-probe wafer resistance meter at 5 random positions on the electrode surface, then the average value was taken as the sheet resistance. The transmittance of the fabricated electrode was determined using a UV-Vis spectrophotometer (SP-3000 nano). Bending tests were carried out using a thin film bending tester that was custom-built. This tester allowed for control of the bending radius and number of bends with great precision. For testing the adhesion of the nanowire network and the PET substrate, 3M Scotch tape was attached to the surface of the electrode and then peeled off. The sheet resistance of the electrode was measured before and after attaching it with 3M scotch tape. The stability of the electrode in solvent was studied by placing the electrode in an ethanol solution and then sonicating for 10 min, drying completely, and then re-measuring the conductivity of the electrode.

3. Results and discussion

3.1. Surface morphology of the electrodes

The morphology and surface roughness of the fabricated electrodes were studied by AFM.

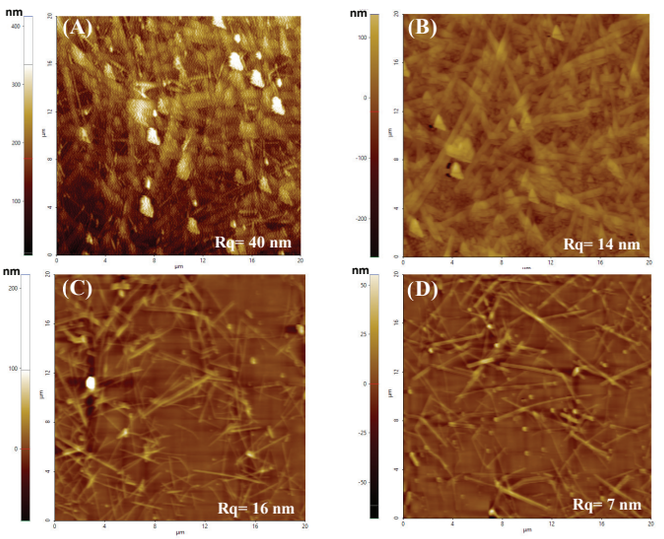

Fig. 1. Surface image of electrodes analysed by AFM. (A) Electrode E1, **(B)** Electrode E2, **(C)** Electrode E3, **(D)** Electrode E4.

The E1 electrode has a root mean square roughness (Rq) of 40 nm. The white areas protruding in the topography image (Fig. 1A) correspond to the intersection points of the AgNW network. These areas have high elevations that were caused by overlapping AgNWs. This issue was improved on the remaining electrodes (Figs. 1B, 1C, 1D). As shown in Fig. 1, the root means square roughness of the electrode decreases to 14 nm (E2), 16 nm (E3), and 7 nm (E4). This result indicates that the GO coating layer and the mechanical pressing method both make the AgNW electrode surface smoother.

The morphology of the electrodes was also studied by SEM images. For the E2 electrode, the AgNWs were tightly connected instead of overlapping as before pressing (Fig. 2A). The compressed connection points can be seen as shown in Fig. 2B. In the case of the E3 electrode, Fig. 2C exhibited GO covering the AgNW junctions. The thin GO layer contributes to tightly pressing the AgNW network onto the PET substrate surface, making the film electrode smoother and more stable.

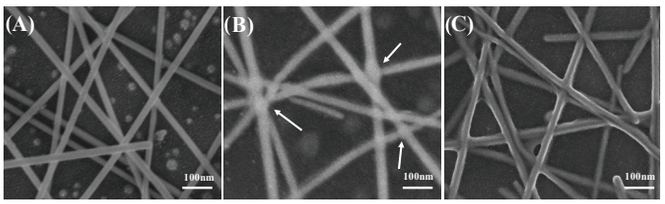

Fig. 2. SEM image of electrode surface in the top view. (A) Before, **(B)** After pressing (white arrows indicate junctions that have been pressed tightly by the pressing method) of AgNW electrodes, **(C)** AgNW/GO electrode.

The off-angle cross-sectional view shows that the AgNWs are not only tightly connected, but also sank into the PET substrate after the pressing process (Fig. 3B).

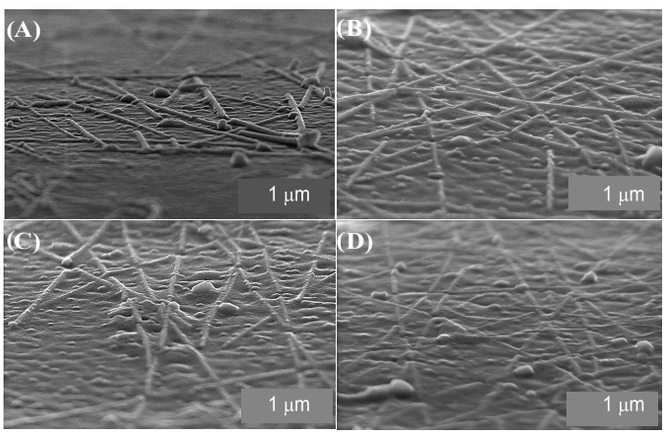

Fig. 3. SEM image of four electrode surfaces with tilt angle. (A) Electrode E1; **(B)** Electrode E2; **(C)** Electrode E3; **(D)** Electrode E4.

For the E3 electrode, GO was coated onto the AgNW network, thereby decreasing the surface roughness of the electrode. Therefore, the E3 electrode surface is smoother than that of E1, as shown in Fig. 3C. The E4 electrode is fabricated by combining both methods and it has a surface roughness value of only 7 nm. This result is better than that of the recently published AgNW/GO electrodes [3, 8, 14]. Off-angle FE-SEM observation indicated that the nanowires networks are tightly pressed onto the substrate, which reduces the protrusion of AgNWs (Fig. 3D).

3.2. Optical and electrical properties of electrodes

The results in Table 1 indicate that the resistance value after pressing the AgNWs and AgNW/GO electrodes significantly decreased from 120 to 33 Ω/sq and from 38 to 22 Ω/sq, respectively. Meanwhile, the transmittances of these electrodes were almost unchanged. After pressing, the conductivity of the electrodes improved significantly because the junctions were tightly bonded, allowing the charge to move easier in the silver nanowire network.

Table 1. Value of resistance, transmittance, and FoM index of 4 electrodes.

Electrode	E1	E2	E3	E4
R (Ω/sq)	120	33	38	22
T (%)	90	89	89	88
FoM×1000	2.9	9	8.2	12.6

As shown in Fig. 4, after pressing, the transmittance of the electrodes tends to decrease in the short wavelength range and increase in the long wavelength range. Fig. 5 illustrates the shape change of the AgNWs after pressing. The pressing method leads to a higher coverage ratio of the AgNW network on the electrode thus the absorption in the short-wavelength range increased. In contrast, after pressing, the AgNWs are thinner. Thus, long-wavelength light can pass through with lower loss. High transmittance in the near IR region in this electrode is an advantage for optoelectronic applications such as OSC devices.

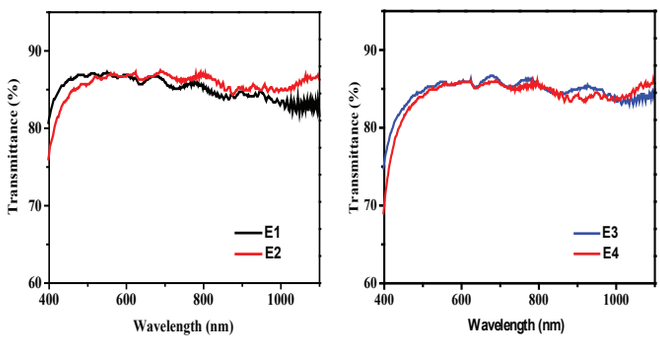

Fig. 4. The transmittance of the electrodes.

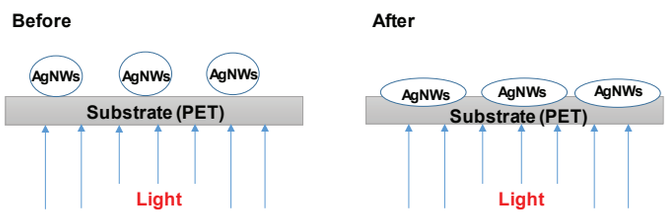

Fig. 5. Illustration the shape of AgNWs before and after pressing.

The FoM value of electrodes was evaluated to compare their performance. The FoM value represents the optimisation between the optical and electrical properties of the electrode and the classical FoM definition of Haacke is commonly used: $FoM = \frac{T^{10}}{R}$ (where T is the optical transmittance measured at a wavelength of 550 nm and R is the resistance value of the electrode) [15-18]. Calculation results (Table 1) show that the AgNW/GO electrode after pressing (E4) has the highest FoM value with an FoM×1000 value of 12.6. The FoM values of the remaining electrodes are 9 (E2), 8.2 (E3), and 2.9 (E1). Thus, the E4 electrode has the best balance between electrical and optical properties. With a FoM value of ~12.6 (sheet resistance value of 22 Ω/sq and a transmittance of 88%), the optical and electrical properties of the E4 electrode in this study are comparable to that of the flexible ITO electrode and higher than some recently announced flexible electrodes [2, 16].

3.3. Investigation of electrode durability

When the E1 electrode was bent with a curve radius of 4 mm, its resistance value increases by 60% after bending 2000 times. For E2 electrodes, which were pressed, their durability increased as shown in Fig. 6A.

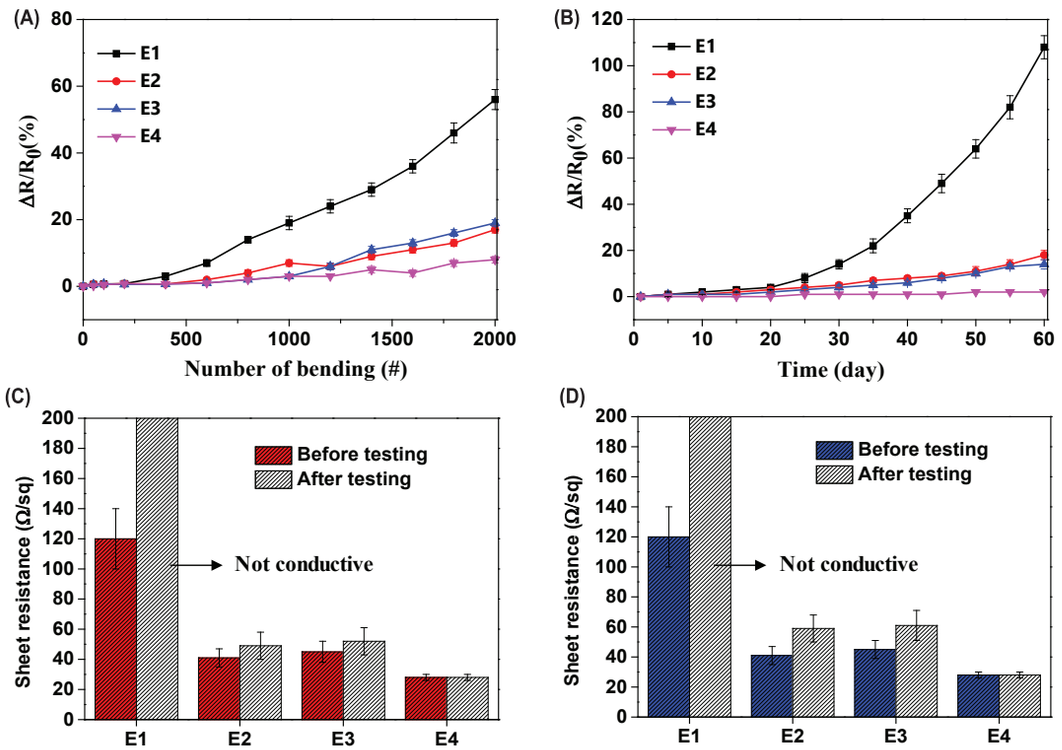

Fig. 6. Resistance changes of the 4 electrode types in the tests. (A) Bending with a radius curve of 4 mm; **(B)** Exposing the electrode to the normal environment; **(C)** Attaching 3M scotch tape to the electrode surface and then tape removal; **(D)** Rinsing the electrode in ethanol and subjecting it to ultrasonic vibration for 10 min.

Through 2000 bends, the resistance value of the E2 electrode rises slightly by 17%, which proves that the pressing method creates a strong interaction between AgNWs as well as the adhesion between the AgNW network and the PET substrate. For that reason, after the pressing process, the AgNW network was less damaged when subjected to mechanical impact. After coating with GO, the sheet resistance of the E3 electrode increased by 19% after 2000 bends. This phenomenon demonstrates that the GO layer also increases the adhesion of the AgNW network to the PET substrate. The E4 electrode has the highest mechanical durability. The sheet resistance of the pressed AgNW/GO electrode was almost unchanged after bending 2000 times. As shown in Fig. 6B, the sheet resistance value of the E1 electrode rapidly increased from 120 to 250 Ω/sq after 60 d of storage. For the E2 electrode, the sheet resistance value only increases by 18% under the same conditions. This demonstrates that the tight contact between the AgNWs makes the electrode more stable. In the case of the E3 electrode, the sheet resistance increased by 14% after the test period. It was reasoned that the coating of GO on AgNWs as a protective layer shielded the AgNWs from the effects of oxidation and humidity. Therefore, GO layers improve the stability of the electrodes. This phenomenon is consistent with the some published results [14, 19]. In this experiment, the E4 electrode still shows superior durability. After 60 d of storage, the sheet resistance value of the E4 electrode remained constant.

In order to study the adhesion between the AgNWs and the PET substrate, 3M Scotch tape was applied to the electrode and then pulled off (Fig. 6C). For the E4 electrode, the sheet resistance value was unchanged. Meanwhile, the sheet resistance value of the remaining electrodes all increased. In particular, in the case of electrode E1, after pulling the tape, this electrode showed very high resistance. In addition, the E4 electrode also exhibits high stability when rinsing and subjecting it to ultrasonic vibration in ethanol (Fig. 6D). The application of the mechanical pressing method and GO layer not only increases the conductivity but also improves the stability of the AgNW electrode.

4. Conclusions

The AgNW/GO transparent flexible hybrid electrode on a PET substrate has been successfully fabricated at room temperature by a simple pressing method. This electrode fabrication method has significantly decreased the surface roughness of the electrode, which was a chronic drawback of silver nanowire electrodes. This pressed AgNW/GO hybrid electrode displayed a low surface roughness, a low sheet resistance of 22 Ω/sq, and a high transmittance of 88% at 550 nm, which are all comparable to the ITO electrodes. Moreover, the electrode shows high mechanical and chemical stability. Thus, this AgNW/GO hybrid electrode could be used to fabricate flexible OSCs.

CRediT author statement

Tien Dat Doan: Conceptualization, Methodology, Writing - Original draft preparation; Nhung Hac Thi: Data curation, Visualisation; Ho Thi Oanh: Conceptualisation, Methodology; Tuyen Nguyen Duc: Investigation; Dong Hoon Choi: Reviewing and Editing; Mai Ha Hoang: Supervision. All authors have read and agreed to the published version of the manuscript.

ACKNOWLEDGEMENTS

This research is funded by Ministry of Science and Technology of Vietnam under grant number NDT.42.KR/18. This research is also supported by Institute of Chemistry under a project entitled "Research and fabrication of energy storage materials and devices" in 2022.

COMPETING INTERESTS

The authors declare that there is no conflict of interest regarding the publication of this article.

REFERENCES

[1] E.L. Lim, C.C. Yap, M.H.H. Jumali, et al. (2018), "A mini review: Can graphene be a novel material for perovskite solar cell applications?", *Nano-Micro Lett*., **10**, pp.1-10, DOI: 10.1007/s40820-017-0182-0.

[2] T. Sannicolo, M. Lagrange, A. Cabos, et al. (2016), "Metallic nanowire-based transparent electrodes for next generation flexible devices: A review", *Small*, **12(44)**, pp.6052-6075, DOI: 10.1002/smll.201602581.

[3] Y.U. Kim, S.H. Park, N.T. Nhan, et al. (2021), "Optimal design of PEDOT: PSS polymer-based silver nanowire electrodes for realization of flexible polymer solar cells", *Macromol. Res.*, **29**, pp.75-81, DOI: 10.1007/s13233-021-9005-8.

[4] R. Chen, S.R. Das, C. Jeong, et al. (2013), "Supporting information: Co-percolating graphene-wrapped silver nanowire network electrodes", *Adv. Funct. Mater.*, **23(41)**, pp.5150-5158, DOI: 10.1002/adfm.201300124.

[5] Y.H. Kim, C. Sachse, M.L. Machala, et al. (2011), "Highly conductive PEDOT: PSS electrode with optimized solvent and thermal post-treatment for ITO-free organic solar cells", *Adv. Funct. Mater*., **21(6)**, pp.1076-1081, DOI: 10.1002/adfm.201002290.

[6] T. Tokuno, M. Nogi, M. Karakawa, et al. (2011), "Fabrication of silver nanowire transparent electrodes at room temperature", *Nano Res*., **4**, pp.1215-1222, DOI: 10.1007/s12274-011-0172-3.

[7] M. Karakawa, T. Tokuno, M. Nogi, et al. (2017), "Silver nanowire networks as a transparent printable electrode for organic photovoltaic cells", *Electrochemistry*, **85(5)**, pp.245-248, DOI:10.5796/electrochemistry.85.245.

[8] K. Naito, R. Inuzuka, N. Yoshinaga, et al. (2018), "Transparent conducting films composed of graphene oxide/Ag nanowire/graphene oxide/PET", *Synth. Met.*, **237**, pp.50-55, DOI: 10.1016/j.synthmet.2018.02.004.

[9] Li Zhang, W. Zhu, Y. Huang, et al. (2019), "Synergetic efects of silver nanowires and graphene oxide on thermal conductivity of epoxy composites", *Nanomaterials*, **9(9)**, DOI: 10.3390/nano9091264.

[10] B.T. Liu, H.L. Kuo (2013), "Graphene/silver nanowire sandwich structures for transparent conductive films", *Carbon*, **63**, pp.390-396, DOI: 10.1016/j.carbon.2013.06.094.

[11] N.T. Nhan, P.D. Linh, D.T. Dat, et al. (2021), "Optimization of silver nanowire synthesis for flexible transparent conductive electrodes", *Vietnam J. Chem*., **59(1)**, pp.98-105, DOI: 10.1002/vjch.202000131.

[12] Y. Sun, B. Mayers, T. Herricks, et al. (2003), "Polyol synthesis of uniform silver nanowires: A plausible growth mechanism and the supporting evidence", *Nano Letters*, **3(7)**, pp.955-960, DOI: 10.1021/nl034312m.

[13] A.M. Dimiev, J.M. Tour (2014), "Mechanism of graphene oxide formation", *ACS Nano*, **8(3)**, pp.3060-3068, DOI: 10.1021/nn500606a.

[14] Y. Ahn, Y. Jeong, Y. Lee (2012), "Improved thermal oxidation stability of solution-processable silver nanowire transparent electrode by reduced graphene oxide", *ACS Appl. Mater. Interfaces*, **4(12)**, pp.6410-6414, DOI: 10.1021/am301913w.

[15] G. Haacke (1976), "New figure of merit for transparent conductors", *J. Appl. Phys*., **47(9)**, pp.4086-4089, DOI: 10.1063/1.323240.

[16] J. Jiu, T. Araki, J. Wang, et al. (2014), "Facile synthesis of very-long silver nanowires for transparent electrodes", *J. Mater. Chem. A*, **2(18)**, pp.6326-6330, DOI: 10.1039/C4TA00502C.

[17] K. Ellmer (2012), "Past achievements and future challenges in the development of optically transparent electrodes", *Nature Photon*., **6**, pp.809-817, DOI: 10.1038/nphoton.2012.282.

[18] T.M. Barnes, M.O. Reese, J.D. Bergeson, et al. (2012), "Comparing the fundamental physics and device performance of transparent, conductive nanostructured networks with conventional transparent conducting oxides", *Adv. Energy Mater*., **2(3)**, pp.353-360, DOI: 10.1002/aenm.201100608.

[19] S. Xu, B. Man, S. Jiang, et al. (2014), "Graphene-silver nanowire hybrid films as electrodes for transparent and flexible loudspeakers", *CrystEngComm*, **16(17)**, pp.3532-3539, DOI: 10.1039/C3CE42656D.

DOI: 10.31276/VJSTE.65(3).32-38

Study on synthesis of carboxymethyl cellulose from pineapple leaf waste and its potential applications as a thickener

Phan Thi Tuyet Mai[1*], Nguyen Hai Linh[1], To Phuong Linh[1], Vu Tien Manh[1], Ngo Hong Anh Thu[1], Pham Ngoc Lan[1], Luu Thi Hue[2]

[1]Faculty of Chemistry, University of Science, Vietnam National University - Hanoi, 19 Le Thanh Tong Street, Phan Chu Trinh Ward, Hoan Kiem District, Hanoi, Vietnam
[2]University of Adelaide, Adelaide SA 5005, Australia

Received 25 August 2022; revised 9 November 2022; accepted 14 November 2022

Abstract:

In this study, cellulose and hemicellulose were successfully extracted from pineapple leaf waste at yields of 58.8 and 16.1% by dried weight, respectively. Carboxymethyl cellulose (CMC) was synthesised from pineapple leaf cellulose by an esterification process using sodium hydroxide (NaOH) and monochloroacetic acid (MCA) with isopropanol as the supporting medium. Preparation of CMC was investigated by varying three free factors, namely, NaOH concentration, MCA dose, and cellulose size. The carboxymethylation process was optimised to produce CMC with differing degrees of substitution (DS). The highest DS of CMC (0.86) was obtained with 15% (w/v) NaOH solution, 0.6 g of MCA/g cellulose, and 50 µm cellulose. The obtained CMC were characterised by FTIR spectroscopy, SEM images and XRD diffractions. Moreover, the thickening performance of obtained CMC was also determined. The influence of the CMC's molecular weight and degree of substitution on the viscosity of 1% (w/v) aqueous solution was tested. The experimental results suggest that the viscosity of the solution increases with increasing molecular weight and degree of substitution of CMC.

Keywords: **carboxymethyl cellulose, cellulose viscosity, hemicellulose, pineapple leaf waste.**

Classification numbers: **2.2, 2.3**

1. Introduction

CMC derivatives are well known and have many applications, for example, they can be used as thickeners, additives, detergents, pharmaceuticals, glues, ceramics, or cosmetics, etc. [1-5]. CMC is obtained when alkali cellulose is reacted with MCA [6]. Some studies show that among the carbon atom positions where sodium carboxymethyl groups are substituted for the OH group, the C2 position is relatively dominant [7]. Hence, the DS is a significant property of CMC particularly because of its water solubility and thickening ability. There are many parameters that affect the DS value of CMC, for example, the concentration of MCA and NaOH, reaction time, reaction temperature, cellulose size, and so on [7, 8]. Several papers have reported that CMC can be synthesised from different cellulose sources like rice straw, corn husk, cotton linter, paper sludge, and pomelo peel [9-15]. Cellulose is usually found in cell walls of plants and is generally associated with lignin and hemicellulose, which make it difficult to extract in pure form. Because of their strong inter- and intra-molecular hydrogen bonds, cellulose molecules associate over extended regions forming polycrystalline, fibrous bundles and several steps must be performed to achieve higher DS, therefore, the extraction process is neither straightforward nor inexpensive [9-12]. Pineapple leaves account for a significant amount of agricultural waste in Vietnam, about 1 million tons annually. After harvesting and processing to obtain a packaged pineapple product, the discarded pineapple leaves make up 70% of the total waste from production. When discharged into the environment, these wastes cause serious pollution. Because pineapple leaves contain about 65-70% dry weight of cellulose, 15-20% hemicellulose, and 4-6% lignin [16-21], they can be used to produce reinforced fibres for polymer composite materials as well as cellulose fibre. However, this resource is yet to be used optimally. In our previous study, Vietnamese pineapple leaves were found to consist of 55% (w/w) cellulose content [22-26]. Thereby, in a scientific aspect, this shows using cellulose from pineapple leaves for applications has high feasibility.

Although hemicellulose is a common polysaccharide, representing about 20-35% of lingo-cellulosic biomass [27-30], it has not yet found wide industrial application. In addition, hemicellulose is a non-food substitute for starch polyols and is also a substitute for petroleum-based polyols [31-35]. Thus, it can be said that hemicellulose is a potential feedstock source for biomaterial synthesis. To the best of our knowledge, no report has been found in the literature where extracts of both hemicellulose and cellulose were prepared from pineapple leaf waste. Thus, it is essential to carry out research on the separation of cellulose and hemicellulose from pineapple leaves. The successful separation and effective use of cellulose and hemicellulose from Vietnamese pineapple leaf waste will be of great significance to environmental protection while adding value to processed fruit products. Therefore, the aim of this research is to confirm the potential separation of both hemicellulose and CMC from Vietnamese pineapple leaf waste and examining if this CMC can be further used as a thickener.

2. Materials and methods

2.1. Materials

Pineapple leaves were supplied by the Pineapple Suoi Hai farm, Ba Vi, Hanoi, Vietnam. They were cut into slices 5 mm in size.

[*]Corresponding author: Email: maimophong@gmail.com

Acetic acid 99.9% and MCA 99.7% were purchased from the UK and nitric acid 65% and sodium hydroxyl 99.9% (Merck) from Japan. Methanol 99.8%, ethanol 99.9% (Xilong Chemical), isopropanol 99.7% (Merck), and acetone 99.8% (Merck) served as solvents.

2.2. Methods

2.2.1. Hemicellulose extraction: The recovery of hemicellulose was conducted by alkaline extraction. Specifically, 10 g of dried pineapple leaf powder was mixed with 250 ml of x mol-NaOH-solution (x=0.25, 0.50, 0.75, 1.00, and 1.25 M) at 90°C while stirring. The mixing time was varied (t=60, 90, 120, and 150 min). The resulting dark slurry was filtered and washed with 250 ml of distilled water. The hemicellulose was separated in an Erlenmeyer flask.

Then, 25% acetic acid solution was used to adjust the filtrate pH 5-6. Afterward, 96% ethanol was added while maintaining the temperature at 4°C. Then the mixture was allowed to rest for 24 hours for the hemicellulose to precipitate. The liquid part was removed by vacuum. The obtained hemicellulose was washed out 3 times with a 70% ethanol solution. Then, the hemicellulose was dried in an oven at 40°C for 30 hours. Powdered hemicellulose was obtained by grinding. The final yield of hemicellulose was calculated as the average yield of three extractions and expressed as the ratio of its dried weight to 100 g of dried pineapple leaf powder before extraction using the following formula:

$$H(\%) = \frac{m}{m_0} x100 \quad (1)$$

where H is the yield of hemicellulose; m is the weight of the obtained hemicellulose; m_0 is the weight of initial dried pineapple leaf powder.

2.2.2. Cellulose recovery: The obtained solid residual was treated with 150 ml of HNO_3 solution with y M concentration (y=0.25, 0.50, 0.75, 1.00, 1.25 M). Then, it was thermally treated at 90°C for 90 min. The mixture was filtered and washed out many times with cold distilled water until the indicator colour of the filtrate did not change. The residue was thoroughly dried at 60°C, then ground into a fine powder, and finally placed in a plastic bag. Then, the cellulose yield (H) was calculated according to Eq. (1).

2.2.3. Synthesis of CMC: To synthesise CMC, 5 g of cellulose powder was added to 150 ml of isopropanol under continuous stirring for 60 min. Next, 15 ml of x NaOH solution (x=10, 15, 20, 25% w/v) was added dropwise while stirring. The stirring was continued for 1 hour at room temperature. Finally, y g of MCA (y=1.0, 2.0, 3.0, 4.0, and 5.0 g) was added to the mixture. It was stirred for another 90 min at 60°C. The solid part was neutralised by acetic acid to pH=7.0 and immersed in 20 ml of ethanol three times for 10 min each. The filtered CMC was thoroughly dried in an oven at 60°C and stored in a plastic bag. CMC productivity was calculated according to the following formula:

$$H_{CMC}(\%) = \frac{m_{CMC}}{m_C} x100 \quad (2)$$

where H_{CMC} is CMC yield; m_{CMC} is the weight of obtained CMC; m_C is the weight of initial cellulose.

2.2.4. Infrared spectroscopy: FTIR spectra were obtained on an FT/IR-6300 spectrometer with a resolution of 4 cm^{-1}. The absorption band was 600-4000 cm^{-1}.

2.2.5. X-ray diffraction studies: The X-ray diffraction (XRD) curves were recorded on an X-ray diffractometer XRD-6100 (SHIMADZU) with Cu K_α radiation at 30 kV and 15 mA. The diffraction angle was in the range of 5 to 80° (0.05°/min).

2.2.6. Scanning electron microscopy: To study the surface structure, SEM images were taken on a JSM-5000 model scanning electron microscope at 5.0 kV (Hitachi).

2.2.7. Determination of DS: The DS of CMC was determined according to ASTM (1994) [23]. To prepare the sample, 5 g of sample was added to a 500 ml conical flask containing 350 ml of ethanol. The contents were shaken for 30 min. The solution was filtered through a porous funnel. The solvent was evaporated at 100°C for 60 min under light vacuum. Finally, the sample was thoroughly dried in a crucible at 110°C.

The measurement procedure began with 2 g of the dry substance, prepared as above, placed into a tared porcelain crucible. The crucible was carefully charred with a low flame, then with a larger one for 10 min. Then, the residue was treated with 3-5 ml of concentrated sulfuric acid. Finally, it was heated carefully until no smoke was seen. Next, the crucible contents were mixed with 1 g of ammonium carbonate. The crucible was further heated with a low flame until no smoke was seen. Finally, the crucible was cooled and weighed. The sodium content was calculated using the following formula:

$$A(\%) = \frac{a \times 32.28}{b} \quad (3)$$

where the weight of residual sodium sulphate is represented by a and the weight of the dry sample by b.

The following formula was used to calculate the DS.

$$DS = \frac{162 \times A}{2300 - 80 \times A} \quad (4)$$

where 162 denotes the molecular weight of an anhydrous glucose unit; 80 represents the net increment in the anhydrous glucose unit for every substituted carboxymethyl group.

2.2.8. Viscosity measurement method: In this study, viscosity was determined by using an Ubbelohde capillary viscometer. Through the Mark-Houwink-Sakurada equation, the intrinsic viscosity was calculated as follows:

$$[\eta] = K.M^{\alpha} \quad (5)$$

where $[\eta]$ ($cm^3.g^{-1}$) represents the intrinsic viscosity and K and α are the specific solvents and polymers, respectively. For example, in the case of CMC, $K=7.3\times10^{-3}$ and $\alpha=0.93$ measured at 25°C in a 6% NaOH solution [24-26].

To carry out the rheological measurements, a Gilmont viscosimeter was used with 1% (w/w) CMC solution prepared in water. The temperature was maintained at 25°C during the reaction.

3. Results and discussion

3.1. Hemicellulose and cellulose extraction from Vietnamese pineapple leaf waste

3.1.1. Extraction of hemicellulose: Effect of the NaOH concentration on the hemicellulose extraction yield: The hemicellulose extraction yield depends on the concentration of the NaOH solution. Fig. 1A shows the highest yield at a NaOH concentration of 0.75 M. A very low yield (about 4.8%) was obtained at an alkaline concentration of 0.25 M NaOH. Indeed, at such a low NaOH concentration, the hemicellulose could not be solubilised since the hemicellulose was still bound to the lignin. Therefore, the hemicellulose extraction yields increased (16.1 and 16.8%) with higher NaOH concentrations (0.5 and 0.75 M, respectively). This is because the higher solubility of hemicellulose relates to the breakdown of the ester bonds between ferulic acid and hemicellulose under these conditions. However, as shown in Fig. 1A, further increasing the concentration of NaOH solution (1.00 and 1.25 M) leads to decreasing hemicellulose yield (15.1 and 13.7%, respectively). This is due to the degradation of hemicellulose [26-28]. Notably, no significant change in the hemicellulose yield could be seen in the NaOH concentration range of 0.5-0.75 M. Thus, 0.5 M NaOH is considered the most suitable.

3.1.2. Dependency of the hemicellulose extraction yield on the extraction time: Fig. 1B shows the dependence of the hemicellulose extraction yield on extraction time (60, 90, 120, and 150 min). In this research, the extraction temperature was 90°C and the NaOH concentration was maintained at 0.5 M. This shows that the hemicellulose yield increased upon increasing extraction time to 90 min. However, the hemicellulose yield declined with further increase of the extraction time to 120 min and 150 min. The partial degradation of hemicellulose may be the reason for this [25-27]. Thus, the extraction time of 90 min was considered the most appropriate.

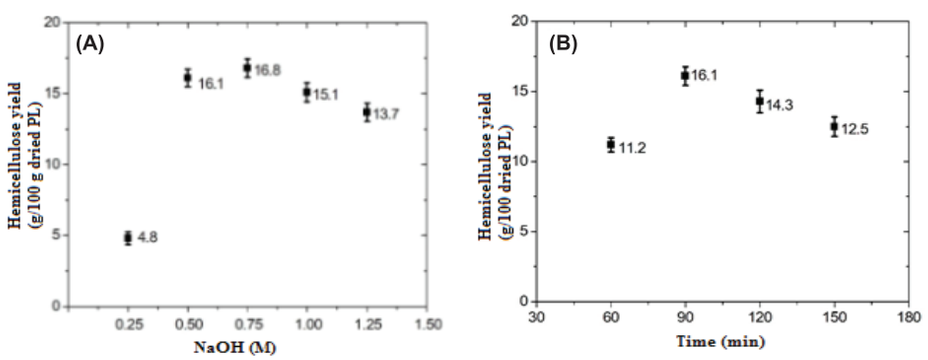

Fig. 1. Dependence of the hemicellulose extraction yield on NaOH concentration (A) and extraction time (B).

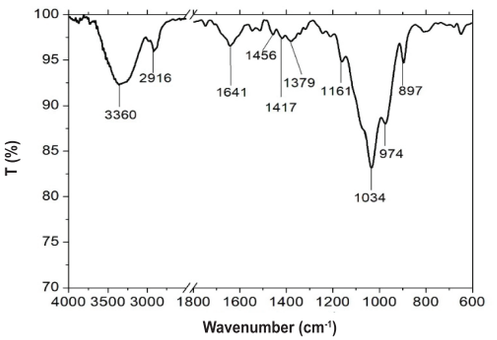

Fig. 2. FTIR spectroscopy of hemicellulose.

The FTIR spectroscopy analysis is shown in Fig. 2. In this figure, the absorption peaks at 1456, 1417, 1379, 1161, 1034, 974, and 897 cm^{-1} are specific for hemicellulose [29, 30]. The C-O-C stretching of the glycosidic linkages of the xylans were demonstrated by a band at 1034 cm^{-1} [29, 31]. The signal at 974 cm^{-1} was due to the presence of arabinose units [32]. The β-(1,4)-glycosidic linkages between the sugar units were characterised by a strong absorption band at 897 cm^{-1} [27, 33]. The broadband at 3360 cm^{-1} belonged to the OH stretching vibration, while the signal at 2916 cm^{-1} was evidence of the stretching vibrations of the CH_2 group. The peak at 1379 cm^{-1} was due to the stretching and deformation vibrations of the C-H group in the glucose unit. It is likely that the 1641 cm^{-1} peak was due to trace amounts of water [26]. In addition, the bands at 1242 and 1161 cm^{-1} were believed to belong to C-H stretching and O-H or C-O bending vibrations. The small peak at 1546 cm^{-1} likely embodies the aromatic skeletal vibrations due to the presence of trace amounts of lignin. Furthermore, the band at 1740-1710 cm^{-1} for the carbonyl groups is not seen, meaning no xylan acetyl groups were present in the alkaline solution. Overall, these FTIR results are similar to those of other studies [29, 34].

3.1.3. Cellulose extraction: Optimal HNO_3 concentration: The yield of cellulose recovery depends on the concentration of HNO_3. The results are shown in Table 1.

Table 1. The yield of carboxymethylation with different concentrations of HNO_3.

C_{HNO_3} (M)	0.25	0.50	0.75	1.00	1.25	1.50
H_c(%)	56.75±0.81	58.80±.65	55.40±1.13	49.20±0.71	43.20±0.42	37.20±0.40

It can be seen from Table 1 that the cellulose recovery yield does not vary much when the concentration of HNO_3 increases from 0.25 to 0.75 M. However, the yield reduces from 55.40±1.13 to 37.20±0.40% when the HNO_3 concentration continues to increase to 1.5 M. This could be due to the 0.75 M HNO_3 solution not only removing the residual hemicellulose but also cutting the cellulose fibres. During washing, some short cellulose

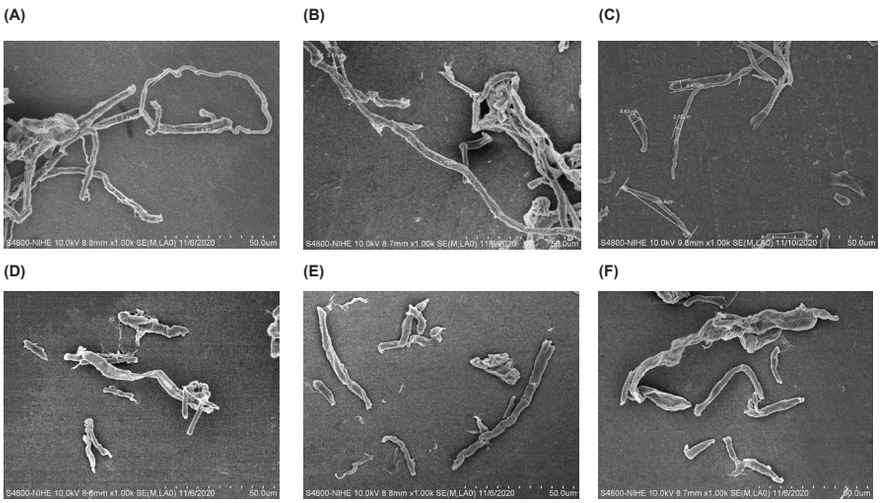

Fig. 3. SEM images of pineapple leaf cellulose treated with different HNO_3 concentrations: (A) 0.25 M, (B) 0.50 M, (C) 0.75 M, (D) 1.00 M, (E) 1.25 M, (F) 1.50 M with 1000x magnification.

fibres may be lost, resulting in smaller cellulose recovery yields. The SEM image in Fig. 3 also supports this point of view.

As Fig. 3 shows, pineapple leaf cellulose are cylindrical fibres with an average diameter of 3-4 µm. At an HNO_3 concentration of 0.25-0.50 M, the length of the cellulose fibres are relatively long, however, at a concentration of 0.50 M, the fibre surface is smoother than that at 0.25 M. It is assumed that the impurities could have been more thoroughly removed at that concentration. It is also clear that from the HNO_3 concentration of 0.75 M that the cellulose fibres were truncated, and the number of short fibres increased with further increase in HNO_3 concentration. However, there was no difference in fibre size in the concentration range of 1.0-1.5 M. Thus, the cellulose fibre length can be adjusted by the concentration of the HNO_3 solution. At a concentration of 0.50-0.75 M, the obtained cellulose fibres have an average size of about 50-200 µm with an average diameter of about 3-4 µm. Thus, a suitable concentration of HNO_3 to treat the pineapple leaves to achieve the highest cellulose recovery efficiency is in the range of 0.50-0.75 M, with the choice depending on the desired fibre length.

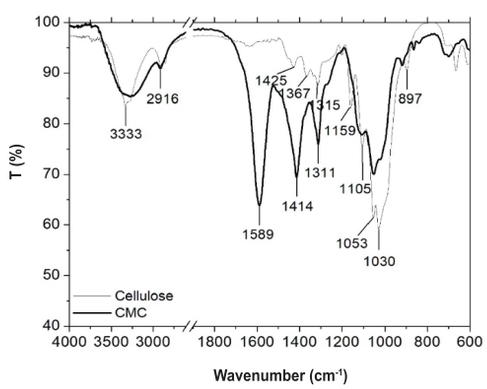

Fig. 4. FTIR spectroscopy of extracted cellulose and CMC from pineapple leaf waste.

FTIR spectroscopy of the cellulose is displayed in Fig. 4. The band at 3333 cm^{-1} characterised the OH stretching mode, while the signal observed at 2916 cm^{-1} was attributed to the stretching and deformation vibrations of the C-H groups in the glucose units. The bands at 1367 and 1425 cm^{-1} characterised the C-H and C-O linkages in the polysaccharide rings, respectively. The absorption peak at 1159 cm^{-1} belongs to the -C-O-C stretch of the β-(1,4)-glycosidic linkage, which is typical for cellulose samples. The peak at 1425 cm^{-1} is typical for the asymmetric bending of the $-CH_2$ group. The absorption band at 1105 cm^{-1} was assigned to the -C-O group of secondary alcohols and ether functions existing on the cellulose chain backbone. Lastly, the band range of 897-1053 cm^{-1} characterised the β-(4,1)-glycosidic linkages between the glucose units in cellulose [26]. Interestingly, there are no peaks at 1600-1800 cm^{-1}, which characterises the C=O groups and the aromatic rings of hemicellulose and lignin molecules [34-36]. This result proves that the obtained cellulose is pure, that is, free from hemicellulose and lignin. It is worth mentioning that the separation of cellulose described in this work is easier and the yield of cellulose is higher compared to that mentioned in our previous report [36]. This interesting result may be due to the different states of starting material. Therefore, the use of fresh pineapple leaves brings higher economic efficiency than its dried state.

3.2. Synthesis of CMC from Vietnam's pineapple leaf cellulose

3.2.1. Effect of NaOH concentration on DS and yield of CMC: The treatment of cellulose with alkali intentionally causes cellulose fibres to swell, making the substitution reaction easier. The relationship between the DS of the CMC and NaOH concentration is shown in Table 2.

Table 2. The yield and DS of CMC with various NaOH concentrations.

NaOH (%wt)	10	15	20	25
H_{CMC} (%)	160.1	172.3	168.8	166.6
DS	0.64	0.86	0.75	0.71

As seen in Table 2, upon increasing NaOH concentration, the DS of the CMC increased. The DS reached a maximum of 0.86 at a NaOH concentration of 15% (w/v). However, the DS value then decreased by further increasing the NaOH concentration. This observation can be explained as follows. At the beginning of the carboxylation process, as NaOH reacts with the cellulose-OH groups, the cellulose morphology is altered. Its crystalline domains transform into amorphous domains [9]. However, this morphology change only occurs up to a certain level, since carboxylation is also influenced by other factors like solvents and reagent ratios. Furthermore, the reaction between MCA and

NaOH can occur during carboxylation. In particular, this reaction is more likely to occur at high concentrations of NaOH, leading to a reduced etherification probability. In addition, at a high NaOH concentration, degradation of CMC polymer chains may occur. The decreasing DS value at high NaOH concentration was previously found in research by K.M. Hong (2013) [8] and J. Chumee, D. Seeburin (2014) [10]. The CMC yields at different NaOH concentrations are also provided in Table 2 and the trend was similar to that of DS.

3.2.2. Effect of MCA dose on DS and yield of CMC: The yield of CMC and the DS value greatly depend on the MCA dose. The weight ratio of MCA to cellulose changed from 0.2 to 1.0. Table 3 shows that the DS of the CMC increases with increasing the weight ratio of MCA to cellulose, from 0.2 to 0.6, then it decreases lightly. The DS reached a maximum at the weight ratio of MCA to cellulose of 0.6. This may relate to undesired side reactions at a high MCA dose, leading to the reducing CMC yield. This similar range of DS values (from 0.58-0.86) can also be seen in another research for passage waste [9, 12]. Like DS, a similar varying trend of CMC yield is also seen in Table 3.

Table 3. The yield and DS of CMC synthesised with various amount of MCA.

m_{MCA} (g)	0.2	0.4	0.6	0.8	1.0
H_{CMC} (%)	143.7	160.7	172.3	154.0	150.1
DS	0.34	0.60	0.86	0.46	0.41

In summary, suitable carboxylation conditions were the weight ratio of MCA to cellulose of 0.6, and 15 ml of 20% w/v NaOH solution. With these conditions, the CMC had a DS of 0.86.

3.2.3. Effect of cellulose size on DS and yield of CMC: The effect of cellulose fibre size on the carboxymethylation reaction was studied. Two fibres with an average diameter of 50 and 200 µm were selected and the results are shown in Fig. 5.

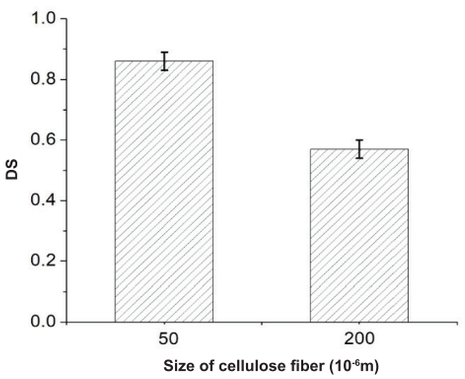

Fig. 5. DS of the synthesised CMC depending on cellulose fibre size.

As Fig. 5 shows, the size of the raw cellulose fibre material greatly affects the DS of CMC. It is well known that increasing cellulose fibre length makes DS decrease. Indeed, for the 200 µm fibre, DS was only 0.57±0.05, while DS reached 0.86±0.03 with the 50 µm fibre.

3.2.4. Structural characterisation of CMC: In our research, cellulose fibres of 200 µm were used to synthesise CMC. The FTIR spectroscopy technique was used to confirm the structure of the extracted cellulose and synthesised CMC (see Fig. 4). It can be seen that the OH-stretching vibrations appear at a broad peak of 3332 cm^{-1}. The peak at 2916 cm^{-1} shows the stretching C-H-linkage. The bands at 1315 and 1159 cm^{-1} are due to C-O-C stretching vibrations in the β-(1,4)-glycosidic linkage. The -C-O- group of secondary alcohols and ethers in the cellulose backbones is characterised by the band at 1105 cm^{-1}. The β-(1,4)-glycosidic linkages between the glucose units in cellulose appear at 1053 and 1022 cm^{-1} [9, 12, 26]. For the CMC, the presence of the -COO and -COONa groups are confirmed by C=O stretching absorption at 1589 and 1414 cm^{-1}, respectively. These peaks do not exist in the cellulose spectrum (Fig. 4), meaning that etherification was successful. These FTIR results are similar to those of J. Chumee and D. Seeburin (2014) [10], S. Sophonputtanaphoca, et al. (2019) [13] research on Thai pineapple leaves. The microstructures of the materials were studied by SEM. Photos of the cellulose and CMC are shown in Fig. 6 and their SEM images are shown in Fig. 7.

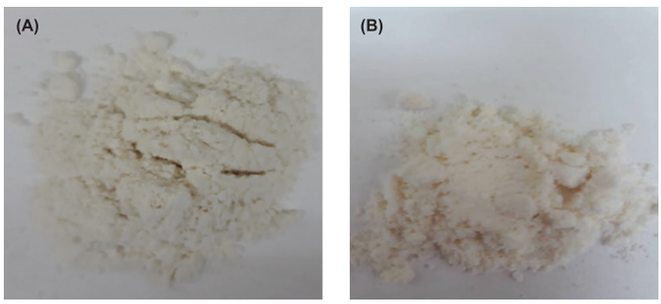

Fig. 6. Images of pineapple leaf cellulose (A) and CMC (B).

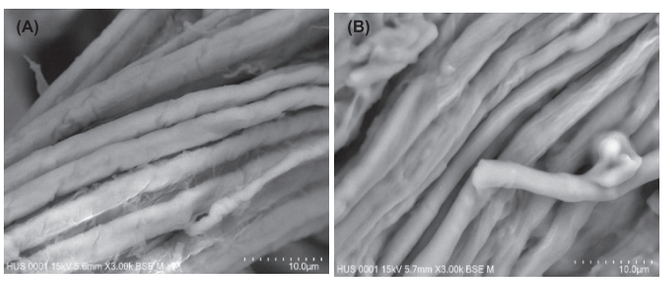

Fig. 7. SEM images of pineapple leaf cellulose (A) and CMC (B) with 3000 x magnification.

As seen in Fig. 7, cellulose and CMC possess a ribbon-shaped or rod-like morphology. The same morphology has been shown by other researchers [13, 14, 19]. This figure also clearly shows the fairly smooth surface of the extracted cellulose fibres. As for CMC, the surface is more extended, rough, and collapsed. The reason for this lies in the fact that the extracted cellulose was treated with sodium hydroxide during carboxymethylation. The size of the cellulose is 3.0-4.0 µm and that of the CMC is 3.5-4.5 µm.

We used XRD to investigate the degree of cellulose crystallinity [12, 13, 20]. Fig. 8 shows the X-ray diffractogram of isolated cellulose and synthesised CMC.

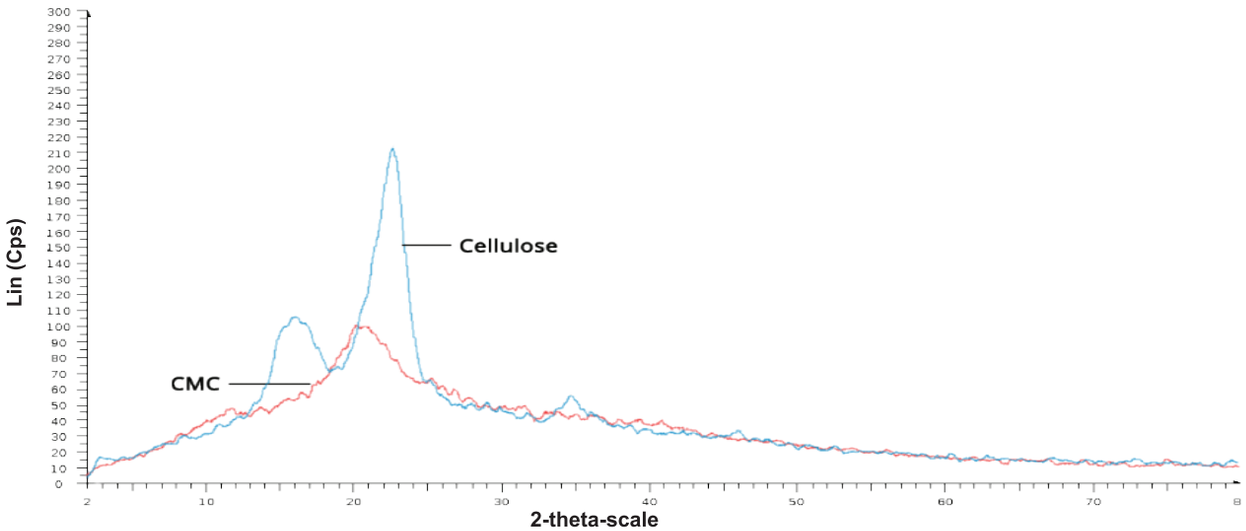

Fig. 8. XRD diffraction pattern of cellulose (blue curve) and synthesised CMC (red curve) from Vietnamese pineapple leaf waste.

Looking at Fig. 8, it can be assumed that holocellulose has a higher crystallinity compared to CMC. Specifically, the holocellulose curve has three peaks at 2θ=16.3, 23.4, and 34.7°. Among them, the two peaks at 2θ=16.3 and 23.4° are sharp, showing larger crystalline phases of the holocellulose core structure. Note that CMC has fewer peaks with lower intensity compared to holocellulose. This is due to a more amorphous structure of CMC compared to that of cellulose. One can assume from the above observation that unlike cellulose, CMC could have a disordered molecular arrangement. This is because of the presence of carboxymethyl moieties in the CMC product. The molecular weight (M) of CMC is one of the most important parameters. By extrapolation of the reduced viscosity [η_{red}] to zero concentration, one can obtain the intrinsic viscosity [η] (Fig. 9). In order to determine the molecular weight by the viscosimetric method, the Mark-Houwink-Sakurada empirical equation (Eq. (5) is used. The [η] values can be estimated from the intercept of the plot, specifically, [η]=188.17 (ml/g). The CMC average molecular weight is 55400±250 g/mol.

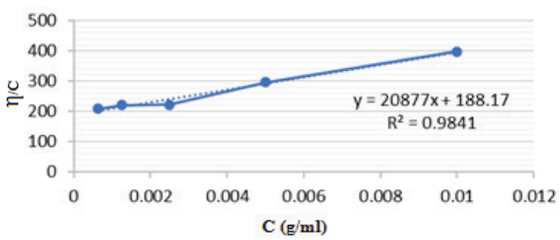

Fig. 9. The Mark-Houwink-Sakurada plot for CMC in 6%wt NaOH at 25°C.

3.3. Evaluation of the thickening ability of CMC products

The thickening ability of the CMC product was evaluated with varying DS values (DS=0.34, 0.60, and 0.86) and different molecular weights (M_w=22000±221 and 55400±250 g/mol). The samples were prepared with a CMC mass concentration of 1% in water. The values of viscosity measurements with a gilmont viscometer are given in Table 4.

Table 4. The dynamic viscosity of the CMC solution at 25°C.

DS	0.34	0.60	0.86	0.86	
M (g/mol)	55400±250			22000±221	55400±250
Viscosity (mPa.s)	385	520	650	250	650

Table 4 shows that DS and M have a great impact on the viscosity of the solution. The viscosity of the 1% CMC solution increases with an increase of DS. This can be explained by the fact that a high value of DS creates a greater number of hydrophilic groups, leading to increasing viscosity (at the constant temperature). This observation is supported by other reports [11, 13, 21].

The molecular mass of CMC has a decisive influence on the thickening ability of CMC. At the same 1% CMC concentration, the viscosity of the solution increases sharply, from 250 to 650 mPa.s, when the molecular weight changes from 22,000 to 55,400 g/mol. This is understandable because the larger the molecular mass, meaning the bulkier the molecules, the harder it is for them to move in solution. This similar observation can be seen in other reports [10, 20]. It is expected that the synthesised CMC may be useful as a thickening agent in many applications.

4. Conclusions

The extraction of cellulose and hemicellulose from Vietnamese pineapple leaf waste was successfully performed. Hemicellulose extraction yield was 16.1% (w/w) at a NaOH concentration of 0.5 M at 90°C for 90 min. The cellulose recovery yield was 58.8% while treating for 90 min with 0.5 M HNO_3. The highest DS of CMC was obtained (0.86) with 15% (w/v) NaOH solution, 0.6 g of MCA/g cellulose, and a cellulose size 50 μm. The CMC yield was 172.3%.

The cellulose fibre size depends on HNO_3 solution concentration. The length of the cellulose chains strongly influences the effectiveness of the carboxymethylation reaction. The DS and molecular weight of CMC have a significant impact on thickening ability. The viscosity of the CMC solution increases with increasing DS and molecular weight. This study shows that using Vietnamese pineapple leaf waste to separate cellulose and hemicellulose has great potential and high feasibility. This research opens a new direction to effectively use pineapple leaf waste while contributing to reducing environmental pollution.

CRediT author statement

Phan Thi Tuyet Mai: Review, Methodology, Formal analysis, Writing, Editing; Nguyen Hai Linh: Data analyst; To Phuong Linh: Data analyst; Vu Tien Manh: Data analyst. Ngo Hong Anh Thu: Editing; Pham Ngoc Lan: Review, Editing; Luu Thi Hue: Review, Editing.

ACKNOWLEDGEMENTS

This research is funded by Hanoi Department of Science and Technology under grant number 01C-03/04-2020-03.

COMPETING INTERESTS

The authors declare that there is no conflict of interest regarding the publication of this article.

REFERENCES

[1] V. Stigsson, G. Kloow, U. Germgård (2001), "A historical overview of "carboxymethyl cellulose" production on an industrial scale", *Paper Asia*, **17(10)**, pp.16-21.

[2] United States Patent (2017), *Thickening Agent for Aqueous Systems, Formulations Containing Same and Use Thereof*, 9pp.

[3] Patent Application Publication (2008), *Improved Paint Formulations Comprising Cellulose Ether/Network Building Polymer Fluid Gel Thickener*, 9pp.

[4] G.B. William, D.B. Valerie (1979), "Dishwashing detergent gel composition", *Patent*, **19**, pp.1-9.

[5] R.C. Sun, J. Tomkinson, P.L. Ma, et al. (2000), "Comparative study of hemicelluloses from rice straw by alkali and hydrogen peroxide treatments", *Carbohydr. Polym.*, **42(2)**, pp.111-122, DOI: 10.1016/S0144-8617(99)00136-8.

[6] S. Zhang, F.X. Li, J.Y. Yu, et al. (2009), "Dissolved state and viscosity properties of cellulose in a NaOH complex solvent", *Cellul. Chem. Technol*., **43(7-8)**, pp.241-249.

[7] V.L. Pushpamalar, S.J. Langford, M. Ahmad, et al. (2006), "Optimization of reaction conditions for preparing carboxymethyl cellulose from sago waste", *Carbohyd. Polym.*, **64(2)**, pp.312-318. DOI: 10.1016/j.carbpol.2005.12.003.

[8] K.M. Hong (2013), "Preparation and characterization of carboxylmethyl cellulose from surgacane bagasse", *B.Sc.(Hons.) Chemistry*, **1**, pp.1-110.

[9] X. He, S. Wu, D. Fu, et al. (2008), "Preparation of sodium carboxymethyl cellulose from paper sludge", *J. Chem. Technol. Biotechnol.*, **84(3)**, pp.427-434, DOI: 10.1002/jctb.2057.

[10] J. Chumee, D. Seeburin (2014), "Cellulose extraction from pomelo peel: Synthesis of carboxymethyl cellulose", *Inter. J. Mater. Metallurgical Eng.*, **8(5)**, pp.435-437, DOI: 10.5281/zenodo.1092854

[11] S.A. Asl, M. Mousavi, M. Labbafi (2017), "Synthesis and characterization of carboxymethyl cellulose from sugarcane bagasse", *J. F. Process. Technol.*, **8**, pp.1-6.

[12] R. Khullar, V.K. Varshney, S. Naithani, et al. (2005), "Carboxymethylation of cellulosic material (average degree of polymerization 2600) isolated from cotton (gossypium) linters with respect to ds and rheological behavior", *J. Appl. Polym. Sci*., **96(4)**, pp.1477-1482, DOI: 10.1002/app.21645.

[13] S. Sophonputtanaphoca, S. Chutong, P. Cha-aim (2019), "Potential of Thai rice straw as a raw material for the synthesis of carboxymethylcellulose", *Inter. Food Research. J.*, **26(3)**, pp.969-978.

[14] I.H. Mondal, M.S. Yeasmin, M.S. Rahman (2015), "Preparation of food grade carboxymethyl cellulose from corn husk agrowaste", *Int. J. Biol. Macromol*., **79**, pp.144-150, DOI: 10.1016/j.ijbiomac.2015.04.061.

[15] M.S. Rahman, M.H. Mondal, M.S. Yeasmin (2020), "Conversion of lignocellulosic corn agro-waste into cellulose derivative and its potential application as pharmaceutical excipient", *Processes*, **8(6)**, 16pp, DOI: 10.3390/pr8060711.

[16] M.E.R. Cassellis, M.E.S. Pardo, M.R. López, et al. (2014), "Structural, physicochemical and functional properties of industrial residues of pineapple", *Cellul. Chem. Technol*., **48(7-8)**, pp.633-641.

[17] M.E.S. Pardo, M.E.R. Cassellis, R.M. Escobedo, et al. (2014), "Chemical characterisation of the industrial residues of the pineapple", *J. Agri. Chem. Environ.*, **3(2)**, pp.53-56, DOI: 10.4236/jacen.2014.32B009.

[18] G.I. Bolio, R.E. Ross-Alcudia, L. Veleva, et al. (2016), "Extraction and characterization of cellulose from agroindustrial waste of pineapple (*Ananas comosus* L. Merrill) crowns", *Chem. Sci. Rev. Lett*., **5(17)**, pp.198-204.

[19] I.M. Fareez, N.A. Ibrahim, W.M.H. Wan Yaacob, et al. (2018), "Characteristics of cellulose extracted from Josapine pineapple leaf fibre after alkali treatment followed by extensive bleaching", *Cellul.*, **25**, pp.4407-4421.

[20] N.A. Kassim, A.Z. Mohamed, E.S. Zainudin, et al. (2019), "Isolation and characterization of macerated cellulose from pineapple leaf", *Bioresour.,* **14(1)**, pp.1198-1209.

[21] S.B. Suhaimi, I. Patthrare, S. Mooktida, et al. (2017), "Synthesis of methyl cellulose from nang lae pineapple leaves and production of methyl cellulose film", *Current Appl. Sci. Technol.*, **17(2)**, pp.233-244.

[22] T.T. M. Phan, T.H. Pham (2019), "Potential biogas production from wasted pineapple leaves", *Chem. J*., **57(2)**, pp. 235-239, DOI: 10.1155/2021/6639964.

[23] ASTM (1994), *Standard Test Methods for Sodium CMC, ASTM Committee on Standards*, Philadelphia, pp.291-298.

[24] T.T.M. Phan, T.S. Ngo (2020), "Pectin and cellulose extraction from passion fruit peel waste", *Vietnam J. Sci. Technol. Eng.*, **62(1)**, pp.32-37, DOI: 10.31276/VJSTE.62(1).32-37.

[25] A.A.Y. Ahmed, H.M. Taisser (2018), "Synthesis and characteristic of carboxymethyl cellulose from baobab (*Adansonia digitata* L.) fruit shell", *Inter. J. Eng. Appl. Sci.*, **5(12)**, pp.1-10.

[26] M.J. Nayef (2006), "Structure rheology of carboxymethyl cellulose solutions", *B.Sc. in Chemical Engineering*, **1**, pp.1-106.

[27] H. Cheng, H. Zhan, S. Fu, et al. (2011), "Alkali extraction of hemicellulose from depithed corn stover and effects on soda-AQ pulping", *BioResour.*, **6(1)**, pp.196-206.

[28] X. Peng, S. Nie, X. Li, et al. (2019), "Characteristics of the water and alkali-soluble hemicellulose fractionated by sequential acidification and graded ethanol from sweet maize stems", *Molecules*, **24(1)**, pp.212-221, DOI: 10.3390/molecules24010212.

[29] I. Egües, C. Sanchez, I. Mondragon, et al. (2012), "Effect of alkaline and autohydrolysis processes on the purity of obtained hemicelluloses from corn stalks", *Bioresour. Technol*., **103(1)**, pp.239-248, DOI: 10.1016/j.biortech.2011.09.139.

[30] R. Sun, J.M. Lawther, W.B. Banks (1996), "Fractional and structural characterization of wheat straw hemicelluloses", *Carbohydr. Polym*., **29(4)**, pp.325-331, DOI: 10.1016/S0144-8617(96)00018-5.

[31] C. Moine, P. Krausz, V. Chaleix (2007), "Structuralcharacterization and cytotoxic properties of a 4-O-methylglucuronoxylan from *Castanea sativa*", *J. Nat. Prod*., **70(1)**, pp.60-66, DOI: 10.1021/np060354p.

[32] A. Ebringerova, Z. Hromadkova, J. Alföldi, et al. (1992), "Structure and solution properties of corn cob heteroxylans", *Carbohydr. Polym.*, **19(2)**, pp.99-105, DOI: 10.1016/0144-8617(92)90119-B.

[33] M.A.K. Azad, F. Wang, H.R. Kim (2015), "Identification of a novel sugar compound from Korean pine seeds", *Food Sci. Biotechnol*., **24**, pp.2011-2015.

[34] B. Xiao, X.F. Sun, R.C. Sun (2001), "Chemical, structural, and thermal characterizations of alkali-soluble lignins and hemicelluloses, and cellulose from maize stems, rye straw, and rice straw", *Polym. Degrad. Stab*., **74(2)**, pp.307-319, DOI: 10.1016/S0141-3910(01)00163-X.

[35] X.H. Yang, W.L. Zhu (2007), "Viscosity properties of sodium carboxymethylcellulose solutions", *Cellul*., **14**, pp.409-417.

[36] M.T.T. Phan, L.N. Pham, L.H. Nguyen (2021), "Investigation on synthesis of hydrogel starting from Vietnamese pineapple leaf waste - derived carboxymethylcellulose", *Journal of Analytical Methods in Chemistry*, **2021**, DOI: 10.1155/2021/6639964.

Compounds from the ethyl acetate extract of *Pteris multifida* Poir. collected in Nam Dinh province, Vietnam

Duc Thien Dao[1], Hoang Sa Nguyen[2], Huu Thu Do[3], Thanh Tam Nguyen[1, 4*]

[1]*Institute of Chemistry, Vietnam Academy of Science and Technology, 18 Hoang Quoc Viet Street, Nghia Do Ward, Cau Giay District, Hanoi, Vietnam*
[2]*University of Khanh Hoa, 1 Nguyen Chanh, Loc Tho Ward, Nha Trang City, Khanh Hoa Province, Vietnam*
[3]*Institute of Ecology and Biological Resources, Vietnam Academy of Science and Technology, 18 Hoang Quoc Viet Street, Nghia Do Ward, Cau Giay District, Hanoi, Vietnam*
[4]*Graduate University of Science and Technology, Vietnam Academy of Science and Technology, 18 Hoang Quoc Viet Street, Nghia Do Ward, Cau Giay District, Hanoi, Vietnam*

Received 14 September 2022; revised 14 October 2022; accepted 20 October 2022

Abstract:

***Pteris multifida* Poir. is an evergreen herbaceous fern that is distributed in temperate and tropical regions of East Asia and cultivated in many other countries. It is an ethnomedicinal plant used for detoxicating, cooling, reducing pain, and as a treatment for many diseases like dysentery, typhoid, cholecystitis, diarrhoea, enteritis, jaundice, and eczema among others. Several compounds including flavonoids, sesquiterpenoids, diterpenoids, coumarins, lignans, and sterols with anti-spasmodic, anti-bacterial, anti-hyperlipidemic, anti-oxidative, and cytotoxic activities have been isolated from this plant. In the present study, three sesquiterpenoids, (2*S*,3*S*)-pretosin Q (1), (2*R*,3*S*)-pterosin C (2), (2*S*,3*S*)-pterosin C (3); two lignans, pinoresinol (4); lariciresinol 9-O-β-glucopyranoside (5), three flavonoids, naringenin (6), apigenin (7), and luteolin (8) were obtained from the ethyl acetate extract of the whole of *P. multifida* collected in Nam Dinh province, Vietnam. The chemical structures were elucidated by various spectroscopic means including one- and two-dimensional (1D, 2D)-NMR, mass spectrometry, and comparison with published data. Compounds 4-6 were isolated from *P. multifida* for the first time.**

Keywords: **flavonoid, lignan, *Pteris multifida* Poir., sesquiterpenoid.**

Classification numbers: **2.2, 3.4**

1. Introduction

The genus *Pteris* is a large member of the family *Pteridaceae*. It contains about 250 species that mostly occur in the tropical and subtropical regions of the world, with about 28 species found in Vietnam [1]. Some *Pteris* species have been utilised in folk medicines, as food sources, and as phytoremediations [2]. *P. multifida*, an evergreen herbaceous fern, is native to temperate and tropical regions of East Asia and cultivated in many other countries. This plant grows extensively throughout the north and middle regions of Vietnam and is most commonly found in damp and shady locations. *P. multifida* is traditionally used for detoxicating, cooling, reducing pain, and as a treatment for many diseases like dysentery, typhoid, cholecystitis, diarrhoea, enteritis, jaundice, and eczema among others [3]. Pharmacological properties of *P. multifida* include anti-tumour, anti-inflammatory, anti-hyperlipidaemic, antimutagenic, and free radical-scavenging activities [4-7]. Previously, the presence of flavonoids, sesquiterpenoids, diterpenoids, coumarins, lignans, and sterols has been reported in this plant [8-14]. We report herein the isolation and structural elucidation of eight compounds from the ethyl acetate extract of the entire the whole of *P. multifida* fern collected in the Nam Dinh province, Vietnam. Their structures were identified as (2*S*,3*S*)-pretosin Q (**1**), (2*R*,3*S*)-pterosin C (**2**), (2*S*,3*S*)-pterosin C (**3**), pinoresinol (**4**), lariciresinol 9-O-β-glucopyranoside (**5**), naringenin (**6**), apigenin (**7**), and luteolin (**8**) by spectral analysis and comparison with spectroscopic data reported in previous literature.

2. Materials and methods

2.1. General experimental procedures

NMR spectra were recorded with a Bruker Avance II spectrometer at 600 MHz (^{1}H-NMR) and 150 MHz (^{13}C-NMR) using TMS as an internal reference. Mass spectra were carried out on an Agilent LC-MSD-Trap SL system mass spectrometer. Thin layer chromatography was performed on silica gel 60F254 and Rp-18 F254s, and spots were detected with UV light (254 and 365 nm) and then sprayed with a solution of vanillin/sulfuric acid followed by heating to 110^{o}C. Silica gel 60 (0.063-0.2 mm), Sephadex LH-20 (25-100 μm), and silica gel Rp-18 (40-63 μm) were used for normal pressure column chromatography.

2.2. Plant material

The whole *P. multifida* plant was collected in the Nam Truc district, Nam Dinh province, Vietnam, in May 2021 and identified

*Corresponding author: Email: nttam@ich.vast.vn

by Prof. Do Huu Thu, Institute of Ecology and Biological Resources, Vietnam Academy of Science and Technology (VAST). The specimens were kept at the Laboratory of Natural Products Research, Institute of Chemistry, VAST, Hanoi, Vietnam.

2.3. Extraction and isolation

The dried whole plant (1600 g) of *P. multifida* was ground and extracted with methanol-water (95:5, v/v) three times at room temperature. After removing the solvent under vacuum, the concentrated extract was successively partitioned with n-hexane, ethyl acetate, and n-butanol, respectively. The EtOAc-soluble fraction (22 g) was subjected to silica gel chromatography eluted with gradient mixtures of CH_2Cl_2-MeOH (from 10:0 to 4:1, v/v) to give ten fractions (PE1-PE10). Fraction PE3 was re-chromatographed on a silica gel column (n-hexane-acetone, 3.5:2) to afford compound **6** (7 mg). Fraction PE4 was further purified on a silica gel column (n-hexane-acetone, 3:2, v/v) and then on a Sephadex LH-20 column (CH_2Cl_2-MeOH, 1:9, v/v) to give compounds **4** (10 mg) and **7** (3 mg). Fraction PE6 was re-chromatographed on a silica gel column (CH_2Cl_2-MeOH, 10:1, v/v) to give four sub-fractions (PE6.1-PE6.4). Sub-fraction PE6.2 was purified on a silica gel column (n-hexane-acetone, 2.5:2, v/v) to yield mixture compounds **2** and **3** (12 mg). Sub-fraction PE6.3 was purified on a silica gel column (n-hexane-acetone, 2.5:2, v/v) to afford compound **1** (10 mg). Fraction PE7 was purified on a silica gel column (CH_2Cl_2-MeOH, 15:1, v/v) to give compound **8** (6 mg). Compound **5** (6 mg) was obtained from fraction PE8 through column chromatography on silica gel (CH_2Cl_2-MeOH-H_2O, 9:1:0.1, v/v), then silica gel Rp-18 (MeOH-H_2O, 1:1).

(2S,3S)-Pretosin Q ***(1)****:* White powder. ESI-MS *m/z* 251.2 $[M+H]^+$. ^{1}H-NMR (600 MHz, CD_3OD): δ_H 7.36 (1H, s, H-4), 5.34 (1H, dd, *J*=8.4, 5.4 Hz, H-12), 4.70 (1H, d, *J*=4.2 Hz H-3), 3.94 (1H, dd, *J*=11.4, 8.4 Hz, H-13a), 3.65 (1H, dd, *J*=11.4, 5.4 Hz, H-13b), 2.77 (3H, s, H-14), 2.59 (3H, s, H-11), 2.49-2.45 (1H, m, H-2), 1.32 (3H, d, *J*=7.2 Hz, H-10). ^{13}C-NMR (150 MHz, CD_3OD): δ_C 207.52 (C-1), 155.34 (C-9), 146.43 (C-5), 140.33 (C-7), 138.66 (C-6), 132.81 (C-8), 126.69 (C-4), 75.74 (C-3), 72.73 (C-12), 65.56 (C-13), 54.79 (C-2), 22.35 (C-11), 15.06 (C-14), 13.26 (C-10).

(2R,3S)-Pterosin C ***(2)****:* ESI-MS *m/z* 235.3 $[M+H]^+$. ^{1}H-NMR (600 MHz, CD_3OD): δ_H 7.38 (1H, s, H-4), 5.16 (1H, d, *J*=6.6 Hz, H-3), 3.63 (2H, t, *J*=7.8 Hz, H-13), 3.03 (2H, t, *J*=7.8 Hz, H-12), 2.79-2.74 (1H, m, H-2), 2.66 (3H, s, H-14), 2.49 (3H, s, H-11), 1.19 (3H, d, *J*=7.2 Hz, H-10). ^{13}C-NMR (150 MHz, CD_3OD): δ_C 210.31 (C-1), 155.13 (C-9), 146.24 (C-5), 138.54 (C-7), 138.07 (C-6), 132.22 (C-8), 126.68 (C-4), 70.23 (C-3), 61.61 (C-13), 49.66 (C-2), 33.04 (C-12), 21.37 (C-11), 14.00 (C-14), 10.70 (C-10).

(2S,3S)-Pterosin C ***(3)****:* ESI-MS *m/z* 235.3 $[M+H]^+$. ^{1}H-NMR (600 MHz, CD_3OD): δ_H 7.37 (1H, s, H-4), 4.70 (1H, d, *J*=4.2 Hz, H-3), 3.62 (2H, t, *J*=7.8 Hz, H-13), 3.02 (2H, t, *J*=7.8 Hz, H-12), 2.66 (3H, s, H-14), 2.49 (3H, s, H-11), 2.48-2.43 (1H, m, H-2), 1.32 (3H, d, *J*=7.2 Hz, H-10). ^{13}C-NMR (150 MHz, CD_3OD): δ_C 207.59 (C-1), 154.53 (C-9), 146.24 (C-5), 138.21 (C-7), 137.85 (C-6), 132.39 (C-8), 125.63 (C-4), 75.90 (C-3), 61.61 (C-13), 54.68 (C-2), 33.04 (C-12), 21.41 (C-11), 14.07 (C-14), 13.28 (C-10).

Pinoresinol ***(4)****:* White powder. ESI-MS *m/z* 359.3**.** ^{1}H-NMR (600 MHz, DMSO-d_6): δ_H 6.88 (2H, d, *J*=1.8 Hz, H-2, H-2′), 6.75 (2H, dd, *J*=8.4, 1.8 Hz, H-6, H-6′), 6.72 (2H, d, *J*=8.4 Hz, H-5, H-5′), 4.60 (2H, d, *J*=4.2 Hz, H-7, H-7′), 4.11 (2H, dd, *J*=9.0, 6.6 Hz, H-9a, H-9′a), 3.76 (6H, s, 2xOCH_3), 3.72 (2H, dd, *J*=9.0, 4.2 Hz, H-9b, H-9′b), 3.04-3.02 (2H, m, H-8, H-8′). ^{13}C-NMR (150 MHz, DMSO-d_6): δ_C 147.50 (C-3, C-3′), 145.88 (C-4, C-4′), 132.21 (C-1, C-1′), 118.61 (C-6, C-6′), 115.11 (C-5, C-5′), 110.39 (C-2, C-2′), 85.13 (C-7, C-7′), 70.87 (C-9, C-9′), 55.58 (2xOCH_3), 53.56 (C-8, C-8′).

Lariciresinol 9-O-β-glucopyranoside ***(5)****:* White powder. ESI-MS *m/z* 545.3 $[M+Na]^+$. ^{1}H-NMR (600 MHz, CD_3OD): δ_H 6.95 (1H, d, *J*=1.8 Hz, H-2), 6.82 (1H, dd, *J*=7.8, 1.8 Hz, H-6), 6.81 (1H, d, *J*=1.8 Hz, H-2′), 6.78 (1H, d, *J*=7.8 Hz, H-5), 6.73 (1H, d, *J*=8.4 Hz, H-5′), 6.67 (1H, dd, *J*=8.4, 1.8 Hz, H-6′), 4.32 (1H, d, *J*=7.8 Hz, H-1″), 4.23 (1H, dd, *J*=9.6, 7.2 Hz, H-9a), 3.99 (1H, dd, *J*=8.4, 6.6 Hz, H-9′a), 3.89 (1H, dd, *J*=11.4, 1.8 Hz, H-6″a), 3.87 (3H, s, OCH_3), 3.86 (3H, s, OCH_3), 3.76 (1H, dd, *J*=8.4, 6.6 Hz, H-9′b), 3.69 (1H, dd, *J*=11.4, 5.4 Hz, H-6″b), 3.62 (1H, dd, *J*=9.6, 6.0 Hz, H-9b), 3.38-3.36 (1H, m, H-3″), 3.32-3.30 (2H, m, H-4″, H-5″), 3.27-3.24 (1H, m, H-2″), 3.02 (1H, dd, *J*=13.8, 4.8 Hz, H-7′a), 2.78-2.75 (1H, m, H-8′), 2.57-2.51 (2H, m, H-7′b, H-8). ^{13}C-NMR (150 MHz, CD_3OD): δ_C 149.00 (C-3, C-3′), 147.07 (C-4), 145.76 (C-4′), 135.65 (C-1), 133.82 (C-1′), 122.19 (C-6′), 119.89 (C-5), 116.19 (C-5′), 115.99 (C-6), 113.52 (C-2′), 110.80 (C-2), 104.60 (C-1″), 84.15 (C-7), 78.29 (C-3″), 78.04 (C-5″), 75.18 (C-2″), 73.69 (C-9′), 71.71 (C-4″), 68.47 (C-9), 62.84 (C-6″), 56.45, 56.44 (2xOCH_3), 51.70 (C-8), 44.04 (C-8′), 33.72 (C-7′).

Naringenin ***(6)****:* White powder. ^{1}H-NMR (600 MHz, DMSO-d_6): δ_H 12.15 (1H, s, 5-OH), 7.31 (2H, d, *J*=9.0 Hz, H-2′, H-6′), 6.79 (2H, d, *J*=9.0 Hz, H-3′, H-5′), 5.88 (1H, d, *J*=2.4 Hz, H-8), 5.87 (1H, d, *J*=2.4 Hz, H-6), 5.44 (1H, dd, *J*=12.6, 3.0 Hz, H-2), 3.26 (1H, dd, *J*=16.8, 12.6 Hz, H-3a), 2.67 (1H, dd, *J*=16.8, 3.0 Hz, H-3b). ^{13}C-NMR (150 MHz, DMSO-d_6): δ_C 196.40 (C-4), 166.63 (C-7), 163.47 (C-5), 162.93 (C-9), 157.71 (C-4′), 128.84 (C-1′), 128.33 (C-2′, C-6′), 115.14 (C-3′, C-5′), 101.75 (C-10), 95.76 (C-6), 94.94 (C-8), 78.41 (C-2), 41.95 (C-3).

Apigenin ***(7)****:* Yellow powder. ^{1}H-NMR (600 MHz, CD_3OD): δ_H 7.87 (2H, d, *J*=8.4 Hz, H-2′, H-6′), 6.95 (2H, d, *J*=8.4 Hz, H-3′, H-5′), 6.61 (1H, s, H-3), 6.48 (1H, d, *J*=1.8 Hz, H-8), 6.23 (1H, d, *J*=1.8 Hz, H-6). ^{13}C-NMR (150 MHz, CD_3OD): δ_C 184.05 (C-4), 166.14 (C-7), 166.27 (C-2), 163.23 (C-5), 162.67 (C-4′), 159.53 (C-9), 129.53 (C-2′, C-6′), 123.28 (C-1′), 117.11 (C-3′, C-5′), 105.32 (C-10), 102.87 (C-3), 100.17 (C-6), 94.97 (C-8).

Luteolin ***(8)****:* Yellow powder. ^{1}H-NMR (600 MHz, CD_3OD): δ_H 7.40 (1H, dd, *J*=7.8, 2.4 Hz, H-6′), 7.39 (1H, d, *J*=2.4 Hz, H-2′), 6.92 (1H, d, *J*=7.8 Hz, H-5′), 6.55 (1H, s, H-3), 6.45 (1H, d, *J*=1.8

Hz, H-8), 6.22 (1H, d, *J*=1.8 Hz, H-6). ^{13}C-NMR (150 MHz, CD_3OD): δ_C 183.93 (C-4), 166.39 (C-7), 166.10 (C-2), 163.18 (C-5), 159.45 (C-9), 150.98 (C-4′), 147.03 (C-3′), 123.75 (C-1′), 120.38 (C-6′), 116.78 (C-5′), 114.15 (C-2′), 105.32 (C-10), 103.88 (C-3), 100.19 (C-6), 95.06 (C-8).

Chemical structures of compounds **1-8** obtained from *P. multifida* are presented in Fig. 1.

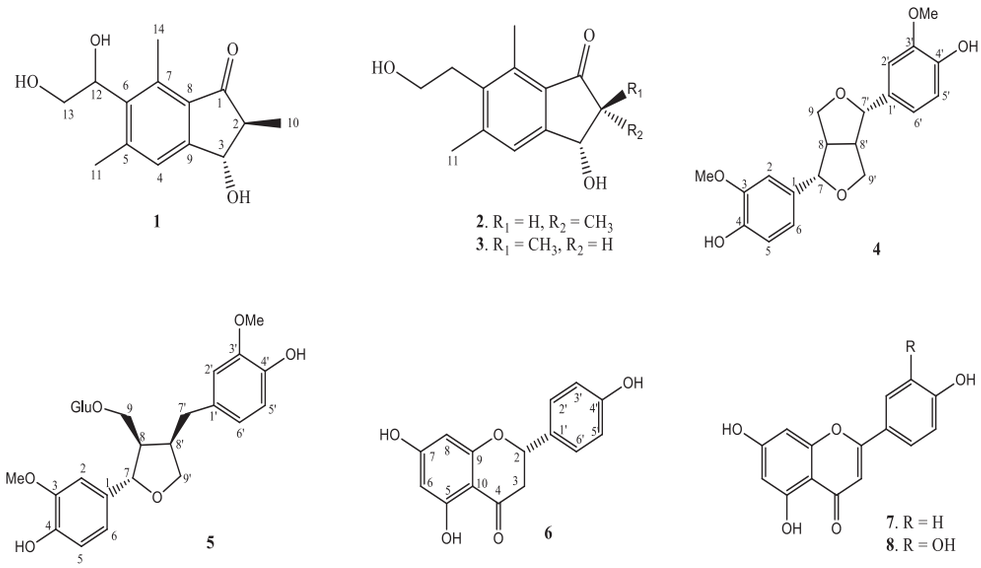

Fig. 1. Chemical structures of compounds 1-8 obtained from *P. multifida*.

3. Results and discussion

Compound **1** was isolated as a white powder and its molecular formula was established as $C_{14}H_{18}O_4$ based on a pseudo-molecular ion peak at 251.2 $[M+H]^+$ and NMR data. The carbon-13 nuclear magnetic resonance (^{13}C-NMR) and heteronuclear single quantum coherence (HSQC) of **1** displayed 14 carbon signals including one ketone group at δ_C 207.52 (C-1), 5 quaternary aromatic carbons, one aromatic methine carbon, 3 aliphatic methine carbons in which two oxygenated methines, 1 oxygenated methylene carbon, and three methyl groups. The ^{1}H-NMR spectrum showed signals of one aromatic proton [δ_H7.36 (1H, s, H-4)], one oxygenated methylene [δ_H 3.94 (1H, dd, *J*=11.4, 8.4 Hz, H-13a), 3.65 (1H, dd, *J*=11.4, 5.4 Hz, H-13b)], three methine protons [δ_H 5.34 (1H, dd, *J*=8.4, 5.4 Hz, H-12), 4.70 (1H, d, *J*=4.2 Hz, H-3), and 2.49-2.45 (1H, m, H-2)] and three methyl groups [δ_H 2.77 (3H, s, H-14), 2.59 (3H, s, H-11), and 1.32 (3H, d, *J*=7.2 Hz, H-10)]. These indicated compound **1** was a pterosin sesquiterpene. The small coupling constant $J_{2\text{-}3}$=4.2 Hz suggested the *trans*-configuration for the protons at C-2 and C-3 in **1** [9]. The HMBC spectrum showed correlations of H-10 to C-1, C-2, and C-3; of H-12 to C-6, C-7, C-13; of H-11 to C-4 and C-5; and of H-4 to C-3 and C-8. Based on the above results, the structure of compound **1** was identified as (2*S*,3*S*)-pretosin Q. This compound was previously obtained from *P. multifida* [3].

Compounds **2** and **3** were obtained as a mixture with a ratio of 1:3 (based on the peak intensities in their ^{1}H- and ^{13}C-NMR spectra). The ESI-MS spectrum showed only one *pseudo*-molecular ion peak at *m/z* 235.3 $[M+H]^+$ suggesting that **2** and **3** are isomers. The ^{1}H- and ^{13}C-NMR spectral data of compounds **2** and **3** were similar to those of **1** except for the presence of an additional methylene group and the absence of one oxymethine group at C-12. The coupling constants ($J_{2\text{-}3}$=6.6 Hz and $J_{2\text{-}3}$=4.2 Hz) confirmed the *cis*-, *trans*-configurations for the protons at C-2 and C-3 in **2** and **3**, respectively. Additionally, the ^{13}C-NMR spectral data of **2** and **3** were similar to those of the (2*R*,3*S*)-acetylpterosin C and (2*S*,3*S*)-acetylpterosin C, except for the absence of signals of the acetyl groups at C-13 and the chemical shifts of C-13 and C-12 significantly changed by -2.2 and +4.1 ppm, respectively [11]. As a result, the chemical structures of **2** and **3** were established as (2*R*,3*S*)-pterosin C and (2*S*,3*S*)-pterosin C, respectively.

The ESI-MS spectrum of **4** showed a *pseudo*-molecular ion peak at *m/z* 359.3 $[M+H]^+$. The ^{13}C NMR and HSQC spectra indicated the presence of only ten carbon peaks, including three aromatic quaternary carbons, three methine carbons, one oxymethylene, one oxymethine, one methine, and one methoxy group. These suggested that compound **4** was a symmetrical molecule and its molecular formula as $C_{20}H_{22}O_6$. The ^{1}H-NMR revealed six aromatic protons in a pair of ABX systems at δ_H 6.88 (2H, d, *J*=1.8 Hz, H-2, H-2′), 6.75 (2H, dd, *J*=8.4, 1.8 Hz, H-6, H-6′), 6.72 (2H, d, *J*=8.4 Hz, H-5, H-5′), two methoxy groups at δ_H 3.76 (6H, s), and aliphatic protons at δ_H 4.60 (2H, d, *J*=4.2 Hz, H-7, H-7′), 4.11 (2H, dd, *J*=9.0, 6.6 Hz, H-9a, H-9′a), 3.72 (2H, dd, *J*=9.0, 4.2 Hz, H-9b, H-9′b), 3.04-3.02 (2H, m, H-8, H-8′). Therefore, the structure of **4** was determined to be pinoresinol. The ^{13}C-NMR data (in DMSO-*d6*) of **4** were in good agreement with those of pinoresinol in [15].

The molecular formula of **5** was determined as $C_{26}H_{34}O_{11}$ from an ESI-MS pseudo-molecular ion peak at 545.3 $[M+Na]^+$ and NMR spectral data. The ^{13}C-NMR and HSQC spectra showed a total 26 carbon signals, which included three methines (δ_C 84.15, 51.70 and 44.04), three methylenes (δ_C73.69, 68.47 and 33.72), two methoxy groups (δ_C 56.45, 56.44), twelve signals for two aromatic rings (δ_C 149.00- 110.80), and six signals for one glucose unit with an anomeric carbon at δ_C 104.60. The ^{1}H-NMR spectrum of **5** revealed the presence of two 1,3,4-trisubstitued benzenes

[δ_H 6.95 (1H, d, *J*=1.8 Hz, H-2), 6.82 (1H, dd, *J*=7.8, 1.8 Hz, H-6), 6.78 (1H, d, *J*=7.8 Hz, H-5); 6.81 (1H, d, *J*=1.8 Hz, H-2′), 6.73 (1H, d, *J*=8.4 Hz, H-5′), 6.67 (1H, dd, *J*=8.4, 1.8 Hz, H-6′)], two methoxy groups [δ_H 3.87 and 3.86 (each 3H, s)]. In addition, the ^{1}H-NMR spectrum also supported the presence of one *β*-glucose moiety with an anomeric proton signal at δ_H 4.32 (1H, d, *J*=7.8 Hz, H-1″). The HMBC correlations between H-1″ (δ_H 4.32) with C-9 (δ_C 68.47) indicated that the sugar unit was attached at the C-9 position. The NOE correlations between H-8 and H-8′ and between H-7 and H-9 confirmed the benzyl group and the glucosyl group were on the same side, while the phenyl group was oriented to the other side of tetrahydrofuran ring. The ^{13}C-NMR data of **5** were similar with those of lariciresinol [16] except for the presence of an additional β-glucose unit. Based on above evidence, the structure of **5** was elucidated to be lariciresinol 9-O-β-glucopyranoside.

Compound **6** was obtained as white powder. The ^{13}C-NMR and HSQC spectra showed 15 carbon signals comprising one carbonyl carbon (δ_C 196.40), six quaternary carbons, seven methine carbons, and one methylene carbon. These suggested **6** was a flavonoid. The ^{1}H-NMR spectrum exhibited a one-proton singlet [δ_H 12.15] for a chelated hydroxyl group at C-5, two *meta*-coupled proton signals [δ_H 5.88 (1H, d, *J*=2.4 Hz) and 5.87 (1H, d, *J*=2.4 Hz)] corresponding to H-8 and H-6 of ring A, one AA′BB′ spin systems of 1’,4’-disubstituted aromatic ring B [δ_H 7.31 and 6.79 (both 2H, d, *J*=7.5 Hz)], and other proton signals of ring C [δ_H 5.44 (1H, dd, *J*=12.6, 3.0 Hz, H-2), 3.26 (1H, dd, *J*=16.8, 12.6 Hz, H-3a), 2.67 (1H, dd, *J*=16.8, 3.0 Hz, H-3b)]. ^{1}H- and ^{13}C-NMR data of **6** were in good agreement with those reported for naringenin [17]. Therefore, **6** was determined to be naringenin.

The structures of the remaining two compounds, **7** and **8,** were determined to be apigenin [18] and luteolin [19], respectively, based on the analysis NMR data and by comparison with the literature. These flavonoids have been found in several plant species and have been previously obtained from *P. multifida.*

Figure 2 shows in simplified form the pathways involved in the biosynthesis of all isolated compounds starting primary metabolism. Farnesyl pyrophosphate is the starting material for all other sesquiterpenes including compounds **1**, **2**, and **3**. The lignan biosynthesis of **4** and **5** were developed through a long sequence of reactions involving the shikimic acid pathway from cinnamic acid to feruloyl-CoA. Flavonoids **6**, **7**, and **8** are synthesised via shikimic acid and HAc-malonic acid pathways, respectively [20-22].

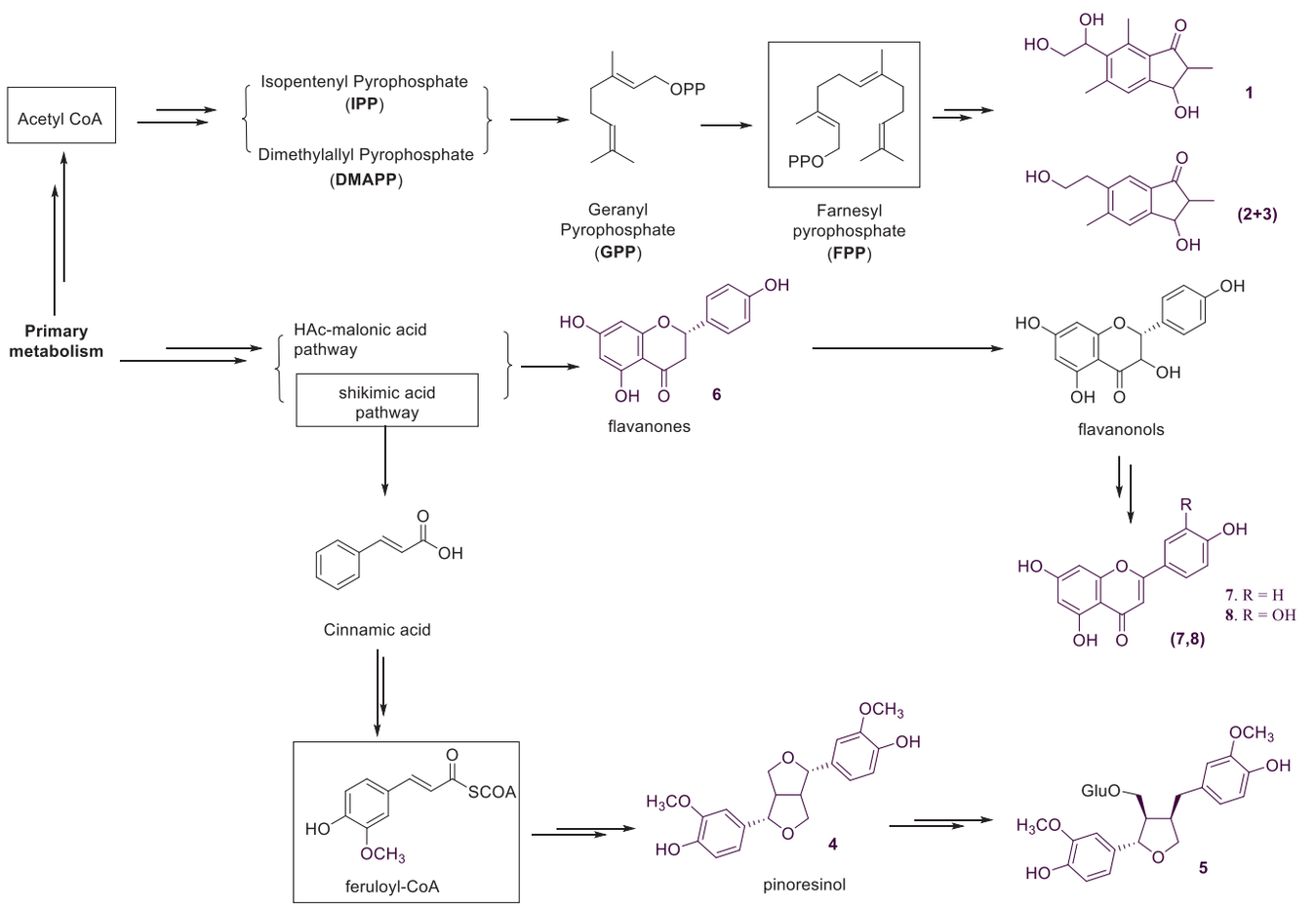

Fig. 2. The proposed biosynthetic pathways of compounds 1-8.

4. Conclusions

The chromatographic investigation of the ethyl acetate extract of the entire whole of *P. multifida* plant collected in the Nam Dinh province, Vietnam, led to the isolation of eight compounds. Their structures were identified as (2*S*,3*S*)-pretosin Q (**1**), (2*R*,3*S*)-pterosin C (**2**), (2*S*,3*S*)-pterosin C (**3**), pinoresinol (**4**), lariciresinol 9-O-*β*-glucopyranoside (**5**), naringenin (**6**), apigenin (**7**), and luteolin (**8**) by analysis of their 1D-NMR (^{1}H-, ^{13}C-NMR), 2D-NMR (HSQC, HMBC, NOESY), ESI-MS spectra, and comparison with published data. This is the first report of the isolation of compounds **4-6** from *P. multifida*.

CRediT author statement

Duc Thien Dao: Methodology, Data curation, Writing - Original draft preparation; Hoang Sa Nguyen: Data curation, Writing - Original draft preparation; Huu Thu Do: Investigation; Thanh Tam Nguyen: Writing - Reviewing and Editing.

ACKNOWLEDGEMENTS

This research was supported by Institute of Chemistry, Vietnam Academy of Science and Technology under grant number VHH.2022.14.

COMPETING INTERESTS

The authors declare that there is no conflict of interest regarding the publication of this article.

REFERENCES

[1] P.H. Ho (2000), *An Illustrated Flora of Vietnam*, Youth Publishing House, **1**, pp.61-68 (in Vietnamese).

[2] W. Hu, M. Hou, K. Hao, et al. (2021), "Phytochemical and chemotaxonomic studies on *Pteris wallichiana* J. Agardh", *Biochemical Systematics and Ecology*, **95**, DOI: 10.1016/j.bse.2021.104242.

[3] M. Hou, Y. Chen, Y. Wang, et al. (2021), "Sesquiterpenoids and flavonoids from *Pteris multifida* Poir.", *Biochemical Systematics and Ecology*, **98**, DOI: 10.1016/j.bse.2021.104320.

[4] J.W. Kim, J.Y. Seo, W.K. Oh, et al. (2017), "Anti-neuroinflammatory *ent*-kaurane diterpenoids from *Pteris multifida* roots", *Molecules*, **22(1)**, pp.27-36, DOI: 10.3390/molecules22010027.

[5] T.C. Wang, C.C. Lin, H.I. Lee, et al. (2010), "Anti-hyperlipidemic activity of spider brake (*Pteris multifida*) with rats fed a high cholesterol diet", *Pharmaceutical Biology*, **48(2)**, pp.221-226, DOI: 10.3109/13880200903085458.

[6] B.B. Hu, X.D. Zheng, H.S. Hu, et al. (2009), "Three antibacterial compounds from the roots of *Pteris multifida*", *Chemistry of Natural Compounds*, **45(1)**, pp.45-48, DOI: 10.1007/s10600-009-9258-5.

[7] T.C. Wang, M.C. Ti, S.C. Lo, et al. (2007), "Free radical-scavenging activity of aqueous extract of *Pteris multifida* Poiret", *Fitoterapia*, **78(3)**, pp.248-249, DOI: 10.1016/j.fitote.2006.11.004.

[8] H.B. Hu, X.D. Zheng, H. Cao, et al. (2006), "Xanthone *O*-glycosides from the roots of *Pteris multifida*", *Journal of the Chinese Chemical Society*, **53(2)**, pp.459-464, DOI: 10.1002/cbdv.202200499.

[9] X. Ge, G. Ye, P. Li, et al. (2008), "Cytotoxic diterpenoids and sesquiterpenoids from *Pteris multifida*", *Journal of Natural Product*, **71(2)**, pp.227-231, DOI: 10.1021/np0706421.

[10] J. Liu, J. Shu, R. Zhang, et al. (2011), "Two new pterosin dimers from *Pteris multifida* Poir.", *Fitoterapia*, **82(8)**, pp.1181-1184, DOI: 10.1016/j.fitote.2011.08.004.

[11] J. Shu, J. Liu, Y. Zhong, et al. (2012), "Two new pterosin sesquiterpenes from *Pteris multifida* Poir.", *Phytochemistry Letters*, **5(2)**, pp.276-279, DOI: 10.1016/j.phytol.2012.01.011.

[12] G. Ni, G.J. Fu, D. Zhang, et al. (2015), "An unusual dihydrobenzofuroisocoumarin and *ent*-kauranediterpenoids from *Pteris multifida*", *Journal of Asian Natural Products Research*, **17(5)**, pp.423-429, DOI: 10.1080/10286020.2015.1040777.

[13] N.D. Chi, L.Q. Long, T.N.H. Thu, et al. (2014), "Some flavonoids were isolated from sedge grass (*Pteris multifida* Poir.) collected in Hanoi (in Vietnamese)", *Journal of Medicinal Materials*, **54(9)**, pp.50-54.

[14] N.D. Chi, L.Q. Long, T.N.H. Thu, et al. (2015), "Some compounds isolated from water fractions of sedge grass (*Pteris multifida* Poir.) collected in Hanoi (in Vietnamese)", *Journal of Medicinal Materials*, **55(3)**, pp.25-29.

[15] S. Nishibe, H. Tsukamoto, S. Hisada, et al. (1984), "Effects of *O*-methylation and *O*-glucosylation on carbon-13 nuclear magnetic resonance chemical shifts of matairesinol, (+)-pinoresinol and (+)-epipinoresinol", *Chemical and Pharmaceutical Bulletin*, **32(11)**, pp.4653-4657, DOI: 10.1248/cpb.32.2622.

[16] L.H. Xie, T. Akao, K. Hamasaki, et al. (2003), "Biotransformation of pinoresinol diglucoside to mammalian lignans by human intestinal microflora, and isolation of *Enterococcus faecalis* strain PDG-1 responsible for the transformation of (+)-pinoresinol to (+)-lariciresinol", *Chemical and Pharmaceutical Bulletin*, **51(5)**, pp.508-515, DOI: 10.1248/cpb.51.508.

[17] C.C. Shen, Y.S. Chang, L.K. Hott, et al. (1993), "Nuclear magnetic resonance studies of 5,7-dihydroxyflavonoids", *Phytochemistry*, **34(3)**, pp.843-845.

[18] L.A.L. Silva, L.G. Faqueti, F.H. Reginatto, et al. (2015), "Phytochemical analysis of *Vernonanthura tweedieana* and a validated UPLC-PDA method for the quantification of eriodictyol", *Revista Brasileira de Farmacognosia*, **25(4)**, pp.375-381, DOI: 10.1016/0031-9422(93)85370-7.

[19] L.M. Ha, N.T. Phuong, D.T.T. Huyen, et al. (2019), "A contribution to study chemical constituents of *Desmodium gangeticum* of Vietnam", *Vietnam Journal of Science and Technology*, **57(1)**, pp.1-6, DOI: 10.15625/2525-2518/57/1/12758.

[20] G.A. Cordell (1976), "Biosynthesis of sesquiterpenes", *Chemical Reviews*, **76(4)**, pp.425-460, DOI: 10.1021/cr60302a002.

[21] N.G. Lewis, L.B. Davin, S. Sarkanen (1998), "Chapter 1: Lignin and lignan biosynthesis: Distinctions and reconciliations", *ACS Symposium Series*, **697**, pp.1-27, DOI: 10.1021/bk-1998-0697.ch001.

[22] M. Rehan (2021), "Biosynthesis of diverse class flavonoids *via* shikimate and phenylpropanoid pathway", *Bioactive Compounds - Biosynthesis, Characterization and Applications*, IntechOpen Publisher, 304pp, DOI: 10.5772/intechopen.96512.

DOI: 10.31276/VJSTE.65(3).44-49

Pencil lead graphite electrochemically modified with polyglutamic acid as a sensor for detection of enrofloxacin in aqueous media

Thi Hai Yen Pham[1*], Thi Kim Ngan Nguyen[2, 3], Thi Thu Hien Chu[4], Thi Thu Ha Vu[1], Quoc Hung Le[1]

[1]*Institute of Chemistry, Vietnam Academy of Science and Technology, 18 Hoang Quoc Viet Street, Nghia Do Ward, Cau Giay District, Hanoi, Vietnam*
[2]*Graduate University of Science and Technology, Vietnam Academy of Science and Technology, 18 Hoang Quoc Viet Street, Nghia Do Ward, Cau Giay District, Hanoi, Vietnam*
[3]*Faculty of Chemistry, University of Sciences, Thai Nguyen University, Tan Thinh Ward, Thai Nguyen City, Thai Nguyen Province, Vietnam*
[4]*Department of Chemistry, Faculty of Building Materials, Hanoi University of Civil Engineering, 55 Giai Phong Street, Dong Tam Ward, Hai Ba Trung District, Hanoi, Vietnam*

Received 13 December 2022; revised 1 March 2023; accepted 6 March 2023

Abstract:

This study investigates the modification of pencil lead graphite electrodes with polyglutamic acid using an effective and fast static method to develop a sensor for the detection of enrofloxacin (ENR). The successful fabrication of pGA on the electrode surface was confirmed by scanning electron microscopy, energy dispersive X-ray analysis, and Fourier-transform infrared spectroscopy. The conditions of electrochemical modification, including the applied potentials and number of cycles in the potentiostatic process, were systematically investigated to determine their effects on the ENR electrochemical response. The pH of the electrolyte media was also explored to elucidate the electrochemical reaction mechanism of ENR. The developed electrochemical sensor was evaluated using square wave stripping voltammetry for ENR detection. Under optimal conditions, the sensor demonstrated good reproducibility with a relative standard deviation of 4.3% (from five measurements) for ENR signal detection. A linear relationship between ENR concentration and its peak current was observed in the concentration range of 0.1 to 5 µM, with a high correlation coefficient of 0.9988. The limit of detection for ENR using the sensor was 0.12 µM. Our findings provide valuable insights into the design and optimisation of pencil lead graphite electrode-based sensors for ENR detection in aqueous media.

Keywords: **electrochemical analysis, electrochemical polymerisation, enrofloxacin detection, glutamic acid, potentiostatic method.**

Classification numbers: **2.2, 5.3**

1. Introduction

ENR has been one of the most widely used antimicrobial drugs for the treatment of infections originating from both gram-positive and gram-negative bacteria in animals [1-3]. The diseases caused by these bacteria include respiratory, mammary, digestive, and dermal infections in livestock and aquaculture [4, 5]. ENR has also been used in the treatment of osteomyelitis, otitis, peritonitis, and pneumonia in humans [6, 7]. Although it has a vital role in preventing humans from microbial infection, the overuse of ENR and its residue can place human health at risk [8, 9]. Besides, the ENR residue generated from human and animal digestion, ENR residues in wastewater is considered a potential risk to the environment due to its accumulation in water and soil [10, 11]. Moreover, antibiotics are considered a factor in the development of anti-bacterial resistant bacteria [12]. Due to these potential dangers, it is crucial to construct analytical methods for the determination of ENR at low concentration ranges in an aqueous environment.

Over past few decades, methods for quantifying ENR have been developed including capillary electrophoresis, high□performance liquid chromatography, liquid chromatography-mass spectrometry, and fluorescence detection [13-17]. These methods provide high accuracy and good sensitivity; however, drawbacks such as extended sample pre-treatment time, complicated operation, requirements for well-trained operators, and high-cost equipment restrict their analytical performance. In recent years, electrochemical determination of ENR has emerged as an effective method owing to advantages like high sensitivity, good selectivity, and convenience [18]. In this method, scientists have mainly focused on modifying the working electrode to improve the electrochemical signal of the target. The modification consists of using nanomaterials like metal nanoparticles, carbon nanomaterials, polymers, organic materials, and metal-organic frameworks [19-25]. These materials have unique properties such as large active surface area, electrochemical catalytic ability, fast electron

[*]*Corresponding author: Email: haiyen25986@gmail.com*

transfer, and customised functional groups, making them beneficial for adsorption and electrochemical reactions of analytes on the electrode surface. Recently, polyglutamic acid (pGA) - a completely biodegradable and non-toxic compound - has attracted much attention in electrochemical research applications because its chain contains a series of free protonated carboxyl groups that facilitate interaction and linkages with desirable targets. In addition, pGA is easily produced on a conductive substrate via an electrochemical process with variable sizes of pGA molecules, making it a promising material in electrochemical applications [26-29].

In this study, we present a new method to modify pencil lead with pGA via a potentiostatic technique that has been employed in the detection of ENR for the first time. The fabrication conditions of the developed electrode were investigated to obtain the most effective sensor for ENR detection. This technique was carried out on a cost-effective electrode substrate with faster and simpler preparation methods compared to previously published ones. Besides, the pGA-based sensor, in combination with an eco-friendly environmental modifier, showed good performance in the quantification of ENR.

2. Materials and methods

2.1. Reagents and apparatus

Pencil lead (diameter of 0.5 mm, length of 15 mm) was purchased from Dong-a Pencil Co., Ltd., Korea. L-GA (99%), potassium ferricyanide (99.9%), potassium dihydrogen phosphate (99.9%), and di-potassium hydrogen phosphate (99.9%), were purchased from Merck, Sigma-Aldrich. ENR (98%) was purchased from Tokyo Chemical Industry Co., Ltd., Japan. All reagents were directly used without further purification.

Electrochemical measurements were performed using a home-made multi-functional potentiogalvanostat manufactured at the Institute of Chemistry, Vietnam Academy of Science and Technology, Hanoi, Vietnam. The electrochemical cell contains a three-electrode system consisting of an Ag/AgCl electrode (reference electrode), a platinum wire (auxiliary electrode), and pencil lead (working electrode).

Cyclic voltammetry was used for the investigation of the modified electrode's properties.

Field emission scanning electron microscopy (FE-SEM) (Hitachi S-4800, Japan) and attenuated total reflectance -Fourier transform infrared spectroscopy (ATR-FTIR) (Perkin Elmer, L1600400 Spectrum Two, UK) was used to characterise the morphology of the electrode surface.

2.2. Preparation of modified electrode

Initially, pencil lead electrodes were polished with tissue paper and rinsed with 90% ethanol and double-distilled water. The electrochemical modification of pGA on the pencil lead electrodes was carried out by using a potentiostatic technique in a 0.1-M phosphate buffer solution (PBS) at pH 7 containing 5.0 g of l-1 glutamic acid (GA). In this step, negative and positive potentials were alternatively applied for 10 s for various numbers of cycles. Both synthesis parameters were examined.

2.3. Characterisation of pGA/PLE

Cyclic voltammetry (CV) was used to study the electrochemical property of GA and the modified electrodes. The measurement was performed in 5.0×10^{-3} M $K_3Fe(CN)_6$/0.1 M PBS solution (pH 7) at various scan rates from 10 mV to 100 mV.

The electrode performance in ENR was conducted by using square wave stripping voltammetry (SW-AdSV) in a PBS solution containing ENR at various concentrations.

All experiments were performed at 25±2°C.

3. Results and discussion

3.1. Electrochemical polymerisation of GA on pencil lead electrode

The electrochemical reaction of GA on pencil lead was characterised by cyclic voltammetry to determine suitable voltametric parameters for the polymerisation of GA. Fig. 1A shows cyclic voltammograms of a pencil lead electrode in PBS solution (pH 7) with and without GA. Obviously, no peak was obtained in the free glutamic solution in the examined potential range. Meanwhile, two peaks at -1 and 1.8 V clearly appeared in the GA solution. These peaks correspond to the electrochemical polymerisation of GA on the electrode surface [30, 31]. Hence, suitable potentials for electrode fabrication were selected in the range from -1.2 to 2.0 V.

To synthesise pGA on the pencil lead, a clean pencil lead bar was immersed in GA solution, then the potentiostatic technique was performed in two successive steps. In step 1, a negative potential was applied to the electrode for 10 s to form −COO−. Subsequently, step 2 was carried out by applying a positive potential for 10 s to form $-NH_2^{\bullet+}$. The process was repeated for a certain period to grow chains of pGA that were created by the combination of −COO− and ($-NH_2^{\bullet+}$) on the pencil lead surface. Fig. 1A illustrates a potentiostatic graph with the anodic and cathodic potentials of 2.0 and -1.0 V. The proposed mechanism of polymerisation of GA is illustrated in Fig. 1B.

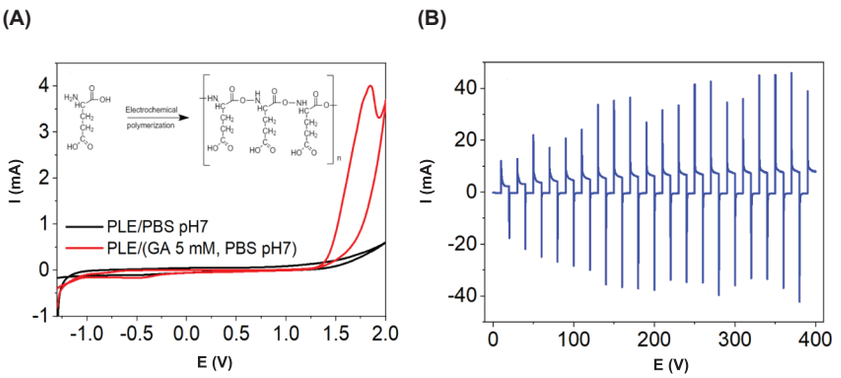

Fig. 1. (A) Cyclic voltammograms and (B) potentiostatic graphic of PLE in pGA solution and during the polymerisation reaction of pGA.

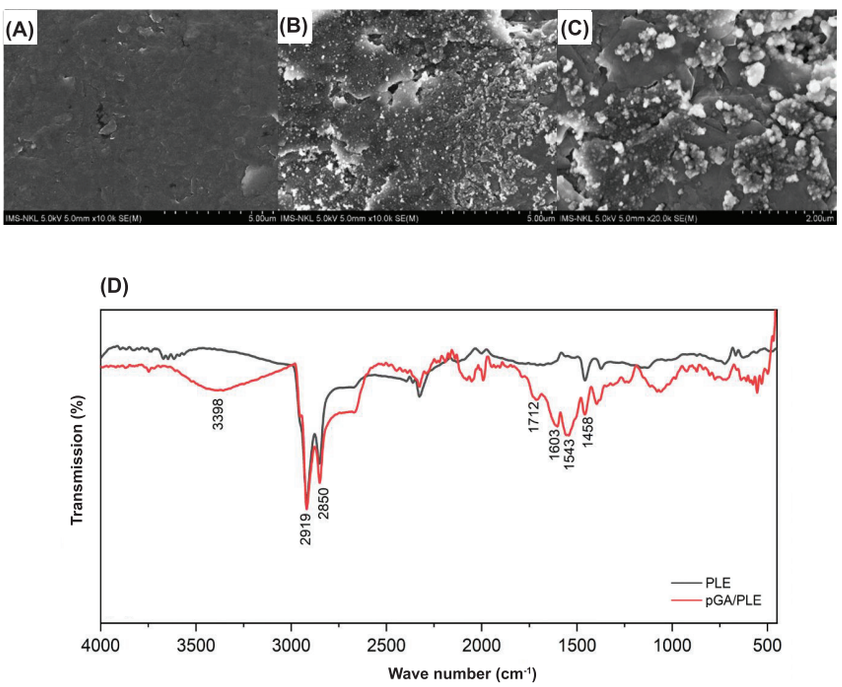

Fig. 2. SEM images of (A) PLE and (B, C) pGA/PLE at different magnifications, (D) ATR-FTIR spectra of PLE and pGA/PLE.

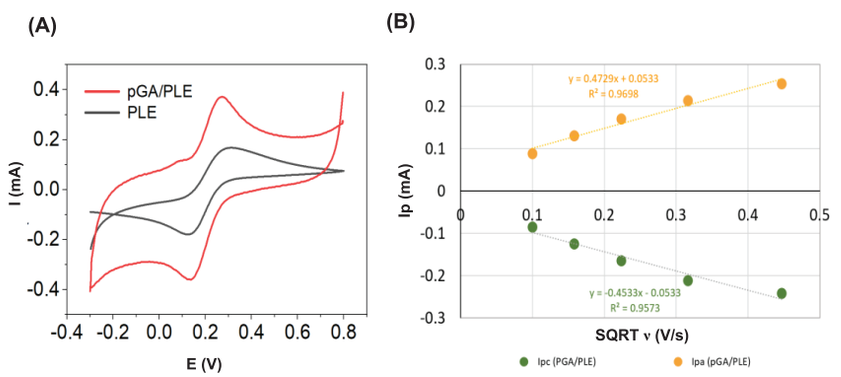

Fig. 3. Cyclic voltammograms of PLE (A) and pGA/PLE (B) in 5 mM $K_3Fe(CN)_6$ solution.

Figure 2 shows the SEM images of pGA/PLE on the electrode surface. As seen in Fig. 2A, the pencil lead electrode has a smooth surface. After modification, pGA clusters are present with a scattered distribution on the pencil lead substrate (Fig. 2B). At higher magnification as seen in Fig. 2C, pGA deposition is clearly identified with a cluster size of several hundred nanometres.

The presence of pGA on PLE can be confirmed by ATR-FTIR spectroscopy, as demonstrated in Fig. 2D. A comparison between the unmodified electrode and the pGA/PLE-modified electrode reveals distinct differences in the spectral peaks. Specifically, the pGA/PLE spectrum exhibits significant peaks at 3398 cm^{-1}, which can be attributed to the stretching vibration of both the N-H and O-H functional groups. Additionally, peaks at 1603, 1543 cm^{-1}, and 1712 cm^{-1}, which correspond to amide I, amide II, and C=O in the carboxylic group, respectively, are observed. These peaks are indicative of the presence of a pGA layer on the PLE electrode surface. Moreover, both the PLE and pGA/PLE electrodes show identical peaks at 2919, 2850, and 1458 cm^{-1}, which can be attributed to C-H stretching and C-C bending in the PLE composition. The obtained results agree with those of previous publications [26, 32-37].

3.2. Electrochemical properties of pGA/PLE

Electrochemical properties of pGA/PLE were examined by cyclic voltammetry. The measurements were performed by cyclic potential scanning from 0.8 to -0.2 V in PBS solution (pH 7) containing 5 mM $K_3Fe(CN)_6$ at different scanning rates. Fig. 3A reveals two clear peaks at 0.18 and 0.25 V, which correspond to the reduction of Fe^{3+} to Fe^{2+} and the oxidation of Fe^{2+} to Fe^{3+}, respectively. It is evident that the reduction peak on PGA/PLE is more symmetric and sharper than that of the pencil lead electrode. Also, the peak current on the modified electrode is higher than that of the unmodified one (Fig. 3A). These indicate that the PGA/PLE exhibited better electron transfer ability and a larger electrochemical active area than the unmodified electrode, which could improve the analytical signal.

Figure 3B illustrates a good linear relationship between peak current and the square root of the potential scanning rate in both oxidation and reduction directions with correlation coefficients of 0.9698 and 0.9573, respectively, indicating the electrochemical process was controlled by diffusion [38].

3.3. The response signal of ENR on the pGA/PLE

The electrochemical response of ENR on the prepared electrode was evaluated by using the SW-AdSV method in a 1 µM ENR solution. As can be seen in Fig. 4A, no peak appeared in the blank solution, while a peak at 0.8 V was clearly observed in the ENR solution. The peak is attributed to the oxidation of ENR on the electrode surface with a reaction mechanism proposed in Fig. 4B [39]. In addition, the result shows a much higher peak current on pGA/PLE than the signal on PLE (13.5 times higher). This increase could be explained by the improvement of ENR accumulation on pGA surface.

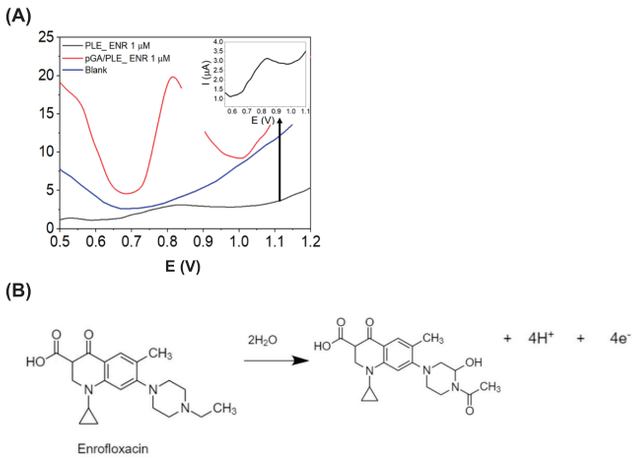

Fig. 4. (A) Square wave graph of PLE (black line) and pGA/PLE (red line) in 1 µM ENR solution; (B) The proposed mechanism of oxidation of ENR.

3.4. Optimisation of pGA/PLE polymerisation and pH of supporting electrolyte

ENR determination significantly depends on the preparation parameters and pH of the supporting electrolyte. This section details the influence of these parameters on the ENR signal.

Influence of polymerisation method on the ENR signal: In comparison with the pencil lead electrode modified with pGA by the cyclic voltammetry method, the ENR peak current on pGA/PLE produced by the potentiostatic method provided a higher ENR peak current (1.45 times higher) (Fig. 5A) and was three times faster. Therefore, to obtain sufficient ENR signal and to reduce preparation time, the potentiostatic method was chosen for electrode modification.

Influence of polymerisation cycle number on the ENR signal: The impact of cycle number in the polymerisation process on ENR signal was investigated by SWV in a PBS solution containing 1 µM ENR. As shown in Fig. 5B, when the cycle number changed from 1 to 20, the peak current significantly increased and reached its highest value at 20 cycles. The peak current gradually decreased over the range of cycles from 30 to 50. Therefore, the 20-cycle polymerisation process was chosen for the next experiment.

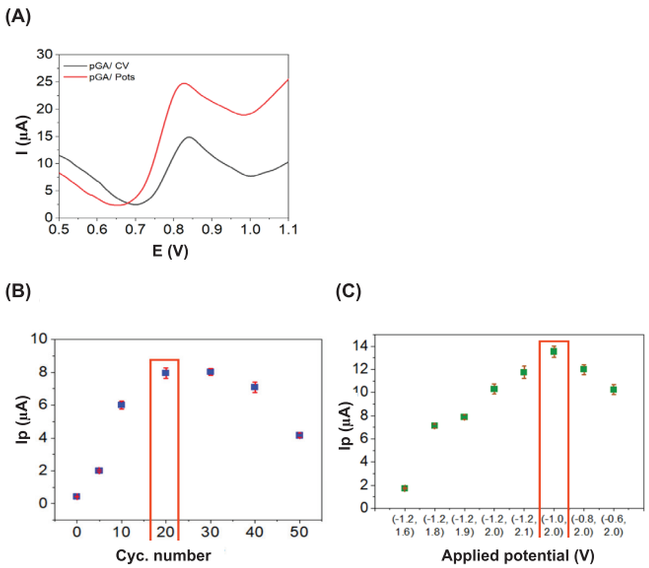

Fig. 5. (A) Square wave voltammograms in ENR solution of pGA/PLE fabricated by cyclic voltammetry and potentiostatic method; (B) Plot of ENR peak current vs cycle numbers; (C) Applied potentials in polymerisation.

Influence of applied polymerisation potential on the ENR signal: The applied potential used in the polymerisation step also plays a crucial role in the improvement of the ENR signal. Cathodic and anodic potential couples of -1.2 and 1.6 V, -1.2 and 1.8 V, -1.2 and 1.9 V, -1.2 and 2.0 V, -1.2 and 2.1 V, -1 and 2 V, -0.8 and 2 V, and -0.6 and 2 V were selected for the investigation. As demonstrated in Fig. 5C, among these potential couples, the highest ENR peak current was obtained when applying a potential couple of -1 and 2 V. These potential values were appropriate for polymerisation in that it supplied sufficient energy for the formation of the ions and free radicals. The decrease in peak current at more negative cathodic potentials and positive potentials could be because of the generation of hydrogen bubbles on the electrode surface, preventing polymer formation. Therefore, the polymerisation potential couple of -1 and 2 V was chosen for the following experiment.

The influence of pH on ENR signal: The pH value of the supporting electrolyte solution has a significant impact on the electrochemical oxidation of ENR. To determine an optimal pH value for ENR analysis, the oxidation signal was recorded in a PBS solution containing 1 µM ENR at different pH values (Fig. 6A). At pH of 4 and 5, relatively low peaks were obtained. Then, the peak currents increased with increasing pH value and the highest current was obtained at pH8. The peak current slightly decreased at pH9. Therefore, the PBS solution with pH8 was chosen as the optimal parameter for the analysis of ENR for the next experiments. Fig. 6B shows a linear relationship of pH value vs. peak potentials of ENR with the slope of the linear curve being 0.049, demonstrating that an equal number of electrons and protons were present in the ENR reaction. It is also observed in Fig. 6C that when pH was changed from 4 to 9, peak positions gradually moved to the negative direction. This result suggests that protons participated in the oxidation reaction of ENR.

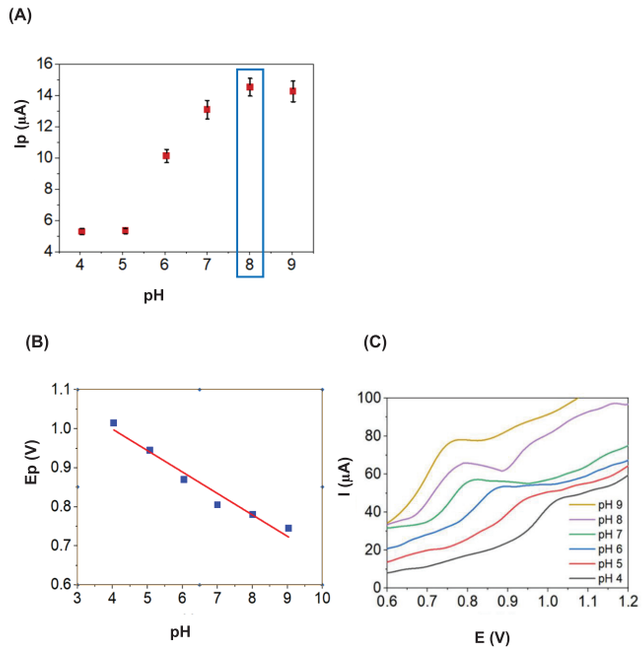

Fig. 6. Plots of ENR peak current vs pH (A) and ENR peak potential vs pH (B); square wave voltammograms of pGA/PLE in ENR solution at pH from 4 to 9 (C).

3.5. Calibration curve for ENR detection

After the optimisation of electrode preparation and analysis conditions, a calibration curve was established to evaluate the performance of ENR detection by SW-AdSV over a concentration range from 0.1 to 5 µM (Fig. 7). Within this concentration range, the peak current and ENR concentration are linearly correlated with the following regression equation: I_p (µA)=14.074 C_{ENR} (µM)-0.353. A correlation coefficient of 0.9988 was obtained. The reproducibility of the measurement was also investigated with an acceptable relative standard deviation of 4.3% (data not shown here). An LOD of 0.122 µM was obtained through the equation LOD=3σ/b; where σ and b are the standard deviation and the linear slope, respectively.

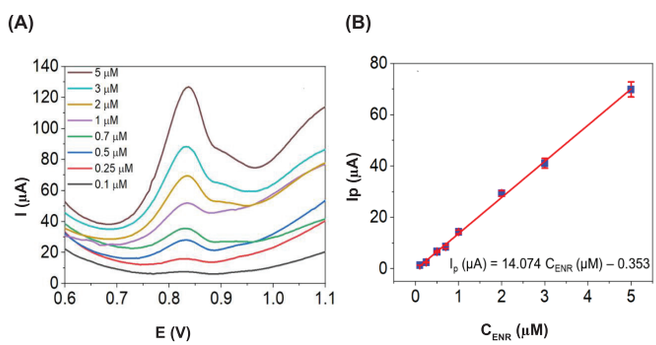

Fig. 7. (A) Square wave voltammograms of pGA/PLE in PBS solution containing ENR over a concentration range from 0.1 to 5 µM; (B) Calibration curve between peak current and concentration.

4. Conclusions

In this study, a novel sensor for ENR detection was successfully developed using polyglutamic-modified pencil lead graphite and a potentiostatic method. Optimal voltametric parameters, including applied cathodic (-1 V) and anodic (2 V) potentials were determined, and the synthesis time was set to 10 s for 20 cycles. The use of a PBS with pH8 was found to be a suitable medium for ENR detection. The sensor demonstrated acceptable reproducibility and a low detection limit of 0.12 µM for ENR. The results of this initial study suggest that the fabrication of the sensor is simple, low-cost, less time-consuming, and environmentally friendly. Thus, it has potential applications in ENR quantification.

CRediT author statement

Thi Hai Yen Pham: Idea and Conceptualisation, Research and Investigation, Revise and Editing, Supervision, Project administration; Thi Kim Ngan Nguyen: Research and Investigation; Thi Thu Hien Chu: Methodology, Writing; Thi Thu Ha Vu: Formal analysis, Writing - Review and Editing; Quoc Hung Le: Resources, Methodology.

ACKNOWLEDGEMENTS

This research is funded by Institute of Chemistry, Vietnam Academy of Science and Technology under grant number VHH.2022.08 and Vietnam National Foundation for Science and Technology Development (NAFOSTED) under grant number 104.06-2019.27.

COMPETING INTERESTS

The authors declare that there is no conflict of interest regarding the publication of this article.

REFERENCES

[1] B.D. Heins, D.V. Nydam, A.R. Woolums, et al. (2014), "Comparative efficacy of enrofloxacin and tulathromycin for treatment of preweaning respiratory disease in dairy heifers", *J. Dairy Sci.*, **97(1)**, pp.372-382, DOI: 10.3168/jds.2013-6696.

[2] E.J. Robb, C.M. Tucker, L. Corley, et al. (2007), "Efficacy of tulathromycin or enrofloxacin for initial treatment of naturally occurring bovine respiratory disease in feeder calves", *Vet. Ther.*, **8(2)**, pp.127-135.

[3] F. Yu, S. Yu, L. Yu, et al. (2014), "Determination of residual enrofloxacin in food samples by a sensitive method of chemiluminescence enzyme immunoassay", *Food Chem.*, **149**, pp.71-75, DOI: 10.1016/j.foodchem.2013.10.024.

[4] A.A. Gouda, A.S. Amin, R. El-Sheikh, et al. (2014), "Spectrophotometric determination of gemifloxacin mesylate, moxifloxacin hydrochloride, and enrofloxacin in pharmaceutical formulations using acid dyes", *Journal of Analytical Methods in Chemistry*, **2014**, DOI: 10.1155/2014/286379.

[5] B. Zhang, L. Lv, X. Ma, et al. (2022), "Au@ZnNi-MOF labeled electrochemical aptasensor for detection of enrofloxacin based on AuPt@h-CeO_2/MoS_2 and DNAzyme-driven DNA walker triple amplification signal strategy", *Biosensors and Bioelectronics*, **210**, DOI: 10.1016/j.bios.2022.114296.

[6] F.M. Salama, K.A. Attia, A.A. Abouserie, et al. (2018), "Potentiometric determination of Enrofloxacin using PVC and coated graphite sensors", *Glob. Drugs Therap.*, **3**, DOI: 10.15761/GDT.1000146.

[7] S. Wu, J. Mao, Y. Zhang, et al. (2023), "Sensitive electrochemical detection of enrofloxacin in eggs based on carboxylated multi-walled carbon nanotubes-reduced graphene oxide nanocomposites: Molecularlyimprintedrecognition versus direct electrocatalytic oxidation", *Food Chemistry*, **413**, DOI: 10.1016/j.foodchem.2023.135579.

[8] S.S. Khaloo, S. Mozaffari, A. Barekat, et al. (2015), "Fabrication of a modified electrode based on multi-walled carbon nanotubes decorated with iron oxide nanoparticles for the determination of enrofloxacin", *Micro & Nano Letters*, **10(10)**, pp.561-566, DOI: 10.1049/mnl.2015.0123.

[9] D. Wang, S. Jiang, Y. Liang, et al. (2022), "Selective detection of enrofloxacin in biological and environmental samples using a molecularly imprinted electrochemiluminescence sensor based on functionalized copper nanoclusters", *Talanta*, **236**, DOI: 10.1016/j.talanta.2021.122835.

[10] C. Canales, E. Peralta, M. Antilen (2019), "Electrochemical techniques to detect and quantify Enrofloxacin in presence of highly potential interferences: Assays in Chilean aqueous-soil matrices", *Journal of Electroanalytical Chemistry*, **832**, pp.329-335, DOI: 10.1016/j.jelechem.2018.10.064.

[11] M. Antilén, C. Valencia, E. Peralta, et al. (2017), "Enrofloxacin behavior in presence of soil extracted organic matter: An electrochemical approach", *Electrochimica Acta*, **244**, pp.104-111, DOI: 10.1016/j.electacta.2017.05.104.

[12] C. Bouki, D. Venieri, E. Diamadopoulos (2013), "Detection and fate of antibiotic resistant bacteria in wastewater treatment plants: A review", *Ecotoxicology and Environmental Safety*, **91**, pp.1-9, DOI: 10.1016/j.ecoenv.2013.01.016.

[13] X. Xu, L. Liu, Z. Jia, et al. (2015), "Determination of enrofloxacin and ciprofloxacin in foods of animal origin by capillary electrophoresis with field amplified sample stacking-sweeping technique", *Food Chemistry*, **176**, pp.219-225, DOI: 10.1016/j.foodchem.2014.12.054.

[14] A.O. Oyedeji, T.A.M. Msagati, A.B. Williams, et al. (2021), "Detection and quantification of multiclass antibiotic residues in poultry products using solid-phase extraction and high-performance liquid chromatography with diode array detection", *Heliyon*, **7(12)**, DOI: 10.1016/j.heliyon.2021.e08469.

[15] H. Tian (2011), "Determination of chloramphenicol, enrofloxacin and 29 pesticides residues in bovine milk by liquid chromatography-tandem mass spectrometry", *Chemosphere*, **83(3)**, pp.349-355, DOI: 10.1016/j.chemosphere.2010.12.016.

[16] J. Dai, Y. Wang, H. Lin, et al. (2023), "Residue screening and analysis of enrofloxacin and its metabolites in real aquatic products based on ultrahigh-performance liquid chromatography coupled with high resolution mass spectrometry", *Food Chemistry*, **404(B)**, DOI: 10.1016/j.foodchem.2022.134757.

[17] M.J.E. Souza, C.F. Bittencourt, L.M. Morsch (2002), "LC determination of enrofloxacin", *Journal of Pharmaceutical and Biomedical Analysis*, **28(6)**, pp.1195-1199, DOI: 10.1016/s0731-7085(01)00673-2.

[18] A.E. Radi (2010), "Application of electrochemical methods for analysis of fluoroquinolones antibacterial agents and fluoroquinolones-DNA interactions", *The Open Chemical and Biomedical Methods Journal*, **3**, pp.27-36, DOI: 10.2174/1875038901003010027.

[19] P. Wei, S. Wang, W. Wang, et al. (2022), "CoNi bimetallic metal-organic framework and gold nanoparticles-based aptamer electrochemical sensor for enrofloxacin detection", *Applied Surface Science*, **604**, DOI: 10.1016/j.apsusc.2022.154369.

[20] S. Han, X. Zhang, H. Sun, et al. (2022), "Electrochemical behavior and voltammetric determination of chloramphenicol and doxycycline using a glassy carbon electrode modified with single-walled carbon nanohorns", *Electroanalysis*, **34(4)**, pp.735-742, DOI: 10.1002/elan.202100354.

[21] E.M. Materón, A. Wong, T.A. Freitas, et al. (2021), "A sensitive electrochemical detection of metronidazole in synthetic serum and urine samples using low-cost screen-printed electrodes modified with reduced graphene oxide and C60", *Journal of Pharmaceutical Analysis*, **11(5)**, pp.646-652, DOI: 10.1016/j.jpha.2021.03.004.

[22] R. Nehru, C.D. Dong, C.W. Chen (2021), "Cobalt-doped Fe_3O_4 nanospheres deposited on graphene oxide as electrode materials for electrochemical sensing of the antibiotic drug", *ACS Applied Nano Materials*, **4(7)**, pp.6768-6777, DOI: 10.1021/acsanm.1c00826.

[23] T.S.K. Sharma, K.Y. Hwa (2021), "Facile synthesis of Ag/AgVO(3)/N-rGO hybrid nanocomposites for electrochemical detection of levofloxacin for complex biological samples using screen-printed carbon paste electrodes", *Inorg. Chem.*, **60(9)**, pp.6585-6599, DOI: 10.1021/acs.inorgchem.1c00389.

[24] A. Feizollahi, A.A. Rafati, P. Assari, et al. (2021), "Development of an electrochemical sensor for the determination of antibiotic sulfamethazine in cow milk using graphene oxide decorated with Cu-Ag core-shell nanoparticles", *Analytical Methods*, **13(7)**, pp.910-917, DOI: 10.1039/D0AY02261F.

[25] A.M. Golkarieh, N. Nasirizadeh, R. Jahanmardi (2021), "Fabrication of an electrochemical sensor with Au nanorods-graphene oxide hybrid nanocomposites for in situ measurement of cloxacillin", *Mater. Sci. Eng. C Mater. Biol. Appl.*, **118**, DOI: 10.1016/j.msec.2020.111317.

[26] Y. Lin, K. Liu, C. Liu, et al. (2014), "Electrochemical sensing of bisphenol A based on polyglutamic acid/amino-functionalised carbon nanotubes nanocomposite", *Electrochimica Acta*, **133**, pp.492-500, DOI: 10.1016/j.electacta.2014.04.095.

[27] X. Liu, L. Luo, Y. Ding, et al. (2011), "Poly-glutamic acid modified carbon nanotube-doped carbon paste electrode for sensitive detection of L-tryptophan", *Bioelectrochemistry*, **82(1)**, pp.38-45, DOI: 10.1016/j.bioelechem.2011.05.001.

[28] Y. Zhang, L. Luo, Y. Ding, et al. (2010), "A highly sensitive method for determination of paracetamol by adsorptive stripping voltammetry using a carbon paste electrode modified with nanogold and glutamic acid", *Microchimica Acta*, **171(1)**, pp.133-138, DOI: 10.1007/s00604-010-0422-1.

[29] J. Thangphatthanarungruang, C. Chotsuwan, W. Siangproh (2023), "A novel and easy-to-construct polymeric l-glutamic acid-modified sensor for urinary 1-hydroxypyrene detection: Human biomonitoring of polycyclic aromatic hydrocarbons exposure", *Talanta*, **253**, DOI: 10.1016/j.talanta.2022.123929.

[30] C. Chen, X. Lv, W. Lei, et al. (2019), "Amoxicillin on polyglutamic acid composite three-dimensional graphene modified electrode: Reaction mechanism of amoxicillin insights by computational simulations", *Analytica Chimica Acta*, **1073**, pp.22-29, DOI: 10.1016/j.aca.2019.04.052.

[31] J.J. Feminus, R. Manikandan, S.S. Narayanan, et al. (2019), "Determination of gallic acid using poly(glutamic acid): Graphene modified electrode", *Journal of Chemical Sciences*, **131(2)**, DOI: 10.1007/s12039-018-1587-0.

[32] O. Suys, A. Derenne, E. Goormaghtigh (2022), "ATR-FTIR biosensors for antibody detection and analysis", *Int. J. Mol. Sci.*, **23(19)**, DOI: 10.3390/ijms231911895.

[33] O. Gördük (2021), "Poly(glutamic acid) modified pencil graphite electrode for voltammetric determination of bisphenol A", *Journal of the Turkish Chemical Society Section A: Chemistry*, **8(1)**, pp.173-186, DOI: 10.18596/jotcsa.728165.

[34] J. Kumirska, M. Czerwicka, Z. Kaczyński, et al. (2010), "Application of spectroscopic methods for structural analysis of chitin and chitosan", *Marine Drugs*, **8(5)**, pp.1567-1636, DOI: 10.3390/md8051567.

[35] E.H. Alsharaeh, A.A. Othman, M.A. Aldosari (2014), "Microwave irradiation effect on the dispersion and thermal stability of RGO nanosheets within a polystyrene matrix", *Materials (Basel)*, **7(7)**, pp.5212-5224, DOI: 10.3390/ma7075212.

[36] B. Sadhasivam, S. Muthusamy (2016), "Synthesis and characterization of optically active polyimides and their octa(aminophenyl) silsesquioxane nanocomposites", *Sage Journals*, **28(5)**, pp.547-561, DOI: 10.1177/0954008315591021.

[37] S. Karamikamkar, M. Fashandi, H.E. Naguib, et al. (2020), "In situ interface design in graphene-embedded polymeric silica aerogel with organic/inorganic hybridization", *ACS Applied Materials & Interfaces*, **12(23)**, pp.26635-26648, DOI: 10.1021/acsami.0c04531.

[38] T.H.Y. Pham, T.T. Mai, H.A. Nguyen, et al. (2021), "Voltammetric determination of amoxicillin using a reduced graphite oxide nanosheet electrode", *Journal of Analytical Methods in Chemistry*, **2021**, DOI: 10.1155/2021/8823452.

[39] M.P. Deepak, G.P. Mamatha (2016), "Simultaneous determination of ciprofloxacin hydrochloride and enrofloxacin at poly (furosemide) modified carbon paste electrode by cyclic voltammetry", *Journal of Chemical and Pharmaceutical Research*, **8(6)**, pp.387-398.

DOI: 10.31276/VJSTE.65(3).50-58

Synthesising nanocomposite Co_2SnO_4@rGO for peroximonosulphate activation in a hybrid ozonation system to effectively degrade cefalexin from wastewater

Van Long Nguyen, Minh Thanh Le, Lan Huong Nguyen*

Ho Chi Minh City University of Industry and Trade (HUIT), 40 Le Trong Tan Street, Tay Thanh Ward, Tan Phu District, Ho Chi Minh City, Vietnam

Received 16 September 2022; revised 13 November 2022; accepted 20 November 2022

Abstract:

This study successfully developed Co_2SnO_4@rGO nanocomposites at various composite ratios of Co_2SnO_4 and rGO using the sol-gel method. These nanocomposites were then used as heterogeneous catalysts to activate PMS in the heterogeneous catalytic oxidation of Co_2SnO_4@rGO/PMS as well as the hybrid ozonation system O_3/Co_2SnO_4@rGO/PMS to degrade cefalexin (CFX). The physical-chemical characteristics of the fabricated catalysts were evaluated through nitrogen adsorption-deadsorption, SEM images, EDS mapping, and XRD. The catalytic activity of the nanocomposite was investigated in a degradation reaction of CFX from an aqueous solution. Besides this, CFX degradation kinetics were determined by fitting experimental data with a first-order model. The results showed that at the composite ratio of 2-Co_2SnO_4 and 1-rGO for CFX degradation had the highest efficiency reaching 95.07 and 99.07% for Co_2SnO_4@ rGO/PMS and O_3/Co_2SnO_4@rGO/PMS systems, respectively. The degradation of CFX in the O_3/Co_2SnO_4@rGO/ PMS system was higher than that of Co_2SnO_4@rGO/PMS. The results were due to a remarkable increase in S_{BET} in 2-Co_2SnO_4@1-rGO compared to both Co_2SnO_4 and rGO, facilitating a catalytic reaction occurring on the catalyst's surface. Moreover, the coupling between O_3 and Co_2SnO_4@rGO/PMS generated a synergetic effect leading to the generation of more $^*SO_4^-$ and $^*OH$ radicals, which enhanced the CFX degradation rate in the hybrid ozonation system. These primary findings illustrated that the nanocomposite catalyst 2-Co_2SnO_4@1-rGO was feasible for the activation of PMS in hybrid ozonation to effectively degrade antibiotic residues from wastewater.

Keywords: **cephalexin, Co_2SnO_4@rGO, hybrid ozonation, O_3, PMS, synthesis.**

Classification numbers: **2.2, 5.3**

1. Introduction

Today, a large amount of antibiotic residues are being found in natural water bodies such as ponds, lakes, rivers, and effluent after secondary treatment [1]. The discharge from hospital, domestic, livestock, and pharmaceutical wastewater has increased antibiotic residues in these receiving water bodies [2]. The presence of antibiotics in aquatic environments is becoming a major concern around the world due to increases in bacterial resistance towards pharmaceuticals [1]. Penicillin and cephalosporin, a group of β-lactam antibiotics that can break down the synthesis of bacterial cell walls and prevent bacterial growth, have been the most widely used around the world to treat bacterial infections accounting for 50-70% of all antibiotics used [3]. Such high consumption of antibiotics inevitably leads to their release into receiving water bodies [4]. Among the antibiotics from the cephalosporin family, CFX is a systemic antibiotic that is most commonly used to treat respiratory tract infections, urinary tract infections, and skin and soft tissue infections caused by sensitive bacteria [5, 6]. Besides, CFX possesses a very low biodegradation rate, nearly 10%, with 90% being excreted through urine causing increasing environmental concern of antibiotic resistance [7, 8]. Recent studies have shown that the CFX concentration found in wastewater, surface water, and even sea water ranges from several ng/l to µg/l [9, 10]. The accumulation of CFX in the environment leads to an occurrence of multi-drug resistant pathogens, which have unpredictable impacts on the environment, human health, and other organisms in the ecosystem [11].

Due to the complex chemical structure and antibacterial properties of CFX, conventional wastewater treatments such as physical, chemical, physicochemical, and biological methods are not effective to remove this compound [11, 12]. Meanwhile, advanced oxidation processes using strong oxidant agents such as O_3, H_2O_2, and PMS in combination

*Corresponding author: Email: huongnl@hufi.edu.vn

with heterogeneous catalysts possess some advantages thanks to generation of free radicals like $^{*}SO_4$, $^{*}OH$, $^{*}O_2$, and $^{1}O_2$. These are very strong oxidation radicals that can oxidize near-persistent organic compounds and antibiotic residues with quick rates and without the formation of by-products. Among these AOPs, advanced sulphate radical ($^{*}SO_4^{-}$)-based oxidation processes using heterogeneous catalysts to activate PMS for the generation of OH, $^{*}SO_4^{-}$, and ozonation have been reported effective in the removal of persistent organic compounds. However, using only heterogeneous catalysts/PMS or O_3 to degrade pollutants have several limitations such as high cost, low stability, and slow oxidation rate. Therefore, to remedy these drawbacks, some hybrid ozonation processes have been recently applied such as O_3/PMS to degrade ibuprofen [13]; O_3/MnO_2@rGO/PMS for removal of 4-nitrophenol [14]; and O_3/PMS to treat para-chlorobenzoic acid [15]. The results of these works indicate that all hybrid ozonation systems demonstrate high removal efficiencies of pollutants compared to using oxidation systems alone due to the synergetic effects between O_3, PMS, and catalysts in the same reactor.

Recently, cobalt-based catalysts have been developed, popularly used, and proven to be the most effective in heterogeneous catalytic systems to activate PMS, thereby promoting the production of $*SO_4^{-}$ radicals due to the high activation efficiency of Co on PMS [16]. For example, M. Stoyanova, et al. (2014) [17] applied $CoFe_2O_4$ to activate PMS for the mineralization of acid orange 7 while others have used MFe_2O_4/PMS for the removal of di-n-butyl phthalate (DBP) (with the highest activation efficiency in the order $CoFe_2O_4$ > $CuFe_2O_4$ > $MnFe_2O_4$ > $ZnFe_2O_4$) [18]; $CoMn_2O_4$ - activated PMS for a Fenton-like reaction to degrade organic dyes [19]; and $Fe_{0.8}Co_{2.2}O_4$ to remove bisphenol A [20]. Co_2SnO_4 was also used to activate PMS for the degradation of rhodamine B and pentachlorophenol with complete removal of both rhodamine B and pentachlorophenol in a 10 - min reaction [21]. However, cobalt oxide exhibits a disadvantage due to the leakage of metal Co into the water after catalysis, especially under acidic conditions [22]. Therefore, to prevent leakage of Co, a cobalt oxide catalyst can be composited with other metal oxides [23], magnetic molecules [24], biochar [25, 26], or graphite (GO, rGO) [27]. Indeed, compositing metal oxides with graphite is considered effective for the prevention of the abovementioned catalyst drawbacks. Among such nanocomposites, the transition metal cobalt has been the most effectively and widely used. For instance, a composite catalyst of nano-$CoFe_2O_4$ and graphite ($CoFe_2O_4$@GO) has been synthesised to degrade amoxicillin (AMX) from water [28]. The results showed that possessed good magnetic properties and was quickly separated from the aqueous medium after the reaction. $CoFe_2O_4$@GO also exhibits a rather good catalytic activity in the activation of PMS to produce $^{*}SO_4^{-}$. To be specific, at optimal conditions, 99.27, 83.1, and 61.11% of AMX, COD, and TOC were removed after 60 min of reaction, respectively [28]. $CoFe_2O_4$@GO was also used for the activation of PMS in the degradation of RB5 [29] and RB [30]. A hybrid nanocomposite of reduced graphite oxide rGO and $CoFe_2O_4$ ($CoFe_2O_4$/rGO) for the activation of PMS for phenol degradation has also been performed [31]. Indeed, catalytic testing showed that $CoFe_2O_4$/rGO exhibits much better catalytic activity compared with $CoFe_2O_4$, indicating that rGO plays an important role in the $CoFe_2O_4$/rGO hybrid-nanocomposite for the degradation of phenol. In the $^{*}SO_4^{-}$-based heterogeneous catalytic system for the degradation of on organic pollutants, $CoFe_2O_4$/rGO was synthesised using a surface hydrothermal method to activate PMS to degrade phenol with a high degradation efficiency thanks to its large specific surface and 3D structure that promotes mass transfer and dispersion of the catalytic sites on the surface of the $CoFe_2O_4$/rGO aerogel [32].

However, rapid oxidation rates cannot be achieved if PMS, PMS activated by catalysts, or ozonation are used separately. Therefore, hybrid processes between O_3 and PMS-activated heterogeneous catalysts are advantageous in the decomposition of difficult-to-biodegrade organic matters due to the creation of synergistic effects that accelerate the decomposition rate of organic pollutants and increase the efficiency of PMS use, which then reduces the dose of PMS necessary for decomposition. The addition of O_3 to a heterogeneous catalytic system has been shown to increase the activation of PMS and generate both $^{*}OH$ and $^{*}SO_4^{-}$ free radicals. However, studies of this hybrid technology in the treatment of difficult-to-biodegrade organic compounds are rare, especially in the treatment of antibiotic residues. Therefore, the aim of this study was to fabricate a nanocomposite catalyst based on a composite of Co_2SnO_4 and rGO, which was used to activate PMS in a hybrid ozonation system for the enhanced degradation of CFX from wastewater. To reach this aim, this study focused on investigating the most suitable conditions for the synthesis of Co_2SnO_4@rGO and using Co_2SnO_4@rGO as a heterogeneous catalyst to activate PMS in a hybrid ozonation system for the degradation of CFX from water medium.

2. Materials and methods

2.1. Chemicals and materials

All chemicals including $KMnO_4$, H_2SO_4, H_2O_2 (30%), HCl, $CoCl_2$, $SnCl_4$, ethylene glycol, and NaOH were purchased from Kyamata (Japan). $NaBH_4$ and CFX ($C_{16}H_{17}N_3O_4S$) were obtained from Sigma Aldrich (Germany). Graphite used for the fabrication of rGO was purchased from Merck (Germany). All chemicals were used as received without further purification.

2.2. Preparation of catalyst materials

In this study, the synthesis procedure of the nanocomposite Co_2SnO_4@rGO consisted of two main steps:

(1) Firstly, Co_2SnO_4NPs and GO were synthesised separately according to the method modified from W.S. Hummers and R.E. Offeman (1958) [33].

Synthesis of GO: Graphene oxide was prepared from natural graphite powder and exfoliated by common chemical agents according to the modified Hummers method. In the first step of the procedure, 3 g of graphite was placed into a beaker containing 150 ml of 98% sulfuric acid, which was cooled in an ice bath (3-5ºC) and completely agitated. Next, 10.5 g of $KMnO_4$ was gradually added into the mixture for 20 min with stirring for a further 20 min. The mixture was then cooled to room temperature and stirred for 72 h. Following that, 250 ml distilled water and 5 ml of 30% H_2O_2 were supplemented in the mixture to achieve a yellow solution. The obtained solid was filtered and repeatedly washed with 3% HCl and distilled water. Finally, the obtained graphene oxide was dispersed overnight into distilled water, reduced metal ions, and protons using a dialysis bag and stored in the dark.

Synthesis of Co_2SnO_4NPs: The magnetic Co_2SnO_4NPs were synthesised using the sol-gel method. Firstly, 93 g of citric acid was poured in a beaker containing 100 ml of distilled water and agitated in a magnetic stirrer at 120 rpm under 60ºC for 15 min to obtain a clear liquid. In the next step, a mixture of 0.36 g $CoCl_2.6H_2O$, 0.63 g $SnCl_4.6H_2O$, and 40 ml ethylene glycol was added in the above beaker and heated to 80ºC until the mixture completely dissolved. Then, the mixture was heated up to 130ºC to obtain a gel mixture. The gel mixture was heated up to 150ºC for 12 h until it became a completely dry solid. The solid was baked at 300ºC for 3 h under oxygen conditions. Finally, the obtained solid was then furnaced to 1000ºC for a further 2 h and cooled to room temperature (25±2ºC). The obtained black solid were Co_2SnO_4NPs and were stored in sealed plastic bags to use as a precursor for the synthesis of nanocomposite Co_2SnO_4@rGO.

(2) Synthesising nanocomposite Co_2SnO_4@rGO: The Co_2SnO_4@rGO at various ratios were prepared using Co_2SnO_4 NPs and GO, which were achieved from the abovementioned procedures. At the beginning of the procedure, a certain amount of GO was dispersed in a beaker containing 20 ml deionised water and sonicated for 60 min. Then, a pre-determined amount of Co_2SnO_4 NPs were also dispersed into the beaker and sonicated for a further 30 min. Afterwards, 10 ml of 0.1 M $NaBH_4$ was gradually added to the mixture. The mixture was sonicated for a further 30 min. Finally, the achieved precipitate was separated by filtration or centrifugation and cleaned by deionised water and ethanol several times. The precipitate was then vacuumed at 80ºC for 6 h. The obtained product was the Co_2SnO_4@ rGO nanocomposite at different composite ratios. The products were stored in sealed plastic bags and labelled as 1-Co_2SnO_4@1-rGO; 2-Co_2SnO_4@1-rGO; 3-Co_2SnO_4@1-rGO; 1-Co_2SnO_4@2-rGO; and 1-Co_2SnO_4@3-rGO for use in the following experiments. The synthesis procedure of the Co_2SnO_4@rGO nanocomposite is summarized in Fig. 1.

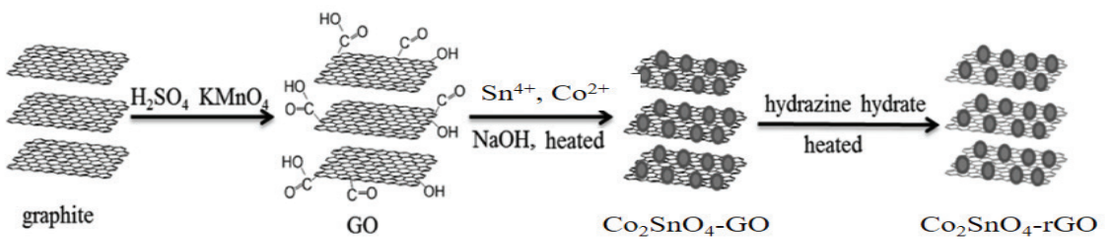

Fig. 1. Schematic description of the synthesis of Co_2SnO_4@rGO nanocomposites.

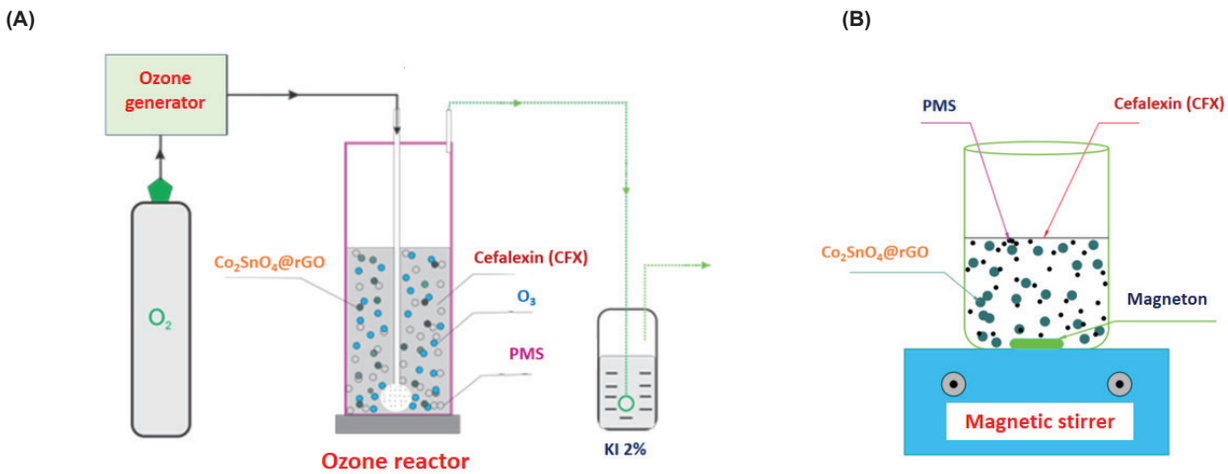

Fig. 2. Scheme of degradation of CFX by O_3/Co_2SnO_4/PMS (A) and Co_2SnO_4/PMS (B).

2.3. Catalytic activity measurement

In this study, CFX was the target pollutant. The CFX degradation experiments were conducted with initial conditions of: CFX concentration of 100 mg/l, pH of 7, catalyst dosage of 0.3 g/l, and PMS dosage of 300 mg/l using Co_2SnO_4@rGO at various composite ratios. All experiments were performed in batch mode. The scheme of CFX degradation by O_3/Co_2SnO_4/PMS and Co_2SnO_4/PMS systems are shown in Fig. 2.

In the O_3/Co_2SnO_4/PMS system, ozone is produced by an ozone generator (NextOzone 20P, Sinh Phu Joint Stock Company, Vietnam). The maximum capacity of O_3 and input O_3 capacity at a flow of 15 ml/min were 5.0 and 3.038 g/h, respectively. The oxygen provided for the O_3 generator was from a pure oxygen container. O_3 is constantly produced and allocated into a tubular borosilicate glass reactor with a height of 450 mm and a diameter of 60 mm through a bubble air stone located at the bottom of the container.

In the Co_2SnO_4/PMS system, the experimental model was set up using a beaker with a volume of 1000 ml containing 500 ml of CFX solution at 100 mg/l and the reaction conditions as abovementioned. The reactor was put on a magnetic stirrer and agitated at 120 rpm.

The reaction kinetics of CFX degradation on the nano-hybrid systems followed a first-order kinetic model (Eq. 1):

$$ln\frac{C_t}{C_o} = -k_d t$$

where C_t is the left concentration of CFX at time t; C_o is the initial concentration of CFX, and k_d is the first-order reaction rate constant. By plotting -ln(C_t/C_o) verse time, k_d and R^2 are determined.

In both reaction systems, the sample was taken out at 40-min intervals to determine the quantity of CFX remaining after reaction.

The CFX removal experiments were triplicated. The results were expressed as average value ±standard deviation.

2.4. Analysis method

The textural characteristic of materials was analysed using N_2 adsorption-desorption isotherms at 77 K (Quantachrome Instruments version 11.0-NOVA). SEM images were applied to observe the morphology of the catalysts using a Hitachi S-4800 (Japan). The EDX data and mapping data were analysed by X-ray energy-dispersive spectroscopy using the JSM-IT200 (InTouchScop). The phase composition and crystal structure of the nanomaterials at various composite ratios were measured by X-ray diffraction with a scanning speed of 1.25°/min at 2θ angles between 20 and 80° using a Bruker D8 device with Cu Kα emission (λ=0.1540 nm).

The degree of CFX degradation was measured using UV-Vis (Shimadzu, model Z2000, Japan) at λ=262 nm. The pH was measured with a pH meter (HANNA, pH HI 2211-02, Romani).

3. Results and discussion

3.1. Characteristics of catalysts

The textural characteristics of the catalysts are presented in Table 1. As can be seen from the data in Table 1, composites of Co_2SnO_4 nanoparticles and rGO led to a remarkable change in the structure of the catalyst. Specifically, at a composite ratio of 2-Co_2SnO_4 and 1-rGO, the S_{BET} of was increased about 17 and 3.9 times compared with Co_2SnO_4 and GO, respectively. Specifically, the S_{BET} of Co_2SnO_4 was 25.43 m^2/g, which agreed with previous work reported by M.B. Ali, et al. (2017) [34]. These results illustrate that the existence of rGO effectively improved the surface property of 2-Co_2SnO_4@1-rGO. The growth of S_{BET} after compositing could be because GO possesses a very large specific surface area in its inherent nature and plays the role of support for Co_2SnO_4. According to IUPAC

Table 1. Nitrogen adsorption-desorption isotherm data of materials.

	Unit	Co_2SnO_4	GO	2-Co_2SnO_4@1-rGO
S_{BET}	m^2/g	25.43	112.9	435.432
V_{pore}	cm^3/g	0.087	0.412	0.383
D_{pore}	nm	0.07	0.94	0.127

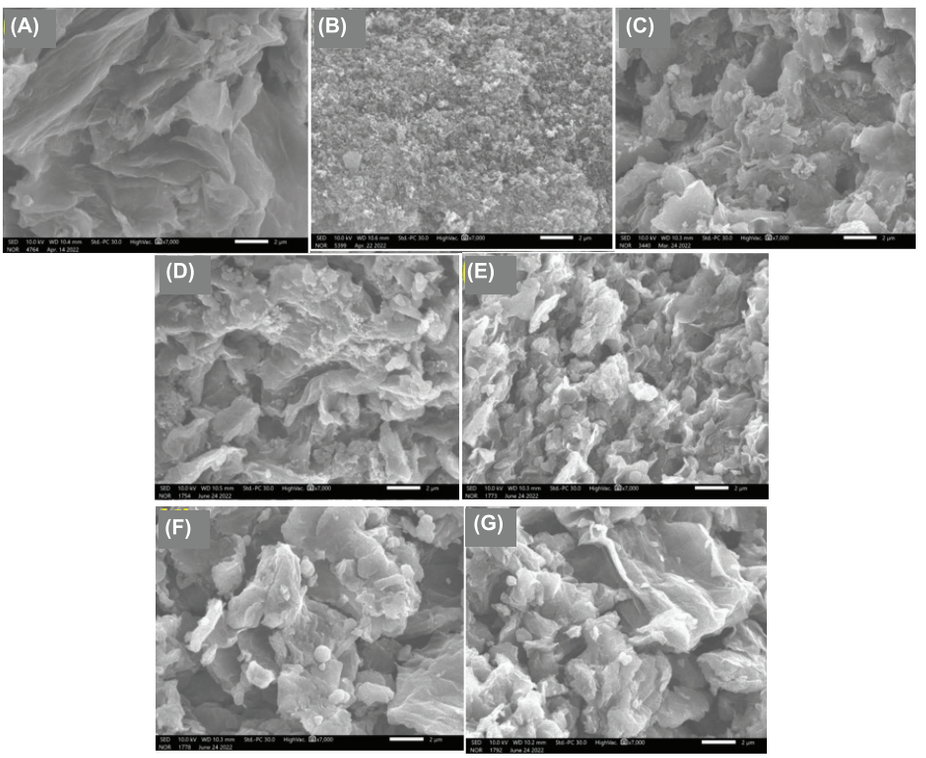

Fig. 3. SEM images of Co_2SnO_4@rGO at various modification ratios. (A) GO, **(B)** Co_2SnO_4, **(C)** 1-Co_2SnO_4@1-rGO, **(D)** 2-Co_2SnO_4@1-rGO, **(E)** 3-Co_2SnO_4@1-rGO, **(F)** 1-Co_2SnO_4@2-rGO, **(G)** 1-Co_2SnO_4@3-rGO.

classification, the 2-Co_2SnO_4@1-rGO nanohybrid had a type-IV isotherm with an H3 hysteresis loop, showing its mesoporous nature. The S_{BET} of 2-Co_2SnO_4@1-rGO was calculated to be 335.432 m^2/g. A similar result was obtained by A.H. Mady, et al. (2019) [27] when compositing γ-MnO_2@$ZnFe_2O_4$ with rGO with an S_{BET} of 376.88 m^2/g. The high surface area provides more adsorption/reaction sites for the activation of PMS during the catalytic reaction, leading to higher catalytic activity.

The morphologies of Co_2SnO_4@rGO at various composite ratios were observed using SEM. The results are demonstrated in Fig. 3. From Fig. 3A, the SEM image of GO showed a regular lamellar structure with drapes of GO. Meanwhile, Fig. 2B displays a typical SEM image of Co_2SnO_4, which indicates particles in an aggregated form with a formation of spherical and cubic nanoparticles. Besides, it is clear that most of the NPs had uniform crystallite size. Figs. 3C-3F, G indicate the morphology of Co_2SnO_4@rGO at various composite ratios. The SEM results showed that Co_2SnO_4@rGO possessed a heterogamous structure with rough surface and Co_2SnO_4 nanoparticles appeared on the surface of nanocomposite. Besides, the transparent silk yarn lamella structure of graphene is more obvious when the GO dosage was increased (Figs. 3E, 3F). Especially, the spherical Co_2SnO_4 particles were more homogeneously loaded on the surface and edges of rGO (Fig. 3D) and the particle size is smaller than those in Fig. 3B, which suggests that agglomeration has been weakened due to the effective fixation and dispersion of rGO on the surface of the Co_2SnO_4 particles. Therefore, it was concluded that the optimum loading ratio of Co_2SnO_4 and rGO was 2:1.

The EDX spectrum of the GO, Co_2SnO_4 NPs, and Co_2SnO_4@rGO at various composite ratios (Fig. 4) essentially show the presence of Co, Sn, C, and O elements indicating good purity of the as-prepared materials. Besides, mapping data also showed a distribution of the constituent elements of Co_2SnO_4@rGO (Fig. 4H). When increasing the composite ratio of Co_2SnO_4, the amounts of Co and Sn elements of Co_2SnO_4@rGO also grew (Figs. 4C-4E). Especially at a composite ratio of 2-Co_2SnO_4 and 1-rGO (Fig. 4D), the amount of Co was the highest. However, when rGO was increased, almost no Co or Sn elements were found in Co_2SnO_4@rGO. The transition metal Co has been proven to effectively activate PMS in catalytic reactions for the degradation of persistent organic compounds. Thus, the Co_2SnO_4@rGO catalyst at a composite ratio of 2-Co_2SnO_4 and 1-rGO was the optimal ratio and used for the rest of this study.

Figure 5 depicts typical XRD patterns of GO, Co_2SnO_4 NPs, and Co_2SnO_4@rGO at various composite ratios synthesised by the sol-gel method. Clearly, the GO pattern has a typical peak at 9.7° corresponding to the (001) crystal plane. However, this characteristic peak was smaller in the Co_2SnO_4@rGO X-ray diffraction and a small diffraction peak appeared at 19°, which suggested that GO was

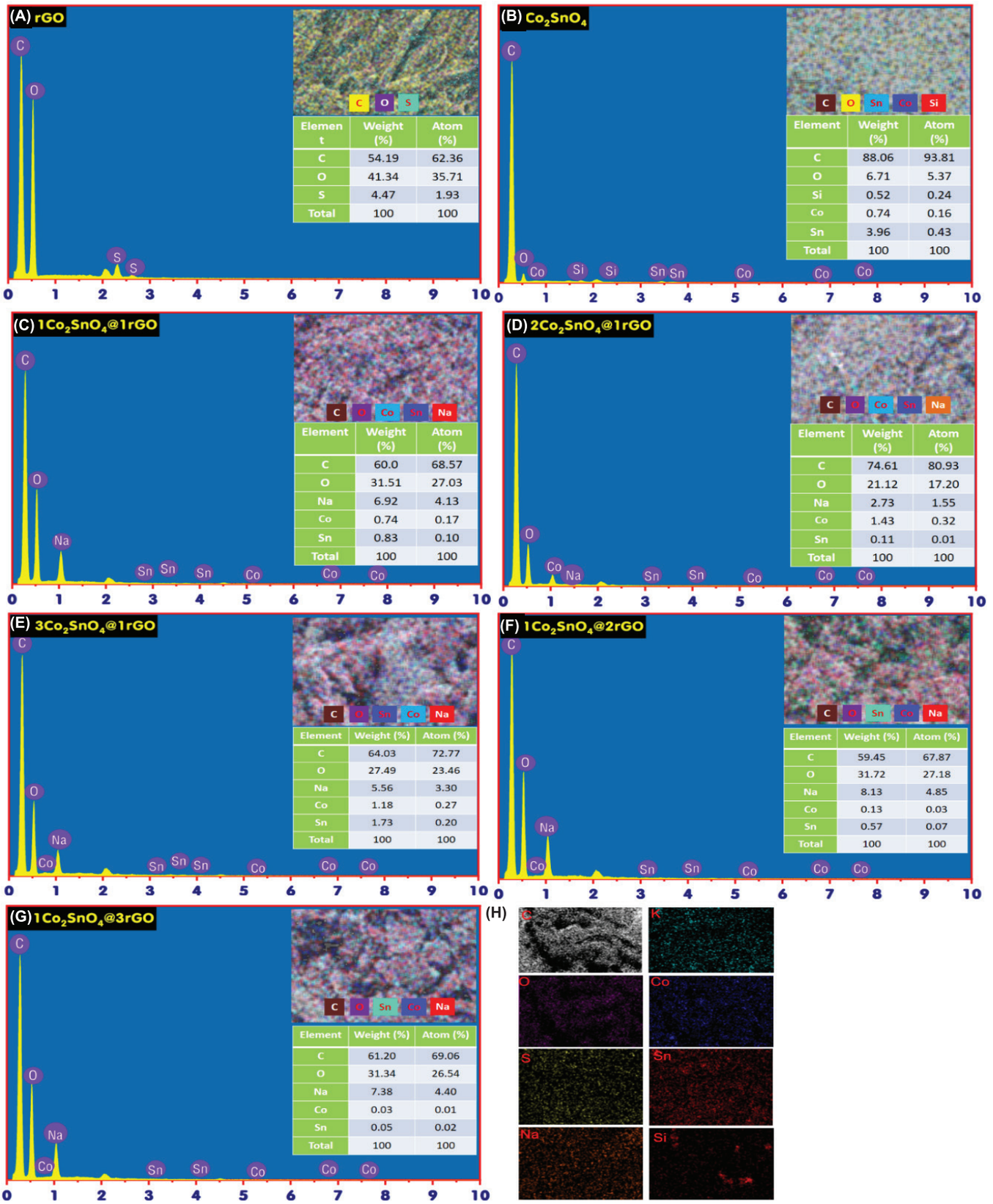

Fig. 4. EDX spectra of Co_2SnO_4@rGO at various modification ratios. (A) rGO, **(B)** Co_2SnO_4, **(C)** 1-Co_2SnO_4@1-rGO, **(D)** 2-Co_2SnO_4@1-rGO, **(E)** 3-Co_2SnO_4@1-rGO, **(F)** 1-Co_2SnO_4@2-rGO, **(G)** 1-Co_2SnO_4@3-rGO, **(H)** Mapping of Co_2SnO_4@rGO.

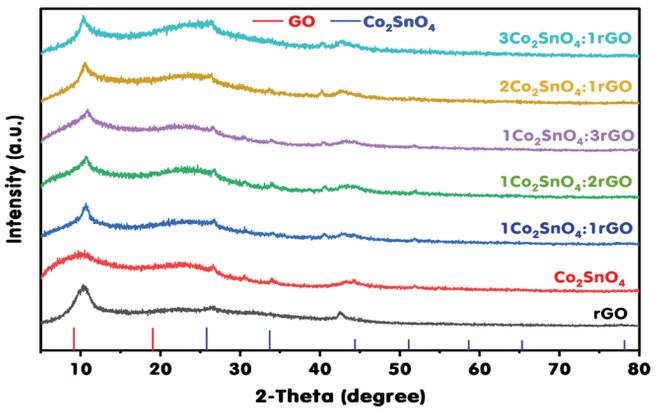

Fig. 5. XRD of catalysts at various modification ratios. (A) rGO, **(B)** Co_2SnO_4, **(C)** $1Co_2SnO_4$@1rGO, **(D)** $2Co_2SnO_4$@1rGO, **(E)** $3Co_2SnO_4$@1rGO, **(F)** $1Co_2SnO_4$@2rGO, **(G)** $1Co_2SnO_4$@3rGO.

successfully reduced to reduced graphene oxide [35] in the synthesis procedure. The observed diffraction peaks at 26.131, 34.321, 35.911, 44.711, 51.761, 57.111, 66.491 and 78.111° are indexed and well matched to cubic Co_2SnO_4 with the space group Fd3m (JCPDS No. 29-0514). The sharp intensity peaks denote the high crystallinity of Co_2SnO_4. It is worth noticing the presence of small diffraction peaks due to SnO_2 and $CoSn(OH)_6$.

The diffraction peaks of Co_2SnO_4@rGO at different composite ratios are consistent with that of Co_2SnO_4 indicating that Co_2SnO_4 was basically deposited on the surface of the graphene layer and its crystal form was unchanged during the synthesis. However, the characteristic peak of Co_2SnO_4@rGO at the ratio of 2-Co_2SnO_4:1-rGO is slightly wider and clearer in comparison with other ratios.

3.2. Catalytic performance of Co_2SnO_4@rGO in the Co_2SnO_4@rGO/PMS and O_3/Co_2SnO_4@rGO/PMS systems

To assess the catalytic activity of Co_2SnO_4@rGO at various composite ratios for PMS activation in Co_2SnO_4@rGO, Co_2SnO_4@rGO/PMS, and O_3/Co_2SnO_4@rGO/PMS systems, degradation experiments of CFX were conducted. The experiment to evaluate catalytic performance of the fabricated heterogeneous catalysts to activate PMS in the Co_2SnO_4@rGO/PMS and O_3/Co_2SnO_4@rGO/PMS systems were conducted with varying composite ratios of Co_2SnO_4:rGO, specifically, 1:1, 2:1: 3:1, 1:2, and 1:3 at an initial CFX concentration of 100 mg/l, PMS dosage of 300 mg/l, catalyst dosage of 0.3 g/l, and at a pH of 7. The results are presented in Fig. 6.

What stands out from the data in Figs. 6A, B is that the CFX degradation efficiencies were varied when the compositing ratios were changed. CFX degradation was completely achieved after 40 min of reaction time. The CFX degradation curves for both Co_2SnO_4@rGO/PMS and O_3/Co_2SnO_4@rGO/PMS systems followed the same trend.

The removal efficiency of CFX reached a peak at a composite ratio of 2-Co_2SnO_4 and 1-rGO in both system (95.07% for Co_2SnO_4@rGO/PMS and 99.07% for O_3/Co_2SnO_4@rGO/PMS).

The degradation of CFX was the lowest in both systems at a composite ratio of 1-Co_2SnO_4 and 1-rGO reaching 23.2 and 82.0%, respectively, for Co_2SnO_4@rGO/PMS and O_3 Co_2SnO_4@rGO/PMS. When increasing the amount of rGO, the degradation of CFX increased. The degradation efficiency of CFX in the O_3/Co_2SnO_4@rGO/PMS system was higher than that of Co_2SnO_4@rGO/PMS, showing a synergetic effect in the hybrid ozonation system for the removal of CFX from wastewater. The results showed that the composite ratio had a significant effect on CFX degradation efficiency in both treatment systems in this study.

Previous works have also suggested that the degradation of CFX by advanced $^{\bullet}SO_4^-$-based oxidation systems using heterogeneous catalysts for the activation of PMS follows a first-order model [28, 34]. Thus, in this work, the experimental degradation data of CFX at various composite ratios were fit with a first-order model and the obtained results are presented in Table 2. As expected, the R^2 values of the fit were very high. Besides, all k_d values agreed well with degradation results of CFX at various composite ratios between Co_2SnO_4 and rGO as discussed earlier. Among the composite ratios tested, 1-Co_2SnO_4 and 1-rGO was the most effective for degrading CFX. The k_d values were determined to be 0.007, 0.076, 0.033, 0.026, and 0.043 min^{-1} and 0.047, 0.112, 0.560, 0.047, 0.049 min^{-1} corresponded with composite ratios of $1Co_2SnO_4$@1rGO, $2Co_2SnO_4$@1rGO, $3Co_2SnO_4$@1rGO, $1Co_2SnO_4$@2rGO, and $1Co_2SnO_4$@3rGO for Co_2SnO_4@rGO/PMS and

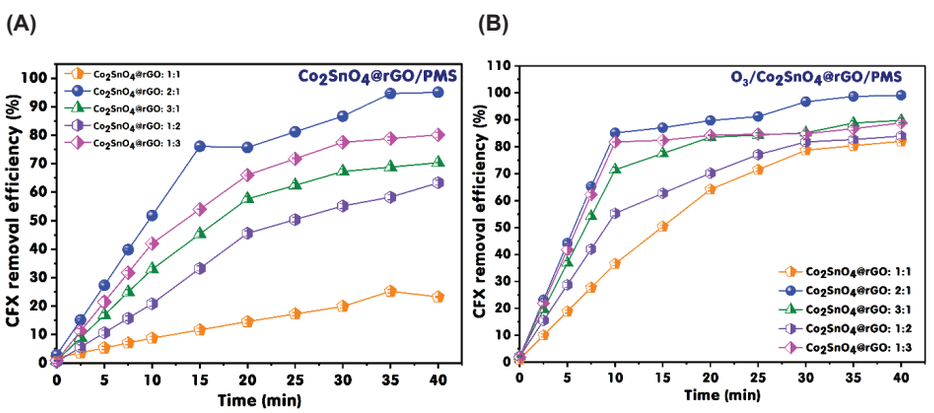

Fig. 6. Time evolution of CFX degradation by Co_2SnO_4@rGO/PMS (A) and O_3/Co_2SnO_4@rGO/PMS (B) at various modification ratios between Co_2SnO_4 and rGO.

Table 2. Degradation kinetic of CFX by Co_2SnO_4@rGO/PMS and O_3/Co_2SnO_4@rGO/PMS.

Reaction conditions		Co_2SnO_4@rGO/PMS		O_3/Co_2SnO_4@rGO/PMS	
		k_d (min^{-1})	R^2	k_d (min^{-1})	R^2
Modification (Co_2SnO_4@rGO)	1:1	0.007	0.9788	0.047	0.9852
	2:1	0.076	0.9736	0.112	0.9649
	3:1	0.033	0.9656	0.560	0.8984
	1:2	0.026	0.9882	0.047	0.9599
	1:3	0.043	0.9733	0.049	0.7308

O_3/Co_2SnO_4@rGO/PMS, respectively. The k_d value reached a peak at a composite ratio of 2-Co_2SnO_4 and 1-rGO for both reaction systems. The k_d values in the O_3/Co_2SnO_4@rGO/PMS system were higher than those in Co_2SnO_4@rGO/PMS at all composite ratios. The results showed that in the addition of O_3 into the Co_2SnO_4@rGO/PMS system promoted the degradation rate of CFX thanks to the synergetic effect of O_3 and Co_2SnO_4@rGO/PMS. Besides, the composition of rGO with Co_2SnO_4 nanoparticles remarkably increased the S_{BET} of the nanocomposite, specifically from 112.9 and 25.43 m^2/g, respectively, for rGO and Co_2SnO_4 to 435.432 m^2/g for 2-Co_2SnO_4@1-rGO. This result proved that the Co_2SnO_4 NPs were successfully loaded onto the surface of rGO. Such a high S_{BET} from the 2-Co_2SnO_4@1-rGO nanocomposite provided more adsorption/catalysis sites for activating PMS during the catalytic process, leading to higher catalytic activities for the degradation of CFX in both systems. Similar results were obtained by previous works. For example, D. Ge, et al. (2016) [36] indicated that the degradation of methyl orange in a O_3/Fe^{2+}/PS reactor increased because inlet ozone concentration enhanced the synergistic effect between ozone and persulphate, thus leading to a higher degradation rate of MO. O_3 was also proved to be enhancement of degradation rate of 4-nitrophenol in the O_3/MnO_2/rGO/PMS system thanks to the synergistic effect between catalytic ozonation and the coupling of PMS activation to generate more $^*SO_4^-$ and *OH radicals, leading to enhancement of pollutants degradation rate [14].

4. Conclusions

In this study, a heterogeneous catalyst derived from a composite of Co_2SnO_4 NPs and rGO at various composite ratios was successfully developed using the sol-gel method. The Co_2SnO_4NPs@rGO at different composite ratios were used to activate PMS in both Co_2SnO_4@rGO/PMS and O_3/Co_2SnO_4@rGO/PMS for the degradation of CFX. The degradation efficiencies of CFX in both systems followed the same trend. However, the removal efficiencies of CFX in hybrid ozonation were higher than those in Co_2SnO_4@rGO/PMS. The degradation of CFX was maximised at a composite ratio of 2-Co_2SnO_4 and 1-rGO. The material characteristics data showed that S_{BET} of the catalyst was remarkably improved at a composite ratio of 2-Co_2SnO_4 and 1-rGO, which facilitated more active sites on the catalyst to degrade CFX. Besides, the presence of Co in 2-Co_2SnO_4@1-rGO was the highest, leading to an enhancement of PMS activation to produce more $^*SO_4^-$. Notably, the combination of O_3 in the Co_2SnO_4@rGO/PMS reactor formed a synergetic effect to increase the generation of *OH radicals, leading to the promotion of CFX degradation rate to reach the standards of QCVN 40:2011/BTNMT (Column A).

CRediT author statement

Van Long Nguyen: Conceptualisation, Methodology, Software; Minh Thanh Le: Visualisation, Investigation, Data curation; Lan Huong Nguyen: Supervision, Writing - Original draft preparation, Writing - Reviewing and Editing.

ACKNOWLEDGEMENTS

The study was supported by Youth Incubator for Science and Technology Program, managed by Youth Development Science and Technology Center - Ho Chi Minh Communist Youth Union and Department of Science and Technology of Ho Chi Minh City under contract number 34/2021/HD-KHCNT-VU.

COMPETING INTERESTS

The authors declare that there is no conflict of interest regarding the publication of this article.

REFERENCES

[1] X.H. Wang, A.Y.C. Lin (2012), "Phototransformation of cephalosporin antibiotics in an aqueous environment results in higher toxicity", *Environ. Sci. Technol.*, **46(22)**, pp.12417-12426, DOI: 10.1021/es301929e.

[2] F. Tavasol, T. Tabatabaie, B. Ramavandi, et al. (2020), "Design a new photocatalyst of sea sediment/titanate to remove cephalexin antibiotic from aqueous media in the presence of sonication/ultraviolet/hydrogen peroxide: Pathway and mechanism for degradation", *Ultrason. Sonochem.*, **65(105062)**, DOI: 10.1016/j.ultsonch.2020.105062.

[3] K. Kümmerer (2009), "Antibiotics in the aquatic environment - A review - Part II", *Chemosphere*, **75(4)**, pp.435-441, DOI: 10.1016/j.chemosphere.2008.12.006.

[4] J. Chen, C. Fang, W. Xia, et al. (2018), "Selective transformation of β-lactam antibiotics by peroxymonosulfate: Reaction kinetics and nonradical mechanism", *Environ. Sci. Technol.*, **52(3)**, pp.1461-1470, DOI: 10.1021/acs.est.7b05543.

[5] Y. Qian, G. Xue, J. Chen, et al. (2018), "Oxidation of cefalexin by thermally activated persulfate: Kinetics, products, and antibacterial activity change", *J. Hazard. Mater.*, **354,** pp.153-160, DOI: 10.1016/j.jhazmat.2018.05.004.

[6] C. Su, X. Lin, P. Zheng, et al. (2019), "Effect of cephalexin after heterogeneous Fenton-like pretreatment on the performance of anaerobic granular sludge and activated sludge", *Chemosphere*, **235**, pp.84-95, DOI: 10.1016/j.chemosphere.2019.06.136.

[7] P. Bansal, A. Verma, C. Mehta, et al. (2018), "Assessment of integrated binary process by coupling photocatalysis and photo-Fenton for the removal of cephalexin from aqueous solution", *J. Mater. Sci.*, **53(10)**, pp.7326-7343, DOI: 10.1007/s10853-018-2094-x.

[8] R. Mirzaei, M. Yunesian, S. Nasseri, et al. (2018), "Occurrence and fate of most prescribed antibiotics in different water environments of Tehran, Iran", *Sci. Total Environ.*, **619-620**, pp.446-459, DOI: 10.1016/j.scitotenv.2017.07.272.

[9] S. Li, W. Shi, W. Liu, et al. (2018), "A duodecennial national synthesis of antibiotics in China's major rivers and seas (2005-2016)", *Sci. Total Environ.*, **615**, pp.906-917, DOI: 10.1016/j.scitotenv.2017.09.328.

[10] T.B. Minh, H.W. Leung, I.H. Loi, et al. (2009), "Antibiotics in the Hong Kong metropolitan area: Ubiquitous distribution and fate in Victoria Harbour", *Mar. Pollut. Bull.*, **58(7)**, pp.1052-1062, DOI: 10.1016/j.marpolbul.2009.02.004.

[11] S.G. Cordeiro, R. Ziem, Y.A. Schweizer, et al. (2021), "Degradation of micropollutant cephalexin by ultraviolet (UV) and assessment of residual antimicrobial activity of transformation products", *Water Sci. Technol.*, **84(2)**, pp.374-383, DOI: 10.2166/wst.2021.170.

[12] R. Guo, J. Chen (2015), "Application of alga-activated sludge combined system (AASCS) as a novel treatment to remove cephalosporins", *Chem. Eng. J.*, **260**, pp.550-556, DOI: 10.1016/j.cej.2014.09.053.

[13] Z. Yuan, M. Sui, B. Yuan, et al. (2017), "Degradation of ibuprofen using ozone combined with peroxymonosulfate", *Environ. Sci. Water Res. Technol.*, **3(5)**, pp.960-969, DOI: 10.1039/C7EW00174F.

[14] Y. Wang, Y. Xie, H. Sun, et al. (2016), "2D/2D nano-hybrids of γ-MnO_2 on reduced graphene oxide for catalytic ozonation and coupling peroxymonosulfate activation", *J. Hazard. Mater.*, **301**, pp.56-64, DOI: 10.1016/j.jhazmat.2015.08.031.

[15] J. Cong, G. Wen, T. Huang, et al. (2015), "Study on enhanced ozonation degradation of para-chlorobenzoic acid by peroxymonosulfate in aqueous solution", *Chem. Eng. J.*, **264**, pp.399-403, DOI: 10.1016/j.cej.2014.11.086.

[16] F. Chi, G. Zhou, B. Song, et al. (2016), "$CoTiO_3$ nanoparticles as a highly active heterogeneous catalyst of peroxymonosulfate for the degradation of organic pollutants under visible-light illumination", *J. Nano Res.*, **42**, pp.73-79, DOI: 10.4028/www.scientific.net/jnanor.42.73.

[17] M. Stoyanova, I. Slavova, S. Christoskova, et al. (2014), "Catalytic performance of supported nanosized cobalt and iron-cobalt mixed oxides on MgO in oxidative degradation of acid orange 7 azo dye with peroxymonosulfate", *Appl. Catal. A Gen.*, **476**, pp.121-132, DOI: 10.1016/j.apcata.2014.02.024.

[18] Y. Ren, L. Lin, J. Ma, et al. (2015), "Sulfate radicals induced from peroxymonosulfate by magnetic ferrospinel MFe_2O_4 (M=Co, Cu, Mn, and Zn) as heterogeneous catalysts in the water", *Applied Catalysis B: Environmental*, **165**, pp.572-578, DOI: 10.1016/j.apcatb.2014.10.051.

[19] Y. Yao, Y. Cai, G. Wu, et al. (2015), "Sulfate radicals induced from peroxymonosulfate by cobalt manganese oxides (Co_xMn_3-xO_4) for Fenton-Like reaction in water", *J. Hazard. Mater.*, **296**, pp.128-137, DOI: 10.1016/j.jhazmat.2015.04.014.

[20] X. Li, Z. Wang, B. Zhang, et al. (2016), "Fe_xCo_3-xO_4 nanocages derived from nanoscale metal-organic frameworks for removal of bisphenol A by activation of peroxymonosulfate", *Applied Catalysis B: Environmental*, **181**, pp.788-799, DOI: 10.1016/j.apcatb.2015.08.050.

[21] H. Bouchaaba, B. Bellal, R. Maachi, et al. (2016), "Optimization of physico-chemical parameters for the photo-oxidation of neutral red on the spinel Co_2SnO_4", *J. Taiwan Inst. Chem. Eng.*, **58**, pp.310-317, DOI: 10.1016/j.jtice.2015.06.011.

[22] M. Golshan, B. Kakavandi, M. Ahmadi, et al. (2018), "Photocatalytic activation of peroxymonosulfate by TiO_2 anchored on cupper ferrite (TiO_2@$CuFe_2O_4$) into 2,4-D degradation: Process feasibility, mechanism and pathway", *J. Hazard. Mater.*, **359**, pp.325-337, DOI: 10.1016/j.jhazmat.2018.06.069.

[23] Q. Yang, H. Choi, Y. Chen, et al. (2008), "Heterogeneous activation of peroxymonosulfate by supported cobalt catalysts for the degradation of 2,4-dichlorophenol in water: The effect of support, cobalt precursor, and UV radiation", *Applied Catalysis B: Environmental*, **77(3-4)**, pp.300-307, DOI: 10.1016/j.apcatb.2007.07.020.

[24] Y. Wang, H. Sun, H.M. Ang, et al. (2014), "Magnetic Fe_3O_4/carbon sphere/cobalt composites for catalytic oxidation of phenol solutions with sulfate radicals", *Chem. Eng. J.*, **245**, pp.1-9, DOI: 10.1016/j.cej.2014.02.013.

[25] P.R. Shukla, S. Wang, H. Sun, et al. (2010), "Activated carbon supported cobalt catalysts for advanced oxidation of organic contaminants in aqueous solution", *Applied Catalysis B: Environmental*, **100(3-4)**, pp.529-534, DOI: 10.1016/j.apcatb.2010.09.006.

[26] Z. Huang, H. Bao, Y. Yao, et al. (2016), "Key role of activated carbon fibers in enhanced decomposition of pollutants using heterogeneous cobalt/peroxymonosulfate system", *J. Chem. Technol. Biotechnol.*, **91(5)**, pp.1257-1265, DOI: 10.1002/jctb.4715.

[27] A.H. Mady, M.L. Baynosa, D. Tuma, et al. (2019), "Heterogeneous activation of peroxymonosulfate by a novel magnetic 3D Γ-MnO_2@$ZnFe_2O_4$/rGO nanohybrid as a robust catalyst for phenol degradation", *Applied Catalysis B: Environmental*, **244**, pp.946-956, DOI: 10.1016/j.apcatb.2018.11.086.

[28] E.B. Lashkaryani, B. Kakavandi, R.R. Kalantary, et al. (2019), "Activation of peroxymonosulfate into amoxicillin degradation using cobalt ferrite nanoparticles anchored on graphene ($CoFe_2O_4$@Gr)", *Toxin Rev.*, **40(2)**, pp.215-224, DOI: 10.1080/15569543.2019.1582066.

[29] N. Mengelizadeh, E. Mohseni, M.H. Dehghani (2021), "Heterogeneous activation of peroxymonosulfate by GO-$CoFe_2O_4$ for degradation of reactive black 5 from aqueous solutions: Optimization, mechanism, degradation intermediates and toxicity", *J. Mol. Liq.*, **327**, DOI: 10.1016/j.molliq.2020.114838.

[30] R. Tabit, O. Amadine, Y. Essamlali, et al. (2018), "Magnetic $CoFe_2O_4$ nanoparticles supported on graphene oxide ($CoFe_2O_4$/GO) with high catalytic activity for peroxymonosulfate activation and degradation of rhodamine B", *RSC Adv.*, **8(3)**, pp.1351-1360, DOI: 10.1039/C7RA09949E.

[31] Y. Yao, Z. Yang, D. Zhang, et al. (2012), "Magnetic $CoFe_2O_4$-graphene hybrids", *Ind. Eng. Chem. Res.*, **17**, pp.6044-6051, DOI: 10.1021/ie300271p.

[32] L. Zou, X. Xiao, C. Chu, et al. (2021), "Facile synthesis of porous $CoFe_2O_4$/graphene aerogel for catalyzing efficient removal of organic pollutants", *Sci. Total Environ.*, **775**, DOI: 10.1016/j.scitotenv.2020.143398.

[33] W.S. Hummers, R.E. Offeman (1958), "Preparation of graphitic oxide", *J. Am. Chem. Soc.*, **80(6)**, DOI: 10.1021/ja01539a017.

[34] M.B. Ali, A. Barras, A. Addad, et al. (2017), "Co_2SnO_4 nanoparticles as a high performance catalyst for oxidative degradation of rhodamine B dye and pentachlorophenol by activation of peroxymonosulfate", *Phys. Chem. Chem. Phys.*, **19(9)**, pp.6569-6578, DOI: 10.1039/C6CP08576H.

[35] Y. Zhao, G. Nie, X. Ma, et al. (2019), "Peroxymonosulfate catalyzed by rGO assisted $CoFe_2O_4$ catalyst for removing Hg0 from flue gas in heterogeneous system", *Environ. Pollut.*, **249**, pp.868-877, DOI: 10.1016/j.envpol.2019.03.103.

[36] D. Ge, Z. Zeng, M. Arowo, et al. (2016), "Degradation of methyl orange by ozone in the presence of ferrous and persulfate ions in a rotating packed bed", *Chemosphere*, **146**, pp.413-418, DOI: 10.1016/j.chemosphere.2015.12.058.

DOI: 10.31276/VJSTE.65(3).59-65

Combined effects of powdered oyster shell (*Ostreidae*) and lemongrass (*Cymbopogon citratus*) as a feed additive for growth development of quail (*Coturnix coturnix japonica*)

Florieza Mangubat[1*], Cerela Looc[2], Fretzel Mad[2]

[1]*College of Arts and Sciences, Cebu Technological University, Brgy.8 Poblacion, Tuburan, Cebu, Cebu City, Philippines*
[2]*College of Agriculture, Cebu Technological University, Tabotabo Street Barangay 5 Tuburan, Cebu City, Philippines*

Received 27 January 2023; revised 5 March 2023; accepted 3 May 2023

Abstract:

Calcium, obtained from various sources, is essential to fulfil the dietary requirements of birds. Oyster shells are excellent sources of calcium and are widely used in bird diets. Calcium is a critical factor in eggshell deterioration, affecting its absorption. Consequently, this study aimed to determine the combined effects of powdered oyster shell and lemongrass on the growth, development, and egg quality of birds, specifically using 5, 10, and 15 grams of oyster shell powder as a calcium source. A completely randomised design was used to assess the efficacy of varying amounts of powdered oyster shell. Results revealed that there was no significant change in growth development at different inclusion levels of oyster shell powder and lemongrass solution. However, egg quality exhibited a significant variance at different inclusion levels of oyster shell powder. Similarly, lemongrass solution as a supplement for laying quails demonstrated a significant difference. Therefore, supplementing the calcium source with a blend of 15 g of oyster shell powder and 300 ml lemongrass solution enhanced egg performance and eggshell quality of laying quail by 5%.

Keywords: ***Coturnix coturnix japonica*, *Cymbopogon citratus*, egg quality, feed additive, powdered oyster shell, water supplement.**

Classification number: **3.1**

1. Introduction

The quality of poultry egg has become integral to the successful marketing of animal products. As public understanding and awareness of nutrition and health have grown, local communities have begun to select eggs with specific nutritional characteristics, such as low cholesterol and fat content [1-2]. One of the most significant economic losses to the poultry industry is egg breakage, which is still a problem today. It is estimated that 13 to 20% of total production is damaged or lost before reaching its final destination [3]. To prevent eggs from breaking during hatching or handling, and to promote optimal growth and development, laying quails must receive sufficient calcium in their diet [4, 5].

Many farmers raise quail for both meat and eggs as an additional source of household income. Quail meat provides an abundance of vitamin C, iron, minerals, and amino acids [6]. However, as the population grows, so does the demand for egg products. The global population is projected to reach 9 billion by 2050, suggesting that food demand will continue to increase in the coming decades [7]. To meet the needs of Filipinos, some farmers raise quails, leading to an increased demand for ingredients for compound feed. In the Philippines, quail eggs are a primary ingredient in kwekwek, a popular street food.

Various sources of calcium are used to meet the dietary requirements of birds. Oyster shells, abundant sources of calcium, are widely incorporated into bird nutrition [8, 9]. According to M. Alagawany, et al. (2021) [10], lemongrass extract can be obtained from boiled lemongrass and is said to contain a very high amount of vitamin C and antioxidant activity. It also boasts antimicrobial capacity and can serve as a substitute antibiotic in the poultry industry [11].

Problems related to shell quality have been extensively studied in chickens, but minimal information is available on quail. A deficiency of calcium in quail feed leads to decreased egg production. The optimal dietary calcium level for high egg production and hatchability appears to be 5 to 15 g, with higher levels leading to reduced hatchability [5]. Today, some plant-based feed additives are used in poultry and animal nutrition to enhance growth and performance, referred to as phytogenic feed additives [12]. At present, small and medium-sized farmers are attempting to commercially increase the production of quail and poultry products by providing feed additives such as oyster shell powder. Although much work has been done to examine shell quality, there has been minimal research on overall egg quality and egg production of laying quail. Farmers need to produce high-quality shell eggs [13], requiring the selection of a high-quality and inexpensive source of calcium for

*Corresponding author: Email: florieza.mangubat@ctu.edu.ph

their diet. Various sources of calcium are available to as a dietary supplement to improve shell quality, but there is often a debate over which is the most effective. Notably, research on calcium levels reveals a gap between the 5 and 15 g levels. Therefore, the present study aimed to evaluate the effects of powdered oyster shells on egg quality, and the impact of lemongrass solution on the growth development of *Coturnix coturnix*, using 5, 10 and 15 g, respectively.

The research examining the impact of calcium sources on the growth and development of Japanese quail holds considerable valuable for several reasons. Firstly, the study focuses on an essential aspect of poultry production: optimising egg production and eggshell quality to increase marketability, indicating stability among quail farmers. Egg performance and eggshell quality are key factors that determine the profitability of poultry farming. Secondly, the study explores alternative calcium sources, which could have practical implications for poultry farmers. Using powdered oyster shells and lemongrass as calcium sources is innovative and could offer a more sustainable and cost-effective alternative to traditional calcium sources. Thirdly, the study proves that combining 15 g of a powdered oyster shell with 300 ml of lemongrass solution can significantly increase egg performance and eggshell quality of laying quail by 5%. This finding is significant as it offers a practical solution for poultry farmers to improve egg production and quality without incurring substantial costs.

Overall, this study enriches the existing literature on poultry farming and highlights the potential benefits of using alternative calcium sources for improving egg performance and quality. The findings of this study could have practical implications for poultry farmers looking to optimise their production processes and enhance profit. Furthermore, providing an alternative and potentially cost-effective calcium source for the poultry industry could benefit small-scale farmers and reduce reliance on traditional calcium sources such as limestone. Using lemongrass as a supplement is unique and could be a viable alternative to conventional calcium sources, such as limestone, and may have additional benefits for egg performance and eggshell quality in laying quail. This study's findings could contributes to developing new and sustainable feed supplements for the poultry industry.

2. Materials and methods

2.1. Source of the test preparation ingredients

Fresh oyster shells were manually collected at Barangay Lilo-an Cebu, Philippines, primarily because the location is known for breeders of oysters. The shell and oyster were separated, thoroughly washed with clean water, boiled at 80^{o}C for 30 min, and dried under the sun's heat for 2-3 days. Dried shells were smashed into a fine powder using a hammer.

Cymbopogon citratus was obtained from a private farm in the municipality of Asturias. A sufficient quantity of the plant was taken, and, after removing the impurities and cleaning them well, they were air-dried at room temperature. The dried leaves of the lemongrass plant were heated with 1 litre of tap water and boiled at 100^{o}C for 10 min. The solution was cooled, filtered, and set aside in an empty container. The concentration of the solution included 10 g lemongrass for 100 ml concentrated extract of lemongrass per litre of drinking water, a concentration of 20 g for 200 ml concentrated extract of lemongrass per litre of drinking water, and a concentration of 30 g for 300 ml of concentrated extract of lemongrass per litre of drinking water.

2.2. Application of powdered oyster shell and lemongrass solution

Applying powdered oyster shells to the experimental birds included mixing with commercial feed according to the standard treatment recommendations of 540 grams/treatment/day. The solution was administered as a water supplement at 100, 200, and 300 ml/l with every treatment. By testing different levels of oyster shell and lemongrass extract supplementation, this study can determine the most effective combination of these two calcium sources for improving egg performance and eggshell quality in laying quail. This information can be useful for poultry farmers looking to optimise their production processes and improve the profitability of their operations. Overall, the choice of oyster shell and lemongrass extract levels in animal nutrition research is based on a combination of factors including previous research, practical experience, and safety considerations.

2.3. Preparation of experimental birds

A total of 72 female quail heads in a cage were used in the study. These were purchased in Catmon, Cebu and transferred to the breeding unit at Purok 2, Tubigagmanok, Asturias, Cebu, as the animal production experimental area.

2.4. Brooding management

Upon arrival, the quail chicks were placed in the hatchery and given copious amounts of electrolyte water to replenish lost electrolytes. The walls of the incubator were covered to avoid cold temperatures along with artificial light (50 watts). Pieces of cardboard/paper were laid out as flooring, which was changed regularly. When the quails were twenty days old, they were placed in their experimental cage with six birds each for treatment. After one week, the treatment was applied. Each treatment was properly labelled for easy identification. Four treatments over three replicates were performed for a total of seventy-two heads. All the birds received the same conditions, such as good ventilation, slatted floor, light bulbs, and feeding schedule, until the study was completed.

2.5. Experimental pen preparation and management

The quails were placed in a shed-type housing in an experimental pen of dimensions 1.8x1.2x0.40 m. The floor was divided into twelve compartments with six quail heads each for treatment. Each experimental cage was equipped with housing facilities such as feeders and water dispensers. The feeding troughs were placed in the cage and tied according to the height of the prospects to reach the feed, facilitate cleaning, and to avoid feed spillage. The shape and size of the trough were semi-circular and adjustable to allow for effortless adjustment and ease of cleaning.

2.6. Light management

Quails received the same daily light duration at all experimental sites, adjusted with increasing age. The laying quail received 15 hours of light for 20 to 38 days and 16 hours per day for 39 days from the laying stage until the end of the study.

2.7. Application of treatment

The same commercial quail layer mash feeds were given to all experimental quail. Through random selection, quails were treated using powdered oyster shells at three different inclusion levels and replicated three times. In each replication, female quails were fed with 90 g quail layer mash (QLM) feeds (without Ca supplements) in the morning and afternoon, 90 g QLM+5 g POS, 90 g QLM+10 g, and 90 g QLM+15 g powdered oyster shell, respectively. The concentrations encompassed 10 g for a dose of 100 ml concentrated extract of lemongrass/litre of drinking water, a concentration of 20 g for a dose of 200 ml concentrated extract of lemongrass/litre of drinking water, and a concentration of 30 g for a dose of 300 ml concentrated extract of lemongrass/litre of drinking water. This scheme was followed throughout the entire study.

2.8. Application of feeds and treatment for quail

In quail 30-36 days old, the feed intake was 180 g of booster/day without supplementation, at 37-43 days, the feed intake was 180 g of quail layer mash /day without supplementation, and at 44-72 days, the feed intake was 180 g of quail layer mash/day with different levels of powdered oyster shell.

T_0: control (100% commercial feeds) + water; T_1: 900 ml of tap water with 100 ml of lemongrass extract + 5 g oyster shell powder; T_2: 800 ml of tap water with 200 ml of lemongrass extract + 10 g oyster shell powder; T_3: 700 ml of tap water with 300 ml of lemongrass extract + 15 g oyster shell powder.

2.9. Feeding management

In this study, the experimental birds were fed twice daily at 7:30 a.m. and 5:00 p.m.

2.10. Statistical analysis

The study was statistically analysed through Sirichai Statistics Version Significant for complete randomised block design. Duncan's Multiple Range Test (DMRT) was used to determine the significant difference among treatments. This was laid out in a Complete Block Design (CBD) consisting of four treatments, six heads per treatment. Commercial growers/finishers with powdered oyster shells as a feed additive and lemongrass extracts for water supplement.

2.11. Experimental unit

The quails were placed in shed-type housing with 12 compartments, each containing six quails for each treatment, resulting in a total of 216 quails with compartment dimensions of 1.8x1.2x0.40 m. Each compartment was equipped with housing facilities such as feeders and water dispensers. The quails were given the same daily light duration, adjusted with increasing age, and were fed the same commercial quail layer mash feeds. The treatments consisted of powdered oyster shells at three different inclusion levels (5, 10, and 15 g) and lemongrass extract at three different concentrations (100, 200, and 300 ml/l). The experiment was replicated three times.

3. Results and discussion

Table 1 shows the effect of adding oyster shell powder to the feed and lemongrass solution to the drinking water on the mean week gain within six weeks of coverage. There was no significant difference between T_0 and T_1, and T_2 and T_3 shared similar differences compared to the body weight of laying female quail ranging from 120 to 160 g [14]. This study's results were contradictory to those of previous studies [15, 16] as adding oyster shell powder to the feed for six weeks led to significant improvement in weight and average weekly weight gain compared to the control. The reason for this may be due to the calcium and active compounds in calcium oyster shell and lemongrass such as flavonoids and linalool solution, which improves digestion and increases the secretion of digestive enzymes in birds. The process of benefiting from food intake improves and is reflected in laying quails' growth and weight gain. As presented herein, there is no significant difference between the oyster shell powder and lemongrass solution when used as a supplement to laying quail.

Table 1. The weekly gain of laying quail with varied levels of oyster shell powder and lemongrass.

Treatment	Week 1	Week 2	Week 3	Week 4	Week 5	Week 6
T_0	149.20^a	150.97^a	152.67^a	154.03^a	154.85^a	156.36^a
T_1	146.36^a	148.77^a	151.17^a	153.20^a	154.63^a	156.45^a
T_2	147.96^a	151.26^a	154.09^a	156.86^a	158.71^a	160.99^a
T_3	150.36^a	153.96^a	157.46^a	160.78^a	163.27^a	166.41^a

T_0: control (100% commercial feeds) + water; T_1: 900 ml of tap water with 100 ml of lemongrass extract + 5 g oyster shell powder; T_2: 800 ml of tap water with 200 ml of lemongrass extract + 10 g oyster shell powder; T_3: 700 ml of tap water with 300 ml of lemongrass extract + 15 g oyster shell powder. Different letters indicate statistically significant differences ($p \leq 0.05$).

Table 2 indicates the mean average feed consumption from the experiment across different inclusion levels. For the mean average consumption of the first and second week of the experiment, T_3 (15 g oyster shell powder) exhibited a significant difference compared to other treatments. During the third week of the experiment, T_1 (5 g oyster shell powder) demonstrated a significant effect compared to T_2 (10 g oyster shell powder) and T_3 (15 g oyster shell powder). In the fourth week of the experiment, T_0 (control) had significant differences compared to all the oyster shell powder treatments. In the fifth week, T_1 (5 g oyster shell powder) significantly differed from T_3 (15 g oyster shell powder). Finally, during the last week of the experiment, T_3 (15 g oyster shell powder) and T_0 (control) had significant differences in comparison to T_1 (5 g oyster shell powder) and T_2 (10 g oyster shell powder). The results of this study are consistent with M. Dian, et al. (2017) [17] in that calcium and active compounds in oyster shells as well as lemongrass flavonoids and linalool improve digestion, increase digestive enzyme secretion, and increase feed consumption in the experimental birds. This information can be helpful to poultry producers in optimising the nutrition of their laying hens for better performance and health [18].

Table 2. The result of mean feed consumption with different inclusion levels of lemongrass and oyster shell powder.

Treatment	Week 1	Week 2	Week 3	Week 4	Week 5	Week 6
T_0	162.05^{a}	162.61^{a}	170.11^{ab}	176.44^{a}	163.39^{ab}	175.33^{a}
T_1	161.17^{a}	160.50^{a}	176.50^{a}	167.17^{b}	169.61^{a}	164.22^{b}
T_2	159.05^{a}	162.31^{a}	154.16^{c}	160.89^{b}	162.167^{ab}	166.72^{b}
T_3	144.67^{b}	157.66^{b}	142.33^{c}	162.78^{b}	156.61^{b}	175.33^{a}

T_0: control (100% commercial feeds) + water; T_1: 900 ml of tap water with 100 ml of lemongrass extract + 5 g oyster shell powder; T_2: 800 ml of tap water with 200 ml of lemongrass extract + 10 g oyster shell powder; T_3: 700 ml of tap water with 300 ml of lemongrass extract + 15 g oyster shell powder. Different letters indicate statistically significant differences ($p \leq 0.05$).

In Table 3, quails fed with commercial layer feeds showed the highest value among treatments. Those given high calcium levels showed the lowest feed conversion ratio. As presented above, laying quails fed commercial feed + 15 g oyster shell powder had the most efficient results compared to the rest of the oyster shell powder treatments. It is evident that poor results were exhibited by laying quails fed with commercial layer feeds without Ca supplements. The result of this present study is in agreement with M. Dian, et al. (2017) [17] in that active compounds such as Ca in oyster shell improve digestion, increases the secretion of digestive enzymes, and increase feed consumption in the laying quail.

Table 3. The result of feed conversion ratio with different inclusion levels of lemongrass and oyster shell.

Treatment	Week 1	Week 2	Week 3	Week 4	Week 5	Week 6
T_0	2.58	2.49	2.60	2.68	2.45	2.63
T_1	2.57	2.53	2.72	2.57	2.55	2.45
T_2	2.47	2.47	2.29	2.38	2.39	2.39
T_3	2.21	2.47	2.17	2.37	2.29	2.50

T_0: control (100% commercial feeds) + water; T_1: 900 ml of tap water with 100 ml of lemongrass extract + 5 g oyster shell powder; T_2: 800 ml of tap water with 200 ml of lemongrass extract + 10 g oyster shell powder; T_3: 700 ml of tap water with 300 ml of lemongrass extract + 15 g oyster shell powder.

The study investigates the effect of various levels of lemongrass solution added to the drinking water on the total water consumption rate in quail birds over six weeks (Table 4). In the first week, T_3 (300 ml lemongrass solution) recorded the highest rate of water consumption and showed a significant difference among treatments. During the second week, T_1 (100 ml lemongrass solution) was significantly different from both T_0 (control) and T_3 (300 ml lemongrass solution). In the third and fourth weeks, T_3 (300 ml lemongrass solution) displayed a significant variance between T_0 (control) and T_1 (100 ml lemongrass extract). In agreement with X. Cheng and N. Zhonghua (2023) [4], the rise in water consumption can potentially increase feed intake. The lemongrass solution may enhance the flavour and taste of the drinking water, thus increasing palatability and subsequentially boosting water consumption, particularly in treatments involving the aforementioned drinking solution.

Table 4. Mean water consumption with different inclusion levels of lemongrass and powdered oyster.

Treatment	Week 1	Week 2	Week 3	Week 4	Week 5	Week 6
T_0	976.11^{b}	1021.83^{b}	869.96^{c}	805.78^{c}	864^{d}	994.83^{c}
T_1	1055.39^{b}	1263.72^{ab}	872^{c}	851.11^{c}	950.72^{c}	871.33^{d}
T_2	1074.33^{b}	1347.55^{a}	1163.94^{b}	1158.44^{b}	1357.53^{a}	1126.17^{b}
T_3	1187.89^{a}	1048.17^{b}	1382.28^{a}	1384.83^{a}	1184.89^{b}	1340.11^{a}

T_0: control (100% commercial feeds) + water; T_1: 900 ml of tap water with 100 ml of lemongrass extract + 5 g oyster shell powder; T_2: 800 ml of tap water with 200 ml of lemongrass extract + 10 g oyster shell powder; T_3: 700 ml of tap water with 300 ml of lemongrass extract + 15 g oyster shell powder. Different letters indicate statistically significant differences ($p \leq 0.05$).

The results in Table 5 demonstrate significant differences ($p<0.05$) in the water conversion factor at six weeks, particularly between T_3 (300 ml lemongrass solution) and T_0 (control). T_3 (300 ml lemongrass solution) recorded the most efficient water conversion factor, exhibiting a significant

improvement ($p \leq 0.05$) in comparison to T_0 (control). These results align with Y.A. Attia, et al. (2020) [18], which posited that the improvement in the efficiency of nutritional conversion may be attributable to the active compounds in lemongrass solution. These compounds may have a role in improving the flavour and taste of drinking water, thereby increasing its palatability and consequentially boosting water consumption, particularly for treatments involving lemongrass solution.

Table 5. Results of water conversion ratio with different inclusion levels of lemongrass and powdered oyster.

Treatment	Week 1	Week 2	Week 3	Week 4	Week 5	Week 6
T_0	6.5	6.75	5.65	5.25	5.59	6.39
T_1	7.27	8.60	5.77	5.56	6.16	5.57
T_2	7.79	8.90	7.56	7.39	8.56	7
T_3	7.92	6.82	8.91	8.62	7.27	8.06

T_0: control (100% commercial feeds) + water; T_1: 900 ml of tap water with 100 ml of lemongrass extract + 5 g oyster shell powder; T_2: 800 ml of tap water with 200 ml of lemongrass extract + 10 g oyster shell powder; T_3: 700 ml of tap water with 300 ml of lemongrass extract + 15 g oyster shell powder.

Laying quails with 15 g of oyster shell powder had the highest number of eggs laid, followed by 5 g and 10 g of oyster shell powder. However, laying quails given pure commercial feed and plain water had the lowest number of eggs among feed treatments across all inclusion levels. Table 6 shows that the number of eggs increased with the highest oyster shell powder treatment. This result is contrary to a study by A. Khalifaha, et al. (2021) [19], who found that the addition of Ca adversely affected feed intake and egg production due to excessive levels of Ca and other minerals such as magnesium, present in Ca sources. Additionally, they suggested that the extreme amounts of Ca added to their diet was not absorbed by the digestive tract, thus significantly affecting some egg yields.

Table 6. The total number of eggs laid with different inclusion levels of lemongrass and oyster powder.

Treatment	Week 1	Week 2	Week 3	Week 4	Week 5	Week 6	Total
T_0	-	16	69	58	64	87	294
T_1	-	15	75	82	60	98	330
T_2	-	9	50	64	68	113	304
T_3	-	12	74	91	83	115	375
Total	-	52	268	295	275	413	1303

T_0: control (100% commercial feeds) + water; T_1: 900 ml of tap water with 100 ml of lemongrass extract + 5 g oyster shell powder; T_2: 800 ml of tap water with 200 ml of lemongrass extract + 10 g oyster shell powder; T_3: 700 ml of tap water with 300 ml of lemongrass extract + 15 g oyster shell powder.

Mean egg weight: As observed in Table 7, laying quails given 15 g of oyster shell powder obtained the highest weight, followed by 10 g and then 5 g of oyster shell powder. The result showed a relatively minor difference in egg weights when the calcium source was given at different inclusion levels. However, laying quails without oyster shell inclusion had the poorest performance. Table 7 highlights the effects of calcium source, the oyster shell powder, added in the diets of laying quails, indicating that T_1 and T_2 were marginally significant compared to T_0 and T_3. Laying quails supplemented with 15 g of oyster shell powder were not significantly different from those given 10 g of oyster shell powder, but they did significantly differ from those receiving 5 g and pure commercial feeds. Generally speaking, the normal egg weight of quail ranges from 6 to 8 g, with an average weight of 9 g [9, 12]. These results align with A. Mako, et al. (2017) [8], which proposed that increased calcium levels improve eggshell thickness and egg weight with three calcium levels (3.75, 4.15 and 4.55%) in laying phase diets. Thus, 5 g of oyster shell powder and the control group, which were given only pure commercial feed, offered a lower Ca amount to laying quails. Calcium is one of the critical nutrients required for optimum egg production and eggshell quality in laying quails [20], and appropriate levels should be identified and considered.

Table 7. The mean egg quality with different inclusion levels of lemongrass and oyster powder.

Treatment	Weight (g)	Length (mm)	Width (mm)	Eggshell percentage (%)	Shell thickness (mm)	Egg yolk colour
T_0	7.95^{c}	28.91^{a}	23.37^{a}	0.45^{c}	0.12^{b}	More yellow
T_1	8.32^{bc}	29.27^{a}	23.52^{a}	0.56^{b}	0.17^{b}	Light yellow
T_2	8.69^{ab}	29.87^{a}	24.07^{a}	0.65^{b}	018^{b}	Lighter yellow and less orange
T_3	9.01^{a}	29.40^{a}	3.97^{a}	0.93^{a}	0.21^{b}	Light orange

T_0: control (100% commercial feeds) + water; T_1: 900 ml of tap water with 100 ml of lemongrass extract + 5 g oyster shell powder; T_2: 800 ml of tap water with 200 ml of lemongrass extract + 10 g oyster shell powder; T_3: 700 ml of tap water with 300 ml of lemongrass extract + 15 g oyster shell powder. Different letters indicate statistically significant differences ($p \leq 0.05$).

Egg length and width: The mean egg quality in terms of length and width of laying quail eggs given oyster shell as a calcium source at different inclusion levels is discussed here. Egg height and width were classified based on the USDA's guidelines. According to A. Saki, et al. (2019) [21], the longest length is attributed to the oldest quail-laid eggs at 32.6 mm, and the maximum width at 25.8 mm. The analysis of variance demonstrates that the supplementation

of oyster shell powder was not significantly different when compared across different inclusion levels. Oyster shell powder at different inclusion levels did not significantly affect the laying quail egg's quality in terms of length and width across all treatment levels. This result implies that addition of oyster shell powder at various levels does not significantly improve egg length and width.

Egg shell percentage: Among the treatment levels, oyster shell powder given at 15 g had the highest shell percentage, sequentially followed by 10 and 5 g. Conversely, laying quails given only pure commercial feeds had the lowest percentage. Therefore, the supplementation of oyster shell powder significantly varied. Oyster shells given to laying quails at 15 g and 10 g yielded a significantly different result at a 5% level ($p<0.005$) compared to 5 g and birds fed purely on commercial feeds. Most research reported that increased dietary calcium levels showed a linear improvement in eggshell quality [22]. Also, a linear increase in eggshell quality was observed when feeding calcium above 6.5 g/day. An increase in calcium intake from 4.08 to 4.64 g/day improves eggshell thickness in aged Brown Layers [23], an outcome not consistent with the results of this study. In another study, results led to the definition of a linear effect on dietary Ca with eggshell quality, which reported that using 90- and 108-week laying hens showed no effects of dietary Ca on eggshell strength and thickness [24]. Still, the eggshell percentage and weight per surface area (ESWSA) increased by increasing the Ca concentration in the diet. Likewise, the present study showed a linear effect on eggshell percentage and thickness.

Egg shell thickness: Laying quail eggs supplemented with 15 g oyster shell had the thickest shell (0.21 mm), followed by a calcium level at 10 g (0.18 mm). However, laying quails receiving only commercial feeds had the thinnest eggshell (0.17 mm) amongst all treatment levels. The average shell thickness is reported to range between 0.08 and 0.17 mm [20]. As reflected in this study's results, supplementing calcium in suitable quantities greatly affects eggshell quality. However, the shell thickness of different inclusion levels of oyster shell treatment showed no significant difference. The results indicated that varying levels of calcium inclusion from oyster shells do not significantly impact eggshell thickness. These results align with those in study of M. Islam and M. Nishibori (2021) [9], who observed no significant difference in shell thickness when limestone was replaced with oyster shells.

Egg yolk colour: Visual scoring, conducted using a Roche Colour Fan, revealed that T_3, treated with 15 g of oyster shell powder, has the highest value of 14, boasting a more orange egg yolk colour amongst the different inclusion levels. According to a study published by the *Journal of Food Science*, egg yolks with darker colours (such as mustard yellow or light orange) typically contain more omega-3s and vitamins than lighter egg yolks.

4. Conclusions

Oyster shell powder and lemongrass solution, used as supplements for laying quails, exhibited significant differences. The growth development of the quails was not significantly impacted at various inclusion levels of oyster shell powder and lemongrass solution. On the other hand, egg quality significantly differed with different inclusion levels, the supplementation of these two ingredients had substantial effects. The administration of calcium sources at a 15 g level notably increased egg performance and eggshell quality of laying quail. Consequently, quail growers are advised to utilise this promising feed additive at a higher inclusion level, as this supplement offers a favourable return on investment.

CRediT author statement

Florieza Mangubat: Data analysis and Interpretation, Writing and Revising manuscript; Cerela Looc: Method, Data analysis and Writing; Fretzel Mad: Method, Data analysis and Writing.

COMPETING INTERESTS

The authors declare that there is no conflict of interest regarding the publication of this article.

REFERENCES

[1] J. Miranda, X. Anton, C. Valbuena, et al. (2015), "Egg and egg-derived foods: Effects on human health and use as functional foods", *Nutrients*, **7(1)**, pp.706-729, DOI: 10.3390/nu7010706.

[2] S.R. Godbert, N. Guyot, Y. Nys (2019), "The golden egg: Nutritional value, bioactivities, and emerging benefits for human health", *Nutrients*, **11(3)**, DOI: 10.3390/nu11030684.

[3] L. Johnson, R. Dunninga, D. Bloom, et al. (2018), "Estimating on-farm food loss at the field level: A methodology and applied case study on a North Carolina farm", *Resources, Conservation and Recycling*, **137**, pp.243-250, DOI: 10.1016/j.resconrec.2018.05.017.

[4] X. Cheng, N. Zhonghua (2023), "Research progress on bird eggshell quality defects: A review", *Poultry Science*, **102(1)**, pp.1-10, DOI: 10.1016/j.psj.2022.102283.

[5] S. Świątkiewicz, A. Arczewska-Włosek, J. Krawczyk, et al. (2015), "Effects on performance and eggshell quality of particle size of calcium sources in laying hens' diets with different Ca concentrations", *Arch. Anim. Breed*., **58,** pp.301-307, DOI: 10.5194/aab-58-301-2015, 2015.

[6] C.M. Mnisi, M. Marareni, F. Manyeula, et al. (2021), "A way forward for the South African quail sector as a potential contributor to food and nutrition security following the aftermath of COVID-19: A review", *Agriculture & Food Security*, **10**, DOI: 10.1186/s40066-021-00331-8.

[7] E. Fukase, W. Martin (2020), "Economic growth, convergence, and world food demand and supply", *World Development*, **132**, DOI: 10.1016/j.worlddev.2020.104954.

[8] A. Mako, B.S. Jemiseye, F.O. Abokede, et al. (2017), "Comparative use of oyster shell and limestone as calcium sources in the chickens' diet", *Nigerian Journal of Animal Production*, **44(1)**, pp.275-281, DOI: 10.51791/njap.v44i1.804.

[9] M. Islam, M. Nishibori (2021), "Use of extruded eggshell as a calcium source substituting limestone or oyster shell in the diet of laying hens", *Vet. Med. Sci.*, **7(5)**, pp.1948-1958, DOI: 10.1002/vms3.544.

[10] M. Alagawany, M.T. El-Saadony, S.S. Elnesr, et al. (2021), "Use of lemongrass essential oil as a feed additive in quail's nutrition: Its effect on growth, carcass, blood biochemistry, antioxidant and immunological indices, digestive enzymes and intestinal microbiota", *Poult. Sci.*, **100(6)**, DOI: 10.1016/j.psj.2021.101172.

[11] A.B. Lagha, B. Haas, M. Gottschalk, et al. (2017), "Antimicrobial potential of bacteriocins in poultry and swine production", *Veterinary Research*, **48**, DOI: 10.1186/s13567-017-0425-6.

[12] N. Abdelli, D.S. Oriol, J.P. Pérez (2021), "Phytogenic feed additives in poultry: Achievements, prospective and challenges", *Animals (Basel*), **11(12)**, DOI: 10.3390/ani11123471.

[13] A. Kavtarashvili, V. Buyarov (2021), "The reasons for the deterioration of chicken eggshell quality at high temperatures: A review", *E3S Web of Conferences*, **247**, DOI: 10.1051/e3sconf/202124701015.

[14] M.D.C. Ludke, A.C.S. Pimentel, J.V. Ludke, et al. (2018), "Laying performance and egg quality of Japanese quails fed diets containing castor meal and enzyme complex", *Rev. Bras. Cienc. Avic.*, **20(4)**, pp.781-788, DOI: 10.1590/1806-9061-2018-0732.

[15] J.H. Seo, S.M. Park, B.J. Yang, et al. (2019), "Calcined oyster shell powder as an expansive additive in cement mortar", *Materials (Basel)*, **12(8)**, DOI: 10.3390/ma12081322.

[16] Y. Wang, M. Ji, M. Wu, et al. (2022), "Toward green farming technologies: A case study of oyster shell application in fruit and vegetable production in Xiamen", *Sustainability*, **15(1)**, DOI: 10.3390/su15010663.

[17] M. Dian, L. Trilianty, D. Fransisca, et al. (2017), "Antioxidant and anti-glycation activity of ethanol lemongrass (cymbopogon's citrate) leaves extract", *Inter. J. Pharm. and Phytochem. Res.*, **9(5)**, pp.710-715, DOI: 10.25258/phyto.v9i5.8153.

[18] Y.A. Attia, M.A. Al-Harthi, H.A.M.A. El-Maaty (2020), "Calcium and cholecalciferol levels on late phase-laying hens' diets: Effects on productive and egg quality traits, blood biochemistry, and immune responses", *Frontiers in Veterinary Science*, **7**, DOI: 10.3389/fvets.2020.00389.

[19] A. Khalifaha, S. Abdalla, W. Dosoky, et al. (2021), "Utilization of lemongrass essential oil supplementation on growth performance, meat quality, blood traits and caecum microflora of growing quails", *Annals of Agricultural Sciences*, **66(2)**, pp.169-175, DOI: 10.3390/nu13020509.

[20] L. Pinotti, M. Manoni, L. Ferrari, et al. (2021), "The contribution of dietary magnesium in farm animals and human nutrition", *Nutrients*, **13(2)**, DOI: 10.3390/nu13020509.

[21] A. Saki, A. Rahmani, A. Yousefi (2019), "Calcium particle size and feeding time influence eggshell quality in laying hens", *Acta Sci. Anim. Sci.*, **41**, DOI: 10.4025/actascianimsci.v41i1.42926.

[22] A. Wilkanowska, K. Dariusz (2012), "Layer age and quality of pharoh quail eggs", *Journal of Central European Agriculture*, **13(1)**, pp.10-21.

[23] J.H. Park, S. Shanmugam, I.H. Kim (2020), "Egg production, egg quality, nutrient digestibility, and excreta microflora of laying hens fed with a diet containing brewer's yeast hydrolysate", *Journal of Applied Animal Research*, **48(1)**, pp.492-498, DOI: 10.1080/09712119.2020.1825446.

[24] H. Jiaying (2013), *Effects of Housing and Calcium-deficient diet on Health and Egg Production in Bovans Brown Hens*, Master of Science Thesis, Purdue University, 116pp.

DOI: 10.31276/VJSTE.65(3).66-74

Soybean yield, seed quality and thresh efficiency by mechanisation at different harvesting stages and postharvest ripening

Thi Thuy Hang Vu*, Ngoc Thang Vu, Thi Tuyet Cham Le, Thi Ngoc Pham

Faculty of Agronomy, Vietnam National University of Agriculture, Trau Quy Town, Gia Lam District, Hanoi, Vietnam

Received 17 November 2022; revised 22 December 2022; accepted 28 December 2022

Abstract:

This study determined the most appropriate and earliest soybean harvesting stage and the number of days of postharvest ripening with minimal effects on seed losses and quality when mechanical harvest and threshing were applied. Harvesting stages at four physiological maturities (60, 70, 80, and 90%) and various days of postharvest ripening treatment (1, 2, and 3 days) were applied for two soybean varieties DT12 and DT26. Harvesting at physiological maturity of 90% recorded the highest seed-shattering loss but the least seed damage (<5%) and highest seed quality, followed by a physiological maturity of 80%. There were no significant differences in seed yields between harvesting stages of 80 and 90% maturity. Harvesting soybeans at a physiological maturity of 60 and 70% resulted in no seed losses but a significant reduction in seed quality. To avoid adverse weather, an early harvest stage at a physiological maturity of 80% is suggested. Although postharvest ripening of soybeans for early harvest caused seed shattering losses (2-5%), it was necessary to ensure seed quality. These results indicate effective and practical methods for farmers at small households to use in early mechanical harvesting of soybeans.

Keywords: **early harvest, mechanical, physiological maturity, postharvest ripening.**

Classification numbers: **3.1, 3.4**

1. Introduction

Harvesting time is critical to seed quality in soybean seed production since the seeds deteriorate either in the field, during harvesting, or after harvesting [1, 2]. Therefore, appropriate harvesting stages of soybeans are important to minimize losses at harvest and to ensure seed quality for the next growing season. Seed yield and quality largely depend on the stage of maturity. Physiological maturity in soybeans reached the reproductive development stage R7 with pods yellowing and 50% of leaves yellowing [3]. The seed moisture content at that physiological maturity ranged from 54-62% [1, 4], which is unsuitable for mechanical harvesting and threshing. The R8 stage was featured by 95% of pods reaching the mature pod colour [5].

Common practice is to harvest soybeans when 90% of the pods on the plant turn brown [6]. Early harvest often results in very poor seed quality due to a greater number of immature and undeveloped seeds [7], high seed moisture content (e.g., 60.9% for soybean seed harvest early at R7), and a low percentage of seed germination (<75%) [1]. In addition, the study by D.F. Miles, et al. (1988) [8] on harvested pods at four developmental stages (full seed, mid-pod fill, expanded pod, and yellow pod) showed that near maximum radicle protrusion occurred at only 35% seed dry weight accumulation, and maximum germination did not occur until physiological maturity. Soybean seeds harvested too early, such as less than 34 days after flowering, were still able to germinate before maximum seed dry weight was reached; but seeds harvested at less than one-half their full size had very little potential to withstand desiccation [9].

Delayed harvesting by one to two weeks after physiological maturity can result in significant seed yield loss [6, 10] and low seed germination and vigour [1, 11-13]. Germination and vigour were reduced in seeds harvested at 15 and 30 days after the R8 stage (when 95% of pods have typical coloration of mature pods) [11]. Oil

*Corresponding author: Email: vtthang.nh@vnua.edu.vn

contents of seeds harvested at R8 stage or 1 to 4 weeks after physiological maturity were not significantly different from and even lower after 1-2 months of storage than that of seeds harvested early at the R7 stage [1, 6]. Maximum protein content was obtained at physiological maturity and decreased with delaying harvest [14]. Total protein was not significantly affected by four harvest times (R7, R7+5 days, R7+10 days (R8), and R7+20 days) [15].

In addition, soybean seed quality is also affected by the field weather environment during harvest dates. Adverse weather, especially highly humid and wet weather or even alternating periods of wet and dry weather during harvest dates, accelerated seed deterioration and shatter loss [13, 16]. Additionally, shrinking and breaking of seeds were some of the physical changes that occurred in soybean seeds after harvesting [17].

Soybean seeds are quite susceptible to mechanical damage, especially at high seed moisture content. One way to minimize the negative effects of harvesting high moisture soybeans on seed viability and vigour is to harvest and dry the seeds within intact pods [18]. Indeed, N.H. Samarah, et al. (2009) [19] found that harvesting and drying soybeans within intact pods helped maintain soybean seed quality (viability and vigour). Drying the seeds within intact pods can also reduce the seed moisture, which consequently reduces seed damage during mechanical threshing. Drying soybean seeds of 9-cm-high seed layer using a prototype dryer showed that seed quality was maintained by drying high moisture seeds (22%) with an average temperature of 34^{o}C and relative humidity of 24.6% [20].

Several studies on soybean harvesting time have been done with emphasis given to effects on commercial values and storage, but not on the use of seeds for the next crop [1, 21]. Additionally, there have been many studies on effects of early harvesting stages and postharvest ripening treatment on seed losses and quality in soybeans. In practice and on small household scales in developing countries like Vietnam [22], farmers are continually faced with the challenge of loss of seed viability and germination. Winter soybeans are a common crop after summer rice - an important rotation sequence in the rice-based cropping system in North Vietnam. However, adverse weather such as high humidity and wet conditions on harvest days in the Vietnamese winter season place pressure on farmers to harvest soybeans early. Moreover, mechanisation at harvest should be increasingly applied for more efficient soybean production. Moreover, there have not yet been any studies providing information on possible early harvesting stages for small farmers to apply in practice with mechanical harvesting to minimize seed losses and quality.

Thus, this study aims to determine the most appropriate stage for early soybean harvesting and number of days of postharvest ripening on seed loss, yield recovery, and seed quality in aspects of seed germination and vigour. This will provide valuable and useful information for small farmers in Vietnam to apply mechanical harvesting and seed threshing to avoid adverse weather at harvest dates.

2. Materials and methods

2.1. Plant materials

Two soybean varieties, DT12 and DT26, were sown in Hung Ha district, Thai Binh province (Northern Vietnam) during the winter season (from September 2019 to January 2020). Soybean varieties suitable for mechanical harvest should have the first pod insertion height ≥10cm, a resistance to logging, and pod shattering [23-25]. DT12 has a short growth duration of 75-80 days, is commonly grown by farmers here, and thus was used as the control variety. DT26 has a growth duration of 85-95 days and is suitable for the winter crop in Thai Binh [25].

2.2. Cultural details and experimental design

The field experiment was a randomised complete block design with three replications. Each experimental plot area was 100 m^2 with a plant density of 45 plants/m^2 and 4 plant rows per plot with row spacing at 15x30x15 cm. Irrigation was provided to ensure plants had sufficient water access, especially around 7-10 days after germination and at flowering and pod filling stages. Chemical sprays were applied to mostly control stem and pod borers. At harvest, the entire plant was mechanically cut and collected in the field. The harvested whole plants with intact pods were mechanically threshed after drying depending on particular treatments. The methods used in this study attempted to

approach the real farmers' practice of drying the soybean seeds within intact pods under the sun.

Experiment 1. Determination of appropriate harvesting stages.

Two soybean varieties (DT12 and DT26) were harvested at four stages, viz., when 60, 70, 80 and 90% of pods on the plant turned brown (designated as T1, T2, T3, and T4, respectively). These four stages were between the R7 and R8 reproductive stages of the soybean [3, 5]. The harvested whole plants with intact pods were left to dry for one day under the sun before being mechanically threshed. Before mechanical harvest, the shattered seeds on the ground were collected from 5 sites that were 2 m^2 each per experimental plot, counted and weighted (number of seed loss, No.SL1 and weight of seed loss, WSL1 prior to harvest). After the mechanical harvest, the seeds that fell to the ground on the 5 2m^2 sites per experimental plot were counted and weighted (number of seed loss, No.SL2 and weight of seed loss, WSL2 after harvest). From those same sites, seed yield (g/m^2) was determined from the total weight of harvested seeds taken off the weight of seed loss WSL1 and WSL2.

Five kilograms of harvested plants (including leaves, stem, and pods) of each harvesting stage were threshed mechanically. Seeds were then examined for seed damage and germination. The percentage of damaged seeds (SD1) (thresh efficiency) was calculated from the weight of broken or damaged seeds out of 500 g with three replications. The standard germination test was conducted in the laboratory. Seeds were arranged in 5 replicates of 50 seeds on each petri dish with moistened filter paper. The percentage of seed germination (PG1), hypocotyl length (HL1), and root length (RL1) were evaluated after 7 days. One hundred seed weights (P100) were determined in three replicates

Experiment 2. Evaluation of early harvesting stages and postharvest ripening.

The plants were mechanically cut when 60, 70, and 80% of pods on the plant turned brown (T1, T2, and T3, respectively). Harvested whole plants with intact pods were left for one day at ambient temperature before beginning the 1, 2, and 3 days of postharvest ripening (D1, D2, and D3, respectively) under the sun.

Measurements consisted of (1) percentage of seed-shattering loss during ripening (SL1); (2) percentage of seed loss by mechanical threshing (SL2); (3) total percentage of seed loss (SL3); (4) percentage of damaged seeds (SD2); (5) percentage of seed germination (PG2) after 7 days; (6) seedling hypocotyl length (HL2) and (7) root length (RL2) after 7 days of germination; (8) and weight of 100 seeds (P100).

Five kilograms of harvested plants (including leaves, stem, and pods) from each treatment were used for seed loss measurements. The percentage of seed-shattering losses (SL1) was determined by the ratio between weight of all loose seeds collected on the ground at postharvest ripening over the total weight of seeds from 5 kg of harvested plants. Percentage of seed loss by threshing (SL2), indicating thresh efficiency, was determined by the ratio between weight of seed left in the pods after threshing over the total weight of seeds from 5 kg of harvested plants. SL3 was the sum of SL1 and SL2.

$$\text{Seed loss (\%)(SL1, SL2)} = \frac{\text{Weight of collected seeds}}{\text{Total weight of seeds collected of harvested plants (5 kg)}} \times 100$$

SD2, PG2, HL2, RL2, and P100 were measured as described in Experiment 1.

2.3. Data analysis

The analysis of variance was done by R version 4.0.2 software to determine the effects of harvesting stages and days of postharvest ripening of soybean on seed yield and quality characteristics when applying mechanical harvest and seed threshing. All experiments were performed with three replications.

3. Results

3.1. Yield, seed quality, and thresh efficiency by mechanisation at different harvesting stages

Seed-shattering occurred at a physiological maturity of 80% (T3) and 90% (T4) for both DT12 and DT26 and caused seed loss (Table 1, Supplement Table 1). Seed shattering loss (No.SL1) occurred at T3 for DT12 and DT26 with 9.87 seeds/m^2 (1.33 g/m^2) and 2.47 seeds/m^2 (0.35 g/m^2) respectively. The loss increased nearly double at T4 with 22.80 seeds/m^2 (3.17 g/m^2) and 5.40 seeds/m^2 (0.80 g/m^2) for DT12 and DT26, respectively.

Table 1. Effects of harvesting stages on seed shattering loss before and at harvest, and yield when applying mechanical harvest.

Variety	Harvesting stages	Seed-shattering loss before harvest		Seed-shattering loss at harvest		P100 (g)	Seed yield (g/m²)
		No.SL1 (seeds/m²)	*WSL1 (g/m²)*	*No.SL2 (seeds/m²)*	*WSL2 (g/m²)*		
DT12	T1	0^{e}	0^{e}	0^{d}	0^{d}	13.22	23.67^{ab}
	T2	0^{e}	0^{e}	0^{d}	0^{d}	13.41	27.33^{a}
	T3	9.87^{b}	1.33^{b}	9.07^{c}	1.23^{c}	13.62	23.67^{ab}
	T4	22.80^{a}	3.17^{a}	21.20^{a}	2.96^{a}	13.91	18.67^{b}
DT26	T1	0^{e}	0^{e}	0^{d}	0^{d}	13.49	27.0^{a}
	T2	0^{e}	0^{e}	0^{d}	0^{d}	13.42	26.33^{a}
	T3	2.47^{d}	0.35^{d}	9.20^{c}	1.31^{c}	14.36	27.33^{a}
	T4	5.40^{c}	0.80^{c}	12.47^{b}	1.79^{b}	14.43	25.0^{a}
	SE	0.80	0.11	0.89	0.13	0.44	1.12
Mean for variety	DT12	8.17^{f}	1.13^{f}	7.56^{e}	1.05^{e}	13.54	23.33^{d}
	DT26	1.97^{g}	0.29^{g}	5.42^{f}	0.78^{f}	13.93	26.42^{c}
	SE	0.40	0.05	0.46	0.07	0.22	0.56
Mean for harvesting stages	T1	0^{j}	0^{j}	0^{i}	0^{i}	13.36	25.33^{e}
	T2	0^{j}	0^{j}	0^{i}	0^{i}	13.42	26.83^{e}
	T3	6.2^{i}	0.84^{h}	9.13^{h}	1.27^{h}	13.99	25.5^{e}
	T4	14.1^{h}	1.99^{h}	16.83^{g}	2.38^{h}	14.17	21.83^{f}
	SE	0.56	0.08	0.63	0.09	0.31	0.79

Note: T1, T2, T3, T4: harvesting stages at physiological maturity of 60, 70, 80, and 90% respectively; No.SL1: number of seed-shattering loss before harvest; No.SL2: number of seed shattering loss at harvest; WSL1: weight of seed shattering loss before harvest; WSL2: weight of seed shattering loss at harvest. Mean within a column followed by the same superscript letter are not significantly different at p=0.05 according to Tukey test.

Under mechanical harvesting, there were additional seed-shattering losses (No.SL2). The loss for DT12 at harvest was quite similar to that before harvest. However, the loss for DT26 at harvest was nearly four times greater at 80% maturity (9.20 seeds/m^2) and two times greater at 90% maturity (12.47 seeds/m^2) compared to those before harvest. Across varieties, DT12 had higher seed-shattering loss than DT26. Across harvesting stages, number and weight of seed shattering loss at physiological maturity of 90% were highest and significantly different from other earlier harvesting stages (T1-T3).

Seed loss, harvesting stages and varieties significantly affected the yield. The yield was least at 90% maturity for both DT12 (18.67 g/m^2) and DT26 (25.0 g/m^2) and for the

Supplement Table 1. ANOVA for effects of harvesting stages on seed shattering loss and quality when applying mechanical harvesting.

Traits	Source of variation	df	SS	MS	F-value	p
No.SL1	Var	1	813.39	813.39	62.3818	7.31E-11***
	T	3	2891.17	963.72	73.9114	<2.20E-16***
	Var:T	3	1187.17	395.72	30.3494	4.59E-12***
No.SL2	Var	1	122.7	122.72	3.996	0.05014
	T	3	4464.3	1488.11	48.4551	4.93E-16***
	Var:T	3	423.2	141.06	4.593	0.00584***
WSL1	Var	1	14.942	14.9422	63.8999	5.02E-11***
	T	3	57.285	19.095	81.6591	<2.20E-16***
	Var:T	3	22.232	7.4107	31.6918	2.10E-12***
WSL2	Var	1	2	2	3.1685	0.080133
	T	3	88.049	29.3496	46.4979	1.17E-15***
	Var:T	3	8.084	2.6948	4.2693	0.008472**
Seed yield	Var	1	57.04	57.04	13.535	0.00248**
	T	3	82.12	27.38	6.496	0.00558**
	Var:T	3	41.46	13.82	3.279	0.05269
SD1	Var	1	58.86	58.86	66.772	2.00E-11***
	T	3	280.95	93.65	106.235	<2E-16***
	Var:T	3	1.44	0.48	0.543	0.654
P100	Var	1	2.64	2.645	1.621	0.208
	T	3	9.02	3.0056	1.841	0.149
	Var:T	3	1.32	0.4409	0.27	0.847
PG1	Var	1	158.7	158.7	29.815	3.06E-07***
	T	3	996.1	332	62.379	<2.00E-16***
	Var:T	3	46.5	15.5	2.912	0.0378*
HL1	Var	1	30.4	30.36	10.05	0.00164**
	T	3	298.1	99.38	32.896	<2.00E-16***
	Var:T	3	49.9	16.64	5.508	0.00103**
RL1	Var	1	0.5	0.53	0.328	0.567
	T	3	252.2	84.07	52.525	<2.00E-16***
	Var:T	3	117.3	39.12	24.437	1.67E-14***

Note: significant codes: 0(***): 0.001; (**): 0.01; (*): 0.05; '.': 0.1; ' ': 1. Var: variety; T: harvesting stages at physiological maturity of 60, 70, 80, and 90%; No.SL1: number of seed-shattering loss before harvest; No.SL2: number of seed-shattering loss at harvest; WSL1: weight of seed-shattering loss before harvest; WSL2: weight of seed-shattering loss at harvest; SD1: percentage of seed damage; P100: weight of 100 seeds; PG1: percentage of germination; HL1: hypocotyl length; RL1: root length.

overall (21.83 g/m^2). No seed losses at early harvest of 60-70% maturity (T1 and T2) resulted in higher seed yield. However, there were no significant differences in the weight of 100 seeds (P100) between the two soybean varieties and among harvesting stages (Table 1).

Both variety and harvesting stages had significant effects on seed damage (SD1) (Table 2). SD1 varied from 5.27-10.73% for DT12 and 3.92-8.88% for DT26. DT26 also had lower seed damage than DT12 (6.63 compared to 8.43% respectively). Harvesting at earlier stages resulted in a higher percentage of seed damage with the mean ranging from 6.98 (80% maturity) to 9.81% (60% maturity). Thus, harvest at a physiological maturity of 90% caused the least percentage of seed damage with an average of 4.59%.

Seed quality is indicated through seed germination and development of seedlings after 7 days of germination. The analysis showed that there were significant differences in the percentage of germination (PG1), hypocotyl length (HL1), and root length (RL1) between DT12 and DT26 and among the four harvesting stages (Table 2). Seed germination varied from 87.33 at 60% maturity to 95.60 at 90% maturity for DT12. DT26 had higher seed germination than DT12 with a range of 90.67-96.53%. In general, seed germination at the harvesting stage of 90% maturity was the highest but not significantly different from that of 80% maturity. Similarly, harvesting time closer to physiological maturity resulted in higher vigour of seedlings, which was indicated by the longer hypocotyl and root lengths. There seemed to be no significant differences between 80 and 90% maturity for germination, hypocotyl, and root length.

Table 2. Effects of harvesting stages on soybean seed quality after mechanical seed threshing.

Variety	Harvesting stages	SD1 (%)	PG1 (%)	HL1 (cm)	RL1 (cm)
DT12	T1	10.73^{a}	87.33^{c}	10.34^{d}	6.54^{d}
	T2	9.76^{b}	90.53^{b}	11.55^{bc}	6.53^{d}
	T3	7.99^{d}	95.20^{a}	12.30^{ab}	8.45^{ab}
	T4	5.27^{e}	95.60^{a}	12.54^{ab}	8.91^{a}
DT26	T1	8.88^{c}	90.67^{b}	9.97^{d}	6.29^{d}
	T2	7.73^{d}	94.27^{a}	10.82^{cd}	8.04^{bc}
	T3	5.97^{e}	96.40^{a}	12.73^{a}	8.46^{ab}
	T4	3.92^{f}	96.53^{a}	11.01^{cd}	7.37^{c}
	SE	0.22	0.60	0.25	0.19
Mean for variety	DT12	8.43^{g}	92.17^{e}	11.68^{e}	7.61^{e}
	DT26	6.63^{h}	94.47^{d}	11.13^{f}	7.54^{e}
	SE	0.11	0.30	0.14	0.11
Mean for harvest	T1	9.801^{i}	89.0^{h}	10.15^{i}	6.42^{h}
	T2	8.74^{j}	92.4^{g}	11.19^{h}	7.29^{g}
	T3	6.98^{k}	95.8^{f}	12.51^{g}	8.46^{f}
	T4	4.59^{l}	96.07^{f}	11.78^{h}	8.14^{f}
	SE	0.15	0.42	0.18	0.14

Note: T1, T2, T3, T4: harvesting stages at physiological maturity of 60, 70, 80, and 90% respectively; SD1: percentage of seed damage; P100: weight of 100 seeds; PG1: percentage of germination; HL1: hypocotyl length; RL1: root length. Mean within a column followed by the same superscript letter is not significantly different at p=0.05 according to Tukey test.

3.2. Seed loss and quality, and thresh efficiency by mechanisation at early harvesting stages and postharvest ripening

Generally, variety, early harvesting stages, and number of days of postharvest ripening had significant effects on seed losses depending on cases. There were significant differences between DT12 and DT26 for seed loss at threshing (SL2), but no differences for seed shattering loss (SL1) and total seed loss (SL3). Harvesting stages significantly affected all seed losses (SL1-SL3). The number of days of postharvest ripening also caused significant differences in all seed losses except for seed loss at threshing (Supplemental Table 2).

Seed losses occurred with higher percentages at postharvest ripening (around 2-5%) than at threshing (around 1-2%) (Table 3). The total seed losses across varieties, early harvesting stages, and number of days of postharvest ripening varied from 2.45 to 7.87%. Early harvest resulted in fewer total seed losses, such as 4.06% at 60% maturity (T1), 6.21% at 70% maturity (T2), and 7.16% at 80% maturity (T3). Similarly, fewer days of postharvest ripening provided significantly fewer total seed losses at 1-day than those at 2- and 3-days.

There were significant differences in seed damage (SD2) among the three early harvesting stages and number of days of postharvest ripening (Supplemental Table 2). Obviously, later harvest at physiological maturity of 80% and 3 d of postharvest ripening resulted in the least seed damage with 5.36 and 6.19%, respectively. Seed damage was not different between DT12 and DT26. Similar to Experiment 1, the weight of 100 seeds was not affected by variety, harvesting stages, or number of days of postharvest ripening.

Supplement Table 2. ANOVA for effects of early harvesting stages and postharvest ripening on seed losses and quality when applying mechanical harvesting and threshing.

Traits	Source of variation	df	SS	MS	F-value	P
SL1	Var	1	0.06	0.056	0.128	0.72288
	T	2	41.82	20.91	47.68	1.36E-10***
	D	2	8.35	4.176	9.522	0.00052***
	Var:T	2	1.84	0.92	2.098	0.13828
	Var:D	2	0.97	0.487	1.11	0.34127
	T:D	4	3.52	0.88	2.006	0.11578
	Var:T:D	4	4.04	1.01	2.304	0.07842
SL2	Var	1	1.4114	1.4114	15.3362	0.000412***
	T	2	9.1983	4.5992	49.9762	7.53E-11***
	D	2	0.4227	0.2114	2.2967	0.115992
	Var:T	2	0.0602	0.0301	0.3273	0.723105
	Var:D	2	1.0633	0.5317	5.7772	0.006921***
	T:D	4	2.2107	0.5527	6.0055	0.00091
	Var:T:D	4	2.454	0.6135	6.6666	0.00045***
SL3	Var	1	2.132	2.132	2.9257	0.096293
	T	2	90.898	45.449	62.3657	4.21E-12***
	D	2	12.635	6.318	8.6692	0.000907***
	Var:T	2	1.828	0.914	1.2542	0.29816
	Var:D	2	4.019	2.009	2.7574	0.077666
	T:D	4	8.436	2.109	2.8941	0.036501*
	Var:T:D	4	12.073	3.018	4.1417	0.007708**
SD2	Var	1	0.0541	0.0541	0.3621	0.55136
	T	2	18.5777	9.2889	62.1064	4.45E-12***
	D	2	5.2804	2.6402	17.6526	5.52E-06***
	Var:T	2	0.1874	0.0937	0.6267	0.540436
	Var:D	2	0.4724	0.2362	1.5791	0.220904
	T:D	4	3.1664	0.7916	5.2928	0.002007**
	Var:T:D	4	1.3995	0.3499	2.3393	0.074868
P100	Var	1	3.276	3.2757	2.0934	0.15709
	T	2	1.388	0.6941	0.4436	0.64541
	D	2	1.263	0.6313	0.4034	0.67117
	Var:T	2	0.209	0.1047	0.0669	0.93538
	Var:D	2	2.975	1.4877	0.9508	0.39648
	T:D	4	16.046	4.0116	2.5637	0.05591
	Var:T:D	4	19.963	4.9908	3.1894	0.02505*
PG2	Var	1	4.3	4.3	0.359	0.549364
	T	2	1496.6	748.28	62.4449	<2.20E-16***
	D	2	124	62.01	5.1748	0.006017**
	Var:T	2	116.3	58.14	4.8521	0.008247**
	Var:D	2	81.6	40.78	3.4033	0.034164*
	T:D	4	130.8	32.7	2.7291	0.028852*
	Var:T:D	4	48.2	12.06	1.0066	0.403713
HL2	Var	1	1465.6	1465.61	311.5935	<2.20E-16***
	T	2	144.9	72.43	15.3997	2.67E-07***
	D	2	11.3	5.65	1.2011	0.301354
	Var:T	2	319.8	159.89	33.993	6.04E-15***
	Var:D	2	67.7	33.85	7.1973	0.000794***
	T:D	4	83.7	20.93	4.4501	0.001449**
	Var:T:D	4	34.2	8.56	1.82	0.122849
RL1	Var	1	93.3	93.251	20.5953	6.46E-06***
	T	2	69.8	34.895	7.7068	0.000481***
	D	2	47.4	23.698	5.2338	0.005501**
	Var:T	2	7.1	3.543	0.7826	0.457556
	Var:D	2	10.3	5.171	1.1421	0.319609
	T:D	4	91.9	22.976	5.0744	0.00048***
	Var:T:D	4	59.8	14.943	3.3002	0.010716*

Note: significant codes: 0(***): 0.001; (**): 0.01; (*): 0.05; '.': 0.1.; ' ': 1. Var: variety; T: harvesting stages at physiological maturity of 60, 70, and 80% respectively; D: days of postharvest ripening of 1, 2, and 3 days; SL1: percentage of seed-shattering loss when applying postharvest ripening; SL2: percentage of seed loss by threshing; SL3: percentage of total seed loss; SD2: percentage of seed damage after threshing; PG2: percentage of seed germination; HL2: hypocotyl length; RL2: root length; P100: weight of 100 seeds.

Table 3. Effects of early harvesting stages and days of postharvest ripening on seed losses of soybean when applying mechanical harvesting and threshing.

Variety	Harvesting stages	Days of postharvest ripening	SL1 (%)	SL2 (%)	SL3 (%)	SD2 (%)	P100 (g)
DT12	T1	D1	1.89^{d}	0.90^{de}	2.45^{f}	10.30^{a}	14.1
		D2	3.08^{abcd}	1.30^{cde}	4.44^{def}	7.97^{bcde}	13.2
		D3	3.82^{abcd}	1.46^{bcde}	5.33^{abcdef}	7.33^{bcdef}	13.1
	T2	D1	3.19^{abcd}	1.51^{bcde}	4.75^{cdef}	7.10^{cdefg}	14.5
		D2	4.23^{abc}	1.77^{abcd}	6.00^{abcd}	8.47^{abcd}	13.2
		D3	4.8^{a}	2.1^{abc}	6.89^{abcd}	6.47^{defgh}	12.9
	T3	D1	4.13^{abc}	1.93^{abc}	6.30^{abcd}	6^{efgh}	12.6
		D2	5.25^{a}	2.61^{a}	7.87^{a}	5.53^{fgh}	13.8
		D3	4.26^{abc}	2.20^{abc}	6.46^{abcd}	5.1^{gh}	13.0
DT26	T1	D1	2.4^{bcd}	0.90^{ab}	4.78^{bcdef}	9.10^{abc}	14.8
		D2	2.07^{cd}	0.76^{e}	2.85^{ef}	9.33^{ab}	13.6
		D3	2.96^{abcd}	1.46^{bcde}	4.49^{def}	6.9^{defg}	13.7
	T2	D1	3.81^{abcd}	1.51^{abc}	5.7^{abcde}	8.23^{abcd}	12.2
		D2	5.17^{a}	2.54^{a}	7.66^{abc}	8.23^{abcd}	13.8
		D3	4.13^{abc}	2.09^{abc}	6.28^{abcd}	6.9^{defg}	15.6
	T3	D1	4.48^{ab}	1.93^{abc}	6.78^{abcd}	5.77^{fgh}	13.7
		D2	5.25^{a}	2.57^{a}	7.78^{a}	5.3^{fgh}	15.1
		D3	5.16^{a}	2.20^{a}	7.76^{ab}	4.47^{h}	12.2
	SE		0.44	0.18	0.56	0.41	0.74
Mean for variety	DT12		3.87^{e}	1.75^{g}	5.61^{f}	7.14^{i}	13.4
	DT26		3.93^{e}	2.08^{f}	6.0^{f}	7.14^{i}	13.9
	SE		0.15	0.06	0.19	0.14	0.25
Mean for harvesting stages	T1		2.70^{h}	1.37^{j}	4.06^{i}	8.49^{j}	13.8
	T2		4.22^{g}	2.0^{j}	6.21^{h}	7.57^{j}	13.7
	T3		4.79^{f}	2.37^{h}	7.16^{g}	5.36^{k}	13.4
	SE		0.18	0.08	0.23	0.17	0.30
Mean for postharvest ripening	D1		3.35^{j}	1.80^{k}	5.13^{k}	7.75^{l}	13.6
	D2		4.17^{j}	1.93^{k}	6.10^{j}	7.47^{l}	13.8
	D3		4.19^{i}	2.01^{k}	6.20^{j}	6.19^{m}	13.4
	SE		0.18	0.08	0.23	0.17	0.30

Note: T1, T2, T3: harvesting stages at physiological maturity of 60, 70, and 80% respectively; D1, D2, D3: 1, 2, and 3 days of postharvest ripening respectively; SL1: percentage of seed shattering loss when applying postharvest ripening; SL2: percentage of seed loss by threshing; SL3: percentage of total seed loss; SD2: percentage of seed damage after threshing. Mean within a column followed by the same superscript letter are not significantly different at p=0.05 according to Tukey test.

Table 4. Effects of early harvesting stages and days of postharvest ripening on soybean seed quality.

Variety	Harvesting stages	Days of postharvest ripening	PG2 (%)	HL2 (cm)	RL2 (cm)
DT12	T1	D1	87.5^{fg}	10.7^{de}	6.6^{bcd}
		D2	87.0^{g}	10.8^{cd}	7.0^{abcd}
		D3	90.4^{bcdefg}	10.5^{def}	7.1^{abcd}
	T2	D1	91.3^{abcde}	8.8^{g}	6.9^{bcd}
		D2	90.7^{abcdef}	9.1^{fg}	6.9^{abcd}
		D3	92.0^{abcde}	9.2^{efg}	5.8^{d}
	T3	D1	93.9^{a}	10.8^{d}	6.0^{cd}
		D2	93.2^{abc}	12.6^{ab}	8.0^{ab}
		D3	93.4^{ab}	10.8^{de}	7.9^{ab}
DT26	T1	D1	89.3^{efg}	13.1^{ab}	6.8^{bcd}
		D2	89.8^{defg}	13.2^{ab}	7.8^{ab}
		D3	90.2^{bcdefg}	12.9^{ab}	7.4^{abc}
	T2	D1	91.5^{abcde}	13.1^{ab}	7.5^{ab}
		D2	89.8^{cdefg}	12.3^{bc}	7.3^{abc}
		D3	91.1^{abcde}	13.9^{a}	7.4^{abc}
	T3	D1	93.2^{abc}	12.4^{b}	7.6^{ab}
		D2	92.8^{abcd}	12.4^{b}	7.8^{ab}
		D3	92.7^{abcd}	12.9^{ab}	8.3^{a}
	SE		0.7	0.3	0.3
Mean for variety	DT12		91.1^{h}	10.4^{i}	6.9^{f}
	DT26		91.2^{h}	12.9^{h}	7.5^{e}
	SE		0.2	0.1	0.1
Mean for harvesting stages	T1		89^{k}	11.9^{j}	7.1^{h}
	T2		91.1^{j}	11.1^{k}	6.9^{h}
	T3		93.2^{i}	12^{j}	7.6^{g}
	SE		0.3	0.1	0.1
Mean for postharvest ripening	D1		91.1^{l}	11.5^{l}	6.9^{j}
	D2		90.6^{l}	11.7^{l}	7.4^{i}
	D3		91.6^{l}	11.7^{l}	7.3^{ij}
	SE		0.3	0.1	0.1

Note: T1, T2, T3: harvesting stages at physiological maturity of 60, 70, and 80% respectively; D1, D2, D3: 1, 2, and 3 days of postharvest ripening respectively; PG2: percentage of seed germination after 7 days; HL2: hypocotyl length after 7 days of germination; RL2: root length after 7 days of germination; P100: weight of 100 seeds. Mean within a column followed by the same superscript letter are not significantly different at p=0.05 according to Tukey test.

There were significant differences in seed germination and seedling development after 7 days of germination (Table 4).

DT12 and DT26 had a similar percentage of germination (PG2) (91.1 and 91.2%, respectively) but DT26 had the vigour of seedlings with longer hypocotyl length HL2 (12.9 cm) and root length RL2 (7.5 cm). Seed germination significantly increased from 89.0% at 60% maturity to 93.2% at 80% maturity. Hypocotyl and root lengths were also longest at 80% maturity with 12.0 and 7.6 cm, respectively. Two or three days of postharvest ripening also resulted in better seedling development (Table 4).

4. Discussion

Harvesting time is a critical step in soybean seed production because it affects both yield losses and seed quality. The common practice is to harvest soybeans at a physiological maturity of 90% when 90% of the pods on the plant turn brown. This harvesting time results in the highest yield, germination percentage, vigour, and fat content than a delayed one and two weeks after physiological maturity [1, 6, 13]. Soybeans are also suggested to be harvested as soon as seed moisture is suitable for mechanisation (12-14% moisture content) [1]. Early harvest stage, such as R7 (beginning maturity - one normal pod on the main stem reaching mature colour) also caused low seed germination percentage (76%) and vigour. In addition, the seed quality of various varieties responded differently to harvesting stages. Similar to previous studies, both experiments in this study generally showed a lower seed germination percentage at early harvesting (60-70%) than that at physiological maturities of 80 or 90%. Seedling development was also less vigorous with shorter hypocotyl and root length (Table 2, Table 4). Interestingly, there seemed to be no significant differences between harvesting stages of 80 and 90% for those measured characteristics (Table 2).

Yield losses due to seed-shattering losses in nature can be significant from 49.4 to 63.2%. Seed-shattering losses when delaying harvesting by one and two weeks after physiological maturity could reach 20 and 31.22% of the total seed weight, respectively [6]. These experiments also indicated that seed-shattering losses started occurring at early harvest stages of 80% and occurred not only on the field before harvest but also at harvest, during drying and postharvest ripening, and seed threshing (Table 1, Table 3). As a consequence, seed yield was reduced with later harvest stages of 80 and 90% maturity. A. Toledo, et al. (2008) [26] summarised the causes for losses from the action of mechanical harvesting of soybean such as losses due to deficiency of cutting height (remaining lodged to the stalk), the threshing system for grains maintained inside residuals, and the separation system. With different sizes of sample areas (1, 2, and 3 m^2) for quantifying soybean losses in mechanical harvesting, [27] found total losses of 3.61-3.77 kg/ha[1]. This study also showed similar losses at harvest of 1.27-2.38 g/m^2 at harvest stages of 80 and 90% physiological maturity, respectively, for sample areas of 2 m^2 (Table 2).

Early harvest for soybeans is sometimes necessary for soybean production to avoid adverse conditions, especially humid and wet conditions in winter seasons in northern Vietnam. This study showed that early harvest stages required postharvest ripening treatment to minimize adverse effects on seed damage and quality. The number of the postharvest ripening days increased as soybeans were harvested earlier. Soybeans harvested early at 60% maturity required at least 3 days of postharvest ripening so that pods and stems turned brown and became drier with the leaves dried and dropping off the stem. This is preferred for mechanical seed threshing since green leaves and stems cause clogs in the machine. Soybeans harvested at 70% maturity required 1-2 days of postharvest ripening for plants to be sufficiently dried before threshing. Similarly, soybeans harvested at 80% maturity only required 1 day of postharvest ripening to reach the ideal physiological maturity of 90%.

Comparable to Experiment 1, seed losses increased as the soybeans were harvested at stages closer to physiological maturity. However, the total percentage of seed losses was much lower (2.16-3.57%) than in other studies (Table 3) [6]. In contrast, seed damage significantly decreased at harvesting stages of 80 and 90% maturity (Table 2) and with more days of postharvest ripening (Table 4). Thus, postharvest ripening treatment is an effective method to reduce seed damage and ensure seed quality if early harvest stages of soybeans are necessary.

5. Conclusions

In conclusion, harvesting stages affect seed-shattering losses and seed quality. Harvesting stages of 90% maturity provide the best seed quality. However, early harvest at a physiological maturity of 80% can also be practical to avoid adverse weather conditions. In that case, at least one day of postharvest ripening should be applied. Thus, careful monitoring of the harvest stages and ripening of different soybean varieties should help to minimize seed damage and ensure seed quality, especially in a practice where farmers apply mechanical harvesting and threshing.

CRediT author statement

Thi Thuy Hang Vu: Writing and Editing the manuscript, Data analysis; Ngoc Thang Vu: Data collection, Data analysis; Thi Tuyet Cham Le: Experimental design, Writing manuscript; Thi Ngoc Pham: Data collection, Data analysis.

ACKNOWLEDGEMENTS

The authors would like to thank the financial support from Thai Binh Department of Science and Technology, Thai Binh province, Vietnam and also the support by Vietnam National University of Agriculture for their contribution to this research project.

COMPETING INTERESTS

The authors declare that there is no conflict of interest regarding the publication of this article.

REFERENCES

[1] J.M. Filho, H.M.C.P. Chamma, J.R.R. Casagrande, et al. (1994), "Effect of harvesting time on seed physiological quality, chemical composition and storability of soybeans", *Sci. Agric.*, **51(2)**, pp.298-304, DOI: 10.1590/S0103-90161994000200016.

[2] F.B.F.D. Lima, M.A.F.D. Silva, R.P.D. Silva (2017), "Quality of mechanical soybean harvesting at two travel speeds", *Eng. Agric.*, **37(6)**, pp.1171-1182, DOI: 10.1590/1809-4430-Eng.Agric.v37n6p1171-1182/2017.

[3] W.R. Fehr, C.E. Caviness, D.T. Burmood, et al. (1971), "Stage of development descriptions for soybeans, *Glycine max* (L.) Merrill1", *Crop. Sci.*, **11(6)**, pp.929-931, DOI: 10.2135/cropsci1971.0011183X001100060051x.

[4] D.M. Tekrony, D.B. Egli, J. Balles, et al. (1979), "Physiological maturity in soybeans", *Agron. J.,* **71**, pp.771-775, DOI: 10.2134/agronj1981.00021962007300030034x.

[5] W.R. Fehr, C.E. Caviness (1977), *Stages of Soybean Development*, Special Report 87, Agriculture and Home Economics Experiment Station, Iowa State University of Science and Technology, 13pp.

[6] O.T. Isaac, B. Banful, S. Amoah, et al. (2016), "Effects of harvesting stages on seed quality characteristics of three soybean (*Glycine max* (L.) Merrill) varieties", *J. Sci. Eng. Res.*, **3(4)**, pp.326-333.

[7] S.N. Vasudevan, J.S. Sudarshan, M.B. Kurdikeri, et al. (2008), "Influence of harvesting stages on seed yield and quality in Fenugreek", *Karnataka J. Agric. Sci.*, **21(1)**, pp.122-124, DOI: 10.15302/J-FASE-2017196.

[8] D.F. Miles, D.M. TeKrony, D.B. Egli (1988), "Changes in viability, germination, and respiration of freshly harvested soybean seed during development", *Crop Sci.*, **28(4)**, pp.700-704, DOI: 10.2135/cropsci1988.0011183X002800040030x.

[9] R.L. Obendorf, E.N. Ashworth, G.T. Rytko (1980), "Influence of seed maturation and germinability in soybean", *Crop Sci.*, **20(4)**, pp.483-486, DOI: 10.2135/cropsci1980.0011183X002000040015x.

[10] A.M. Zuffo, J.G. Aguilera, E.R. Carvalho, et al. (2020), "Harvest times with chemical desiccation and the effects on the enzymatic expression and physiological quality of soybean seeds", *Rev. Caatinga*, **33(2)**, pp.361-370, DOI: 10.1590/1983-21252020v33n209rc.

[11] F.O. Diniz, M.S. Reis, L.A.S. Dias, et al. (2013), "Physiological quality of soybean seeds of cultivars submitted to harvesting delay and its association with seedling emergence in the field", *J. Seed Sci.*, **35(2)**, pp.147-152, DOI: 10.17221/512/2020-PSE.

[12] A.M. Zuffo, J.M.Z. Junior, E.R. Carvalho, et al. (2017), "Physiological and enzymatic changes in soybean seeds submitted to harvest delay", *Pesqui. Agropecu. Trop.*, **47(4)**, pp.488-496, DOI: 10.1590/1983-40632017v4749811.

[13] I.M, Ali, R. Nulit, M.H. Ibrahim, et al. (2018), "Effect of delay harvest on seed quality and germination of three varieties of soybean (*Glycine max*) seeds", *Plant Arch.*, **18(2)**, pp.1961-1966.

[14] R.N. Tripathi, N. Nath, A.P. Gandhi (2009), "Effect of time of harvesting on physico-chemical characteristics of soybean (*Glycine max* M)", *As. J. Food Ag-Ind.*, **2(1)**, pp.44-50, DOI: 10.20546/ijcmas.2017.604.136.

[15] V. Mathias, C.M.M. Coelho, J. Garcia (2019), "Soluble protein as indicative of physiological quality of soybean seeds", *Rev. Caatinga*, **32(3)**, pp.730-740, DOI: 10.1590/1983-21252019v32n317rc.

[16] A.M. Gillen, J.R. Smith, A. Mengistu, et al. (2012), "Effects of maturity and on germination and vigour of soybean seed of near-isogenic lines", *Crop Sci.*, **52(6)**, DOI: 10.2135/cropsci2011.10.0566.

[17] R. Narayan, G.S. Chauhan, N.S. Verma (1988), "Changes in the quality of soybean during storage. Part 1 - Effect of storage on some physic-chemical properties of soybean", *Food. Chem.*, **27(1)**, pp.12-23, DOI: 10.1016/0308-8146(88)90032-5.

[18] R.D. Ennen (2011), *Earlier Harvest and Drying of Soybean Seed Within Intact Pods Maintain Seed Quality*, M.Sc. Diss., Dept. Agronomy., Iowa State Uni., Iowa, United States, 62pp.

[19] N.H. Samarah, R.E. Mullen, S. Goggi, et al. (2009), "Effect of drying treatment and temperature on soybean seed quality during maturation", *Seed Sci. Technol.*, **37(2)**, pp.469-473, DOI: 10.15258/sst.2009.37.2.20.

[20] F.C. Kryzanowski, S.H. West, J.D.B.F. Neto (2006), "Drying soybean seed using air ambient temperature at low relative humidity", *Rev. Bras. Sementes.*, **28(2)**, pp.77-83, DOI: 10.1590/S0101-31222006000200010.

[21] V. Rafael, R.N.O. da Silva, A.P. Nadal, et al. (2019), "Harvest delay, storage and physiological quality of soybean seeds", *Journal of Seed Science*, **41(4)**, pp.506-513, DOI: 10.1590/2317-1545v41n4222413.

[22] H.V. Khai, M. Yabe (2013), "The comparative advantage of soybean production in Vietnam: A policy analysis matrix approach", *A Comprehensive Survey of International Soybean Research: Genetics, Physiology, Agronomy and Nitrogen Relationships*, pp.161-179, DOI: 10.5772/51000.

[23] E. Muresanu, R. Marginean (2012), "The new competitive soybean varieties created at agricultural research and development turda", *Bulletin UASVM Agriculture.*, **69(1)**, pp.330-332, DOI: 10.15835/buasvmcn-agr:8711.

[24] M.B. Beikufner, H.D. Trautz, I. Kuhling (2019), "Comparative harvest efficiency of soybeans between cropping systems affected by first pod height and plant length", *Org. Farming*, **5(1)**, pp.3-13, DOI: 10.12924/of2019.05010003.

[25] N.T. Vu, T.T.H. Vu, T.T.C. Le, et al. (2020), "Effect of soil preparation technique in mechanization on growth and yields of soybean in autumn - winter season at Hung Ha, Thai Binh province", *J. Viet Agric. Sci. Tech.*, **6(115)**, pp.26-31 (in Vietnamese).

[26] A. Toledo, R.A. Tabile, R.P. Silva, et al. (2008), "Characterisation of losses and distribution of vegetation cover in mechanised soybean harvesting", *Eng. Agricola*, **28(4)**, pp.710-719, DOI: 10.1590/S0100-69162008000400011 (in Portuguese).

[27] A.L. Junior, R.P. Silva, M.T. Cassia, et al. (2014), "Influence of the sample area in the variability of losses in the mechanical harvesting of soybeans", *Eng. Agricola*, **34(1)**, pp.74-85, DOI: 10.1590/S0100-69162014000100009.

DOI: 10.31276/VJSTE.65(3).75-79

Several prognosis factors of severe pertussis in children treated at Vietnam National Children's Hospital (2019-2020)

Do Thi Thuy Nga[1*], Nguyen Manh Cuong[2], Phung Thi Bich Thuy[2], Tran Minh Dien[3, 4]

[1]Centre for Tropical Disease, Vietnam National Children's Hospital, 18/879 La Thanh Street, Lang Thuong Ward, Dong Da District, Hanoi, Vietnam
[2]Department of Pediatrics, Military Hospital 103, Vietnam Military Medical University, 261 Phung Hung Street, Phuc La Ward, Ha Dong District, Hanoi, Vietnam
[3]Department of Molecular Biology of Infectious Diseases, Vietnam National Children's Hospital, 18/879 La Thanh Street, Lang Thuong Ward, Dong Da District, Hanoi, Vietnam
[4]Vietnam National Children's Hospital, 18/879 La Thanh Street, Lang Thuong Ward, Dong Da District, Hanoi, Vietnam

Received 11 May 2023, revised 21 June 2023; accepted 23 June 2023

Abstract:

A prospective, descriptive study was conducted on 382 pediatric patients diagnosed with pertussis at Vietnam National Children's Hospital over a two-year period, from January 1st, 2019, to December 31st, 2020. Of all patients participating in this study, children with severe conditions accounted for 30.1% (115/382). Several factors were found to be associated with the risk of this condition with odds ratios (OR) and 95% confidence intervals (CI), including a decrease in the duration of the onset phase by 5 days [OR 1.53, 95% CI: 1.002-2.34], fever [2.49, 1.18-5.24], cyanosis [9.59, 2.9-31.7], pneumonia [14.45, 6.06-34.5], pulmonary hypertension [4.15, 1.02-16.83], an increase of 10 g/l in white blood cell (WBC) count in the full blood count (FBC) test [1.39, 1.05-1.84], a 5-cycle reduction in Cycle threshold (Ct) value in the pertussis real-time PCR test [1.36, 1.01-1.84], and superinfection [3.94, 1.84-8.48 times]. A WBC count in FBC of ≥30 g/l could be used as a prognostic factor for the risk of severe illness condition (sensitivity 46.1%, specificity 90.6%), the requirement for mechanical ventilation (sensitivity 57.1%, specificity 88.5%), and mortality (sensitivity 100%, specificity 91%).

Keywords: **children, severe pertussis, Vietnam National Children's Hospital.**

Classification number: **3.2**

1. Introduction

Pertussis is an acute respiratory tract infection caused by Bordetella pertussis. Despite the discovery of the pertussis vaccine nearly a century ago, the disease has never been completely under control. According to the World Health Organization (WHO) in (2019) [1], there were approximately 24.1 million annual cases of infection, resulting in 160,700 deaths among children under 5 years old, with infants accounting for 53% of the recorded deaths. Over the past three decades, reports from many countries have indicated the risk of pertussis outbreaks, even in countries with high vaccination coverage rates [2]. This re-emerging disease has posed significant challenges to the public health system [3]. Furthermore, the illness itself, along with severe disease conditions and intractable complications such as severe pneumonia and pulmonary hypertension, has placed a substantial burden on medical personnel [4, 5].

In Vietnam, pertussis has not been completely controlled. In fact, since 2015, the number of pertussis cases has been steadily increasing [6-8]. The fatality rate of pertussis in the inpatient population is estimated to be around 1.5-2.8% [9-11], with deaths predominantly occurring in infants under 3 months of age [9, 10]. Identifying risk factors for severe conditions helps clinicians accurately prognose each patient, enabling timely intervention and reducing the risk of fatal outcomes. Considering these factors, the primary objective of this study is to "Identify prognostic factors of severe pertussis in children treated at Vietnam National Children's Hospital (2019-2020)".

2. Participants and method

2.1. Participants

The study included paediatric patients under 16 years old who were diagnosed with pertussis and received treatment at the National Children's Hospital between January 1st, 2019, and December 31st, 2020.

The diagnosis of pertussis was based on the criteria outlined by the Global Pertussis Initiative 2011 (GPI 2011) and a positive pertussis real-time PCR test.

[*]Corresponding author: Email: dr.ngado83@gmail.com

Exclusion criteria: Participants whose parents or caregivers did not consent to participate in the study.

2.2. Method

Study design: This was a prospective descriptive study of a case series.

Sampling method: Convenience sampling was employed to collect a sample size of 382 pediatric patients.

Severe pertussis was defined as follows: Children with respiratory failure requiring continuous oxygen supplementation for at least 24 hours (excluding cases where children only required oxygen support during paroxysmal coughing episodes and stable children without oxygen needs outside of coughing episodes), children requiring endotracheal intubation and mechanical ventilation, and/or children with circulatory collapse and multiorgan failure necessitating additional resuscitation measures such as blood transfusion, dialysis, or extracorporeal membrane oxygenation (ECMO).

Processed software: The data were processed using SPSS 22.0, a statistical software.

Ethical considerations: The study received approval from the Medical Ethics Committee of the Vietnam National Children's Hospital and the National Institute of Malariology, Parasitology, and Entomology.

3. Results

3.1. Rate of severe disease

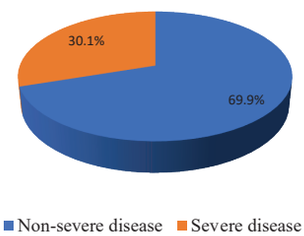

Fig. 1. Severe disease rate.

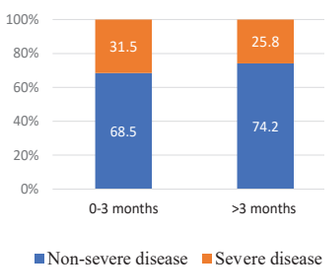

Fig. 2. Severe disease rate by age group.

The rate of children with severe pertussis was 30.1% (115/382) (Fig. 1), with infants aged 0-3 months accounting for 31.5% (91/289). In the group of children over 3 months old, the rate was 25.8% (24/93) (Fig. 2). However, this difference was not statistically significant (p=0.3>0.05).

3.2. Factors associated with severe disease conditions

Relationships between epidemiological characteristics and severe disease: Physiological factors such as preterm birth, malnutrition, underlying medical conditions, and lack of pertussis vaccination are likely to increase the risk of severe illness by 2.5 (95% CI: 1.1-5.6), 6.6 (95% CI: 1.7-25.3), 2.7 (95% CI: 1.3-5.7), and 3.3 (95% CI: 1.4-7.5) times, respectively (Table 1).

Table 1. The relationship between epidemiological characteristics and severe disease.

Features	Severe disease (n=115)		Non-severe disease (n=267)		p	OR (95% CI)
	Number	*%*	*Number*	*%*		
Premature birth	13	11.3	13	4.9	0.026	2.5 (1.1-5.6)
Malnutrition	8	7.0	3	1.1	0.04	6.6 (1.7-25.3)
Base diseases	16	13.9	15	5.6	0.008	2.7 (1.3-5.7)
No pertussis vaccination	108	93.9	220	82.4	0.005	3.3 (1.4-7.5)

Clinical symptoms and complications: Table 2 demonstrates that symptoms of fever, cyanotic cough, apnoea, convulsions, and complications of pneumonia and pulmonary arterial hypertension are associated with an increased risk of severe pertussis (p<0.01).

Table 2. Symptoms and complications associated with severe disease.

Symptom	Severe disease (n=115)		Non-severe disease (n=267)		p	OR (95% CI)
	Number	*%*	*Number*	*%*		
Fever	50	43.5	61	22.8	<0.001	2.6 (1.6-4.1)
Stridor	7	6.1	16	6.0	0.9	
Cyanotic cough	110	95.7	157	58.8	<0.001	15.4 (6.1-39.0)
Apnoea	29	27.8	13	4.9	<0.001	6.6 (3.3-13.2)
Convulsion	15	13.0	2	0.7	<0.001	19.9 (4.5-88.5)
Pneumonia	107	93.0	79	29.6	<0.001	31.8 (14.8-68.4)
Pulmonary arterial hypertension	30	26.1	7	2.6	<0.001	13.1 (5.6-30.9)

Subclinical signs: Table 3 presents a comparison of average leukocyte count, lymphocyte count, neutrophil count, platelet count, and CRP levels between children with severe and non-severe disease, which revealed significantly higher values in the severe disease group (p<0.01). Thus, these results indicate that an increase in these indicators is associated with the severity of the disease in children.

Table 3. Complete blood count and indicators related to severe disease.

Indicator	Severe disease (n=115)		Non-severe disease (n=267)		p
	$\bar{x}$	*SD*	$\bar{x}$	*SD*	
WBC(G/1)	28.6	19.1	17.1	8.9	<0.001
Lym. (G/1)	16.3	9.9	11.9	6.9	<0.001
Neut (G/1)	8.4	7.7	3.4	2.7	<0.001
PLT (G/1)	507.9	181.0	457.4	153.2	0.006
CRP (mg/l)	13.4	30.3	2.5	9.1	<0.001
Ct (cycle threshold)	23.8	6.2	26.1	5.9	0.001

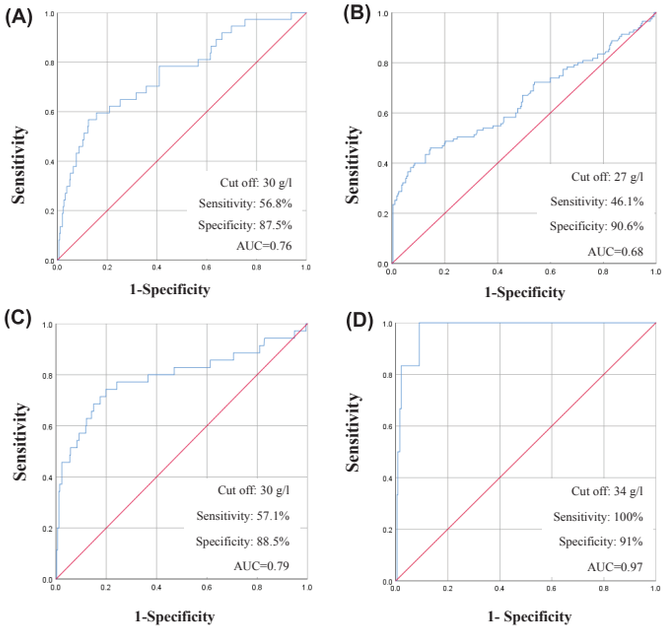

Fig. 3. The ROC curve of the white blood cell count predicting. (A) The risk of pulmonary hypertension; **(B)** The risk of severe disease; **(C)** The risk of mechanical ventilation; **(D)** The risk of death. Note: Cut off: cut point; AUC: area under the curve.

The peripheral blood total leukocyte count has demonstrated predictive value for pulmonary hypertension, severe disease, mechanical ventilation, and mortality in children with pertussis (Fig. 3): An increase in white blood cell count of more than 30 g/l was found to predict the risk of developing pulmonary hypertension, with a sensitivity of 56.8% and specificity of 87.5%. A white blood cell count of ≥27 g/l could predict the risk of severe pertussis, with a sensitivity of 46.1% and specificity of 90.6%. A white blood cell count of ≥30 g/l was shown to predict the risk of requiring mechanical ventilation, with a sensitivity of 57.1% and specificity of 88.5%. A white blood cell count of ≥34 g/l was identified as a predictor for mortality due to pertussis, with a sensitivity of 100% and specificity of 91%.

Table 4. Cycle threshold (Ct) values associated with the complications of pulmonary hypertension, severe illness, risk of mechanical ventilation, and mortality.

Ct value/(-5)		B	p	OR (95% CI)
pH	Ct/(-5)	0.723	<0.001	2.06 (1.47-2.88)
Severe disease	Ct/(-5)	0.326	0.001	1.39 (1.15-1.67)
Mechanical ventilation	Ct/(-5)	0.628	<0.001	1.87 (1.35-2.61)
Mortality	Ct/(-5)	0.578	0.134	

Table 4 demonstrates that a low Ct value is associated with an elevated risk of complications, including increased pulmonary arterial pressure, severe pertussis, and the need for mechanical ventilation (p<0.01). Specifically, a 5-cycle reduction in Ct value is associated with: A 2.06-fold increase in the risk of elevated pulmonary arterial pressure (95% CI: 1.47-2.88). A 1.39-fold increase in the risk of severe pertussis (95% CI: 1.15-1.67). A 1.87-fold increase in the risk of requiring mechanical ventilation (95% CI: 1.35-2.61).

Table 5. Other tests.

Indicator	Severe disease			Non-Severe disease			p
	Quantity	$\bar{x}$	*SD*	*Quantity*	$\bar{x}$	*SD*	
Glucose (mmol/l)	79	5.5	1.2	31	5.7	1.1	0.65
NT-proBNP (pmol/l)	39	1373.0	2819.6	15	217.0	552.7	0.019
Troponin(ng/ml)	15	0.236	0.642	11	0.018	0.018	0.20

Table 5 reveals that the average NT-proBNP value in the severe group was 1373.0 pmol/l, whereas in the non-severe group, it was 217 pmol/l. This disparity was statistically significant (p<0.05). Conversely, the average serum glucose and troponin concentrations did not differ significantly between the severe and non-severe groups (p>0.05).

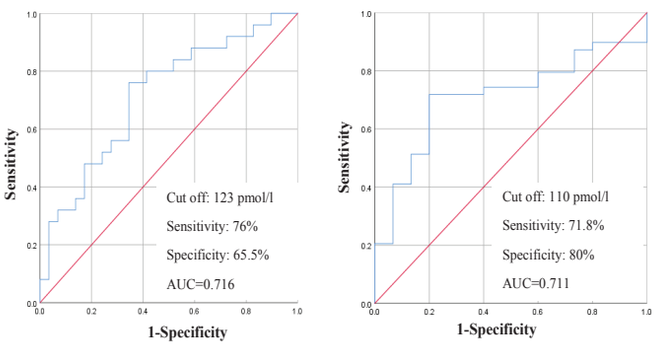

Fig. 4. ROC curve of NT-proBNP serum concentration predicting the risk of pulmonary arterial hypertension complications and severe disease.

The optimal cutoff point of NT-proBNP serum concentration for predicting the risk of pulmonary arterial hypertension in children with pertussis was found to be 123 pmol/l, yielding a sensitivity of 76% and specificity of 65.5%. The area under the ROC curve was 0.716 (95% CI 0.578-0.854). Similarly, the optimal cutoff point of NT-proBNP serum concentration for predicting the risk of severe pertussis was determined to be 110 pmol/l, with a sensitivity of 71.8% and specificity of 80%. The area under the ROC curve was 0.711 (95% CI 0.568-0.854) (Fig. 4).

Superinfection with other microorganisms: Based on the findings presented in Table 6, the proportion of pertussis-infected children with superinfection in the severe disease group was 43.5% (50/115), which was significantly higher than the non-severe disease group, which recorded a rate of 15,0% (40/267) with p<0.01.

Table 6. Superinfection associated with severe disease.

	Severe disease (n=115)	Non-severe disease (n=267)	p	OR (95% CI)
Superinfection	50 (43.5%)	40 (15.0%)	<0.001	4.4 (2.7-7.2)
Non-superinfection	65 (56.5%)	227 (85.0%)		

Determining prognostic factors for the disease through multivariate regression analysis: Multivariable logistic regression analysis revealed the following factors to be associated with severe disease status, with their respective odds ratios (OR) and 95% confidence intervals (CI): Time from onset of symptoms/(-5): [1.53, 1.002-2.34]; Presence of fever: [2.5, 1.18-5.24]; Cyanosis: [9.59, 2.9-31.7]; Pneumonia: [14.45, 6.06-34.5]; Elevated mean pulmonary arterial pressure: [4.15, 1.02-16.83]; Increase of 10 g/l in leukocyte count: [1.4, 1.05-1.84]; Decreased Ct value in Real-time PCR pertussis: [1.36, 1.01-1.84]; Superinfection with other microorganisms: [3.94, 1.84-8.48] (Table 7).

Table 7. Multivariate logistic regression analysis of prognostic factors for severe disease.

Associated factors	B	p	OR (95% CI)
Age (months)	0.027	0.096	1.03 (0.99-1.06)
Onset time/(-5)	0.43	0.049	1.53 (1.002-2.34)
Fever	0.91	0.017	2.49 (1.18-5.24)
Cyanosis	2.26	0.000	9.59 (2.90-31.70)
Apnoea	0.72	0.18	2.05 (0.73-5.78)
Pneumonia	2.67	0.000	14.45 (6.06-34.50)
Pulmonary hypertension	1.42	0.047	4.15 (1.02-16.83)
Leukocytes/(10)	0.33	0.023	1.390 (1.05-1.84)
Ct/(-5)	0.31	0.045	1.36 (1.01-1.84)
Superinfection	1.37	0.000	3.94 (1.84-8.48)

4. Discussion

According to the analysis of the correlation between various epidemiological and clinical characteristics with severe pertussis (as presented in Tables 1 and 2), certain factors stood out as being associated with an increased risk of severe pertussis. These factors included premature birth (gestational age <37 weeks), the presence of underlying diseases, and lack of pertussis vaccination. Additionally, children exhibiting symptoms such as fever, cyanosis, apnoea, seizures, or complications such as pneumonia and pulmonary hypertension were found to be at higher risk of developing severe pertussis.

Laboratory indicators, as shown in Table 3, including total leukocyte count, lymphocyte count, neutrophil count, platelet count, and CRP value, were found to be higher in the severe group compared to the non-severe group, suggesting a correlation between these indicators and the severity of the disease.

By analysing the ROC curve (as shown in Fig. 3), we determined that a white blood cell count of 27 g/l could predict the risk of severe disease with a sensitivity of 46.1% and specificity of 90.6% (AUC 0.68, 95% CI 0.62-0.74). A white blood cell count of 30 g/l could predict the risk of pulmonary arterial hypertension with a sensitivity of 56.8% and specificity of 87.5% (AUC 0.76, 95% CI 0.67-0.84), as well as the risk of requiring mechanical ventilation with a sensitivity of 57.1% and specificity of 88.5% (AUC 0.79, 95% CI 0.69-0.89). Notably, a white blood cell count of 34 g/l could predict the risk of death due to severe respiratory failure with a sensitivity of 100% and specificity of 91% (AUC 0.97, 95% CI 0.94-1). These results align with a study conducted by Tran Minh Dien (2015) [9] on the prognostic factor of severe respiratory failure, which found a significant association between a total blood white blood cell count ≥30.0 g/l and severe illness (OR: 4.1, 95% CI: 2.44-17.25). Similarly, F. Palvo, et al. (2017) [6] reported that an elevated white blood cell count of ≥30,000/mm^3 was associated with severe illness, and they established a cutoff value of 41.2 g/l for predicting the risk of ICU admission with a sensitivity of 64.7% and specificity of 89.5% (AUC 0.75, 95% CI 0.59-0.90). They also found a sensitivity of 100% and specificity of 81.6% in predicting the risk of death (AUC 0.93, 95% CI 0.84-0.98).

Therefore, our study results demonstrate a correlation between white blood cell count and complications such as pulmonary hypertension, severe illness, and death due to pertussis. A white blood cell count of ≥30 g/l has significant prognostic value for severe pertussis. Moreover, a low Ct value in pertussis real-time PCR testing was associated with an increased risk of pulmonary hypertension, severe illness, and the need for mechanical ventilation ($p<0.01$), as indicated in Table 4. This could be explained by the hypothesis that a low Ct value corresponds to a high bacterial load (per unit of the specimen) and an increased concentration of bacterial toxins (in serum or body tissue), thus increasing the risk of severe complications, illness severity, and the need for mechanical ventilation The association between Ct value and severe pertussis has been reported in previous study of R.A. Lewis, et al. (2020) [12]. Additionally, superinfection with other microorganisms was found to increase the risk of severe disease in children, as shown in Table 6.

Another indicator, NT-proBNP, was also found to be associated with severe disease (Table 6). Fig. 4 demonstrates that NT-proBNP levels can contribute to the prediction of the risk of pulmonary hypertension (with a cutoff value of 123 pmol/l, sensitivity of 76%, and specificity of 65.5%) and severe pertussis (with a cutoff value of 110 pmol/l, sensitivity of 71.8%, and specificity of 80%). Although the association between NT-proBNP and pulmonary hypertension has been reported by previous authors [13, 14], the association of NT-proBNP with severe pertussis has received little recognition.

Multivariate logistic regression analysis of factors associated with severe pertussis (Table 7) revealed that a shorter duration of disease onset, symptoms of fever and cyanosis, presence of pneumonia, pulmonary hypertension, elevated white blood cell count, low Ct value, and superinfection with other pathogens were closely associated with severe pertussis.

Previous studies by Tran Minh Dien (2015) [9] identified age (infants ≤3 months old), pneumonia, and peripheral blood leukocyte count ≥30.0 g/l as prognostic factors for severe pertussis (OR: 4.1, 95% CI: 2.44-17.25). C. Liu, et al. (2020) [14] recognised apnoea, elevated white blood cell count, and pulmonary hypertension as key determinants related to severe pertussis in infants under

120 days old. L. Kang, et al. (2022) [5] reported several factors related to severe disease, including age at onset, exposure history to individuals with pertussis, lack of pertussis vaccination, and symptoms such as paroxysmal cough, post-tussive vomiting, cyanotic or flushed face, and fever, which were more common in the severe disease group compared to the non-severe disease group. Furthermore, they found a higher percentage of peripheral blood leukocyte count, CRP levels, and pneumonia complications in the severe disease group.

Therefore, our study's findings align with the trends observed in most previous studies, highlighting several key factors associated with severe pertussis, including fever, cyanosis, pneumonia complications, and an elevated white blood cell count. Additionally, our study investigated the correlation between the duration of infection onset and disease severity. Specifically, we found that if the onset duration was reduced by 5 days, the risk of severe illness would increase by 1.53 times. Notably, pulmonary arterial hypertension was identified as a severe complication associated with an increased risk of severe illness, with 26.1% of children in the severe group and 2.6% in the non-severe group classified as having pulmonary arterial hypertension, and the difference between the groups was statistically significant. The pulmonary arterial hypertension group had a 4.15 times higher risk of severe disease compared to the non-pulmonary arterial hypertension group. The Ct value in the pertussis real-time PCR test was also found to be a factor associated with severe disease, as a 5-cycle reduction in the Ct value increased the risk of severe disease by 1.36 times (95% CI: 1.01-1.84). Furthermore, superinfection with other microorganisms increased the risk of severe disease by 3.94 times (95% CI: 1.84-8.48).

5. Conclusion

Our study revealed that 30.1% of children had severe pertussis, with infants aged ≤3 months accounting for approximately 31.5% of those cases. We identified several key factors associated with an elevated risk of severe pertussis, including a shorter duration of the onset phase, the presence of fever and paroxysmal cyanosis, complications such as pneumonia, elevated pulmonary artery pressure, an increased white blood cell count, a low Ct value on real-time PCR, and superinfection with other pathogens. Notably, a white blood cell count ≥30 g/l served as a significant indicator of an increased risk of pulmonary hypertension, severe illness, the need for mechanical ventilation, and fatality.

CRediT author statement

Do Thi Thuy Nga: Data collection, Conceptualisation, Methodology, Validation, Writing - Review and Editing; Nguyen Manh Cuong: Conceptualisation, Methodology, Validation, Writing; Phung Thi Bich Thuy: Writing - Review and Editing; Tran Minh Dien: Review and Editing.

COMPETING INTERESTS

The authors declare that there is no conflict of interest regarding the publication of this article.

REFERENCES

[1] World Health Organization (2019), "Immunization country profile 2019", https://apps.who.int/immunization_monitoring/globalsummary/countries?countrycriteria%5Bcountry%5D%5B%5D=VNM, accessed 5 May 2022.

[2] K.H.T. Yeung, P. Duclos, E.A.S. Nelson, et al. (2017), "An update of the global burden of pertussis in children younger than 5 years: A modeling study", *The Lancet Infect. Dis.*, **17(9)**, pp.974-980, DOI: 10.1016/S1473-3099(17)30390-0.

[3] D.W. Jackson, P. Rohani (2014), "Perplexities of pertussis: Recent global epidemiological trends and their potential causes", *Epidemiology & Infection*, **142(4)**, pp.672-684, DOI: 10.1017/S0950268812003093.

[4] J.A. Melvin, E.V. Scheller, J.F. Miller, et al. (2014), "*Bordetella pertussis* pathogenesis: Current and future challenges", *Nat. Rev. Microbiol.*, **12**, pp.274-288, DOI: 10.1038/nrmicro3235.

[5] L. Kang, X. Cui, J. Fu, et al. (2022), "Clinical characteristics of 967 children with pertussis: A single-center analysis over an 8-year period in Beijing, China", *Eur. J. Clin. Microbiol. Infect. Dis.*, **41**, pp.9-20, DOI: 10.1007/s10096-021-04336-w.

[6] F. Palvo, A.T. Fabro, M.C. Cervi, et al. (2017), "Severe pertussis infection", *Medicine (Baltimore)*, **96(48)**, DOI: 10.1097/MD.0000000000008823.

[7] National Institute of Hygiene and Epidemiology (2018), "Final report on expanded immunization in 2018", https://www.afro.who.int/sites/default/files/2019-09/Final%202018%20EPI%20Annual%20Report%20for%20WHO%20Ethiopia.pdf, accessed 7 May 2022.

[8] Expanded Program on Immunisation (2022), "Outcome of the expanded vaccination program in Vietnam", http://www.tiemchungmorong.vn/vi/content/thanh-qua.html, accessed 5 May 2022 (in Vietnamese).

[9] T.M. Dien (2015), "Characteristics of pertussis patient at Vietnam National Children's Hospital in 2015", *Vietnam Journal of Preventive Medicine*, **27(6)**, pp.69-76 (in Vietnamese).

[10] H.T.T. Ha, H.H. Mai, D.T. Hai (2019), "Clinical epidemiological characters of pertussis at children aged from under 3 months at Vietnam National Children's Hospital", *Vietnam Journal of Preventive Medicine*, **6**, pp.93-101 (in Vietnamese).

[11] D.T.T. Nga, H.T.T. Ha, D.T. Hong (2016), "Effectiveness for treatment of the pertussis in children at Vietnam National Children's Hospital", *Vietnam Journal of Preventive Medicine*, **5(178)**, pp.57-62 (in Vietnamese).

[12] R.A. Lewis, C. Durrington, R. Condliffe, et al. (2020), "BNP/NT-proBNP in pulmonary arterial hypertension: Time for point-of-care testing?", *European Respiratory Review*, **29(156)**, DOI: 10.1183/16000617.0009-2020.

[13] T.M. Berghaus, J. Kutsch, C. Faul, et al. (2017), "The association of N-terminal pro-brain type natriuretic peptide with hemodynamics and functional capacity in therapy-naive precapillary pulmonary hypertension: Results from a cohort study", *BMC Pulm. Med.*, **17**, DOI: 10.1186/s12890-017-0521-4.

[14] C. Liu, L. Yang, Y. Cheng, et al. (2020), "Risk factors associated with death in infants <120 days old with severe pertussis: A case-control study", *BMC Infect. Dis.*, **20(1)**, DOI: 10.1186/s12879-020-05535-0.

DOI: 10.31276/VJSTE.65(3).80-84

Standardised flavonoid extract from *Diospyros kaki* L.f leaves alleviates high blood pressure and ventricular hypertrophy on cortisone acetate-induced hypertensive rats

Thi Thanh Loan Nguyen[1, 2], Thi Van Anh Pham[2], Thi Xoan Le[1*]

[1]*Department of Pharmacology and Biochemistry, National Institute of Medicinal Materials, 3B Quang Trung, Trang Tien Ward, Hoan Kiem District, Hanoi, Vietnam*
[2]*Department of Pharmacology, Hanoi Medical University, 1 Ton That Tung Street, Khuong Thuong Ward, Dong Da District, Hanoi, Vietnam*

Received 18 November 2022; revised 20 December 2022; accepted 28 December 2022

Abstract:

The current study was designed to investigate the anti-hypertensive effects of a standardised flavonoid extract from *Diospyros kaki* L.f leaves (DK extract) on cortisone acetate-induced hypertensive rats. Hypertension was induced in *Wistar* rats by subcutaneously injecting 2.5 mg cortisone acetate daily and by maintaining the rats on a 1% sodium chloride diet for a period of 28 days. The hypertensive rats were treated daily with DK extract (50 and 100 mg/kg of body weight; p.o.) or captopril (20 mg/kg of body weight; p.o.), a reference drug, for 14 consecutive days. The blood pressure and heart rate of awake rats were measured using a non-invasive tail-cuff method. The heart weight and left ventricular wall thickness of rats were measured. *In vitro* angiotensin-converting enzyme (ACE) inhibition activity of the DK extract and captopril were analysed. DK extract significantly and dose-dependently reduced systolic and diastolic blood pressure in the hypertensive rats. There were no significant changes observed in heart rate. The cortisone acetate-induced hypertensive rats had increased heart weight and left ventricular wall thickness. These actions were attenuated by the treatment of DK extract (100 mg/kg) and captopril. Moreover, DK extract inhibited ACE activity *in vitro* with an IC_{50} of 4.71±0.53 µg/ml. Our findings demonstrate that DK extract exerted anti-hypertensive effects and alleviated ventricular hypertrophy in the cortisone acetate-induced hypertensive rats and these actions occurred at least in part via ACE activity inhibition.

Keywords: **angiotensin-converting enzyme inhibitor, anti-hypertensive effect, *Diospyros kaki* L.f leaves, ventricular hypertrophy.**

Classification numbers: **3.2, 3.3**

1. Introduction

Hypertension is a medical condition characterised by persistently elevated blood pressure in the arteries. This condition is a leading cause of ischemic stroke and a major risk factor for coronary artery disease and myocardial infarction [1]. Globally, the goal is to reduce the prevalence of hypertension by 25% by 2025 [2]. To date, treatments for hypertension aim to reduce not only systolic and diastolic blood pressure but also its long-term complications, such as end-organ damage. First-line pharmacotherapy for hypertension typically involves the use of ACE inhibitors, although their efficacy may be limited in some cases because of side effects such as cough, mild skin itching, and numbness [1]. Therefore, there is growing interest in developing natural source-based antihypertensive drugs.

Persimmon (*Diospyros kaki* L.f) is a plant species belonging to the family *Ebenaceae*. This plant is widely distributed in Asian countries such as China, Japan, Korea, India, and Vietnam. Traditionally, persimmon leaves have been used for medicinal, cosmetic, and health beverage purposes. In particular, persimmon leaf tea is a popular preparation in China and Japan due to its purported ability to lower blood pressure [3]. In a previous study, we demonstrated that a standardised flavonoid extract from *Diospyros kaki* L.f leaves (DK extract) exerted antihypertensive effects in rats with two-kidney one-clip induced hypertension [4]. However, the anti-hypertensive mechanism of DK leaves and its potential effects on cardiac hypertrophy, an important long-term complication of hypertension, have not yet been clarified.

The administration of glucocorticoids together with a high-salt diet is an animal model widely used for evaluating the antihypertensive activity of drugs. This model induces volume overload hypertension in rats through the combined administration of glucocorticoids and sodium chloride. The most important advantage of this model is markedly depressed renin-angiotensin-aldosterone system activity, which enables its use in studies as an angiotensin-independent model. Furthermore, this experimental model immediately induces hypertension and cardiac hypertrophy. Therefore, it is useful for the investigation of antihypertensive effects and its complications, especially those affecting the cardiovascular system [5].

*Corresponding author: Email: xoanle@nimm.org.vn

In this study, we aim to investigate whether DK extract possesses antihypertensive effects and, if so, to elucidate the underlying mechanism. Specifically, we examined the effect of persimmon leaf extract on blood pressure and myocardial hypertrophy in cortisone acetate-induced hypertensive rats. We also assessed the ACE inhibitory activity of the persimmon leaf extract.

2. Materials and methods

2.1. Preparation of the standardized flavonoid extract from Diospyros kaki L.f leaves (DK extract)

The *Diospyros kaki* L.f leaves used in this study were collected from Lang Son Province in June 2019 and identified by Dr. Pham Thanh Huyen (Department of Medicinal Plant Resources, National Institute of Medicinal Materials, Vietnam). A voucher specimen of the herb was deposited in National Institute of Medicinal Materials. In this study, the standardised flavonoid extract was prepared as previously reported [6]. Briefly, 10 kg of the persimmon leaves were dried at 40-50°C and then crushed. The dried leaves were extracted three times with 70% ethanol (10/8/8 ml/g) by refluxing for 2, 1.5, and 1 h, respectively. The collected extracts were pooled and evaporated to form a 40% alcohol concentrated extract. This ethanol extract was then adsorbed onto the column containing D101 macroporous resin. After absorption, the column was washed with 30% ethanol until the colour faded. Then, the column was eluted with 60% ethanol. After recovery of ethanol by rotary evaporation, the extract was evaporated by a water bath at 60°C. The extract was dried in a vacuum oven at 50°C to obtain 302 g dry extract (DK extract) with a moisture content of less than 5%.

The flavonoid contents in the DK extract were analysed as described in a previous study [6]. Briefly, the DK extract was hydrolysed in a 2-M HCl /methanol solution at 90°C for 2 h. Quercetin and kaempferol contents in the hydrolysed DK extract solution were determined by HPLC (Shimazu 20A, Japan) using a Vertisep C18 column (250×4.6 mm, 5 µm) (Vertical Chromatography Co., Ltd, Bangkok, Thailand). The content of flavonoids in the DK extract was calculated as in the following formula:

Total content of flavonoids in DK extract = quercetin content × 2.55 + kaempferol content × 2.59.

According to the analysis method, the total content of flavonoids in the DK extract was calculated as 21%.

2.2. Cortisone acetate-induced hypertension and drug administration

2.2.1. Cortisone acetate-induced hypertensive model: Both male and female *Wistar* rats 8-12 weeks of age and weighing between 200 and 250 grams were provided by the Military Medical Academy, Hanoi, Vietnam. The rats were housed and maintained at a temperature of 25±1°C under 65±5% humidity and a 12 h dark-light cycle (from 7:00-19:00). The rats were kept for one week to acclimatise them before the commencement of experiments. Food and water were made available for rats *ad libitum*. The present protocol of this study was approved by the Scientific Board Committee of Hanoi Medical University, Vietnam (No. 777/QD-DHYHN).

Hypertension was induced in the *Wistar* rats by daily subcutaneous injection of 2.5 mg cortisone acetate and a constant diet of 1% sodium chloride/water for a period of 28 days. Cortisone acetate was dissolved in olive oil and administered by subcutaneous injection. The rats' blood pressure and the heart rate of awake rats were measured using a non-invasive tail-cuff method [7, 8]. After 28 days of cortisone acetate administration and 1% sodium chloride diet, the blood pressure and heart rate were measured using the tail-cuff method in conscious rats. Only rats with systolic blood pressure ≥140 mmHg were used to evaluate anti-hypertensive property.

DK extract was suspended in distilled water and given to the hypertensive rats at doses of 50 and 100 mg/kg/day, p.o. Captopril (Across Organics, USA) was also dissolved in water and given to the animals at a daily dose of 20 mg/kg/day, p.o. The physiological control (sham) and the model control rats were administered tap water (Fig. 1).

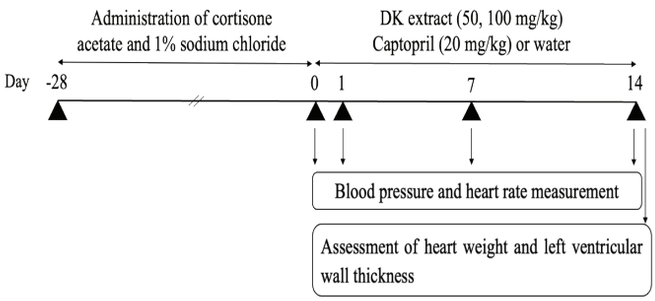

Fig. 1. Experimental schedule.

2.2.2. Measurement of the blood pressure and heart rate in awake rats: The blood pressures and heart rates of awake rats were measured using a non-invasive tail-cuff method as previously described [4]. Briefly, rats were individually placed in a warming chamber and then immobilised in a dedicated mini cage. A cuff with a pulse sensor was fixed to the tail of rats and connected to a pressure transducer. Results were recorded and analysed using Labchart Pro software (ADInstruments, Pty Ltd. Australia). Blood pressure and heart rate was measured on the first day (1 hour after the first drug was administered), and 7 and 14 days after starting the treatment. On the day of blood pressure and heart rate measurements, the rats were given medications 1 hour before the measurement (Fig. 1).

2.2.3. Assessment of heart weight and left ventricular wall thickness: After the final measurement of blood pressure on day 14, the rats were anesthetised with chloral hydrate (250 mg/kg, i.p). The heart was immediately removed and weighed, then cut into 1 mm-thick slices. Left ventricular wall thickness (9 measurements for each section) was evaluated using Image-J software (ver. 1.41, NIH; Bethesda, MD, USA) [9].

2.3. ACE inhibition assay

DK extract was dissolved in DMSO to obtain a stock solution (100 mg/ml). To determine the half-maximal inhibitory concentration (IC_{50}), a stock solution of DK extract was diluted in a borate buffer (pH 8.3) to obtain test concentrations of 1.563, 3.125, 6.250, 12.500, and 25.000 µg/ml.

Determination of the ACE inhibitory activity was conducted as described by previous studies [9-11]. Briefly, 12.5 µl of test sample (DK extract) or a reference drug, captopril (Across Organics), and a borate buffer (27.5µl) were mixed with 10 µl ACE solution (0.02 U/ml) in a 96 well-plate. This mixture was incubated at 37°C for 5 min. Then, 75 µl of N-Hippuryl-His-Leu solution (Sigma-Aldrich, USA) was added and subsequently incubated at 37°C for 30 min. The reaction was terminated using 1 M HCl. Quinoline (150 µl, Across Organics) and benzene sulfonyl chloride (75 µl, Sigma-Aldrich, USA) were added to the mixture. After diluting with 300 µl ethanol, the absorbance at 490 nm was measured using an ELISA system (EL x 808 Biotek, USA). Control samples were made similarly to the test samples with DK extract or captopril replaced by borate buffer. Each reaction was run in duplicate. ACE inhibitory activity (I%) was determined using the following formula:

$$I\ \% = (OD_{control} - OD_{test})/OD_{control} \times 100\ (\%),$$

where $OD_{control}$: absorbance value (optical density) of control sample; OD_{test}: absorbance (optical density) value of test sample.

2.4. Statistical analysis

The data were statistically analysed using SigmaPlot 12.0 (SYSTA Software Inc, Richmond, CA, USA). The results of systolic and diastolic blood pressure and heart rate were expressed as mean ± standard error of the mean (SEM). Differences between groups were assessed using two-way ANOVA followed by a Student-Newman-Keuls post hoc test for multiple comparisons. Differences of *p* value <0.05 were considered significant.

3. Results

3.1. DK extract reduced blood pressure without affecting the heart rate of the hypertensive rats

As shown in Fig. 2, the cortisone acetate-induced hypertensive model resulted in a significant development of hypertension as indicated by increases in both systolic and diastolic blood pressure when compared to the sham group ($p<0.001$). In the sham and untreated hypertensive rats, blood pressure remained stable throughout the study period. The daily administration of 50 mg/kg DK extract did not show blood pressure reducing effects one hour after the first administration compared to the vehicle-treated 2K1C rats. However, after 7 and 14 days of administration, the hypertensive rats treated with DK extract at a dose 50 mg/kg had significantly reduced blood pressure ($p<0.05$). Treatment of DK extract at a dose of 100 mg/kg significantly decreased the systolic and diastolic blood pressure of the hypertensive rats after 1 h, 7 days, and 14 days of administration compared to the control hypertensive model ($p<0.001$). Treatment with captopril at a dose of 20 mg/kg resulted in a reduction of the systolic and diastolic blood pressures that was apparent from the first administration and maintained during the following 14 days ($p<0.001$). Moreover, there was no change in heart rate across all animal groups ($p>0.05$) (Fig. 3).

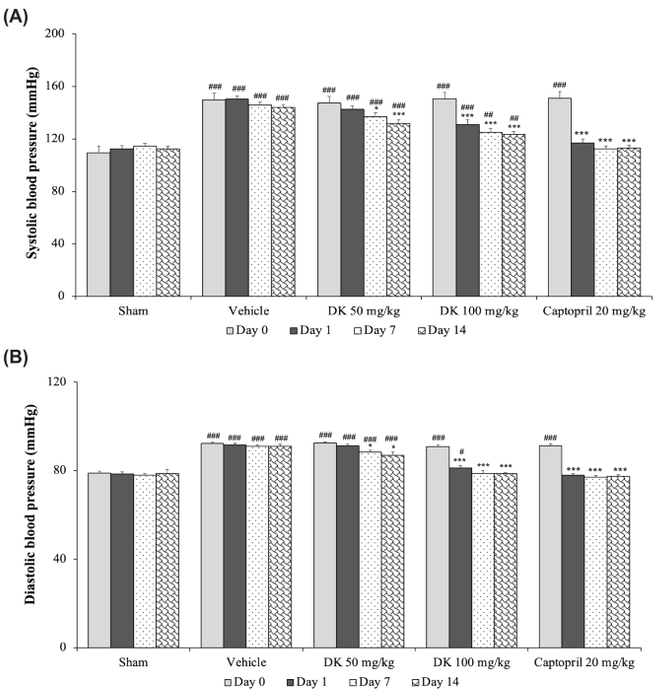

Fig. 2. Effects of DK extract on systolic and diastolic blood pressures of cortisone acetate-induced hypertensive rats: (A) systolic blood pressure and (B) diastolic blood pressure (n=10). Note: *: $p<0.05$, ***: $p<0.001$ compared to vehicle-treated hypertensive rats; ###: $p<0.001$ compared to sham animals. Data represents mean ± SEM.

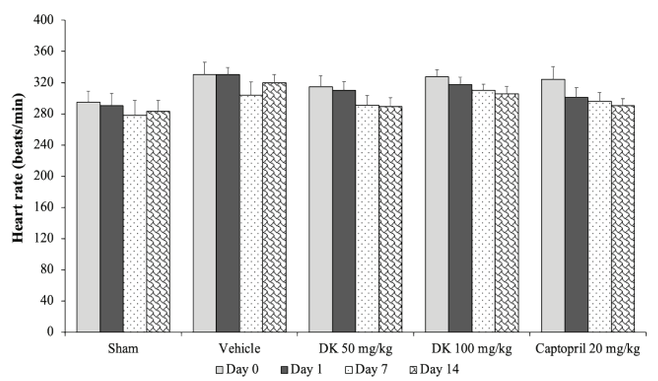

Fig. 3. Effects of DK extract on heart rate of cortisone acetate-induced hypertensive rats (n=10). Data represents mean ± SEM.

3.2. DK extract reduced ventricular hypertrophy in the hypertensive rats

Myocardial hypertrophy is a known complication of hypertension [12]. Therefore, we investigated the effects of

persimmon leaf extract (DK extract) on heart weight and left ventricular wall thickness in hypertensive rats. As shown in Table 1, cortisone acetate-induced hypertensive rats exhibited a significant increase in heart mass compared to the sham rats ($p<0.001$). However, administration of captopril (20 mg/kg) or DK extract (100 mg/kg) for 14 days led to a marked decrease in heart weight compared to the vehicle-treated hypertensive group ($p<0.05$). Additionally, treatment with captopril (20 mg/kg) or DK extract (100 mg/kg) significantly attenuated left ventricular hypertrophy in hypertensive rats. Notably, treatment with DK extract at a dose of 50 mg/kg had no significant effect on heart mass or left ventricular wall thickness in hypertensive rats (Table 1 and Fig. 4).

Table 1. Effects of DK extract on heart weight/body weight ratio and left ventricular wall thickness (n=10).

Groups	Dose (mg/kg)	Heart weight/body weight ratio (*10^3)	Left ventricular wall thickness (mm)
Sham	-	2.95 ± 0.11	2.23 ± 0.08
Vehicle-treated hypertensive rats	-	4.07 ± 0.17$^{###}$	3.29 ± 0.15$^{###}$
DK-treated hypertensive rats	50	3.64 ± 0.20$^{#}$	2.98 ± 0.12$^{###}$
	100	3.47 ± 0.15*	2.88 ± 0.09$^{###}$*
Captopril-treated hypertensive rats	20	3.24 ± 0.13**	2.79 ± 0.11$^{##}$*

*: $p<0.05$; **: $p<0.01$ compared to vehicle-treated hypertensive rat; $^{#}$: $p<0.05$; $^{##}$: $p<0.01$; $^{###}$: $p<0.001$ vs. sham animal. Data represents mean ± SEM.

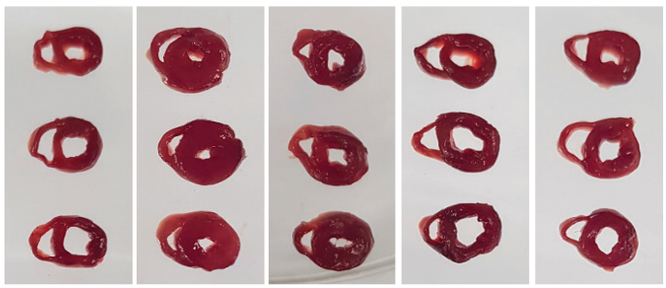

Fig. 4. Effects of DK extract on ventricular hypertrophy in the cortisone acetate-induced hypertensive rats. One mm-thick slices of heart were prepared from rats after 14 days of drug administration.

3.3. In vitro ACE inhibitory activity of DK

To investigate the possible mechanism underlying the antihypertensive effects of DK extract, we performed an ACE inhibition assay using a spectrophotometric method. The dose-response curves for ACE inhibition activity (%) in the presence of various concentrations of DK extract and captopril are shown in Fig. 5. The IC_{50} values of captopril and DK extract were calculated as 17.95±1.99 nM and 4.71±0.53 µg/ml, respectively.

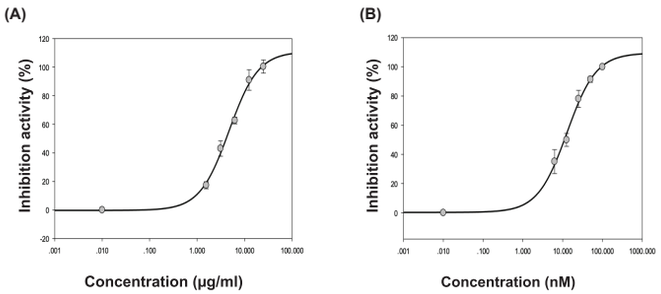

Fig. 5. *In vitro* ACE inhibitory activity of DK extract (A) and captopril (B).

4. Discussion

Hypertension is the most prevalent cardiovascular disease, and its pathophysiology in humans is multifactorial and complex. Therefore, experimental research models are used to investigate the aetiology, pathophysiology, complications, and treatment of hypertension [5]. In this study, we demonstrated that daily administration of DK extract at a dose 100 mg/kg reduced blood pressure and alleviated the left ventricular hypertrophy in cortisone acetate-induced hypertensive rats. Indeed, our findings were supported by an *in vitro* study indicating that the extract possessed ACE inhibitory activity with an IC_{50} of 4.71±0.53 µg/ml.

We employed the glucocorticoid-salt induced hypertensive model in rats to evaluate the antihypertensive effects of DK extract. This model, which combines glucocorticoid treatment and high-salt intake, induces hypertension by promoting increases in extracellular fluid volume, providing a reliable animal experimental model [3]. In a previous study, we demonstrated that a flavonoid-enriched extract from *Diospyros kaki* L.f leaves at a dose of 100 mg/kg exerted antihypertensive effects in rats with two-kidney one-clip-induced hypertension [4]. However, this renovascular hypertensive model has limitations, such as a difficulty in controlling the degree of renal damage and a large failure rate of the number of hypertensive rats. In addition, renovascular hypertension represents only a small fraction of human hypertension [13, 14]. Therefore, we conducted the glucocorticoid-salt hypertension model to evaluate the antihypertensive effects of DK extract and its underlying mechanism. Our results demonstrated that daily treatment with DK extract reduced systolic and diastolic blood pressures in a dose-dependent manner. Furthermore, the extract's antihypertensive mechanism was supported by an *in vitro* study indicating that it possessed ACE inhibitory activity with an IC_{50} of 4.71±0.53 µg/ml. The total flavonoid content in the DK extract was calculated as 21% using the HPLC method. On the other hand, it has been reported that some isolated flavonoid components from the *Diospyros kaki* leaves growing in Vietnam, such as quercetin and astragalin, reduced blood pressure *via* ACE inhibition [15-19]. Therefore, the present findings suggest that flavonoid components, through ACE inhibition activity, play a role in the anti-hypertensive effects of DK extract. In addition, quercetin decreased blood pressure by activating the Na□-K□-2Cl$^-$ cotransporter 1 in renal epithelial cells [20], while kaempferol enhanced relaxation of smooth muscle

cells by activating large-conductance calcium-activated potassium channels [21]. Hence, it is possible that these mechanisms also contributed to the antihypertensive effect of DK extract.

Our study also demonstrated that daily administration of DK extract at a dose of 100 mg/kg, as well as captopril at a dose of 20 mg/kg, significantly mitigated the increase in heart mass and the left ventricular wall thickness caused by hypertension. These findings provide evidence for the first time that flavonoids extracted from *Diospyros kaki* L.f leaves can reduce myocardial hypertrophy. An association between long-term hypertension and left ventricular hypertrophy has been reported [12], and preventing myocardial hypertrophy is an important endpoint in the treatment of hypertension [22]. ACE inhibitors, calcium channel blockers, beta-blockers, and diuretics have been shown to reduce left ventricular mass, while direct-acting vasodilators and alpha-adrenergic blockers do not affect myocardial hypertrophy [12]. Therefore, the suppression of left ventricular hypertrophy observed in DK-treated hypertensive rats suggests that DK extract possesses a beneficial effect on the cardiovascular system in addition to blood pressure-lowering activity.

5. Conclusions

Our study demonstrated that the daily administration of DK extract mitigated hypertension and alleviated ventricular hypertrophy in hypertensive rats, possibly through its ACE inhibition activity. These findings suggest that DK extract may be a useful treatment for hypertension and cardiovascular disease.

CRediT author statement

Thi Thanh Loan Nguyen: Investigation, Formal analysis, Writing-original draft; Thi Van Anh Pham: Conceptualisation, Interpretation of findings, Drafting the manuscript; Thi Xoan Le: Conceptualisation, Interpretation of findings, Writing - Review and Editing.

ACKNOWLEDGEMENTS

DK extract sample in this study was provided by Dr. Nguyen Van Tai - National Institute of Medicinal Materials.

COMPETING INTERESTS

The authors declare that there is no conflict of interest regarding the publication of this article.

REFERENCES

[1] L.L. Brunton, R.H. Dandan, B.C. Knollmann (2018), *Goodman and Gilman's: The Pharmacological Basis of Therapeutics*, New York (NY): McGraw-Hill, 13th Edition, pp.507-526.

[2] World Health Organisation (2020), "Hypertension", https://www.who.int/news-room/fact-sheets/detail/hypertension, accessed 26 August 2020.

[3] C. Xie, Z. Xie, X. Xu, et al. (2015), "Persimmon (*Diospyros kaki* L.) leaves: A review on traditional uses, phytochemistry and pharmacological properties", *The Journal of Ethnopharmacology*, **163**, pp.229-240, DOI: 10.1016/j.jep.2015.01.007.

[4] N.T.T. Loan, L.T. Xoan, P.T.N. Hang, et al. (2020), "Anti-hypertensive effects of flavonoid-enriched extract from *Diospyros kaki* L.f leaves on reno-vascular hypertensive rats", *Journal of Medicinal Materials*, **25(5)**, pp.246-250 (in Vietnamese).

[5] A. Polak, E.H. Symbor, A. Chabowski (2018), "Animal models of hypertension - revisited", *Progress in Health Sciences*, **8(1)**, pp.167-175, DOI: 10.5604/01.3001.0012.1116.

[6] L.T. Xoan, P.T.N. Hang, N.V. Tai, et al. (2017), "Neuroprotective effects of *Diospyros kaki* and *Gardenia jasminoides* against ischemic neuronal injury in mice", *Vietnam Journal of Science, Technology and Engineering*, **59(3)**, pp.60-64, DOI: 10.31276/VJSTE.59(3).60.

[7] N.T.B. Anh, V.T.N. Thanh, P.T.V. Anh, et al. (2017), "Evaluation of antihypertensive action of Geraniin purified from the rambutan's peel in experimental animals", *Journal of Medical Research*, **108(3)**, pp.74-80 (in Vietnamese).

[8] A.I. Knowlton, E.N. Loeb, H.C. Stoerk, et al. (1952), "Induction of arterial hypertension in normal and adrenalectomised rats given cortisone acetate", *Journal of Experimental Medicine*, **96(3)**, pp.187-205, DOI: 10.1084/jem.96.3.187.

[9] L.T. Xoan, N.T.T. Loan, N.T. Phuong, et al. (2022), "Anti-hypertensive effects of *Callisia fragrans* extract on Reno-vascular hypertensive rats", *Clinical Experimental Hypertension*, **44(5)**, pp.411-418, DOI: 10.1080/10641963.2022.2065286.

[10] L.T. Xoan, N.T.T. Loan, N.T. Phuong, et al. (2020), "Angiotensin-converting enzyme inhibitory activity of some Vietnamese medicinal plants", *Vietnam Journal of Science, Technology and Engineering*, **62(2)**, pp.77-82, DOI: 10.31276/VJSTE.62(2).77-82.

[11] J. Chen, Y. Wang, R. Ye, et al. (2013), "Comparison of analytical methods to assay inhibitors of angiotensin I-converting enzyme", *Food Chemistry*, **141(4)**, pp.3329-3334, DOI: 10.1016/j.foodchem.2013.06.048.

[12] W.S. Aronow (2017), "Hypertension and left ventricular hypertrophy", *Annals of Translational Medicine*, **5(15)**, pp.310-314, DOI: 10.21037/atm.2017.06.14.

[13] L.O. Lerman, T.W. Kurtz, R.M. Touyz, et al. (2019), "Animal models of hypertension, a scientific statement from the American heart association", *AHA Scientific Statement*, **73(6)**, pp.87-120, DOI: 10.1161/HYP.0000000000000090.

[14] S.P. Chelko, C.W. Schmiedt, T.H. Lewis, et al. (2012), "A novel vascular clip design for the reliable induction of 2-kidney, 1-clip hypertension in the rat", *Journal of Applied Physiology*, **112(3)**, pp.362-366, DOI: 10.1152/japplphysiol.01015.2011.

[15] J. Duarte, R.P. Palencia, F. Vargas, et al. (2001), "Antihypertensive effects of the flavonoid quercetin in spontaneously hypertensive rats", *Br. J. Pharmacol.*, **133(1)**, pp.117-124, DOI: 10.1038/sj.bjp.0704064.

[16] M.T. Olaleye, O.O. Crown, A.C. Akinmoladun, et al. (2014), "Rutin and quercetin show greater efficacy than nifedipin in ameliorating hemodynamic, redox, and metabolite imbalances in sodium chloride-induced hypertensive rats", *Human & Experimental Toxicology*, **33(6)**, pp.602-608, DOI: 10.1177/0960327113504790.

[17] M.C. Serban, A. Sahebkar, A. Zanchetti, et al. (2016), "Effects of quercetin on blood pressure: A systematic review and meta-analysis of randomised controlled trials", *J. Am. Heart Assoc.*, **5(7)**, DOI: 10.1161/JAHA.115.002713.

[18] K. Kameda, T. Takaku, H. Okuda, et al. (1987), "Inhibitory effects of various flavonoids isolated from leaves of persimmon on angiotensin-converting enzyme activity", *Journal of Natural Products*, **50(4)**, pp.680-683, DOI: 10.1021/np50052a017.

[19] L.P. Hackl, G. Cuttle, S.S. Dovichi, et al. (2002), "Inhibition of angiotesin-converting enzyme by quercetin alters the vascular response to brandykinin and angiotensin I", *Pharmacology*, **65(4)**, pp.182-186, DOI: 10.1159/000064341.

[20] Y. Marunaka, R. Marunaka, H. Sun, et al. (2017), "Actions of quercetin, a polyphenol, on blood pressure", *Molecules*, **22(2)**, DOI: 10.3390/molecules22020209.

[21] Y.C. Xu, S.W.S Leung, G.P.H Leung, et al. (2015), "Kaempferol enhances endothelium-dependent relaxation in the porcine coronary artery through activation of large-conductance Ca^{2+}-activated K^+ channels", *British Journal of Pharmacology*, **172(12)**, pp.3003-3014, DOI: 10.1111/bph.13108.

[22] T. Unger, C. Borghi, F. Charchar, et al. (2020), "2020 International society of hypertension global hypertension practice guidelines", *Hypertension*, **75(6)**, pp.1334-1357, DOI: 10.1161/HYPERTENSIONAHA.120.15026.

DOI: 10.31276/VJSTE.65(3).85-90

In silico screening of alkaloids as potential inhibitors of epidermal growth factor receptor

Bui Thanh Tung[1*], Pham Thi Kim Dung[2], Nguyen Nhu Son[1], Nguyen Bao Kim[1], Nguyen Hai Ha[1], Nguyen Thanh Tra[3]

[1]University of Medicine and Pharmacy, Vietnam National University-Hanoi, 144 Xuan Thuy Street, Dich Vong Hau Ward, Cau Giay District, Hanoi, Vietnam
[2]Hanoi Obstetrics and Gynecology Hospital, 929 La Thanh Street, Ngoc Khanh Ward, Ba Dinh District, Hanoi, Vietnam
[3]Research and Development Department, Phap Viet Xnk and Investment Joint Stock Company (PHAVIMEX), Lane 63, Phu Do Ward, Nam Tu Liem District, Hanoi, Vietnam

Received 25 January 2023; revised 14 April 2023; accepted 20 April 2023

Abstract:

The epidermal growth factor receptor (EGFR) belongs to the HER/erbB receptor tyrosine kinase (RTK) family, serving as a crucial target for cancer treatment. Anti-EGFR drugs, used as a primary treatment for patients with advanced EGFR gene mutations such as T790M, C797S, and L858R, have shown greater efficacy and safety compared to standard chemotherapy. This study aimed to screen alkaloid compounds with anticancer activity, extracted from the Selleckchem database that inhibit EGFR enzyme activity. The structure of the EGFR receptor was retrieved from the Protein Data Bank, whilst compounds were gathered from the alkaloids library within the Selleckchem database, with their structures downloaded from the PubChem database. Molecular docking was performed using Autodock Vina software. Lipinski's rule of five was employed to distinguish between compounds with drug-like and non-drug-like properties. The pharmacokinetic parameters of potential compounds were evaluated using the pkCSM tool. Our research indicates that amongst the screened alkaloids, four compounds - peiminine, sanguinarine chloride, dauricine, and irinotecan - are the most promising inhibitors of the EGFR receptor for the treatment of lung cancer. These compounds exhibit high binding affinity for the active sites of EGFR, thus inhibiting its activity. All aforementioned compounds adhere to Lipinski's rule and possess pharmacokinetic properties (absorption, distribution, metabolism, excretion, and toxicity - ADMET) that render them suitable for development into drugs.

Keywords: **alkaloid, cancer, epidermal growth factor receptor (EGFR), Lipinski's rule, molecular docking.**

Classification number: **3.3**

1. Introduction

The EGFR gene, located on the short arm of chromosome 7 (7p11.2), encodes a 170-kDa type I transmembrane growth factor receptor with tyrosine kinase (TK) activity [1]. EGFR forms part of the HER/erbB family of RTKs, encompassing HER1 (EGFR/erbB1), HER2 (neu, erbB2), HER3 (erbB3), and HER4 (erbB4). EGFR is comprised of an extracellular ligand-binding domain and an intercellular TK domain. As a cell surface protein, EGFR interacts with endogenous epidermal growth factor (EGF), instigating the EGFR receptor homo- or heterodimerisation process, followed by autophosphorylation and activation of several downstream pathways (STAT, MAPK, PI3K, AKT, PKC). This triggers cell proliferation, growth, and differentiation [2, 3]. Given EGFR's pivotal role in cell signalling and pathway involvement, it constitutes a significant target for cancer treatment [4]. Anti-EGFR drugs, used as first-line therapy in patients with advanced EGFR gene mutations such as T790M, C797S, and L858R, have exhibited superior efficacy and safety compared to conventional chemotherapy [5]. To date, numerous tyrosine kinase inhibitors (TKIs) have been employed to inhibit EGFR kinase overexpression, particularly erlotinib and gefitinib, which are highly selective for treating non-small cell lung cancer (NSCLC) and pancreatic cancer, while lapatinib is a dual inhibitor of EGFR and HER2 kinase, useful in metastatic breast cancer [6, 7]. However, these drugs can also induce adverse side effects, including vomiting, nausea, bleeding, diarrhoea, dry skin, skin rashes, and lung disease [8, 9].

Alkaloids, a highly diverse group of compounds, encompass approximately 3000 distinct entities derived from plants, fungi, and animals [10]. Alkaloids are low molecular weight organic nitrogen-containing compounds often classified chemically as pyrrolidines, pyridines, tropanes, pyrrolizidines, isoquinolines, indoles, quinolines and terpenoids and steroids. They have been shown to inhibit the topoisomerase

*Corresponding author: Email: tungbt.ump@vnu.edu.vn

enzyme, thereby blocking DNA replication and inducing cell death [11]. Thus, alkaloids have formed the basis for various drugs for diverse diseases, such as the asthma-relieving action of ephedrine, the analgesic action of morphine, and the anticancer effects of vinblastine [12]. Among phytochemicals, alkaloids demonstrate potential as anticancer agents.

Molecular docking is a highly applicable modelling technique in the research and development of novel drugs. This method aids in determining enzyme and ligand topology, offering an evaluation of the drug's pharmacological potential. The lower the binding energy (Gibbs free energy) of a protein-ligand complex (substance), the greater the pharmacological potential. This *in silico* method provides substantial cost and time savings for compound screening compared to experimental methods [13]. Our study was undertaken with the goal of screening alkaloids with anticancer potential to identify potential inhibitors of HER2 receptors via the molecular docking method.

2. Methodology

2.1. Molecular docking

Preparation of the protein structure: The crystal structures of the EGFR receptor (ID: 1M17) were collected from the RCSB protein data bank (http://www.rcsb.org/) [14]. Water molecules and co-ligand erlotinib (4-anilinoquinazoline inhibitor) were removed from the protein structure with the help of Discovery Studio Visualizer 4.0 software, while hydrogen atoms were added afterward using Autodock Vina. The binding site of the TK enzyme EGFR was re-established by MGL Autodock tools 1.5.7 within a 24 x 24 x 24 Å-sized gridbox, spacing of 1 Å, and (x,y,z) centre coordinates at (20.663, 4.206, 56.920). Finally, the protein structure files were saved in .pdbqt format for the docking process.

Preparation of the ligand structure: Data from 204 highly potential anticancer alkaloid compounds were collected and sorted from the Alkaloid Compound Library and Anti-cancer Compound Libraries I and II (http://www.selleckchem.com/). Their 3D structures were retrieved from the PubChem database (https://pubchem.ncbi.nlm.nih.gov/). All compounds were optimised by Avogadro software using Conjugate Gradients and converted to .pdbqt format using Autodock tools.

Performance of molecular docking: Docking and screening of the 204 bioactive alkaloids against the EGFR receptor were performed using AutoDock Vina software. Molecular interactions of protein-ligand complexes showing promising binding free energies and molecular targets were visualized using Discovery Studio Visualizer 2020.

Validation of docking: To validate the docking protocol, the co-ligand of the co-crystal structure was docked in the target active site. The docking process was considered valid if the root mean square deviation (RMSD) value was less than or equal to 1.5 [15]. The binding capacity of the ligands was determined by their interactions with amino acids in the binding pocket as well as the binding energies calculated by the Autodock Vina scoring function.

2.2. Lipinski's rule of five

Lipinski's rule of five aids in the comparison of drug-like and non-drug-like molecules [16]. We evaluated Lipinski's rule of five with an online tool (http://www.scfbio-iitd.res.in/software/drugdesign/lipinski.jsp) [17]. The chemical structures were downloaded from the PubChem database and adjusted to pH 7.0.

2.3. Prediction of ADMET

The ADMET profile includes five parameters: absorption, distribution, metabolism, excretion, and toxicity, which play a critical role in demonstrating the likelihood of success of a compound to become a drug. In this study, PkCSM tools (http://biosig.unimelb.edu.au/pkcsm/prediction) were used to predict the ADMET profile [18].

3. Results and discussion

3.1. Molecular docking

Docking protocol validation: To validate the docking protocol, a separated co-ligand is re-docked back into target protein's binding site to calculate the RMSD value between the redocked conformation and protein-bound ligand conformation. The results showed that the docking process was valid for EGFR with RMSD values of 1.40108 Å<1.5 Å. Therefore, the docking procedure can be performed (Fig. 1).

Fig. 1. Superposition of the re-docking pose and the original complexed ligand.

Screening of potential EGFR inhibitor: Molecular docking between 204 alkaloid ligands with anticancer potential against EGFR receptor was performed. The results were shown in Table 1.

Table 1. The docking results of 204 alkaloid compounds into EGFR receptor.

No	Compound	Binding energy (kcal/mol)
1	(-)-Huperzine A (HupA)	-7.0
2	(-)-Norepinephrine	-6.0
3	(-)-Sparteine sulfate	-6.5
4	(+)-Bicuculline	-10
5	(+)-Isocorynoline	-8.2
6	(+)-Matrine	-7.8
7	(S)-10- Hydroxycamptothecin	-9.3
8	2'-Deoxyguanosine monohydrate	-7.5
9	2'-Deoxyinosine	-7.6
10	3,3'-Diindolylmethane	-8.6
11	4-Aminoantipyrine	-6.9
12	4-Hydroxyquinazoline	-6.3
13	5'-Adenylic acid	-7.4
14	6-Biopterin	-7.1
15	7-Ethylcamptothecin	-9.9
16	9-Methoxycanthin-6-one	-8.4
17	Abiraterone acetate	-9.3
18	Acarbose	-7.9
19	Acetylcysteine	-4.6
20	Acetylcholine chloride	-4.3
21	Adenosine	-7.2
22	ADP	-7.5
23	Ajmaline	-8.6
24	Albendazole	-6.7
25	Allantoin	-5.9
26	Aloperine	-7.0
27	Aminocaproic acid	-4.8
28	Ampiroxicam	-9.4
29	Anamorelin	-8.5
30	Anisomycin	-6.9
31	Aristolochic acid A	-8.6
32	Atropine sulfatemonohydrate	-7.5
33	Benzamide	-5.7
34	Berbamine (dihydrochloride)	-8.3
35	Berberine chloride	-9.2
36	Berberrubine	-9.2
37	Bestatin	-7.2
38	Beta-alanine	-3.6
39	Betaine	-3.7
40	Boldine	-8.2
41	Brevianamide F	-8.4
42	Butylscopolamine Bromide	-7.5
43	Camptothecin	-10
44	Canertinib (CI-1033)	-8.0
45	Capecitabine	-7.0
46	Capsaicin (Vanilloid)	-6.8
47	Catharanthine	-7.6
48	Cephalotaxine	-8.3
49	Cepharanthine	-9.6
50	Cinchonine(LA40221)	-7.8
51	Colchicine	-7.7
52	Coptisine chloride	-9.8
53	Cordycepin	-7.4
54	Corynoline	-9.8
55	Corynoxine	-7.5
56	Crebanine	-8.9
57	Cyclocytidine HCl	-7.1
58	Cytidine	-7.1
59	Cytisine	-6.8
60	Chelidonine	-9.5
61	Chlorhexidine HCl	-8.6
62	Danofloxacin mesylate	-8.8
63	Dasatinib monohydrate	-8.6
64	Dauricine	-10.1
65	Daurisoline	-9.9
66	Decitabine	-6.6
67	Dehydrocorydalin	-8.1
68	Demethyleneberberine	-8.6
69	Dihydrocapsaicin	-6.5
70	DL-Norvaline	-4.7
71	Dopamine HCl	-5.6
72	Efavirenz	-8.1
73	Ellipticine hydrochloride	-8.7
74	Epigoitrin	-4.2
75	Ethionamide	-5.2
76	Evodiamine	-9.1
77	Fangchinoline	-9.4
78	Fenspiride HCl	-7.7
79	Fingolimod	-6.1
80	Folic acid	-8.4
81	Galanthamine HBr	-7.8
82	Gefitinib (ZD1839)	-8.5
83	Gelsemine	-7.9
84	Glutathione	-5.6
85	Gramine	-6.0
86	Guanosine	-7.4
87	Halofuginone	-8.0
88	Harmaline	-6.8
89	Harmine hydrochloride	-6.9
90	Harringtonine	-8.1
91	Higenamine hydrochloride	-8.0
92	Histamine	-4.6
93	Homatropine bromide	-7.5
94	Homoharringtonine	-8.3
95	Hydroquinidine	-7.8
96	Hydroxycamptothecin	-10
97	Hyoscyamine	-7.5
98	Indigo	-8.4
99	Indirubin	-9.0
100	Indole-3-acetic acid	-6.3
101	Indole-3-carbinol	-5.9
102	Irinotecan	-10.1
103	Isatin	-6.1
104	Isoguanosine	-7.5
105	isoleucine	-5.0
106	Isoliensinine	-10
107	Jatrorrhizine	-8.5
108	Jervine	-9.9
109	Kynurenic acid	-7.0
110	L-5-Hydroxytryptophan	-7.0
111	Lappaconite HBr	-9.1
112	Lappaconitine	-9.2
113	L-Arginine HCl (L-Arg)	-5.4
114	L-carnitine	-4.5
115	L-Cycloserine	-4.5
116	Leonurine	-6.6
117	Levoleucovorin calcium	-8.7
118	Liensinine	-9.8
119	L-Kynurenine	-6.5
120	Lobeline hydrochloride	-8.7
121	L-Ornithine hydrochloride	-5.2
122	L-serine	-4.0
123	L-Tryptophan	-6.6
124	Lycorine hydrochloride	-8.2
125	Melatonin	-7.0
126	Metronidazole	-5.4
127	Monocrotaline	-7.7
128	N-(5-Aminopentyl)acetamide	-4.9
129	N-Benzoyl-(2R,3S)-3-phenylisoserine	-7.7
130	Neferine	-9.6
131	Nicergoline	-8.2
132	Nicotinamide (VitaminB3)	-5.4
133	Nicotinamide N-oxide	-5.7
134	Nifuratel	-5.4
135	Nitidine chloride	-9.4
136	Nonivamide	-6.3
137	Nuciferine	-8.8
138	Nudifloric acid	-6.2
139	Orotic acid (6Carboxyuracil)	-5.9
140	Oxcarbazepine	-8.0
141	Oxindole	-5.7
142	Oxymatrine	-8.3
143	Palmatine chloride	-8.2
144	Palonosetron HCl	-8.7
145	Peiminine	-10.6
146	Penicillamine	-4.5
147	Pilocarpine HCl	-6.3
148	Pioglitazone	-8.0
149	Piperine	-7.9
150	Piperlongumine	-7.2
151	Primaquine diphosphate	-7.1
152	Procaine HCl	-6.1
153	Protopine	-8.4
154	Proxyphylline	-7.0
155	Puromycin 2HCl	-8.1
156	Quinine HCl dihydrate	-7.4
157	Raceanisodamine	-7.6
158	Reserpine	-9.1
159	Roquinimex	-7.8
160	Rutaecarpine	-9.3
161	Ruxolitinib phosphate	-8.4
162	S-(-)-Cotinine	-5.9
163	S-allyl-L-cysteine	-4.4
164	Santacruzamate A (CAY10683)	-6.7
165	Sanguinarine chloride	-10.3
166	Sarcosine	-3.7
167	Scopine	-5.6
168	Scopolamine HBr	-7.4
169	Scopolamine N-Oxide HydrobroMide Monohydrate	-7.8
170	Securinine	-7.4
171	Silodosin	-7.9
172	Sinapine thiocyanate	-6.4
173	Sinomenine hydrochloride	-6.8
174	S-Methyl-L-cysteine	-4.3
175	Songorine	-8.4
176	Sophocarpine	-7.6
177	Sophoridine	-8.4
178	Sorafenib	-8.9
179	Stachydrine hydrochloride	-5.0
180	Synephrine	-6.3
181	Taurine	-3.9
182	Tetrahydroberberine	-8.9
183	Tetrahydropapaverine HCl	-7.8
184	Tetramethylpyrazine	-4.9
185	Tetrandrine	-9.1
186	Tigecycline	-8.5
187	Tioconazole	-7.4
188	Topotecan HCl	-9.6
189	Tubercidin	-7.3
190	Tyramine	-5.5
191	Thymine	-5.3
192	Tranexamic Acid	-5.5
193	Trigonelline hydrochloride	-5.5
194	Tropisetron	-7.8
195	Tryptamine	-6.3
196	Tryptanthrin	-8.9
197	Uracil	-4.8
198	Uridine	-7.3
199	Veratramine	-9.6
200	Vidarabine	-6.9
201	Vincamine	-8.7
202	Vindoline	-7.4
203	Vinpocetine	-8.7
204	Vortioxetine	-7.5
205	Lapatinib (Positive control)	-9.2

The docking results from Table 1 show that 13/204 alkaloids had binding energies (kcal/mol) lower than the reference compound Lapatinib: (+)-Bicuculline; camptothecin, 7-Ethylcamptothecin, Coptisine chloride, Dauricine, Daurisoline, Hydroxycamptothecin, Irinotecan, Peiminine, Isoliensinine, Jervine, Liensinine and Sanguinarine chloride with binding energies (kcal/mol) of -10,0 (kcal/mol); -9,9 (kcal/mol); -10,0 (kcal/mol); -9,8 (kcal/mol); -10,1 (kcal/mol); -9,9 (kcal/mol); -10,0 (kcal/mol); -10,1 (kcal/mol); -10,0 (kcal/mol), -9,9 (kcal/mol), -9,8 (kcal/mol), -10,6 (kcal/mol) and -10,3 (kcal/mol), respectively. Lapatinib, the first dual inhibitor of EGFR and human epidermal growth factor receptor 2 (HER2) TKs, was approved by the US Food and Drug Administration (FDA) in 2007 [19]. The interactions of thirteen compounds with amino acids in the 1M17 receptor are shown in Table 2.

Table 2. Interactions of amino acids in the binding pocket with the 13 compounds.

Compound	Receptor	Hydrogen bonds	p-anion bonds	Other interactions
(+)-Bicuculline	1M17	MET769, PRO770		THR830, LEU800, LEU694, LEU820, VAL702
7 Ethylcamptothecin		THR766, ASP831		LEU820, VAL702, LEU694, CYS773
Camptothecin		THR766, ASP831		LEU820, VAL702, LEU694
Coptisine chloride		GLU738, ASP776		LEU820, LEU694, CYS773, VAL702, ALA719, LYS721
Dauricine		LYS721, ASP831	CYS773	LEU820, VAL702, ALA719, PHE699, ARG817
Daurisoline		LYS721, THR766	ASP831	LEU820, VAL702, ALA719, PHE699, ARG817, CYS773, MET742, GLY772, LEU 768
Hydroxy camptothecine		CYS751, ASP831		LEU820, VAL702, LEU694
Irinotecan		MET769, PRO770, ASP831		LEU820, LEU694, CYS773, VAL702, ALA719, LYS721
Isoliensinine		GLY697, GLY695, ASP831	ASP831	VAL702, ALA719, LYS721, PHE699, LEU694, MET742, THR766
Jervine		GLU738, ASP776		LEU820, VAL702, ALA719, LYS721
Liensinine		GLY695, ASP831	ASP831	LEU820, VAL702, ALA719, LEU694, PHE699, THR766
Peiminine		MET769		ASP831, PHE699, LEU694, VAL702
Sanguinarine chloride		CYS751, ASP831		LEU820, VAL702, ALA719, LYS721, PHE699, THR766

3.2. Lipinski's rule of five

Lipinski's rule of five aids in distinguishing between drug-like and non-drug-like molecules for the development of oral drugs. It predicts high probabilities of drug-like effectiveness or failure for molecules complying with two or more of the following rules: a molecular mass (MW) below 500 Dalton; high lipophilicity (expressed as LogP below 5); less than 5 hydrogen bond donors (HBD); less than 10 hydrogen bond acceptors (HBA1); and a molar refractivity (MR) between 40-130. The result of Lipinski's rule of five showed that all compounds satisfied more than two criteria. Thus, we focus on analysing the pharmacokinetic properties, including absorption, distribution, metabolism, excretion, and toxicity, of these drugs.

3.3. Prediction of ADMET profile

The prediction of absorption, distribution, metabolism, excretion, and toxicity profile of four selected compounds are shown in Table 3.

Table 3. The results of ADMET profile of four selected compounds.

Properties	Dauricine	Irinotecan	Peiminine	Sanguinarine chloride
Absorption				
Water solubility (log mol/l)	-3.952	-3.57	-3.881	-4.848
Caco2 permeability (log P_{app} in 10^{-6} cm/s)	0.386	0.648	1.341	1.05
Intestinal absorption (human) (%)	88.177	99.879	91.574	70.472
Distribution				
VDss (human) (log l/kg)	-0.525	-2.741	0.1	0.142
BBB permeability (log BBB)	-1.054	-1.303	-0.009	0.41
Metabolism				
CYP2D6 substrate	Yes	No	No	No
CYP3A4 substrate	Yes	Yes	Yes	Yes
CYP2D6 inhibitor	No	No	No	No
CYP3A4 inhibitor	Yes	Yes	No	Yes
Excretion				
Total clearance (log ml/min/kg)	0.987	0.939	-0.064	1.406
Toxicity				
AMES toxicity	No	No	No	Yes
Hepatotoxicity	No	Yes	Yes	No

In the absorption process, the human intestinal absorption (HIA) and human colon adenocarcinoma-2 cell line (Caco2) are two important parameters determining the absorption of a drug. A substance is considered poorly absorbed if the percentage absorbed in the human intestine is less than 30% [20]. The (human) intestinal absorption percentage of the four selected compounds was comparatively high/medium, especially irinotecan with a maximum absorption percentage of 99.879%. The Caco-2 cell line consists of human colon adenocarcinoma cells. A compound has high Caco-2 permeability if it has a Papp>$8x10^{-6}$ cm/s, i.e., logPapp>0.9 [20]. The results show two compounds with a Caco-2 permeability greater than 0.9, namely peiminine and sanguinarine chloride.

The distribution of a substance is expressed through several parameters including lipid-solubility, concentration, as well as the binding capability to plasma proteins and transfer proteins. The steady-state volume of distribution (VDss) is the theoretical volume to which the total dose of a drug should be uniformly distributed to obtain the same plasma concentrations [20]. The higher the VDss, the more a drug will be distributed in tissue rather than plasma. Compounds are said to be well distributed to tissues if logVDss>0.45 and poorly distributed if logVDss<-0.15 [20]. All four compounds, dauricine, irinotecan, peiminine, and sanguinarine chloride, distributed poorly to tissues with logVDss values of -0.525, -2.741, 0.1, and 0.142, respectively. No compounds were well distributed. The ability of a drug to cross the blood-brain barrier is a factor to consider to help reduce toxicities and side effects or to improve the effectiveness of drugs whose pharmacological activity is within the brain [20]. There are two compounds (dauricine and irinotecan) which have poor blood-brain barrier ability because their logBBB values were all less than -1. This limits the effectiveness of the compound in treating conditions that affect the brain, because the compound is unable to reach its target site in the brain.

The cytochrome P450 enzymes play an important role in the metabolism of many drugs. The results show that all compounds are substrates of CYP3A4, thus indicating that these compounds are potentially metabolized by P450.

Regarding elimination, we predicted total clearance, which is shown in Table 3. The results demonstrate that the total clearance of dauricine, irinotecan, and sanguinarine chloride are the highest compared with peiminine.

In terms of toxicity, dauricine has no toxicity, while all remaining compounds have at least one toxicity.

In this study, we screened 204 alkaloids, which have anticancer abilities, from the alkaloid compound library and anti-cancer compound libraries I and II in order to evaluate their potential as EGFR inhibitors. Docking results show that 13 compounds had the lowest binding energies. Among these, dauricine, irinotecan, peiminine, and sanguinarine chloride were chosen as potential compounds for development into drugs. Although dauricine has not been studied as a potential treatment for lung cancer, there have been some studies showing that dauricine has the ability to suppresses the growth of pancreatic cancer *in vivo* [21, 22]. For many years, irinotecan, which has been used to treat a variety of cancers, is a flexible chemotherapeutic agent that works effectively in combination with a wide range of anticancer medicines. More clinical trials are needed to demonstrate the efficacy of this medication for lung cancer. Peiminine is an alkaloid derived from the bulb of *Fritillaria thunbergii* Miq and possesses anticancer and anti-inflammatory properties. Peiminine inhibits the progression of colorectal cancer through up-regulating miR-760 and inducing apoptosis and autophagy [23, 24]. Sanguinarine chloride, a benzophenanthridine alkaloid produced from the root of *Sanguinaria Canadensis*, can exhibit a clear-cut anticancer potential by inducing apoptosis and/or antiproliferative effects on tumour cells. This alkaloid's anti-tumour activity is the consequence of a combination effect on tumour cell proliferation and invasiveness, as well as modulation of the complicated phenomenon of tumour angiogenesis [25]. Sanguinarine, in particular, is a promising option for the development of novel lung anticancer medicines, either alone or in conjunction with existing chemotherapy regimens, due to its pro-apoptotic capability.

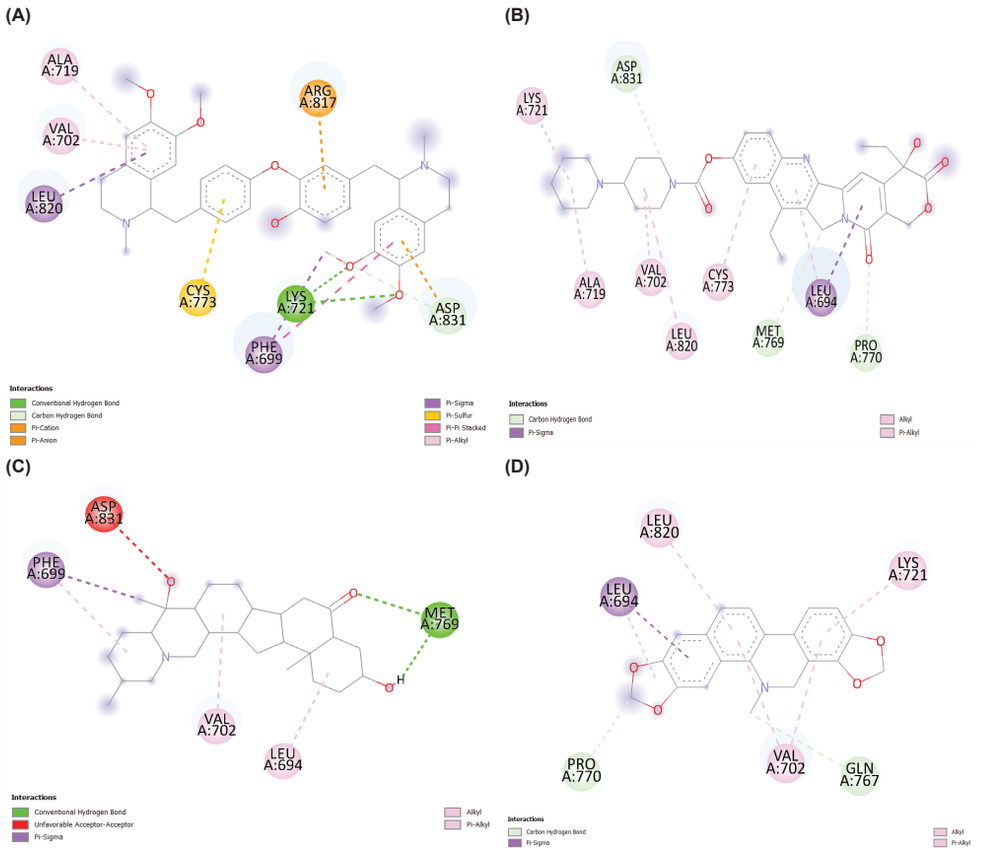

Fig. 2. Interactions between four potential compounds and the EGFR receptor. (A) Dauricine; **(B)** Irinotecan; **(C)** Peiminine; **(D)** Sanguinarine chloride.

In this study, we also evaluated the interactions between the four compounds with EGFR using Discovery Studio Visualizer 4.0 software, as shown in Fig. 2. The lapatinib positive control, with a binding energy of -9.2 kcal/mol, has hydrogen bonds and π interactions with amino acids MET769, ASP831, LEU820, VAL702, ALA719, and LYS721. All four compounds showed good binding ability at the active site of the enzyme through many important amino acids such as LEU820, VAL702, ALA719, LYS721, and ASP831 [26-29].

4. Conclusions

Our study elucidated that four alkaloid compounds (dauricine, irinotecan, peiminine, and sanguinarine chloride) are potential inhibitors of the EGFR enzyme for the treatment of lung cancer. These compounds exhibit strong binding affinity for the active sites of EGFR, thus inhibiting the activity of this enzyme. All the aforementioned compounds comply with Lipinski's rule and possess pharmacokinetic properties suitable for drug development. Hence, we propose to conduct further *in vitro* and *in vivo* studies of these four compounds with the aim of treating cancer.

CRediT author statement

Bui Thanh Tung: Conceptualization, Methodology, Supervision; Pham Thi Kim Dung and Nguyen Thanh Tra: Data curation, Writing - Original draft preparation; Nguyen Nhu Son, Nguyen Bao Kim, Nguyen Hai Ha: Software, Visualisation, Investigation, Writing - Reviewing and Editing.

COMPETING INTERESTS

The authors declare that there is no conflict of interest regarding the publication of this article.

REFERENCES

[1] Y. Yarden, M.X. Sliwkowski (2001), "Untangling the ErbB signalling network", *Nat. Rev. Mol. Cell Biol.*, **2(2)**, pp.127-137, DOI: 10.1038/35052073.

[2] A. Ayati, S. Moghimi, S. Salarinejad, et al. (2020), "A review on progression of epidermal growth factor receptor (EGFR) inhibitors as an efficient approach in cancer targeted therapy", *Bioorg. Chem.*, **99**, DOI: 10.1016/j.bioorg.2020.103811.

[3] P.A. Schwartz, B.W. Murray (2011), "Protein kinase biochemistry and drug discovery", *Bioorg. Chem.*, **39(5-6)**, pp.192-210, DOI: 10.1016/j.bioorg.2011.07.004.

[4] R. Rosell, T. Moran, C. Queralt, et al. (2009), "Screening for epidermal growth factor receptor mutations in lung cancer", *N. Engl. J. Med.*, **361(10)**, pp.958-967, DOI: 10.1056/NEJMoa0904554.

[5] K. Ohashi, L.V. Sequist, M.E. Arcila, et al. (2013), "Characteristics of lung cancers harboring NRAS mutations", *Clin. Cancer Res.*, **19(9)**, pp.2584-2591, DOI: 10.1158/1078-0432.CCR-12-3173.

[6] J.C. Soria, Y.L. Wu, K. Nakagawa, et al. (2015), "Gefitinib plus chemotherapy versus placebo plus chemotherapy in EGFR-mutation-positive non-small-cell lung cancer after progression on first-line gefitinib (IMPRESS): A phase 3 randomised trial", *Lancet Oncol.*, **16(8)**, pp.990-998, DOI: 10.1016/S1470-2045(15)00121-7.

[7] J.C. Yang, Y.L. Wu, M. Schuler, et al. (2015), "Afatinib versus cisplatin-based chemotherapy for EGFR mutation-positive lung adenocarcinoma (LUX-Lung 3 and LUX-Lung 6): Analysis of overall survival data from two randomised, phase 3 trials", *Lancet Oncol.*, **16(2)**, pp.141-151, DOI: 10.1016/S1470-2045(14)71173-8.

[8] B. Forsythe, K. Faulkner (2004), "Overview of the tolerability of gefitinib (IRESSA) monotherapy: Clinical experience in non-small-cell lung cancer", *Drug Saf.*, **27(14)**, pp.1081-1092, DOI: 10.2165/00002018-200427140-00002.

[9] S.R. Johnston, A. Leary (2006), "Lapatinib: A novel EGFR/HER2 tyrosine kinase inhibitor for cancer", *Drugs Today (Barc)*, **42(7)**, pp.441-453, DOI: 10.1358/dot.2006.42.7.985637.

[10] B. Salehi, J.S. Rad, E. Capanoglu, et al. (2019), "Cucurbita plants: From farm to industry", *Applied Sciences*, **9(16)**, DOI: 10.3390/app9163387.

[11] D. Jain, P. Chaudhary, N. Varshney, et al. (2021), "Tobacco smoking and liver cancer risk: Potential avenues for carcinogenesis", *J. Oncol.*, **2021(1)**, DOI: 10.1155/2021/5905357.

[12] J.J. Lu, J.L. Bao, X.P. Chen, et al. (2012), "Alkaloids isolated from natural herbs as the anticancer agents", *Evid. Based Complement. Alternat. Med.*, **2012**, DOI: 10.1155/2012/485042.

[13] I.W. Cheung, S. Nakayama, M.N. Hsu, et al. (2009), "Angiotensin-I converting enzyme inhibitory activity of hydrolysates from oat (*Avena sativa*) proteins by *in silico* and *in vitro* analyses", *J. Agric. Food Chem.*, **57(19)**, pp.9234-9242, DOI: 10.1021/jf9018245.

[14] K. Aertgeerts, R. Skene, J. Yano, et al. (2011), "Structural analysis of the mechanism of inhibition and allosteric activation of the kinase domain of HER2 protein", *J. Biol. Chem.*, **286(21)**, pp.18756-18765, DOI: 10.1074/jbc.M110.206193.

[15] K.E. Hevener, W. Zhao, D.M. Ball, et al. (2009), "Validation of molecular docking programs for virtual screening against dihydropteroate synthase", *J. Chem. Inf. Model.*, **49(2)**, pp.444-460, DOI: 10.1021/ci800293n.

[16] C.A. Lipinski (2004), "Lead- and drug-like compounds: The rule-of-five revolution", *Drug Discov. Today Technol.*, **1(4)**, pp.337-341, DOI: 10.1016/j.ddtec.2004.11.007.

[17] B. Jayaram, T. Singh, G. Mukherjee, et al. (2012), "Sanjeevini: A freely accessible web-server for target directed lead molecule discovery", *BMC Bioinformatics*, **13(Suppl 17):S7**, DOI: 10.1186/1471-2105-13-S17-S7.

[18] pkCSM, "Pharmacokinetic properties", http://biosig.unimelb.edu.au/pkcsm/prediction, accessed 20 November 2022.

[19] P.J. Medina, S. Goodin (2008), "Lapatinib: A dual inhibitor of human epidermal growth factor receptor tyrosine kinases", *Clin. Ther.*, **30(8)**, pp.1426-1447, DOI: 10.1016/j.clinthera.2008.08.008.

[20] D.E. Pires, T.L. Blundell, D.B. Ascher (2015), "PkCSM: Predicting small-molecule pharmacokinetic and toxicity properties using graph-based signatures", *J. Med. Chem.*, **58(9)**, pp.4066-4072, DOI: 10.1021/acs.jmedchem.5b00104.

[21] Y.B. Zhang, H.X. Fei, J. Guo, et al. (2019), "Dauricine suppresses the growth of pancreatic cancer *in vivo* by modulating the hedgehog signaling pathway", *Oncol. Lett.*, **18(5)**, pp.4403-4414, DOI: 10.3892/ol.2019.10790.

[22] L. Jiang, T. Guo, Y. Jiang, et al. (2021), "Dauricine inhibits human pancreatic carcinoma cell proliferation through regulating miRNAs", *Mol. Omics*, **17(4)**, pp.630-640, DOI: 10.1039/d1mo00156f.

[23] J. Li, Y. Qin, W. Wang, et al. (2021), "Peiminine inhibits the progression of colorectal cancer through up-regulating miR-760 via declining the expression of long noncoding RNA LINC00659", *Anticancer Drugs*, **32(2)**, pp.148-156, DOI: 10.1097/CAD.0000000000000981.

[24] Z. Zheng, L. Xu, S. Zhang, et al. (2017), "Peiminine inhibits colorectal cancer cell proliferation by inducing apoptosis and autophagy and modulating key metabolic pathways", *Oncotarget*, **8(29)**, pp.47619-47631, DOI: 10.18632/oncotarget.17411.

[25] R. Gaziano, G. Moroni, C. Bue, et al. (2016), "Antitumor effects of the benzophenanthridine alkaloid sanguinarine: Evidence and perspectives", *World J. Gastrointest. Oncol.*, **8(1)**, pp.30-39, DOI: 10.4251/wjgo.v8.i1.30.

[26] J. Stamos, M.X. Sliwkowski, C. Eigenbrot (2002), "Structure of the epidermal growth factor receptor kinase domain alone and in complex with a 4-anilinoquinazoline inhibitor", *J. Biol. Chem.*, **277(48)**, pp.46265-46272, DOI: 10.1074/jbc.M207135200.

[27] B.D. Palmer, S.T. Kallmeyer, D.W. Fry, et al. (1997), "Tyrosine kinase inhibitors. 11. Soluble analogues of pyrrolo- and pyrazoloquinazolines as epidermal growth factor receptor inhibitors: Synthesis, biological evaluation, and modeling of the mode of binding", *J. Med. Chem.*, **40(10)**, pp.1519-1529, DOI: 10.1021/jm960789h.

[28] S. Mahernia, M. Hassanzadeh, N. Sharifi, et al. (2018), "Structure-based pharmacophore design and virtual screening for novel potential inhibitors of epidermal growth factor receptor as an approach to breast cancer chemotherapy", *Mol. Divers.*, **22(1)**, pp.173-181, DOI: 10.1007/s11030-017-9799-7.

[29] I.S. Yadav, P.P. Nandekar, S. Srivastavaa, et al. (2014), "Ensemble docking and molecular dynamics identify knoevenagel curcumin derivatives with potent anti-EGFR activity", *Gene*, **539(1)**, pp.82-90, DOI: 10.1016/j.gene.2014.01.056.

DOI: 10.31276/VJSTE.65(3).91-96

Assessment of growth and fermentation of some yeasts on soybean residue hydrolysate

Thi Van Anh Mai[1, 2*], Kim Loan Nguyen[1], Dinh Trien Dang[1], Thi Xuan Sam Nguyen[1], Thanh Hang Nguyen[1]

[1]Hanoi University of Science and Technology, 1 Dai Co Viet Street, Bach Khoa Ward, Hai Ba Trung District, Hanoi, Vietnam
[2]University of Economics - Technology for Industries, 456 Minh Khai Street, Minh Khai Ward, Hai Ba Trung District, Hanoi, Vietnam

Received 6 April 2023; revised 23 June 2023; accepted 8 August 2023

Abstract:

This study explored the growth and fermentation capabilities of four distinct yeast strains, including *Saccharomyces cerevisiae var. boulardii* CNCM I-745, *S. cerevisiae* 7012, *S. cerevisiae* 7028, and *S. cerevisiae var. diastaticus* BE-134, with the aim of identifying the most suitable strain for the production of a fermented beverage from soybean residue hydrolysate (SRH). The results were as follows: *S. cerevisiae* 7012 exhibited the most efficient fermentation, with residual sugar content of 2.16 g/100 ml, an ethanol concentration of 1.39% v/v, and a favourable aroma, receiving a sensory score of 4.3/5 points. Within this sensory profile, the aromatic compound 2-phenylethanol was found to be the predominant component. Additionally, *S. cerevisiae var. boulardii* CNCM I-745 demonstrated superior biomass production ability, achieving a cell density of 7.71 log CFU/ml after 48 hours of fermentation solution also showed the highest antioxidant activity, equivalent to 1.63 mg of ascorbic acid per 100 ml. Consequently, these two yeast strains were selected for combined use in fermentation to leverage the probiotic characteristics of *S. cerevisiae var. boulardii* CNCM I-745 and the flavouring capacity of *S. cerevisiae* 7012 in creating fermented beverages from SRH.

Keywords: **fermentation, *S. cerevisiae*, soybean residue, yeast.**

Classification number: **3.5**

1. Introduction

Soybean residue, a by-product of the soy milk and tofu industries, contains an array of valuable nutrients that can be exploited. Through enzymatic hydrolysis, the concentration of solutes in soybean residue can be significantly enhanced, rendering it appropriate for the growth and fermentation of microorganisms. Fermentation not only facilitates the digestion and absorption of nutrients but also augments the nutritional value of soybean residue. This process can eliminate undesired odours, augment the quantity of digestible fibre, and synthesise aromatic compounds that enrich the sensory appeal of the product. In fact, soybean residue has been successfully fermented to produce a diversity of products, including soy sauce, jam, animal feed, food additives, and beverages [1, 2].

One strategy for altering the odour of soybean residue is through bioconversion using yeast. Certain yeasts and soybean lipases can break down the lipids in soybean residue, generating free fatty acids that can be partially metabolised via β-oxidation to create methyl ketones, secondary alcohols, esters, alkanes, and lactones [3]. Unwanted aldehydes can be oxidised by aldehyde dehydrogenases to form fatty acids or reduced by yeast alcohol dehydrogenases to form alcohols. Yeast alcohol acyltransferase can catalyse the reaction between alcohols and yeast metabolic intermediates to form esters. Yeast proteinases and peptidases can further decompose the proteins in soybean residue, and the resultant free amino acids can be metabolised by yeasts via the Ehrlich pathway to generate higher alcohols and esters [4].

Solid-state fermentation (SSF) of yeast on soybean residue has been demonstrated to enhance its nutritional quality. Fermentation leads to a rise in protein, ash, total polyphenolics, and antioxidant activity, whilst simultaneously reducing the raw fibre content, carbohydrates, and lipids. Furthermore, SSF promotes the bioconversion of isoflavones β-D-glucoside to aglycone forms via the action of β-glucosidases [5, 6].

Yeast fermentation may be employed to produce bio-flavours from soybean residue or to create a food ingredient with improved sensory characteristics. Dairy yeasts, owing to their enhanced lipolytic capability, typically metabolise the fat fraction of soybean residue into methyl ketones. Conversely, soybean residue fermented by wine yeasts contains a higher concentration of esters than that fermented by dairy yeasts [7].

Yarrowia lipolytica yeast was discovered to biotransform soybean residue by catabolising aldehydes and their metabolites mainly to methyl ketones. This resulted in a reduction in grassy, off-odour and a slightly pungent, musty, and cheese-like odour in the fermented soybean residue. The fermentation process yielded volatile aromatics, such as 3-methylbutanal and 2-phenylethanol, from amino acids. The fermented soybean residue exhibited increased levels of umami-tasting substances, a cheese-like odour, improved digestibility, and enhanced antioxidant capacity [8].

*Corresponding author: Email: mtvanh@uneti.edu.vn; maichipbong@gmail.com

According to research, the synergy of carbohydrase from Celluclast® 1.5L and Viscozyme® L with protease from *Y. lipolytica* resulted in soybean residue with elevated antioxidant activity and higher concentrations of total amino acids and ferulic acid post-fermentation. The interaction between carbohydrase and *Y. lipolytica* disrupted the secondary cell wall of the soybean residue, which may elucidate these findings [9].

S. cerevisiae var. boulardii is acknowledged as a probiotic and a vital constituent in producing biologically active substances through fermentation. This yeast strain aids in the synthesis of active phytochemicals, such as isoflavones [10] and phenolics [11], thus increasing the antioxidant capacity of the end product. Additionally, its utilisation enhances the bioavailability of essential minerals and B vitamins, whilst reducing the concentration of antinutrients like phytates [12]. The extracellular fraction of *S. boulardii* culture is enriched with polyphenolic metabolites, including vanillic acid, cinnamic acid, phenyl ethyl alcohol (rose oil), erythromycin, amphetamine, and vitamin B6. *S. boulardii* exhibits growth patterns comparable to *S. cerevisiae* but possesses greater stress tolerance. Moreover, *S. boulardii* comparatively produces 6-10 times more antioxidant potential, and 20-70 times higher total phenolics and flavonoids in the extracellular fraction [13].

Recently, there has been burgeoning interest in employing yeast to biosynthesise natural aromatic compounds from by-products, and yeast fermentation is regarded as a promising technique. Numerous yeasts have the ability to produce 2-phenylethanol (2-PE) from L-phenylalanine. 2-PE has varied applications in several industries, particularly in food and beverage, as it enhances the organoleptic properties of the final product [14].

In this study, four yeasts were evaluated for their growth and fermentation ability on soybean residue hydrolysed by protease and carbohydrase complexes. The study aimed to select a suitable yeast for producing fermented beverages from SRH.

2. Subject and methodology

2.1. Subject

Four yeasts were employed in this study, including *S. cerevisiae var. boulardii* CNCM I-745 as a yeast used for probiotic production activated from Bioflora (Biocodex, France); *S. cerevisiae* 7012 and *S. cerevisiae* 7028 as yeasts used in ethanol production obtained from the collection of School of Biotechnology and Food Technology, Hanoi University of Science and Technology; and *S. cerevisiae var. diastaticus* SafAle™ BE-134 as a dry yeast used in beer production obtained from Fermentis, France. These four yeast strains, *S. cerevisiae var. boulardii* CNCM I-745, *S. cerevisiae* 7012, *S. cerevisiae* 7028, and *S. cerevisiae var. diastaticus* SafAle™ BE-134, were marked as I-745, 7012, 7028, and BE-134, respectively.

SRH used in the study was prepared as follows: each soybean residue sample from Vinasoy Bac Ninh factory was autoclaved and mixed with water to achieve 5% w/w. The slurry was adjusted to pH 7.0 and hydrolysed with Alcalase® 2.4 L for 1 hour; further adjusted to pH 4.5 with H3PO4 10%, and hydrolysed with Viscozyme® L and Pectinex® Ultra SP-L for 3 hours [15]. The treated SRH was then supplemented with 2% w/w sucrose, boiled in water for 15 minutes and cooled to approximately 30°C before being inoculated with yeasts in sterile conditions.

The starter culture medium is 10°Brix malt, a 10% w/v of yeast extract, autoclaved at 121°C for 15 minutes. To prepare the secondary culture medium, pretreated SRH was centrifuged to remove the undissolved part, and the supernatant was autoclaved at 121°C for 15 minutes. The determination of yeast cell number and mass is discussed in a subsequent section.

2.2. Research methodology

Evaluation of growth ability of four yeasts on SRH: These strains, grown on malt-extracted agar, were inoculated with 10 ml of starter culture medium at 30°C for 24 hours. Then, 10 ml of inoculations with the same initial cell density were subcultured in 90 ml of secondary culture medium at 30°C for 48 hours. The number of yeast cells was determined every 2 hours using a Neubauer counting chamber.

Evaluation of fermentation ability of four yeasts on SRH: Four yeasts from malt-extracted agar were cultured in glass tubes containing 10 ml of starter culture medium at 30°C for 24 hours. Grade 1 seed was drawn up 1 ml into 9 ml of secondary medium for further propagation at 30°C for 24 hours. Ten ml of the secondary medium from each strain was transferred to a fermentation vessel containing 90 ml of SRH, to form a density of 6.7 log CFU yeast/ml. The amount of CO_2 released was determined based on the decreasing weight of the fermenter every 2 hours for 48 hours. Analysis was conducted both before and after 48 hours of fermentation for all four yeasts, including parameters such as: pH, acidity, total sugar content, soluble protein and soluble protein in TCA, phenolic content, antioxidant activity, alcohol content, composition of volatiles, and sensory analysis of flavour.

2.3. Analysis methodology

Analysis of total sugar: The analytical solution was completely hydrolysed in 2 hours with 25% HCl, then neutralised to pH 7.0 with 10% NaOH, titrated to the specified volume and then centrifuged to collect the supernatant before analysis. The reducing sugar content in the solution was determined by the DNS method through absorbance at 540 nm of the final product with DNS reagent using a D-glucose standard curve [16].

Analysis of soluble protein and soluble protein in TCA: The analytical solution was neutralised to pH 7.0 and centrifuged to collect the supernatant. The content of soluble protein or soluble protein in 20% (w/w) trichloroacetic acid (TCA) was determined by the Lowry method. The amount of protein in the sample was determined by the absorbance at 750 nm of the supernatant with Folin reagent using the BSA standard curve [17, 18].

Analysis of phenolic: The slurry was centrifuged to collect the supernatant, after which it was precipitated with absolute ethanol at a ratio of 1:1 to remove proteins. The phenolic content in the supernatant was determined by the Folin-Ciocalteu method through absorbance at 760 nm of the final product with the Folin-Ciocalteu reagent, using the gallic acid standard curve [19].

Analysis of ethanol: The slurry was centrifuged to collect the supernatant. Ethanol content was determined by the high-performance liquid chromatography (HPLC) method, using the HPLC system of Agilent Technologies 1200 series (Germany) with a Biorad 87H analytical column, RID detector.

Analysis of antioxidant capacity: 2,2-Diphenyl-1-picrylhydrazyl (DPPH) analysis was carried out to determine the changes in antioxidant activity before and after fermentation. The supernatant of the slurry was precipitated with absolute methanol at a ratio of 1:1 to remove proteins before analysis. The scavenging activity of the analysis sample could be assayed by measuring the decrease in absorbance at 517 nm of the stable free radical DPPH. The antioxidant content in the solution was expressed as mg ascorbic acid equivalent (mg AAE) per 100 ml [20, 21].

Analysis of volatiles: The slurry sample was extracted with ethyl acetate at a ratio of 1:1, then centrifuged to collect the supernatant. This supernatant was further filtered through a 0.2 µm membrane and analysed by GC-MS using a SCION 456-GC gas chromatograph (Netherlands). Based on the NIST 17 spectral library, containing information on retention time and mass spectrometry data, the presence of different volatiles in the analyte was determined. Semi-quantitative analysis was performed using peak areas on an equal amount of analytical samples [22]. The relative peak area (RPA) for each major group of volatiles was expressed as a percentage of the total peak areas of those compounds over the total peak area of all compounds.

Sensory evaluation: Comparison of the samples before and after fermentation was done by a scoring test according to Vietnamese Standard 3215-79 to determine the degree of aroma difference between samples. The sensory panel consisted of 10 members who had been trained. Each tester received one answer sheet and all samples to be evaluated. The tester would rate the aroma intensity of each product through a corresponding score on a 6-point scale with terms describing the intensity of that property already specified. The results were then statistically processed. Scores on the 6-point scale are: 0 - Odour of spoiled or odourless product; 1 - Strange odour; 2 - Less fragrant, beany odour; 3 - Weak aroma, very little beany odour; 4 - Light scent, relatively harmonious, slightly alcoholic smell; 5 - Mild aroma, smelling like fermented fruit, creating a feeling of liking.

Statistical analysis: The test of significance for experimental data was performed using one-way analysis of variance (One-Way ANOVA) and Tukey's test using SPSS® 22.0 software for Windows (SPSS Inc., Chicago, IL, USA) to evaluate any statistical differences between the treatments at $p \leq 0.05$.

3. Results

The growth and fermentation capabilities of four distinct yeast strains are shown in growth curves (Fig. 1), amount of CO_2 produced during 48 hours of fermentation (Fig. 2), composition of fermentation slurries (Table 1) and the changes in the major groups of volatiles in the slurries before and after fermentation (Table 2), as outlined below.

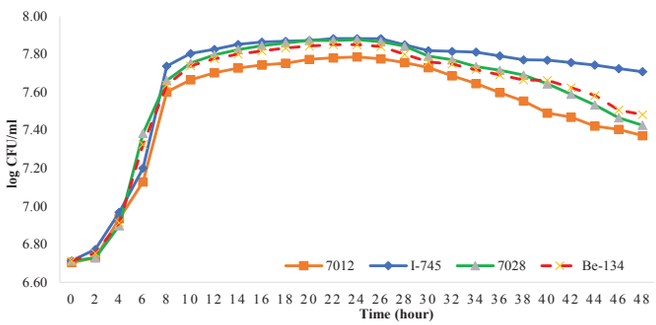

Fig. 1. Growth curves of the four yeast strains in pretreated SRH.

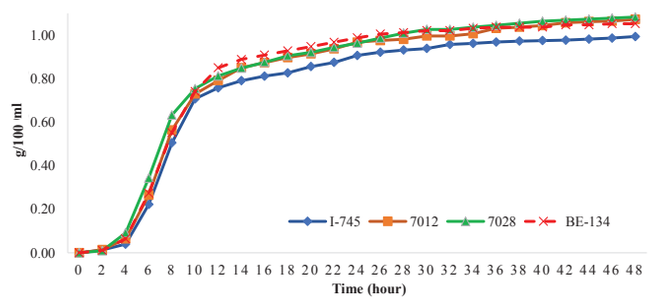

Fig. 2. Amount of CO_2 produced during 48 hours of fermentation by the four yeast strains.

Table 1. Composition of slurries before and after fermentation.

Analytical indicators	Before fermentation	After 48 hours of fermentation			
		I-745	*7012*	*7028*	*BE-134*
pH	$4.24^{a}\pm0.02$	$4.03^{b}\pm0.07$	$4.04^{b}\pm0.06$	$4.03^{b}\pm0.07$	$4.04^{b}\pm0.06$
Acidity (mg lactic/100 ml)	$385.9^{ab}\pm5.7$	$400.5^{a}\pm6.4$	$373.5^{b}\pm6.4$	$373.5^{b}\pm6.4$	$380.3^{b}\pm3.2$
°Brix	$5.25^{a}\pm0.07$	$3.15^{b}\pm0.07$	$3.00^{b}\pm0.14$	$3.00^{b}\pm0.14$	$3.05^{b}\pm0.07$
Total sugar (g/100 ml)	$4.70^{a}\pm0.04$	$2.29^{b}\pm0.04$	$2.16^{d}\pm0.02$	$2.20^{cd}\pm0.01$	$2.25^{bc}\pm0.01$
Ethanol (% v/v)	-	$1.23^{b}\pm0.07$	$1.39^{a}\pm0.03$	$1.25^{b}\pm0.07$	$1.36^{b}\pm0.02$
Soluble protein (mg/100 ml)	$617.7^{a}\pm11.8$	$451.3^{b}\pm16.6$	$468.3^{b}\pm20.7$	$465.0^{b}\pm23.0$	$459.3^{b}\pm21.5$
TCA-soluble protein (mg/100 ml)	$518.6^{a}\pm13.0$	$418.5^{b}\pm20.3$	$410.0^{b}\pm20.7$	$402.3^{b}\pm19.3$	$417.0^{b}\pm8.2$
Phenolic content (mg GAE/100 ml)	$31.10^{a}\pm2.31$	$30.08^{ab}\pm0.56$	$28.94^{b}\pm0.61$	$30.34^{ab}\pm0.87$	$31.60^{a}\pm1.83$
@ mgAAE/100 ml	$0.63^{c}\pm0.04$	$1.63^{b}\pm0.02$	$1.50^{a}\pm0.02$	$1.50^{a}\pm0.04$	$1.51^{a}\pm0.04$
Sensory score	$1.20^{d}\pm0.42$	$2.90^{c}\pm0.57$	$4.30^{a}\pm0.48$	$2.70^{c}\pm0.48$	$3.60^{b}\pm0.52$

$^{a, b, c, d}$: Statistical analysis using ANOVA at 95% confidence interval. Values with the same letter indicate no significant difference between the groups.
@ Antioxidant capacity measured using DPPH scavenging assay. Antioxidant capacity is expressed as mg ascorbic acid equivalent (AAE)/100 ml.

Table 2. Some volatiles in the slurries before and after 48 hours of fermentation.

No	Content	Before fermentation		After 48 hours of fermentation							
				I-745		7012		7028		BE-134	
		S peak x 10^7	*RPA (%)*	*S peak x 10^7*	*RPA (%)*	*S peak x 10^7*	*RPA (%)*	*S peak x 10^7*	*RPA (%)*	*S peak x 10^7*	*RPA (%)*
1	2,4-Decadienal, (E,E)-	25.6	2.5	ND	ND	ND	ND	ND	ND	ND	ND
2	E-14-Hexadecenal	45.3	4.4	ND	ND	ND	ND	ND	ND	ND	ND
3	Oleic acid	96.2	9.4	80.7	4.4	21.1	1.3	44.5	1.2	67.4	3.5
4	Octadecanoic acid	79.7	7.8	ND	ND	ND	ND	ND	ND	ND	ND
5	2-Phenylethanol	7.53	0.7	502	27.3	648	39.0	564	15.3	614	31.6
6	Octanoic acid, ethyl ester	7.01	0.7	17.5	1.0	15.3	0.9	18.1	0.5	15.9	0.8
7	Decanoic acid, ethyl ester	ND	ND	10.5	0.6	12.5	0.9	12.5	0.3	14.6	0.8
8	Hexadecenoic acid, ethyl ester	ND	ND	68.8	3.7	52.7	3.2	64.2	1.7	63.1	3.3
9	Decanoic acid, 2-phenylethyl ester	ND	ND	9.58	0.5	6.02	0.4	12.6	0.3	12.3	0.6
10	Linoleic acid ethyl ester	ND	ND	137	7.4	63.0	3.8	93.3	2.5	117	6.0

ND: not detected.

4. Discussion

4.1. Evaluation of the growing ability of yeasts

The results in Fig. 1 demonstrate that, with the same initial cell density, all yeast strains grow well on the slurries. In this, the cell density increased from hour 2 to hour 10, then stabilised from hour 10 to hour 24 and began decreasing gradually from hour 26. All yeasts increased in density 10-12 times (from 6.7 to 7.8 log CFU/ml). I-745 is the yeast with the highest cell density in the fermentation broth. In the first 6 hours of culture, the density of this strain was equivalent to or even lower than the other 3 strains, but from the 8th hour, this strain increased in biomass very quickly and consistently reached the highest cell density until the end of fermentation. This result is consistent with the findings of Joaquín Mulero-Cerezo, et al. (2019) [23]. Thus, yeast strain I-745 is a probiotic that can grow well and maintain a large cell density in the SRH. High yeast growth is advantageous since our purpose aimed to create probiotic drinks from the SRH.

4.2. Evaluation of the fermentation ability of yeasts

The results in Fig. 2 show that, with the same cell density at hour 0, all yeasts have fermented well on the enzymatically treated slurries. Three yeast strains 7012, 7028 and BE-134 released almost the same amount of CO_2. I-745 has the highest cell density in the fermentation broth but the amount of CO_2 released by this yeast is the lowest.

The results in Table 1 demonstrate that although the pH of the post-fermentation slurries has not been reduced compared to that of the pre-fermentation, the acidity of the post-fermentation slurries has not changed substantially. The fermented slurry from I-745 has the highest fermentation acidity at 400.5 mg/100 ml.

After 48 hours of fermentation, all 4 yeast strains reduced the soluble dry matter content of the slurries from about 5 to 3°Brix. The total sugar content after fermentation differed; the remaining total sugar after fermentation by 7012 was the lowest, and was the highest remaining by I-745. The ethanol content generated by the four yeasts after 48 hours of fermentation fluctuated in the range of 1.23-1.39% v/v. In which 7012 produced the most, I-745 produced the least ethanol among the four strains. Due to the characteristics of a probiotic strain, *S. boulardii* CNCM I-745 tends to generate biomass mainly and does not favour the production of alcohol. Thus, 7012 was the best fermenting strain among the four yeast strains with the lowest residual sugar of 2.16 g/100 ml and the highest amount of ethanol generated at 1.39% v/v.

Soluble protein contents were significantly reduced after fermentation in all samples; this is due to the proteolytic activity of yeasts [24]. The contents of TCA-soluble protein also decreased after fermentation but still a certain amount of about >400 mg/100 ml (varied by each strain). This amount was quite close to the amount of soluble protein. Thus, it can be confirmed that soluble proteins are mainly short-chain peptides and amino acids. These differences were not significant among strains after 48 hour of fermentation.

The phenolic content of the samples did not increase after fermentation; even some samples decreased slightly compared to before fermentation. According to W.C. Vong, et al. (2019) [25], some phenolics metabolised during fermentation may be reduced or produced. Therefore, this amount changes without a specific rule and needs further research, but the reduction is insignificant, and after fermentation, there was still a certain amount of phenolics in the slurries.

The antioxidant capacity after fermentation of all four yeasts increased compared to the unfermented slurry. In the fermented slurries, there were certain amounts of short-chain peptides and certain contents of phenolics; these components contributed to the antioxidant capacity of the slurries. In addition, yeast cells themselves have also been recognised as a source of antioxidants.

Yeast has the ability to synthesise a number of biologically active compounds that can act as antioxidants such as glutathione [26], coenzyme Q or ubiquinone [27], carotenoids, etc. Some products metabolised by yeast after fermentation, some substances in cell components such as soluble proteins, sulphur-containing amino acids, β-glucan in yeast cell walls... also contribute to the ability to create this antioxidant ability [28]. The fermented slurries of I-745 exhibited the highest antioxidant activity. The antioxidant activity of *S. boulardii* higher than that of S. cerevisiae has also been reported by some authors [23, 29].

In terms of organoleptic quality, all yeasts showed a significant improvement in the aroma of the slurry compared to before fermentation, and the differences were statistically significant. The fermentation sample using 7012 was evaluated as the best aroma sample among the four yeasts with a sensory score of 4.3/5 points. The fermentation slurry has a light aroma, similar to that of fermented rice, relatively harmonious, with a slight alcohol smell.

4.3. Changing of volatile compounds after 48 hours fermentation of four yeasts

The results in Table 2 show that the hydrolysate slurry before fermentation still contains some undesirable odorous components, which are aldehydes that cause unpleasant odours such as 2,4-Decadienal, (E,E), E-14-Hexadecenal. But after fermentation, the aldehyde components were completely lost. This result is consistent with the report of W.C. Vong, et al. (2016) [8], in fresh soybean residue, volatile components are mainly aldehydes, these substances tend to decrease during heat treatment and fermentation.

The SRH also contained a large number of fatty acids such as oleic, octadecanoic, which were fatty acids available in the raw materials. Fatty acids tended to be completely or partially reduced in the post-fermentation slurry depending on the yeast strain, the most in the fermentation slurry of strain 7012 and the least in that of I-745.

The fermentation products by four yeasts contained several higher alcohols, typically 2-phenylethanol and esters. The results in Table 2 show that the composition of esters produced by the fermenting strains varied depending on the strain. The total amount was about 5.3-13.2% of the total volatile matter in the fermentation solution. I-745 was the most ester-producing strain of the four yeast strains.

2-phenylethanol was significantly high in the aroma spectrum of all strains, accounting for about 27.3-39.0% depending on the yeast strain, so this component greatly affected the sensory value of the fermentation slurries. Currently, this compound is considered to be very valuable and is being exploited through the biosynthetic pathway by yeast fermentation. Many yeasts, especially *S. cerevisiae*, are capable of producing 2-phenylethanol using L-Phe as a precursor [14]. The SRH slurry contained a lot of amino acid components, under the action of yeast, it produced volatile aromatic compounds in which 2-phenylethanol accounted for a very high proportion. The 7012 strains had the highest 2-phenylethanol content in the fermentation slurry. This result was consistent with the sensory evaluation results.

5. Conclusions

The experimental results above demonstrate that all four yeast strains thrived and fermented effectively on the SRH. Among them, *S. cerevisiae* 7012 was the best fermenting yeast, with residual sugar at only 2.16 g/100 ml, an ethanol content of 1.39% v/v, and the most appealing aroma, achieving a sensory score of 4.3/5 points. Within this aroma, the aromatic compound 2-phenylethanol accounted for the highest proportion. Conversely, the probiotic *S. boulardii* CNCM I-745 exhibited the most robust biomass production ability, achieving a cell density of 7.71 log CFU/ml after 48 hours, and the fermentation solution possessed the highest antioxidant activity, equivalent to 1.63 mg of ascorbic acid per 100 ml. Consequently, these two yeast strains were selected to be used in tandem for fermentation, capitalising on the probiotic properties of *S. boulardii* CNCM I-745 and the flavouring capacity of *S. cerevisiae* 7012 for fermented beverages derived from SRH.

CRediT author statement

Thi Van Anh Mai: Collected data and Wrote the paper; Kim Loan Nguyen and Dinh Trien Dang: Co-authors who collected a part of data; Thi Xuan Sam Nguyen and Thanh Hang Nguyen: Co-authors who provided research guidance.

COMPETING INTERESTS

The authors declare that there is no conflict of interest regarding the publication of this paper.

REFERENCES

[1] S. Li, D. Zhu, K. Li, et al. (2013), "Soybean curd residue: Composition, utilization, and related limiting factors", *ISRN Industrial Engineering*, **2013**, pp.1-8, DOI: 10.1155/2013/423590.

[2] W.C. Vong, S.Q. Liu (2016a), "Biovalorisation of okara (soybean residue) for food and nutrition", *Trends in Food Science & Technology*, **52**, pp.139-147, DOI: 10.1016/j.tifs.2016.04.011.

[3] Y.F. Collins, P.L.H. McSweeney, M.G. Wilkinson (2003), "Lipolysis and free fatty acid catabolism in cheese: A review of current knowledge", *International Dairy Journal*, **13(11)**, pp.841-866, DOI: 10.1016/S0958-6946(03)00109-2.

[4] L.M. Sørensen, K. Gori, M.A. Petersen, et al. (2011), "Flavour compound production by Yarrowia lipolytica, Saccharomyces cerevisiae and Debaryomyces hansenii in a cheese-surface model", *International Dairy Journal*, **21(12)**, pp.970-978, DOI: 10.1016/j.idairyj.2011.06.005.

[5] M.M. Rashad, E.A. Mahmoud, M.H. Abdou, et al. (2011), "Improvement of nutritional quality and antioxidant activities of yeast fermented soybean curd residue", *African Journal of Biotechnology*, **10(30)**, pp.5750-5759, DOI: 10.5897/ajb10.1658.

[6] V.A. Queiroz Santos, C.G. Nascimento, C.A.P. Schimidt, et al. (2018), "Solid-state fermentation of soybean okara: Isoflavones biotransformation, antioxidant activity and enhancement of nutritional quality", *LWT*, **92**, pp.509-515, DOI: 10.1016/j.lwt.2018.02.067.

[7] W.C. Vong, S.Q. Liu (2016b), "Changes in volatile profile of soybean residue (okara) upon solid-state fermentation by yeasts", *J. Sci. Food Agric.*, **97(1)**, pp.135-143, DOI: 10.1002/jsfa.7700.

[8] W.C. Vong, K.L. Au Yang, S.Q. Liu (2016c), "Okara (Soybean residue) biotransformation by yeast *Yarrowia lipolytica*", *Int. J. Food Microbiol.*, **235**, pp.1-9, DOI: 10.1016/j.ijfoodmicro.2016.06.039.

[9] W.C. Vong, X.Y. Lim, S.Q. Liu (2017), "Biotransformation with cellulase, hemicellulase and *Yarrowia lipolytica* boosts health benefits of okara", *Appl. Microbiol. Biotechnol.*, **101**, pp.7129-7140, DOI: 10.1007/s00253-017-8431-1.

[10] C.R. Rekha, G. Vijayalakshmi (2010), "Bioconversion of isoflavone glycosides to aglycones, mineral bioavailability and vitamin B complex in fermented soymilk by probiotic bacteria and yeast", *Journal of Applied Microbiology*, **109(4)**, pp.1198-1208, DOI: 10.1111/j.1365-2672.2010.04745.x.

[11] Nurcan Degirmencioglu, Ozan Gurbuz, Yasemin Sahan (2016), "The monitoring, via an *in vitro* digestion system, of the bioactive content of vegetable juice fermented with Saccharomyces cerevisiae and Saccharomyces boulardii", *Journal of Food Processing and Preservation*, **40(4)**, pp.798-811.

[12] S.C. Chandrasekar Rajendran, Bhawani Chamlagain, Susanna Kariluoto, et al. (2017), "Biofortification of riboflavin and folate in idli batter, based on fermented cereal and pulse, by Lactococcus lactis N8 and Saccharomyces boulardii SAA655", *Journal of Applied Microbiology*, **122(6)**, pp.1663-1671, DOI: 10.1111/jam.13453.

[13] M.A. Lazo Velez, S.O. Serna Saldivar, M.F. Rosales-Medina, et al. (2018), "Application of Saccharomyces cerevisiae var. boulardii in food processing: A review", *Journal of Applied Microbiology*, **125(4)**, pp.943-951, DOI: 10.1111/jam.14037.

[14] Sara Mitri, Mohamed Koubaa, R.G Maroun, et al. (2022), "Bioproduction of 2-phenylethanol through yeast fermentation on synthetic media and on agro-industrial waste and by-products: A review", *Foods*, **11(1)**, DOI: 10.3390/foods11010109.

[15] M.T.V. Anh, N.T.X. Sam, N.K. Loan, et al. (2022), "Studying on using Viscozyme® L and Pectinex® Ultra SP-L to increase efficiency of soy bean curd residue digestion", *Agriculture & Rural Development*, **15(1)**, pp.41-48 (in Vietnamese).

[16] Gail Lorenz Miller (1959), "Use of dinitrosalicylic acid reagent for determination of reducing sugar", *Analytical Chemistry*, **31(3)**, pp.426-428, DOI: 10.1021/ac60147a030.

[17] O.H. Lowry, N.J. Rosebrough, A. Lewis Farr, et al. (1951), "Protein measurement with the Folin phenol reagent", *Journal of Biological Chemistry*, **193(1)**, pp.265-275, DOI: 10.1016/S0021-9258(19)52451-6.

[18] J. H. Waterborg, H. R. Matthews (1984), "The Lowry method for protein quantitation", *Methods in Molecular Biology*, **1**, pp.1-3, DOI: 10.1385/0-89603-062-8:1.

[19] A.L. Waterhouse (2002), "Determination of total phenolics", *Current Protocols in Food Analytical Chemistry*, **6(1)**, pp.11-18, DOI: 10.1002/0471142913.fai0101s06.

[20] W.B. Williams, M.E. Cuvelier, C.L.W.T. Berset (1995), "Use of a free radical method to evaluate antioxidant activity", *LWT-Food Science and Technology*, **28(1)**, pp.25-30, DOI: 10.1016/S0023-6438(95)80008-5.

[21] Jiafei Tang, F.R. Dunshea, H.A.R. Suleria (2019), "LC-ESI-QTOF/MS characterization of phenolic compounds from medicinal plants (hops and juniper berries) and their antioxidant activity", *Foods*, **9(1)**, DOI: 10.3390/foods9010007.

[22] Victoria Ruiz-Hernández, María José Roca, Marcos Egea-Cortines, et al. (2018), "A comparison of semi-quantitative methods suitable for establishing volatile profiles", *Plant Methods*, **14**, pp.1-15, DOI: 10.1186/s13007-018-0335-2.

[23] Joaquín Mulero-Cerezo, Álvaro Briz-Redón, Ángel Serrano-Aroca (2019), "*Saccharomyces cerevisiae var. boulardii:* Valuable probiotic starter for craft beer production", *Applied Sciences*, **9(16)**, DOI: 10.3390/app9163250.

[24] Y.P. Maturano, L.A.R. Assaf, M.E. Toro, et al. (2012), "Multi-enzyme production by pure and mixed cultures of *Saccharomyces* and non-*Saccharomyces* yeasts during wine fermentation", *International Journal of Food Microbiology*, **155(1-2)**, pp.43-45, DOI: 10.1016/j.ijfoodmicro.2012.01.015.

[25] W.C. Vong, S.Q. Liu (2019), "The effects of carbohydrase, probiotic *Lactobacillus paracasei* and yeast *Lindnera saturnus* on the composition of a novel okara (soybean residue) functional beverage", *LWT*, **100**, pp.196-204, DOI: 10.1016/j.lwt.2018.10.059.

[26] D.W.S. Stephen, D.J. Jamieson (1996), "Glutathione is an important antioxidant molecule in the yeast *Saccharomyces cerevisiae*", *FEMS Microbiology Letters*, **141(2-3)**, pp.207-212, DOI: 10.1016/0378-1097(96)00223-6.

[27] Isabel González-Mariscal, Elena García-Testón, Sergio Padilla, et al. (2014), "The regulation of coenzyme q biosynthesis in eukaryotic cells: All that yeast can tell us", *Molecular Syndromology*, **5(3-4)**, pp.107-118, DOI: 10.1159/000362897.

[28] C.A. Abbas (2006), "Production of antioxidants, aromas, colours, flavours, and vitamins by yeasts", *Yeasts in Food and Beverages*., **2**, pp.285-334, DOI: 10.1007/978-3-540-28398-0_10.

[29] Suprama Datta, D.J. Timson, U.S. Annapure (2017), "Antioxidant properties and global metabolite screening of the probiotic yeast *Saccharomyces cerevisiae* var. *boulardii*", *Journal of the Science of Food and Agriculture*, **97(9)**, pp.3039-3049, DOI: 10.1016/j.ijfoodmicro.2012.01.015.

General Instructions on using this template and submitting a manuscript to VJSTE: Thank you for preparing a manuscript for submission to VJSTE. Using this template, or following the guidelines below, will help us in processing your article.

The structure of different types of articles may vary according to the type of study, and the content of the article.

The following are the detailed main components of the original research and review articles submitted to the journal.

From 2023 onwards, you can submit your article at: https://mc04.manuscriptcentral.com/mostvjste

Original research

The original research should have three following parts:

Preliminary section: It includes title, list of all contributing authors with their institutional affiliation, and abstract (160-250 words) with at least 3 keywords.

Title: How to format a science article (replace with your real title)

Author(s): List the author name(s) separated by commas. Use superscript numbers to link affiliations, and symbols *†‡ for author notes. For example, Y. Obsie[1*], S.A. Adem[1, 2]

**Corresponding author(s):* Include the email addresses or telephone numbers of the corresponding author(s). Please use the asterisk (*) symbol for the corresponding author information. This information is at the bottom of the manuscript's first page.

Author's affiliation addresses:

[1]Affiliations should be preceded by superscript numbers corresponding to the author list

[2]For any institutions, please provide the institution name, street, district, city, country

Received ; revised ; accepted

Abstract:
Start your abstract here…
Keywords: **keyword 1, keyword 2, keyword 3…**
Classification number(s): **1.1, 3.4, 5.3, etc.**

Abstract: The abstract should range between 160 and 250 words and be structured in a single paragraph following keywords in a separate line. The abstract should represent the main part of the research manuscript. It should reflect a brief and comprehensive background following the aim of the study (main questions to be addressed), methods used for investigating the problem, a summary of significant findings, main conclusions, and implications of the results.

Keywords: They should come immediately after the abstract and contain 3-7 specific and relevant keywords. They should reflect the research study and the relevant field of research.

Classification numbers: Depend on the Journal's Classification Scheme.

Author(s) are encouraged to write a "Highlights" that summarises the most exciting, interesting points from your manuscript.

Manuscript section: It is the main body of the scientific manuscript including: 1) Introduction; 2) Material(s) and method(s); 3) Results and discussion (separation of these two sections is acceptable); 4) Conclusions; 5) Recommendations/Suggestions/Implications/Study limitations...(if any). These sections may slightly vary depending on the type of research approach and design used in the research. Each section should be numbered.

All of the Figures, Tables, and Equations should be cited in numerical order.

Figures

Fig. #: (Begin each figure caption with a label, "**Fig. 1.**" for example, as a new paragraph).

Fig. 1. The figure caption should begin with an overall descriptive statement of the figure followed by additional text. They should be immediately after each figure. Figure parts are indicated with capital letters **(A)**. If you prefer, you can place both the actual figures and captions logically through the text near where they are cited rather than at the end of the file (but not both). If a paragraph in the main text begins with the name of a figure, write out "Figure" in full (e.g., <para> "Figure 1 shows...").

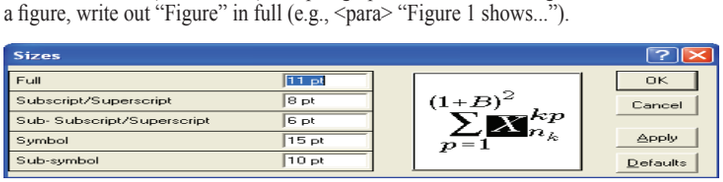

Fig. 1. The figure caption.

Tables

Table #: (Begin each table caption with a label "**Table 1.**", etc. as a new paragraph).

Table 1. Start this caption with a short description of your table. Format tables using the Word Table commands and structures. Do not create tables using spaces or tabs characters.

Table 1. Caption.

a	b	c	d	e
f				
g				
h				

Equations

$$\int_a^b xdx \tag{1}$$

Equations can be included. We do not recommend using the native Word 2007, 2008, 2010 or 2011 equation editor. This can in some cases produce less reliable MathML, the online markup language we use, which may result in display errors. Instead, use the legacy equation editor in Word (Insert menu; select insert object; select word equation) or use MathType (recommended). If you enter equations in simple LaTeX, check that they will convert accurately (Word 2007 and higher can convert simple LaTeX equations).

Closing section: It includes appendices/supplementary materials/data availability statement (if applicable), CRediT author statement (for multiple authors), acknowledgements (if applicable), competing interests, ethics (if any) and a complete list of references corresponding to all the citations given in the text of the manuscript. The appendices/supplementary materials may include data files and other material relevant to the research that should be submitted in separate files if required.

APPENDICES (if any)

The appendices should ideally be under 1000 words (approximately 2 A4 pages) for printing version. With longer appendices, they are only accepted for online publication.

CRediT author statement (for multiple authors)

CRediT offers authors the opportunity to share an accurate and detailed description of their diverse contributions to the published work.

ACKNOWLEDGEMENTS (if applicable)

This section is for the researchers who were funded for the research projects, and it should enclose all sources of financial support.

COMPETING INTERESTS

The author(s) declare(s) that there is no conflict of interest regarding the publication of this article.

REFERENCES

For in-text citation: References should be cited in the bracket with a number [1]. Multiple reference citations are separated by commas [2, 3] or if a series, dashes [4-6]. When citing sources with the author(s) and the year, they should be shortened to the first author's name, followed by et al. (with more than one author) and the year.

For reference list: With less than or equal to three authors, list all the author(s). With more than three authors, the first three should be listed and followed by et al.

References are listed in numerical order, and in the same order in which they are cited in text. The reference list should include all and only those references you have cited in the text. The reference list appears at the end of the article.

The reference consists of: Initial(s) and first/last name of the author(s), author' names separated by commas (Year of publication), "Titles of journal articles or chapter of book", *Title of Journal, Book or Other Publication*, **Volume(Number)** (if any), page numbers (if any), DOI (if any), URL and accessed date (if any) (in its original language if not English).

To cite a website and online/electronic resources, please include the accessed date (day month year).

Example of a reference list:

[1] T. Binzoni, T.S. Leung, D. Boggett, et al. (2003), "Non-invasive laser Doppler perfusion measurements of large tissue volumes and human skeletal muscle blood RMS velocity", *Phys. Med. Biol.*, **48(1)**, pp.2527-2549, DOI: 10.1088/0031-9155-48-15-318.

[2] H.W. Bischoff, H.C. Bold (1963), *Some Soil Algae from Enchanted Rock and Related Algal Species*, University of Texas Publications, 95pp.

[3] R. Busi (2016), "Weedy rice in the Philippines and Vietnam", https://www.aciar.gov.au/publication/technical-publications/weedy-rice-philippines-and-vietnam-final-report, accessed 15 July 2018.

Review articles

They should be different from the original research as they would contain different sections on the literature review. Authors may structure this part as per nature, background, and available literature on the issue argued in the manuscript.

For more detailed instructions, please visit our website: vietnamscience.vn or vietnamscience.vjst.vn

This manuscript template has been used from 2021 onwards.

P-ISSN 2525-2461 • E-ISSN 2615-9937

Vietnam Journal of Science, Technology and Engineering

SEPTEMBER 2023 • VOLUME 65 NUMBER 3

EDITORIAL BOARD

EDITORIAL OFFICE

113 Tran Duy Hung Str., Cau Giay Dist., Hanoi, Vietnam

Tel: (84.24) 39436793; Fax: (84.24) 39436794

Email: vjste@most.gov.vn

Website: vietnamscience.vn or vietnamscience.vjst.vn

PUBLICATION LICENCE

No. 459/GP-BTTTT 20th July 2021

No. 50/GP-BTTTT 1st February 2023